
THE UNIVERSITY *of* EDINBURGH

# Measuring Dark Neutrinos and Light Using External and Internal Components of LArTPCs

Li Jiaoyang

李 娇瑒


Doctor of Philosophy
The University of Edinburgh
September 2024

# Abstract

The so-called MiniBooNE low-energy excess has been a long-standing question for beyond Standard Model (BSM) physics in the neutrino field. The Short Baseline Neutrino (SBN) program was proposed to investigate and provide further insights into this excess. The SBN program utilises Liquid Argon Time Projection Chamber (LArTPC) technology, which allows for precise measurements of neutrino interactions and holds great potential for addressing significant open questions in the field. Within the SBN program, the Short Baseline Near Detector (SBND) plays a crucial role as one of the near detector, positioned just 110 meters from the neutrino source. Being located on the surface, SBND is exposed to cosmic-ray background, and to mitigate this, the Cosmic Ray Tagger (CRT) system has been implemented to identify and veto cosmic background events, thereby enhancing the purity of neutrino interactions. Additionally, the CRT system can be used to search for BSM signatures, such as the dark neutrinos, which have been proposed to explain the MiniBooNE low-energy excess. This thesis presents a novel approach for searching for dark neutrinos using existing SBND CRT data, collected with a unique setup called the CRT Beam Telescope. An extended model-independent search based on the dark neutrino analysis is also presented. The sensitivity plot for the CRT Beam Telescope is compared with an estimated MiniBooNE exclusion limit. Furthermore, this thesis covers the commissioning work conducted for the SBND CRT system, which is vital for ensuring optimal performance. The LArTPC technology also benefits from liquid argon's excellent scintillation properties, producing abundant scintillation light. This thesis describes a method developed to understand the detector response to the scintillation light produced across the LArTPC, enhancing our understanding of the detector's performance and facilitating more accurate measurements.

# Lay Summary

Particle physics is driven by humanity's deep curiosity about the universe, as scientists seek to expand our understanding of elementary particles and their interactions. Among these particles, neutrinos are perhaps the most intriguing. Proposed by Wolfgang Pauli in 1930 as a *"desperate remedy"* to account for missing energy in radioactive decay, neutrinos are often called "ghost particles" because they interact with matter only through the weak force, making them extremely elusive. For a long time, scientists even believed neutrinos could never be detected, adding to their mysterious nature.

Today, neutrino detection and measurement are among the most active areas of research in particle physics, with precision measurements being the ultimate goal. Despite significant progress over the years, many questions about neutrinos remain unanswered, leaving much to explore in this fascinating field. One notable anomaly observed in neutrino experiments is the so-called "low-energy excess", first detected by the Liquid Scintillator Neutrino Detector at Los Alamos National Laboratory, USA, and later confirmed by the MiniBooNE experiment at Fermi National Accelerator Laboratory (Fermilab), USA. Both experiments observed an unexpected excess of low-energy events that could not be explained by our current understanding of physics.

Motivated by the "low-energy excess", the Short-Baseline Neutrino program was proposed to be built at Fermilab to further investigate this anomaly. Three experiments were built: the Short-Baseline Near Detector (SBND), the intermediate detector MicroBooNE, and the far detector ICARUS. Modern particle detectors are complex, comprising multiple systems to achieve precision measurements to the maximum. However, even individual parts of these systems can lead to interesting discoveries. This thesis will focus on two specific systems: the Cosmic Ray Tagger (CRT) in SBND and the Photon Detection system in MicroBooNE.

The work conducted on SBND focuses on a new model proposed to explain the ”low-energy excess”, known as the dark neutrino. This new particle is sought using an innovative approach that relies solely on the CRT system of the detector. This thesis presents a sensitivity plot for this unique detector setup and model for the first time. The hands-on work involved in commissioning the CRT system will also be presented in this thesis.

The work carried out on the MicroBooNE detector focuses on measuring one of its key signals: scintillation light. By using isolated point-like proton tracks, we can map how the detector responds to this light and test the various physics assumptions made in our simulations.

# Declaration

I declare that this thesis was composed by myself, that the work contained herein is my own except where explicitly stated otherwise in the text, and that this work has not been submitted for any other degree or professional qualification except as specified.

(*Li Jiaoyang, September 2024*)

# Acknowledgements

The strongest motivation behind my journey into physics originated from my innate instinct to rebel against stereotypes of women. Despite not always feeling like the smartest in the field, my stubbornness has consistently encouraged me to continue my journey without quitting thus far. Furthermore, without the love, help, and support from so many people throughout this journey, I would not be the person whom I am today. Although I do not have the page length to name everyone, I express my deepest gratitude and would like to say to all of you, "Thank you very much!"

First and foremost, I would like to thank my dearest supervisor, Andrzej. Thank you for your endless kindness, starting from my time as a summer student and later welcoming me back as a PhD student after I ventured into a different field. I am immensely grateful for your support in securing funding for an international PhD student with such trust. I also want to thank you for teaching me how to become a decent researcher and for setting a great example of what a great supervisor should be like. Without you, my academic journey would not have had such an amazing start, and I hope that if I continue on this career path, I will be as good a supervisor as you are. I also want to thank you for the freedom you have given me and for connecting me with other excellent collaborators during my PhD. Lastly, boss, I value all the conversations I've had with you about research and life, and I hope we will have many more in the future.

I would also like to thank my amazing group in Edinburgh and Manchester. It was a pleasure to work with you all. I wish you all the best in the future. I want to give a special thanks to Patrick for setting a great example of what it means to be a PhD student. It has been a pleasure to work with you and to hang out with you and others whenever we met in person. And Marina, thank you for including me in the many activities you organised during and after the pandemic, which made me feel less alone. Thank you for being a good friend to me!

I started my PhD during the pandemic, joining the wonderful MicroBooNE collaboration, where I met so many brilliant people and friends. Thank you, David, for being my first collaborator. I hope working with a newbie like me was not too awful. I truly appreciate your guidance throughout the project and your help in preparing my first collaboration presentation; it meant a lot to me. Thank you, Vincent, for being a good friend and an amazing convenor. I am grateful for our friendship, and thank you for convincing me to stay at Fermilab. Anyssa, sometimes friendships just happen for no reason. The many crazy things we have done together, without any regrets, feel like a miracle to me. We keep saying we will work together one day, but it has not happened yet. Possibilities always lie in the future.

The second part of my PhD gifted me a fantastic team to work with on the SBND CRT Beam Telescope. Thank you, Ornella, for being such a great mentor; my discussions with you about physics are always enjoyable, and I have learned so much from you. Thank you so much for always have faith in me, even when I sometimes don't trust myself! Marco, it was amazing to work with you on my thesis analysis. You have been my go-to person for all my questions for such a long time, and I look forward to continuing our collaboration during my postdoc. I hope to one day be as good as you. Kevin and Pedro, I am incredibly grateful for our collaboration and all the discussions we have had over the past few years. Thank you so much for saving my analysis in the most unexpected way. I truly appreciate it!

During my PhD, I was incredibly lucky to have the opportunity to work closely with my another fantastic experiment, SBND. All my hardware skills were developed while working with the CRT commissioning, and I am grateful for such good companionship with the CRT team! Michelle, I cannot express how much I enjoy working with you and how fortunate I feel to have learned so much from you. I appreciate you as a mentor, and I am thankful for the trust you placed in me from day one, even when I had no experience with hardware at all! I am forever grateful for all our conversations and the opportunities you provided when I wanted to step away from the computer. I look forward to continuing to work with you in the future, if possible!

Working on SBND without all my dearest friends would never be the same. Thank you so much for making physics and research a lot less painful. I love you all so much, pals! Lynn, Mun, Lane, and Bear, I cherish all the small trips we took together with others. Thank you for making America start to feel like home to me. Lan, thank you for always joining me in complaining about various things. I hope to see you soon; if not in Chicago, I will come to California—not for the Sequoias, but for you! Rodrigo, thank you for making my second visit to Fermilab so lovely. Living with you was so much fun and I appreciate all hugs when I felt down. I wish you all the best for your next stage of your life! A special thank goes to Henry! I feel super lucky to have you as a friend; the almost year living with you in 15 Pot was a blast. So many things would never have happened without you. Thank you for everything pal! I hope I will see you in the very near future.

I want to thank all my friends in Edinburgh. André, thank you so much for joining me for my first Céilidh dance. The friendship that grew from our awkward dance was an amazing gift. I appreciate all the coffee breaks/dinners/pubs we had when I was in Edinburgh and the various video calls while I was in the US. I wish you all the best in Germany. Anh and Han, thank you for always providing me with a place to stay whenever I return to Edinburgh temporarily. Han, I am grateful for all the fun activities you organised with me and also for bringing Cabbage into my life. Anh, thank you for being such a great friend. Although we didn't overlap much during our PhD (sadly!), we share so much in common, and I cherish all our late-night conversations. Pal, I hope you find the goal of your next stage in your life soon, and remember there will always be a home for you in Chicago whenever you want.

I want to thank all lovely people I met at Fermilab. Thank you, Namitha, for always bringing fun and smile into my life. Thank you, Adam, for providing me with great advice when I felt lost. Thank you, Annie, for always believing in me and for the kind words you always said to me.

我想感谢我在曼城的所有朋友，特别是老猫。谢谢你在疫情期间的陪伴，和你在一起做饭，聊天，打游戏，旅游都令我非常开心！我非常感激有你这个的朋友！虽然不知道以后我们会在哪里见面，但无论如何，希望我们经常联系，经常见面！祝你未来一切顺利！

睿宁，谢谢你从本科开始就成为我非常好的朋友。我非常非常开心能在美国和你再次重逢，和你一起在加州一起旅游让我非常快乐。谢谢你在疫情期间和我线上打电话一起学习，一起看电影陪伴彼此。虽然和你在国外见面以后可能会变得比较困难，但我希望我能早日在国内见到你！祝你万事胜意！

Thank you, Edinburgh, for providing me with ultimate fun during my time here. I now consider you home and hope to find a way to come back to you in the future.

I never would have thought I could be this incredibly lucky to get to know a brilliant person, a great collaborator, my best friend, and a partner beyond my imagination. Fran, thank you for hugging me when I was feeling extremely down and for holding my hand as we faced all the challenges of our PhD together. Thank you for always being by my side through both the ups and downs. It took a lot of courage to decide to move across the ocean with me, and I am super grateful for that. Fran, I can never thank you enough; just you being yourself makes me feel truly lucky.

最后的最后，我想感谢我的家人，谢谢你们对我的所有的爱和支持。谢谢我的妈妈和爸爸，谢谢你们所有的无条件的爱。谢谢爸爸，你为这个家庭所奉献的一切，虽然成长的道路上你不常物理上地陪伴在我的左右，但我从来没有觉得你的爱和你的教育缺席过。爸爸，谢谢你让我可以坦荡地说爱你和妈妈。谢谢妈妈从小到大对我无微不至的照顾，没有你就不会有今天的我。我会永远记得冬天下大雪的时候你在电动车前面为我挡雪接送我上下学的背影。爸爸妈妈，如果你们的前半辈子有很多时候都是为了我在拼搏，我希望从今天开始，你们可以自由肆意地为你们自己而活。我爱你们！我将这篇论文致敬给你们。

阿公阿婆，我希望你们也能看到这篇论文，我非常非常地想你们。

*To my parents and all the fighters for feminism throughout history,*

*without you, I would not be here pursuing a PhD.*

*May a future with true gender equality, where everyone has power over themselves.*

# Contents

# 1

# Introduction

The Standard Model (SM) of particle physics represents our best understanding of the universe at the microscopic scale. It is a mathematical framework that unifies the description of all observed particles, including the origin of their mass through the Higgs field, and their interactions via three fundamental forces: the strong, electromagnetic, and weak forces, with the exclusion of gravity.

Among the particles included in the SM, neutrinos are arguably the most intriguing. Despite being the second most abundant particles in the universe after photons, they interact only weakly with matter. This challenge in detection has not deterred humankind's drive to understand them. Over the past few decades, numerous experiments have been dedicated to studying these "ghost" particles from various natural and man-made sources. Our journey has progressed from the discovery of neutrinos to identifying the three known types of light active neutrinos—electron, muon, and tau neutrinos—and observing neutrino oscillations. These measurements have provided profound insights into these particles, which were initially thought to be undetectable.

Neutrino detection relies on reconstructing the charged daughter particles resulting from neutrino interactions. As our understanding of neutrinos deepens with the experimental measurements, new questions challenge the completeness of the SM. These include the potential CP violation in the lepton sector, which could help explain the matter-antimatter asymmetry in the universe; the origin of neutrino masses, which are not predicted by the SM; and the question of neutrino mass ordering. Additionally, various experimental anomalies have further added more questions. One of the most famous anomalies is the low-energy excess (LEE) observed in the LSND and confirmed by MiniBooNE experiments.

Motivated by the LEE anomalies, the Short-Baseline Neutrino (SBN) program was proposed to address these issues definitively. The SBN program consists of three detectors: the Short-Baseline Near Detector (SBND), the intermediate detector Micro Booster Neutrino Experiment (MicroBooNE), and the far detector Imaging Cosmic And Rare Underground Signals (ICARUS) T600. This thesis will focus on the SBND and MicroBooNE experiments. All three detectors use LArTPC technology, which provides millimeter-level spatial resolution and excellent calorimetry, enabling precise measurements of neutrinos. The MicroBooNE detector was the first constructed within the SBN program and initiated the search for the LEE. However, no excess has been observed in their search channels to date. New theoretical models are needed to explain the anomaly. The dark neutrino model is one such proposal to explain the MiniBooNE anomaly. This thesis will discuss the search for dark neutrinos and explore a model-independent approach, with a particular focus on a subset system of SBND.

Scintillators have been widely used throughout the history of particle detection as a medium to convert the energy deposited by particles into detectable signals. The usage of Polystyrene as a scintillator dates back to the early 1950s and remains a popular choice for efficiently tagging charged particles. Liquid argon is another excellent scintillator that effectively converts deposited energy into scintillation light. Due to its superior scintillation properties and the potential for secondary ionised electron signals, liquid argon time projection chamber (LArTPC) technology has become a preferred choice for accelerator-based neutrino beam experiments at Fermi National Accelerator Laboratory (Fermilab) in the United States.

Modern particle detectors, such as LArTPC detectors are generally complex, making an understanding of their performance crucial. Scintillation light is one of primary signals in LArTPC detectors and is commonly used to trigger in neutrino experiments. This thesis introduces a position-dependent light yield measurement to study photon detection behaviour in LArTPC detectors.

The thesis will be structured as follows:

**Chapter 2** reviews the history and properties of Standard Model neutrinos, highlighting key discoveries and ongoing challenges. It introduces the dark neutrino model proposed to explain the MiniBooNE low-energy excess and discusses the theory, constraints, and decay of dark neutrinos. Additionally, it explores a model-independent search approach, outlining its framework and providing an example constraint.

**Chapter 3** will give an overview of particle interactions in scintillators, with a focus on both polystyrene and liquid argon. It will discuss the conversion of scintillation light into ionised charge in liquid argon and the physics processes that can affect the propagation of both light and charge.

**Chapter 4** will provide an overview of the SBN program at Fermilab, detailing its objectives and components. It will discuss the production of neutrino beams and the technology behind LArTPC detectors. Additionally, the chapter will offer a description of the detectors relevant to analyses presented in this thesis: the SBND detector and the MicroBooNE detector.

**Chapter 5** provides an overview of simulation and reconstruction workflow in LArTPC detectors.

**Chapter 6** introduces a novel method for measuring position-dependent light yield in the MicroBooNE detector.

**Chapter 7** will describe the Cosmic Ray Tagger (CRT) system in the SBND. It will cover both the design and hardware readouts of the CRT system. Additionally, the chapter will introduce the CRT-only setup, known as the CRT Beam Telescope, and discuss the data collection associated with this setup.

**Chapter 8** will detail the commissioning work on the CRT system undertaken by the author for the SBND detector.

**Chapter 9** discusses the simulation and reconstruction processes, highlighting the improvements made by the author to the CRT system in SBND. It focuses particularly on the CRT-only setup: the Beam Telescope detector.

**Chapter 10** will present a search for dark neutrinos using the signature of $e^+e^-$ in the SBND CRT Beam Telescope.

**Chapter 11** will introduce a model-independent search approach based on the results obtained from the dark neutrino.

# 2

# Neutrinos, Dark Neutrinos and Beyond

> *"... I have hit upon a desperate remedy to save the 'exchange theorem' (1) of statistics and the law of conservation of energy. ..." [1]*
>
> – W. Pauli

The amazing story of neutrinos began with a letter written by Pauli for a nuclear physics conference in Tübingen, Germany, on December 4, 1930 [1]. Pauli proposed the idea of neutrinos as a *desperate remedy* for energy conservation in beta decay. Starting from a mere theoretical concept of an undetectable particle, neutrinos are now known as the second-most abundant particles in the universe after photons. The journey to understand neutrinos and the physics effects that involve them has been full of surprises, and many questions in the field still remain unanswered.

Starting with a brief introduction to the Standard Model (SM), this chapter further outlines the physics of SM neutrinos and introduces the concept of dark neutrinos, a theoretical model that extends the SM. The dark neutrino model was proposed to explain certain anomalies observed in neutrino experiments. Finally, the chapter discusses model-independent searches for physics beyond the Standard Model (BSM).

## 2.1 Standard Model

The SM of particle physics represents our best understanding of the fundamental constituents and interactions in the universe. It was developed through extensive collaborative efforts between experimental and theoretical research. This model stands as a milestone in particle physics and is regarded as one of the greatest scientific achievements of the last century.

The SM contains only elementary particles, meaning those we understand to have no substructure. These elementary particles can be described by basic properties such as mass, electric charge, and spin. Additionally, other properties, such as chirality, are important for describing particles. Chirality is determined by comparing the direction of a particle's spin with its momentum direction, e.g. a right-handed particle typically refers to the situation where the spin and momentum directions are aligned with each other.

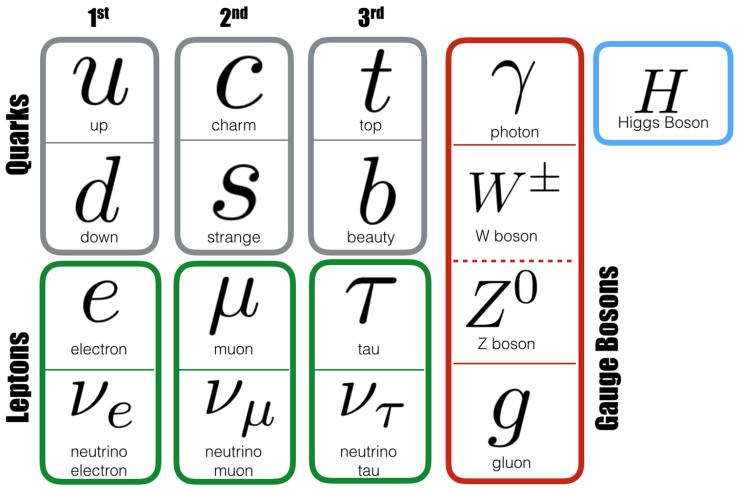


**Figure 2.1** The elementary particles of the SM. Figure from Reference [2].

The model categorises particles into **fermions** and **bosons**. Fermions are spin-$\frac{1}{2}$ particles that obey Fermi-Dirac statistics, while bosons are spin-1 particles that obey Bose-Einstein statistics. Within the SM, fermions are further divided into **quarks** and **leptons**, each organised into three generations as shown in Figure 2.1. Quarks and leptons each consist of six distinct particles. The six quarks are: up ($u$), down ($d$), charm ($c$), strange ($s$), top ($t$), and bottom ($b$). The six leptons are: electron ($e$), muon ($\mu$), tau ($\tau$), electron neutrino ($\nu_e$), muon neutrino ($\nu_\mu$), and tau neutrino ($\nu_\tau$). Quarks serve as the fundamental building blocks of matter.

Fermions interact via four fundamental forces: the strong, weak, electromagnetic, and gravitational forces. Gravity is the weakest of these, but it has an infinite range. The electromagnetic force, which also has an infinite range, is much stronger than gravity. The weak and strong forces, in contrast, operate only over short distances at the subatomic level. While the weak force is stronger than gravity, it is weaker than both the electromagnetic and strong forces. The strong force is the most powerful of the four fundamental forces.

Three of these fundamental forces are mediated by force-carrier particles known as **bosons**. The strong force is carried by gluons ($g$) and acts on quarks. The electromagnetic force is mediated by photons ($\gamma$) and affects only electrically charged particles. The weak force is mediated by $W$ and $Z$ bosons, which can interact with all fermions.

## 2.2 Standard Model Neutrinos

Neutrinos are part of elementary particles in SM. They are electrically neutral and are notoriously difficult to detect because they interact only via the weak force[1]. This section will provide a historical overview of neutrino physics, highlighting key discoveries and outlining the remaining open questions in the field.

### 2.2.1 Discovery of Neutrinos

In the early 20th century, nuclear $\beta$-decay was believed to involve a neutron transforming into a proton only with the emission of an electron. Under the assumption of a two-body decay, the electron's energy should be fixed. However, measurements showed that the electron energy spectrum was continuous, as shown in Figure 2.2.

To resolve this discrepancy and conserve energy in the nuclear $\beta$-decay process, Pauli proposed the existence of a new, neutral, weakly interacting particle with spin $\frac{1}{2}$, which he initially referred to as the "neutron". In 1932, Chadwick discovered a neutral particle with a mass similar to the proton and named it the neutron [4]. A few years later, Fermi [5] and Perrin [6] provided a theoretical interpretation of nuclear $\beta$-decay involving weak interactions and a third neutral particle. This particle was given the name **neutrino** by Fermi.

[1] The gravitational force is negligible due to the very small mass of neutrinos.

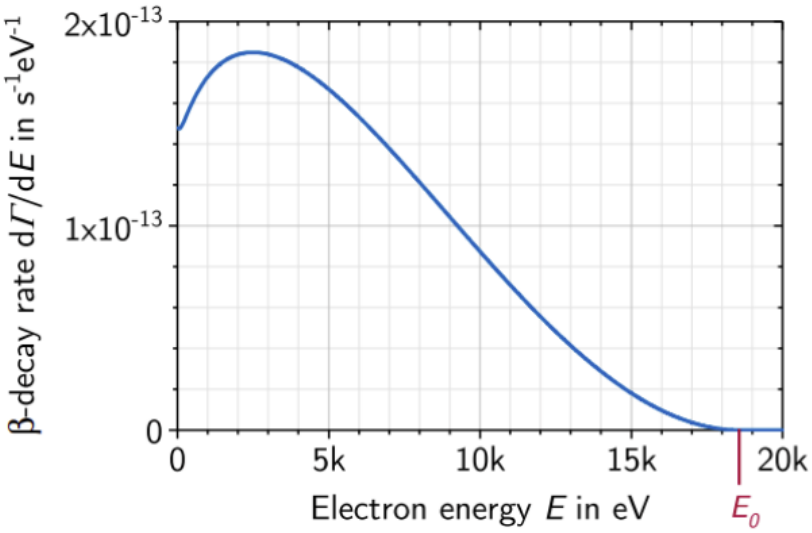


**Figure 2.2** Energy spectrum of $\beta$-decay. The measured spectrum is drawn in blue curve and the expected fixed energy $E_0$ under the two-body decay assumption. Figure from Reference [3].

From then, the quest to detect the neutrino began. Early calculations of neutrino-nucleus interaction cross-sections suggested that observing neutrinos experimentally would be nearly impossible [7]. It took nearly 30 years for the first observation of electron antineutrino by Cowan and Reines in 1956 at the Savannah River Plant in South Carolina [8, 9]. The large flux of antineutrinos from the nuclear reactor compensated for the small interaction cross-section. The detector was made up of layers of scintillator, and between the scintillator was cadmium-doped water, which is sensitive to the inverse $\beta$-decay process,

$$\overline{\nu} + p \rightarrow e^{+} + n. \tag{2.1}$$

The signal consists of a prompt scintillation light produced by the annihilation of the positron, followed by a delayed ($\sim 10\mu s$) scintillation signal produced from neutron capture on $^{144}$Cd. The rate of this process was measured when the reactor was on and off, and the comparison of these results provided evidence for the existence of neutrinos originating from the reactor [8, 9]. This discovery was awarded the Nobel Prize in 1995.

### 2.2.2 Discovery of Neutrino Flavours

The discovery of the neutrino opened the door to experimental neutrino physics. This breakthrough shifted the focus of experimentalists towards studying the newly discovered neutrino particle. Similar to inverse $\beta$-decay (Equation 2.1), the reaction

$$\overline{\nu} + {}^{37}\mathrm{Cl} \rightarrow e^{-} + {}^{37}\mathrm{Ar}, \tag{2.2}$$

was initially proposed for measurement by Pontecorvo [10] and Alvarez [11]. Davis and coworkers later pursued this with the Brookhaven reactor and liquid $CCl_4$ detector [12, 13]. Despite predictions for a non-zero cross-section, no events were observed. The concept of lepton number conservation, proposed by Konopinski and Mahmoud in 1953 [14], provided an explanation for these experimental observations. They assigned a lepton number $L = +1$ to leptons, such as the electron and neutrino, and $L = -1$ to anti-leptons, such as the positron and antineutrino. By requiring the conservation of $L$, the process described in Equation 2.2 is forbidden.

The muon particle was discovered by various groups in cosmic rays [15–17] in 1937. After the discovery, muons were predicted to decay into electrons and two neutral leptons via the process,

$$\mu^{-} \rightarrow e^{-} + \nu + \nu, \tag{2.3}$$

by Sakata and Inoue [18] and later confirmed by Conversi and coworkers in 1947 [19].

In the meantime, another decay process,

$$\mu^{-} \rightarrow e^{-} + \gamma, \tag{2.4}$$

was calculated by Feinberg [20] to be observable in experiments but was not detected [21]. To resolve this discrepancy between theory and experiment, two different flavours of neutrinos were proposed: the electron neutrino and the muon neutrino. Therefore, one of the two neutral particles in Equation 2.3 was identified as $\overline{\nu}_e$, while the other was identified as a muon-related neutrino, $\nu_\mu$. The concept of lepton flavour numbers was accordingly introduced, and by requiring the conservation of the electron lepton number ($L_e$) and the muon lepton number ($L_\mu$), the process described by Equation 2.4 is thus forbidden.

With the rule of the lepton number conservation, the neutrino flavour can be identified based on the leptons involved in the neutrino interaction. Specifically, neutrinos interact weakly with matter through the neutral-current (NC) $Z$ boson and the charged-current (CC) $W$ boson, as illustrated in Figure 2.3. In CC interactions, the outgoing leptons ($l^-$) enables the possibility of determining the neutrino flavour.

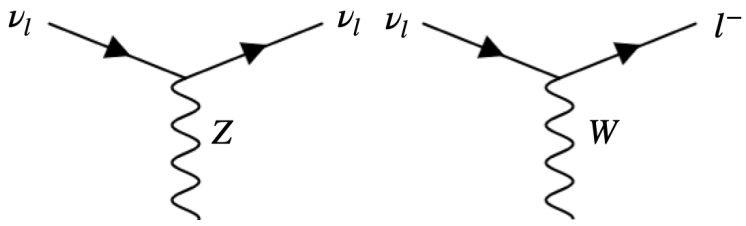


**Figure 2.3** Neutrino interactions via (left) neutral-current $Z$ and (right) charged-current $W$ bosons.

The direct detection of $\nu_\mu$ was achieved by Lederman, Schwartz, Steinberger and others in 1962 [22]. A beam of neutrinos produced by accelerating protons up to 15 GeV and colliding them with a Beryllium target was used for the detection. This collision predominantly produced pions, which primarily decay into $\nu_\mu$ via the reaction,

$$\pi^\pm \rightarrow \mu^\pm + \nu_\mu(\overline{\nu}_\mu). \tag{2.5}$$

In the resulting experiments, 34 single-muon candidates originating from within the shielded spark-chamber detector were identified, along with only 8 electron-like candidates. The observation of muon production from neutrino interactions compared to electron production demonstrated that muon neutrinos are distinct from electron neutrinos. This experimental evidence confirmed the theory of neutrino flavour, establishing the existence of different types of neutrinos associated with their corresponding leptons, once produced.

In 1975, a heavy lepton with a mass of approximately 1.8 GeV was discovered by Perl and coworkers [23] through the process:

$$e^+ + e^- \rightarrow \tau^+ + \tau^-. \tag{2.6}$$

Both experimental and theoretical analyses established that this heavy lepton was a spin $\frac{1}{2}$ fermion and a point-like particle, similar to the electron and muon. The discovery of the $\tau$ lepton led to the prediction of a third neutrino flavour, the $\nu_\tau$. The tau lepton number ($L_\tau$) is also introduced and similarly is required to be conserved in neutrino interactions. The tau neutrino is more challenging to detect compared to the electron and muon neutrinos. Firstly, the GeV-scale mass of the tau lepton requires much higher energy for production. Secondly, the tau lepton has a short lifetime of approximately $10^{-13}$ seconds.

The DONUT experiment achieved the first detection of four tau neutrino interactions in 2001 [24]. Similar to the production of muon neutrino beams, tau neutrinos were produced by colliding 800 GeV protons with a tungsten target. The higher energy of the protons enables the production of $D_s$ mesons, which decay into tau neutrinos with a branching ratio of 6%. The DONUT experiments used tracking detectors and calorimeters to detect neutrino interactions in a dense iron target. Since the outgoing tau lepton ($\tau$) has a very short lifetime (typically corresponding to a 2 mm path), tau-neutrino interactions were identified by observing the decay products, which often displayed a characteristic kink caused by the decay of the tau leptons [25].

### 2.2.3 Number of Light Active Neutrinos

The $Z$ boson, a neutral-current mediator of the weak interaction, was discovered by the UA1 experiment in 1983 [26]. Following this discovery, the Large Electron-Positron (LEP) collider began to study the properties of the $Z$ boson by observing its decay modes. The hadron production around the $Z$ resonance can be described as [27]

$$\sigma_{had} = \frac{12\pi}{m_Z^2} \frac{\Gamma_{ee}\Gamma_{had}}{\Gamma_Z^2}, \tag{2.7}$$

where $m_Z$ is the mass of $Z$ boson, $\Gamma_{ee}$ and $\Gamma_{had}$ are the partial widths of specific decay modes. The $\Gamma_Z$ is the total decay width and can be written as

$$\Gamma_Z = N_\nu \Gamma_\nu + 3\Gamma_{ee} + \Gamma_{had}, \tag{2.8}$$

where the $N_\nu$ is the number of the active light neutrinos. By fitting the data with different numbers of $N_\nu$, the results from LEP experiments such as ALEPH, DELPHI, L3, and OPAL concluded the existence of **three light active neutrinos** coupling to the $Z$ boson. The combined cross-section measurements from these experiments are illustrated in Figure 2.4.

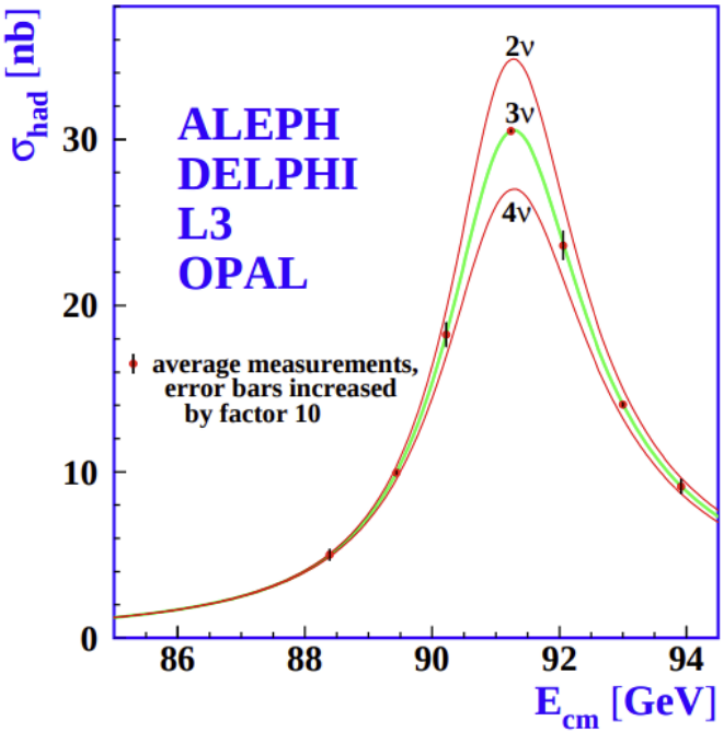


**Figure 2.4** The hadron production cross-section around the $Z$ resonance, together with predictions assuming different numbers of active light neutrinos. Figure from Reference [27].

### 2.2.4 Neutrino Interactions

As mentioned previously, identifying neutrino flavour can be achieved through CC interactions. Therefore, understanding these interactions with nuclei and the resulting particles is crucial. Depending on the neutrino energy, interactions between neutrinos and matter can be categorised into three main types: quasi-elastic (QE), resonance (RES), and deep inelastic scattering (DIS), as illustrated in Figure 2.5.

**QE** scattering dominates neutrino interactions in the sub-GeV range. This process involves a neutrino interacting approximately elastically with a nucleon, resulting in the production of a nucleon from the target. In QE scattering, neutrinos convert into charged leptons in the final state.

**RES** production describes a neutrino with higher energy exciting a target nucleon to a resonance state. The resonance baryon then quickly decays to a ground-state nucleon along with the production of various mesons, such as pions.

**DIS** happens when the neutrino energy is above several GeV. In this process, the neutrino can resolve the internal structure of a nucleon and interact directly with a quark. This interaction breaks apart the nucleon and produces a shower of hadrons.

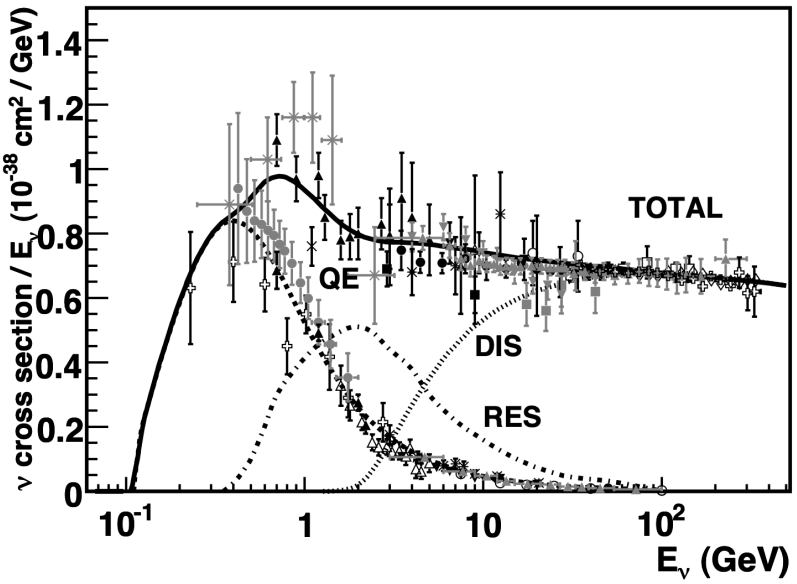


**Figure 2.5** The total muon neutrino charged-current (CC) cross-section per nucleon as a function of neutrino energy is shown. This total cross-section is divided into three distinct modes: **quasi-elastic (QE)**, **resonance (RES)**, and **deep inelastic scattering (DIS)**. Figure from Reference [28].

All three processes mentioned above except for QE can occur in both CC and NC interactions. Additionally, as the neutrino energy decreases further (less than QE), it can interact with the entire target nucleus or atom in a process known as coherent scattering (COH). COH involves low momentum transfer, which can induce pion production, so it is typically associated with the presence of an extra pion in the final state. Another type of neutrino interaction, Meson Exchange Current (MEC), occurs when a neutrino interacts with a pair of nucleons in a nucleus, mediated by mesons, resulting in the ejection of multiple nucleons from the nucleus.

### 2.2.5 Discovery of Neutrino Oscillations

Bahcall's Standard Solar Model [29] predicted the neutrino flux from the Sun. Subsequently, the Homestake experiment [30], led by Davis and his colleagues, measured the solar neutrino flux using a chlorine-based detector. This detector employed radiochemical techniques to detect interactions of solar neutrinos. The Homestake experiment was designed to be sensitive only to electron neutrinos and collected data over a 30-year period. A deficit was observed when comparing the measured neutrino flux to the predictions. This discrepancy became known as the **solar neutrino problem**.

Meanwhile, a deficit of muon neutrinos was also observed in atmospheric experiments. In 1988, the Kamiokande experiment reported a deficit of approximately 60% for muon neutrinos compared to Monte Carlo (MC) calculations [31]. The upgraded Super-Kamiokande experiment, a 50-kton water Cherenkov detector, was designed to detect neutrinos from both the Sun and the atmosphere. The Super-Kamiokande experiment could reconstruct both the direction and the energy of neutrinos and therefore the neutrino disappearance can be studied more accurately. Figure 2.6 shows the ratio of measured to predicted numbers of electron-like and muon-like events as a function of $L/E_\nu$ in the Super-Kamiokande experiment, where $L$ is the distance travelled by the neutrinos and calculated from the angle of the incoming atmospheric neutrino and $E_\nu$ is the neutrino energy. At higher $L/E_\nu$ values, a deficit of around 50% was observed in the $\nu_\mu$ flux.

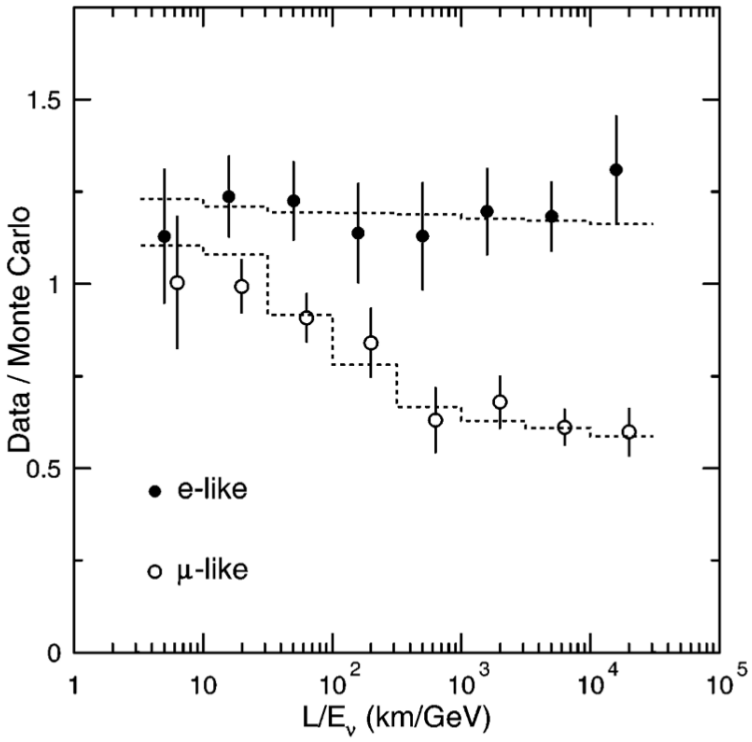


**Figure 2.6** The ratio of measured events to the MC calculations as a function of $L/E_\nu$ in Super-Kamiokande, shown as data points. The dashed line shows the expected shape if the $\nu_\mu \rightarrow \nu_\tau$ oscillation is considered. Figure from Reference [32].

The solar neutrino problem and the deficit of atmospheric muon neutrinos can both be explained by the phenomenon of neutrino oscillation. Pontecorvo was the first to propose the idea of oscillation between neutrinos and antineutrinos in 1957 [33]. With the discovery of the second neutrino flavour, the theory was expanded to include mixing between different flavours by Maki, Nakagawa, and Sakata in 1962 [34], and later by Pontecorvo in 1967 [35]. Pontecorvo proposed neutrino oscillations specifically to explain the solar neutrino problem [35]. According to this theory, an electron neutrino created in the core of the Sun can change its flavour to a muon or tau neutrino on its way to Earth. Similarly, the deficit of atmospheric muon neutrinos can be explained by the oscillation of muon neutrinos into tau neutrinos, as illustrated by the dashed line in Figure 2.6.

The neutrino oscillation explanation of the solar neutrino problem was confirmed by the Sudbury Neutrino Observatory (SNO) experiment [36]. The SNO experiment utilised a heavy water ($D_2O$) Cherenkov detector, which was designed to be sensitive to both electron neutrinos and non-electron neutrinos. The total incident neutrino flux measured by the SNO experiment was in agreement with theoretical predictions. This confirmed that flavour-changing neutrinos along their journey to Earth could explain the solar neutrino problem. SNO and Super-Kamiokande were awarded the Nobel Prize in Physics in 2015 for their work in measuring the total neutrino flux from the Sun and confirming the phenomenon of neutrino oscillation.

In 2002, the KamLAND experiment provided the first evidence for $\overline{\nu}_e$ oscillations from a reactor source [37]. Today, neutrino oscillations have been observed using various sources including the Sun, reactors, cosmic ray interactions, and accelerator beams [38].

### 2.2.6 Neutrino Oscillations

#### Neutrino Mixing

The basic principle behind neutrino oscillations lies in the fundamental difference between the mass eigenstates and the weak interaction eigenstates. Neutrinos $\nu_\alpha$ with flavours $\alpha = e, \mu, \tau$ are produced through weak interaction processes. In the current neutrino oscillation model, these weak (flavor) eigenstates $\nu_\alpha$ are considered to be a mixture of the mass eigenstates $\nu_i$,

$$|\nu_\alpha\rangle = \sum_i U^*_{\alpha i} |\nu_i\rangle \,, \tag{2.9}$$

where $U_{\alpha i}$ represent the components of the Pontecorvo-Maki-Nakagawa-Sakata (PMNS) matrix. The PMNS matrix is a unitary matrix, meaning it satisfies the relation $UU^\dagger = U^\dagger U = \mathbf{1}$, where $\mathbf{1}$ is the identity matrix. For the case of three mass eigenstates and three flavour eigenstates, the PMNS matrix $U$ takes the form:

$$U = \begin{pmatrix} U_{e1} & U_{e2} & U_{e3} \\ U_{\mu 1} & U_{\mu 2} & U_{\mu 3} \\ U_{\tau 1} & U_{\tau 2} & U_{\tau 3} \end{pmatrix}. \tag{2.10}$$

#### Neutrino Oscillations in Vacuum

Let us consider a neutrino produced by a weak interaction process at $t = 0$. The flavour state is created by the superposition of the mass eigenstates, as described by:

$$|\nu(t=0)\rangle = |\nu_\alpha\rangle = \sum_i U^*_{\alpha i} |\nu_i\rangle . \tag{2.11}$$

The time evolution of this state can be described by the free propagation Hamiltonian $H$. In vacuum, the neutrino mass states are eigenstates of $H$, meaning $H|\nu_i\rangle = E_i |\nu_i\rangle$, where $E_i$ is the energy of the neutrino. Therefore, the flavour state with time evolution can be expressed by:

$$|\nu(t)\rangle = e^{-iHt} |\nu(t=0)\rangle = e^{-iE_i t} |\nu(t=0)\rangle = \sum_i e^{-iE_i t} U^*_{\alpha i} |\nu_i\rangle . \tag{2.12}$$

Considering orthonormal mass neutrino states where $\langle \nu_i | \nu_j \rangle = \delta_{ij}$, the probability of detecting this neutrino in a different flavour state $|\nu_\beta\rangle$ is given by:

$$\begin{aligned} P(\nu_\alpha \to \nu_\beta) &= \langle \nu_\beta | \nu_\alpha(t) \rangle^2 \\ &= \left| \sum_i U_{\beta i} U^*_{\alpha i} e^{-iE_i t} \right|^2 \\ &= \sum_{i,j} U^*_{\beta j} U_{\alpha j} U_{\beta i} U^*_{\alpha i} e^{-i(E_i - E_j)t}. \end{aligned} \tag{2.13}$$

In general, neutrinos are produced in an ultra-relativistic regime. Therefore, their energy can be approximated by a Taylor expansion to be

$$E_i = \sqrt{(p_i^2 + m_i^2)} \approx p_i + \frac{m_i^2}{2p_i} \approx E + \frac{m_i^2}{2E_i}, \tag{2.14}$$

where $p_i$ and $m_i$ are the momentum and the mass of neutrino mass state $i$. With

Equation 2.14, it is possible to write:

$$E_i - E_j \approx \frac{\Delta m_{ij}^2}{2E}, \tag{2.15}$$

where $\Delta m_{ij}^2 = m_i^2 - m_j^2$, with the assumption $E_i \approx E_j = E$. In neutrino oscillation experiments, the propagation time $t$ is not measured. Given that neutrinos travel almost at the speed of light, the approximation $t \approx L$ can be made. Therefore, the final probability can be expressed as

$$P(\nu_\alpha \to \nu_\beta) = \sum_{i,j} U_{\beta j}^* U_{\alpha j} U_{\beta i} U_{\alpha i}^* e^{-i(\frac{\Delta m_{ij}^2 L}{2E})}. \tag{2.16}$$

Equation 2.16 illustrates how the oscillation probability depends on the $L/E$ ratio in a given experiment. The discovery of neutrino oscillation, namely that $P$ in Equation 2.16 has a non-zero value, implies that the mass splitting $\Delta m_{i,j} \neq 0$ and therefore neutrinos have mass.

### Neutrino Oscillations in Matter

When neutrinos propagate through electron-rich matter, the propagation Hamiltonian is influenced by both CC and NC interactions. The Feynman diagrams illustrating these processes are shown in Figure 2.7. The NC interaction between neutrinos and electrons is the same for all flavours, whereas the CC interaction is exclusive to electron neutrinos and does not occur with other flavours or antineutrinos. The described effect is normally referred to as the "matter effect" or Mikheyev-Smirnov-Wolfenstein (MSW) effect [39].

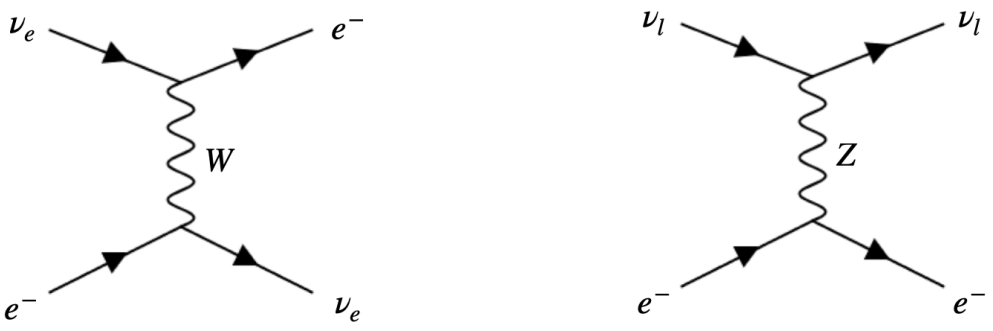


**(a)** **(b)**

**Figure 2.7** Feynman diagrams of (a) charged current and (b) neutral current interactions between neutrinos and electrons in matter.

For electron neutrinos, the presence of electrons in matter introduces an additional potential:

$$V = \sqrt{2} G_F n_e, \tag{2.17}$$

where $G_F$ is the Fermi coupling constant and $n_e$ is the number density of electrons in the matter. The potential modifies the Hamiltonian of the system to $H_1 = H + V$, where $H$ is the Hamiltonian in vacuum. Consequently, the probability that a neutrino oscillates to a different flavour will be different from the probability of neutrino oscillation in vacuum. The MSW effect can enhance neutrino oscillation when the matter-induced potential matches the neutrino oscillation frequency in vacuum, a phenomenon commonly referred to as the MSW resonance. The condition of the resonance is correlated with both the neutrino energy and the local electron density [40].

Moreover, the MSW effect will impact the oscillation probabilities between neutrinos and anti-neutrinos because CC interactions are not available for anti-neutrinos due to the lack of positrons in the Earth. This effect needs to be carefully considered when studying the differences between neutrinos and antineutrinos.

### Overview of Neutrino Oscillation Parameters

Precision measurements of the parameters in the PMNS matrix and the mass splittings have been a major focus of neutrino oscillation experiments. The PMNS matrix, described in Equation 2.10, can be parameterised by three mixing angles $\theta_{12}, \theta_{13}$, and $\theta_{23}$, which are analogous to 2D rotations, along with a charge-parity (CP) violating phase $\delta_{cp}$, which could create a difference in oscillation behaviour between neutrinos and antineutrinos. The Majorana phases $\alpha_1$ and $\alpha_2$ indicate if neutrinos are Majorana particle. The matrix can be written as

$$U = \underbrace{\begin{pmatrix} 1 & 0 & 0 \\ 0 & c_{23} & s_{23} \\ 0 & -s_{23} & c_{23} \end{pmatrix}}_{\text{Atmospheric (+Accelerator)}} \underbrace{\begin{pmatrix} c_{13} & 0 & s_{13}e^{-i\delta_{cp}} \\ 0 & 1 & 0 \\ -s_{13}e^{-i\delta_{cp}} & 0 & c_{13} \end{pmatrix}}_{\text{Reactor (+Accelerator)}} \underbrace{\begin{pmatrix} c_{12} & s_{12} & 0 \\ -s_{12} & c_{12} & 0 \\ 0 & 0 & 1 \end{pmatrix}}_{\text{Solar (+Reactor)}} \underbrace{\begin{pmatrix} e^{i\frac{\alpha_1}{2}} & 0 & 0 \\ 0 & e^{i\frac{\alpha_2}{2}} & 0 \\ 0 & 0 & 1 \end{pmatrix}}_{\text{Majorana}}, \tag{2.18}$$

where $c_{ij} = \cos(\theta_{ij})$ and $s_{ij} = \sin(\theta_{ij})$.

For precision measurements of the mass splitting, because $\Delta m^2$ is fixed by nature, experiments need to be designed to probe different values of $\Delta m^2$ by selecting appropriate values of the $L/E$ ratio. A summary of the energies and distances explored by various neutrino oscillation experiments is shown in Figure 2.8. Oscillation experiments are primarily driven by two different mass splittings: the atmospheric splitting $\Delta m^2_{31}$ and the solar splitting $\Delta m^2_{21}$, which are indicated by the dashed lines. Some experiments that do not follow these dashed lines, such as MiniBooNE and SBN, are designed to address experimental anomalies, which will be further discussed in Section 2.3.4.

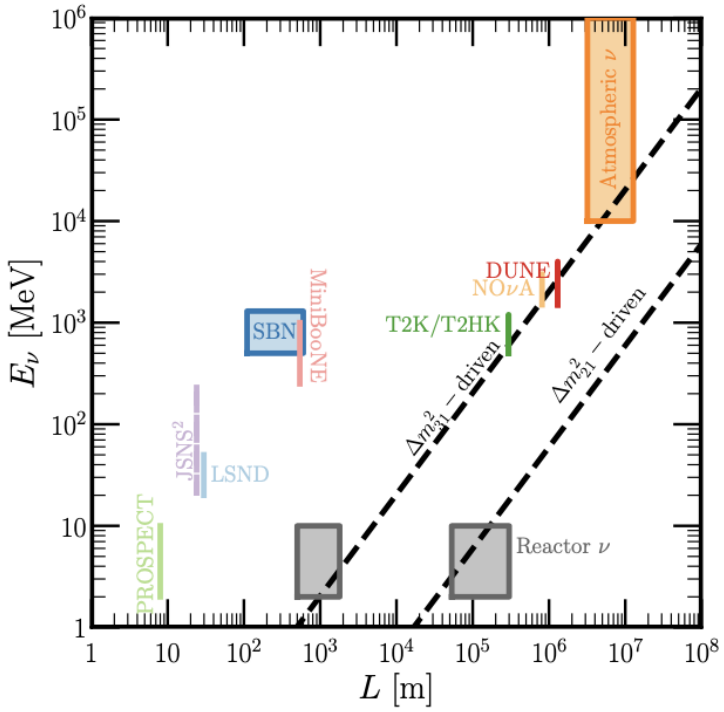


**Figure 2.8** A summary of different energies and distances probed by a variety of different neutrino oscillation experiment. Figure from Reference [41].

The angle describing in the first matrix, $\theta_{23}$, in Equation 2.18 was predominantly determined by **atmospheric neutrino experiments**. Atmospheric neutrinos are produced from the decays of pions and kaons created by cosmic rays interacting with nucleons in the Earth's atmosphere. The energy range for atmospheric neutrinos spans from hundreds of MeV to a few TeV, with travel distances ranging from around 10 km to $10^4$ km. These neutrinos are primarily muon and electron neutrinos, with a ratio of approximately 2:1 [42]. The Super-Kamiokande experiment measured the atmospheric mass splitting $\Delta m^2_{31} \approx 2 \times 10^{-3}$ eV$^2$ and the mixing angle $\theta_{23} \approx 45^\circ$ by observing the disappearance of atmospheric muon neutrinos [43]. With an appropriate $L/E$ ratio corresponding to the measured atmospheric neutrino mass splitting, the accelerator experiment OPERA directly detected tau neutrinos that originated from muon neutrinos [44, 45].

The angle in the third matrix, $\theta_{12}$, was measured by **solar neutrino experiments**. Solar neutrinos are primarily produced through the process $p + p \rightarrow^2 \mathrm{H} + e^+ + \nu_e$, with energies less than 1 MeV. Since solar neutrinos are predominantly electron neutrinos, solar neutrino experiments measure the fraction of solar neutrinos reaching Earth with an electron flavour. The SNO experimental was designed to detect neutrinos via both CC interactions, which are sensitive only to electron neutrinos, and NC interactions, which are sensitive to all neutrino flavours. By comparing the rates of these interactions, SNO could determine the probability of solar electron neutrinos changing into muon and tau neutrinos as a function of neutrino energy. The variation of oscillation probability as a function of energy observed by different experiments made it possible to distinguish between vacuum oscillations at lower energies and matter-enhanced oscillations at higher energies. Combining these results with global fits from other experiments, SNO measured the solar neutrino mass splitting as $|\Delta m^2_{21}| \approx 7.5 \times 10^{-5}$ eV$^2$ and the mixing angle $\theta_{12}$ to be approximately $33^\circ$ [46–49]. These findings were later confirmed by the KamLAND experiment, which measured the oscillation of electron antineutrino flux from nuclear reactors [50].

Finally, the mixing angle in the second matrix, $\theta_{13}$, was measured through the disappearance of electron antineutrinos by **short-baseline reactor neutrino experiments**. Reactor neutrinos are generated by beta decays, with $\overline{\nu}_e$ being the most abundant, and energies up to 10 MeV. The Daya Bay [51], RENO [52] and Double Chooz [53] experiments reported $\theta_{13} \approx 9^\circ$.

The remaining parameters in the neutrino oscillation matrix that are not yet measured include the CP-violating phase $\delta_{CP}$ and the Majorana phases $\alpha_1$ and $\alpha_2$. The CP-violating phase $\delta_{CP}$ will be measured by current and future long-baseline **accelerator oscillation experiments**, with distances as large as $\mathcal{O}(1000\,\text{km})$. More about $\delta_{CP}$ will be covered in Section 2.3.2. The Majorana phases $\alpha_1$ and $\alpha_2$ are only present if neutrinos are Majorana particles, where $\nu = \overline{\nu}$. These Majorana phases are currently studied through neutrinoless double beta decay rather than by oscillation. More details about Majorana particles can be found in Section 2.3.1.

## 2.3 Open Questions in Neutrino Physics

The SM developed in the 1970s describes the three light active neutrino flavours and their interactions with matter but initially predicted that neutrinos have no mass. Subsequent extensions to the SM incorporated the concept of massive neutrinos and their oscillations, yet the origin of neutrino mass remains unknown. Alongside the mechanism of neutrino mass, many other questions remain unresolved in the field of neutrino physics. This section will selectively introduce some of these outstanding open questions.

### 2.3.1 Nature of Neutrino and its Mass Mechanism

The SM introduces mass to particles via the Higgs mechanism. All known particles to date are so-called Dirac particles [54], meaning they are distinct from their antiparticles. For Dirac particles and their antiparticles to acquire mass, both left-handed and right-handed chiral states are required. The Higgs mechanism has successfully explained the origin of mass for all quarks and charged leptons. However, neutrinos (antineutrinos) are observed only in left-handed (right-handed) chirality [55]. For this reason the original SM predicted that neutrinos should have zero mass, which we now know contradicts experimental observations.

To address this, two mechanisms have been proposed for neutrino mass generation, both of which require the introduction of new physics beyond the SM. The first involves using the Dirac mechanism, which requires introducing additional right-handed neutrino states, often referred to interchangeably as neutral fermions, heavy leptons, or sterile neutrinos [56]. These newly introduced neutrinos do not interact via the weak interaction, and, with their presence, the SM neutrino mass can be generated through the Higgs mechanism.

The second mechanism involves introducing a Majorana mass term to the neutrino. If the neutrino were a Majorana particle, the distinction between the neutrino and its antiparticle would vanish [57]. In this case, the mass of the neutrino can be generated without the need to introduce a new right-handed state.

The determination of the nature of neutrinos, whether they are Dirac or Majorana particles, could be achieved through experiments searching for neutrinoless double beta decay ($0\nu\beta\beta$). This process is predicted under the assumption that the neutrino is a Majorana particle and is characterised by the production of two electrons and two protons without accompanying neutrinos, as shown in Figure 2.9. Such a process is forbidden in the SM due to the violation of lepton number conservation. Although $0\nu\beta\beta$ decay has not yet been observed experimentally, many experiments have set stringent constraints on its lifetime, including GERDA [58], KamLAND-Zen [59], and CUORE [60]. Future experiments, such as NEXT [61], LEGEND [62], and SNO+ [63], will continue to push the limits on the presence of the $0\nu\beta\beta$ decay.

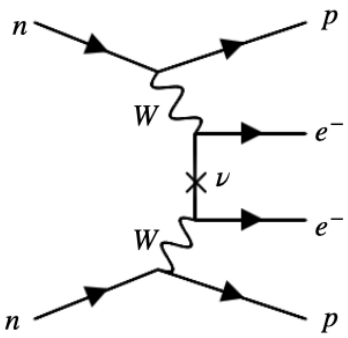


**Figure 2.9** Feynman diagram of a neutrinoless double beta decay ($0\nu\beta\beta$).

### 2.3.2 Charge-Parity Symmetry in the Lepton Sector

According to the Big Bang theory, matter and antimatter were produced in equal amounts. However, living in a matter-dominated universe nowadays naturally raises the question: why is there an imbalance between matter and antimatter? In 1967, Sakharov proposed three key requirements, known as the Sakharov conditions [64], to explain this imbalance. One of these is the violation of CP symmetry.

CP symmetry combines charge conjugation (C) and parity transformation (P). Charge conjugation transforms a particle into its antiparticle, while parity transformation involves reversing spatial quantities and therefore flips chirality, meaning a left-handed particle will be transformed into a right-handed one. The concept of CP symmetry conservation was proposed following Wu's discovery of the violation of both C and P symmetry in weak interactions, observed during the study of $\beta$ decays of Cobalt-60 [65]. However, the violation of CP symmetry was also observed in the quark sector by Val Fitch, Jim Cronin, and collaborators in 1964 during studies of neutral kaon decays [66]. The SM incorporates the theory of CP violation through the Kobayashi-Maskawa mechanism [67].

CP violation has been observed in several channels in the quark sector, but the total value observed is not sufficient to explain the matter-antimatter asymmetry, indicating the need for new sources of CP violation. Among all proposed theories, **Leptogenesis**, as suggested by Fukugita and Yanagida [68, 69], involves expected CP violation in the lepton sector. The $\delta_{CP}$ can be measured by comparing the probabilities of neutrino and antineutrino oscillations. To precisely measure the value of $\delta_{CP}$, other parameters, especially the mass ordering, need to be accurately determined. The violation of CP symmetry in the lepton sector can be confirmed if $\delta_{CP}$ is measured to be neither 0 nor $\pi$.

### 2.3.3 Neutrino Mass Ordering

So far oscillation experiments have measured the magnitudes of both the solar mass splitting $\Delta m^2_{21}$ and the atmospheric mass splitting $\Delta m^2_{31}$, but only the sign of the solar mass splitting has been established. The MSW effect, as described in Section 2.2.6, modifies the probability of neutrino oscillation in electron-rich environments. This change in probability becomes sensitive to the sign of the mass splitting, allowing the sign of the mass splitting to be determined from solar oscillation experiments. More details on the calculation of the oscillation probability can be found in Reference [70].

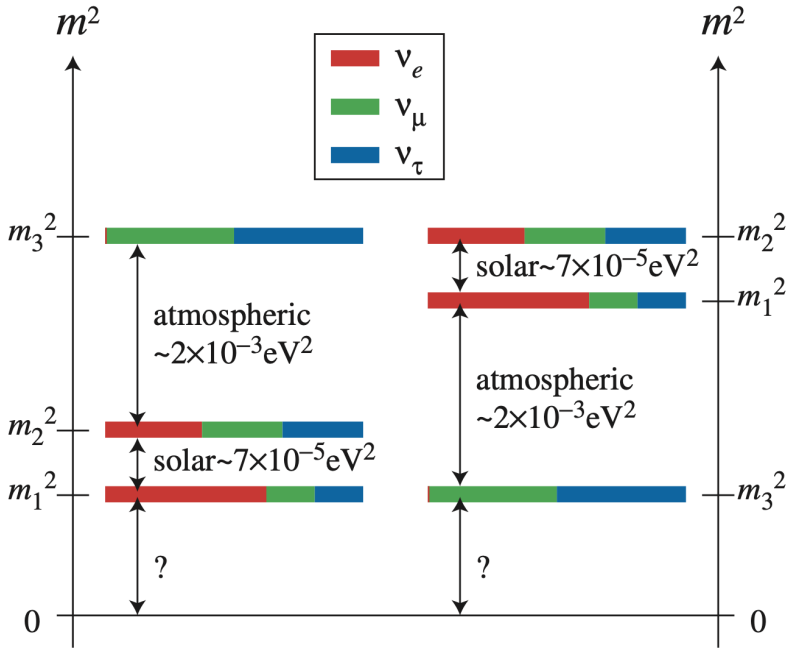


**Figure 2.10** A schematic diagram of the two possible neutrino mass orderings: (left) normal ordering and (right) inverted ordering. The absolute mass scale is unknown but is constrained to be sub-eV. Figure from Reference [71].

Since the sign of the atmospheric mass splitting remains unknown, there are two possible orderings of the three mass eigenstates: **normal ordering** and **inverted ordering**, as illustrated in Figure 2.10. For both orderings, oscillation experiments are unable to determine the absolute scale of neutrino masses due to their insensitivity to this parameter. However, other experimental approaches can provide such measurements. For example, cosmological observations have established a stringent upper limit on the sum of the three neutrino masses, constraining it to less than 0.2 eV [72]. Nonetheless, this is an indirect measurement, so direct experiments remain necessary. The Karlsruhe Tritium Neutrino (KATRIN) experiment is designed specifically to measure the neutrino mass directly through beta decay. Recently, KATRIN set an upper limit on the effective electron antineutrino mass at $m_\nu < 0.45\,\text{eV}$ [73].

Determining the neutrino mass ordering is a fundamental step towards completing the neutrino theory. Firstly, it can help reduce the uncertainty in the $\delta_{cp}$ measurement. Using an electron neutrino appearance oscillation search as an example, the

oscillation probability defined in Equation 2.16 can be rewritten as:

$$
\begin{aligned}
P(\nu_\mu \to \nu_e) \simeq & \sin^2\theta_{23}\sin^2 2\theta_{13}\frac{\sin^2(\Delta_{31}-aL)}{(\Delta_{31}-aL)^2}\Delta_{31}^2 \\
& + \sin 2\theta_{23}\sin 2\theta_{13}\sin 2\theta_{12}\frac{\sin(\Delta_{31}-aL)}{(\Delta_{31}-aL)}\Delta_{31}\frac{\sin(aL)}{(aL)}\Delta_{21}\cos(\Delta_{31}+\delta_{CP}) \\
& + \cos^2\theta_{23}\sin^2 2\theta_{12}\frac{\sin^2(aL)}{(aL)^2}\Delta_{21}^2,
\end{aligned}
\tag{2.19}
$$

where $\Delta_{ij} \equiv \frac{\Delta m_{ij}^2 L}{4E}$ and $a \equiv G_F n_e/\sqrt{2}$. The probability is affected by both the mass effect ($a$) and $\delta_{cp}$, and therefore determining the neutrino mass ordering can help reduce the uncertainty in the $\delta_{cp}$ measurement.

Moreover, the neutrino mass ordering also helps define the relevant domain for future neutrinoless double beta decay experiments, as the mass ordering affects the effective mass for $0\nu\beta\beta$ decay [74, 75]. Additionally, when combined with cosmological measurements, which are sensitive to the sum of the neutrino masses, the mass ordering can aid in determining the absolute scale of neutrino masses.

The current operational long-baseline experiments, NOvA [76] and T2K [77], have both individually shown a slight preference for normal mass ordering but have indicated different preferences for the region of $\delta_{CP}$ in the normal ordering scenario. Recently, NOvA and T2K conducted a joint analysis, which mildly favoured inverted ordering and strongly suggested CP violation in the inverted ordering scenario [78]. The next-generation long-baseline experiments such as DUNE [79, 80] and Hyper-Kamiokande [81], JUNO [82], IceCube-Upgrade [83], and KM3NeT-ORCA [84] are expected to provide definitive answers on the neutrino mass ordering and the measurement of $\delta_{CP}$.

### 2.3.4 Short-Baseline Anomalies

The SM describes weak interactions among three flavours of neutrinos. However, over the past 20 years, many short-baseline neutrino oscillation experiments have reported anomalous results that cannot be explained by the three-flavour neutrino phenomenology alone. A deficit of electron antineutrinos from calibration sources was observed in radiochemical experiments using gallium ($^{71}$Ga) targets [85, 86]. Similarly, reactor experiments also noted a deficit in antineutrino flux [87]. Both observed a 2.5 to 3 $\sigma$ discrepancy.

The Liquid Scintillator Neutrino Detector (LSND) was a neutrino oscillation experiment at Los Alamos National Lab, operating from 1993 to 1998. The detector was filled with mineral oil doped with a scintillator, where the charged particles produced from neutrino interactions generate scintillation and Cherenkov light as signals. The $L/E$ ratio was designed to be 30 m/40 MeV, making the detector sensitive to a mass splitting of approximately 1 eV. In 2001, LSND reported an excess of $\overline{\nu}_e$ in the $\overline{\nu}_\mu \rightarrow \overline{\nu}_e$ channel [88].

The most popular explanation for the LSND anomaly involves introducing a fourth type of neutrino, commonly referred to as a sterile neutrino [89–91]. This sterile neutrino would not interact via the weak interaction, as the hadron production around the $Z$ resonance allows only three flavours of neutrino coupling to the weak interaction, as explained in Section 2.2.3. The simplest extended oscillation model is the 3 (active) + 1 (sterile) model, which can be described by an extended PMNS mixing matrix:

$$U = \begin{pmatrix} U_{e1} & U_{e2} & U_{e3} & U_{e4} \\ U_{\mu 1} & U_{\mu 2} & U_{\mu 3} & U_{\mu 4} \\ U_{\tau 1} & U_{\tau 2} & U_{\tau 3} & U_{\tau 4} \\ U_{s1} & U_{s2} & U_{s3} & U_{s4} \end{pmatrix}. \tag{2.20}$$

The MiniBooNE experiment was built at the Fermi National Accelerator Laboratory (Fermilab) to verify the LSND results [92]. MiniBooNE was a Cherenkov detector that used mineral oil, and it collected data from 2002 to 2019. The experiment was positioned in an independent neutrino beam line with a similar $L/E$ ratio (500 m/700 MeV) to LSND. In 2007, MiniBooNE confirmed the anomalous excess of events in data [93]. Recent results from the full dataset, shown in Figure 2.11, have again reported this excess, achieving a significance of $4.8\sigma$ at low neutrino energies and forward scattering angles [94].

MiniBooNE also performed a fit under the assumption that one type of sterile neutrino oscillates into electron neutrinos, as shown by the dashed histogram in Figure 2.11. Compared with the data, the sterile neutrino oscillation model increased the expected MC predictions, but it is not sufficient to explain the excess in the lower energy region.

The observed excess is clearly understood to be of an electromagnetic shower nature. The MiniBooNE detector, as a Cherenkov detector, is not able to distinguish between photon-induced and electron-induced electromagnetic showers, with photon-induced showers being the primary background. Therefore the origin of this excess is still not known.

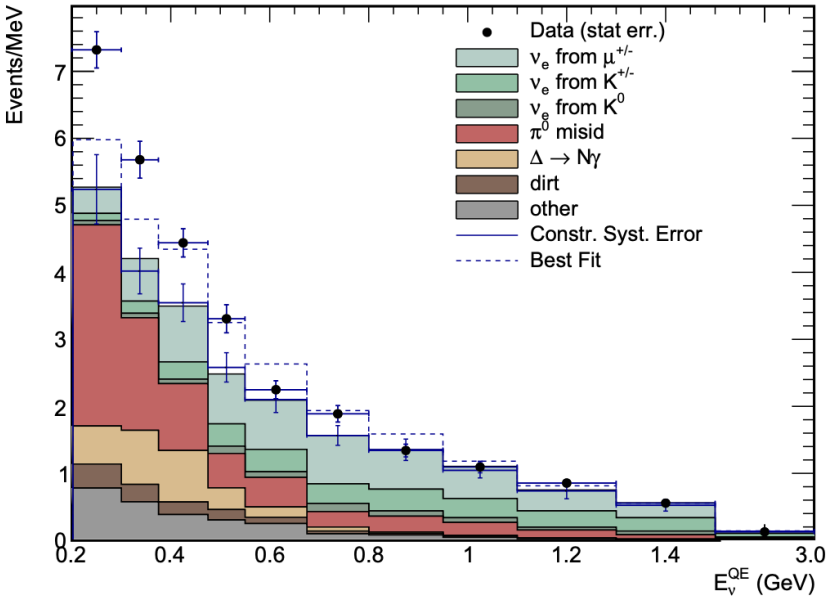


**Figure 2.11** The reconstructed charged-current QE neutrino energy distribution. The dashed line represents the best fit to the neutrino-mode data using the SM oscillation parameters. Figure from Reference [94].

### Recent MicroBooNE Results

MicroBooNE was built to study the MiniBooNE low energy excess (LEE) anomaly and therefore was positioned with a similar baseline to the MiniBooNE detector. MicroBooNE employs liquid argon time projection chamber (LArTPC) technology and collected data from 2015 to 2020. LArTPC detectors are known for their good position resolution (down to millimetres) and their excellent calorimetry. MicroBooNE is able to distinguish a photon from an electron by precisely reconstructing the deposited energy per unit length that particles travel, as illustrated in Figure 2.12. More details about LArTPC detectors will be discussed in Section 4.3.

In 2021, MicroBooNE released their first results for the LEE search using half of their dataset. The initial results focused on single photons resulting from a neutral current $\Delta$ resonance interactions [96] and electron neutrinos with multiple final state topologies [97–100]. Figure 2.13 (a) and (b) show the results of the signal photon study for both $1\gamma 1p$ and $1\gamma 0p$ processes. The study rules out photons from NC$\Delta \rightarrow N\gamma$ as the cause of the LEE at a 94.8% confidence level (C.L). Figure 2.13 (c) presents the results of the $\nu_e$-like searches with different final states. These results also exclude hypotheses of electrons as the only component of the LEE.

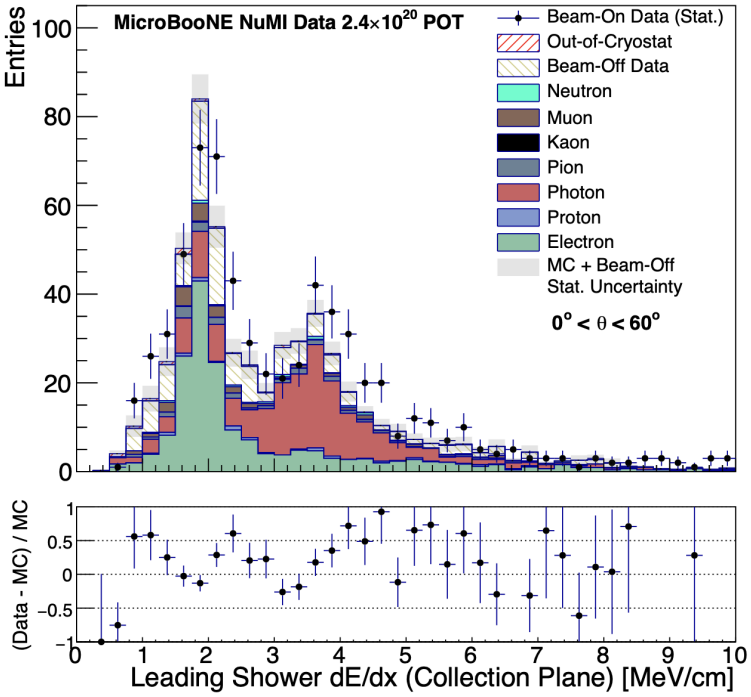


**Figure 2.12** The distribution of deposited energy per unit length ($dE/dx$) for electron and photon showers. Figure from Reference [95].

Since the release of its first results, MicroBooNE has continued searching for LEE signals. The $\nu_e$-like searches have been expanded to use the full dataset, and the data still show inconsistency with the LEE at a confidence level greater than 99% [101]. More channels have been included in the signal $\gamma$ search, and no evidence of the LEE has been observed yet [102–104].

In 2021, MicroBooNE reported their first results with extended sterile neurtino model using half of the dataset [105]. As shown in Figure 2.14 (a), the $4\nu$ model fit to the MicroBooNE data shows good agreement with the SM predictions, and therefore no evidence of light sterile neutrino oscillations was observed. The exclusion plot at 95% C.L. is shown in Figure 2.14 (b), and MicroBooNE is able to exclude part of the LSND-allowed region.

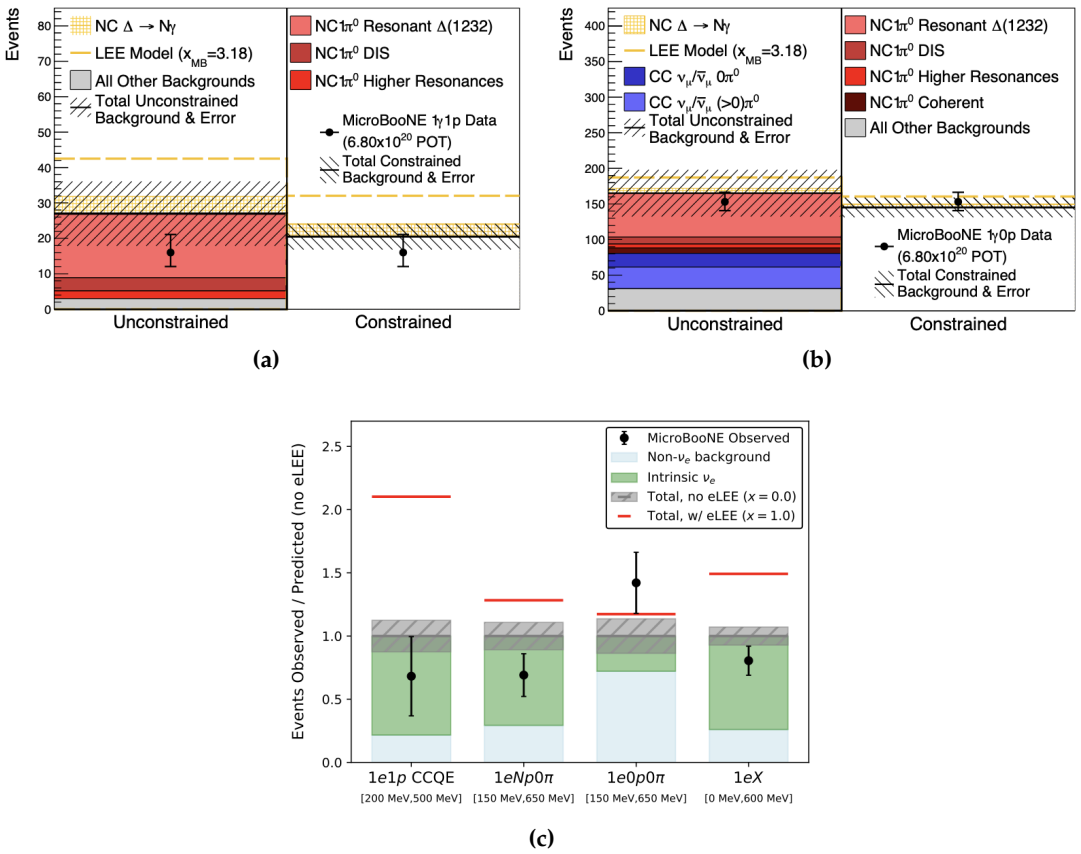


**Figure 2.13** Low energy excess (LEE) results from MicroBooNE: observed event rates for (a) $1\gamma 1p$ (b)$1\gamma 0p$ processes, compared with unconstrained and constrained background, and LEE model. (c) The ratio of observed to predicted $\nu_e$ candidates with different final states, compared with prediction with and without LEE model. Figures from Reference [96, 100].

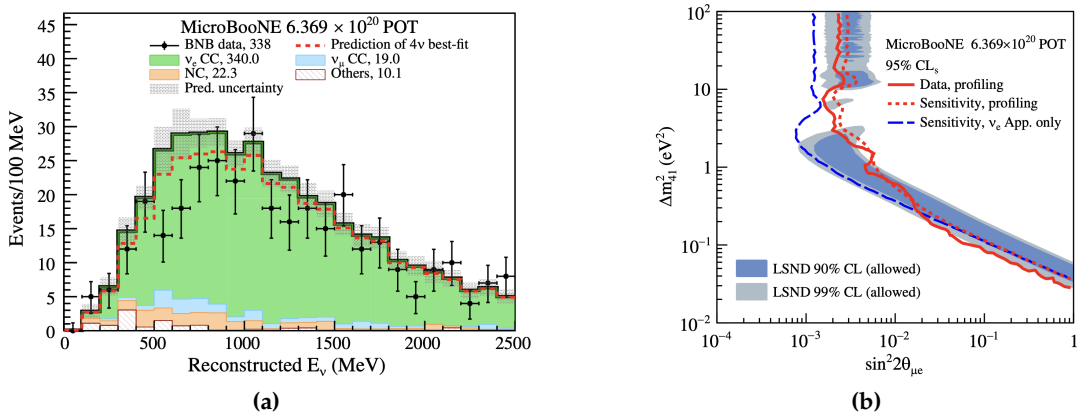


**Figure 2.14** Results from sterile neutrino searches in MicroBooNE: (a) Reconstructed neutrino energy from MicroBooNE data, compared with the 3+1 fit prediction and the SM prediction. (b) MicroBooNE $CL_s$ exclusion plot at 95 % CL in the phase parameter compared with LSND allowed region. Figures are from Reference [105].

## 2.4 Dark Neutrinos

MicroBooNE results suggest that the LEE might not be caused by $\nu_e$-like processes or single-photon mechanisms. Furthermore, the data disfavours the theory of neutrino oscillations into electron neutrinos, including the involvement of sterile neutrino species, as an explanation for the LEE. Moreover, considering the sterile neutrino oscillation model is also not sufficient to explain the MiniBooNE excess in the lower energy region, additional mechanisms are needed to account for the MiniBooNE observation.

Processes from so-called **dark sector** physics can also introduce additional mechanisms to produce EM-like excess. The dark neutrino model [106] is one such model proposed to explain the MiniBooNE LEE. It postulates a dark neutrino, $N_D$, that can be produced by the light active neutrinos and decay into a lepton pair within the detector. If the decay is prompt and produces an electron-positron pair, and considering that the MiniBooNE detector is unable to distinguish a collimated $e^+e^-$ pair from a single electron, the MiniBooNE LEE could potentially be explained by the dark neutrino model. A search for dark neutrinos decaying with an $N_D \to \nu e^+ e^-$ signature using the SBND cosmic ray tagger setup will be the focus of Chapter 10.

### 2.4.1 Model Framework

Dark neutrinos can be produced by light active neutrinos upscattering with nuclei as they propagate along the beam line. Unlike sterile neutrinos, dark neutrinos do not participate in neutrino oscillations but can decay via a new-induced dark-sector boson, $Z_D$, which couples exclusively to a dark neutrino $N_D$. The dark sector boson $Z_D$ will subsequently decay into a lepton pair, as shown in Figure 2.15.

The dark neutrino mixes with the light active neutrinos in the following manner:

$$\nu_\alpha = \sum_{i=1}^{3} U_{\alpha i}\nu_i + U_{\alpha 4}N_D,\ \alpha = e, \mu, \tau, D, \tag{2.21}$$

where $\nu_i$ and $\nu_\alpha$ are neutrino mass and flavour eigenstates respectively. The new dark-sector boson $Z_D$ interacts with the SM sector via either mass mixing or kinetic mixing, and the relevant Lagrangian can be written as,

$$\mathcal{L}_D \supset \frac{m_{Z_D}^2}{2} Z_{D\mu} Z_D^\mu + g_D Z_D^\mu \bar{\nu}_D \gamma_\mu \nu_D + e\epsilon Z_D^\mu J_\mu^{\text{em}} + \frac{g}{c_w}\epsilon' Z_D^i J_\mu^Z, \tag{2.22}$$

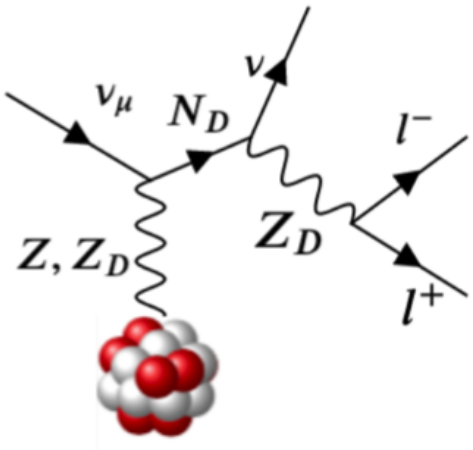


**Figure 2.15** Feynman diagram of the production and the decay of dark neutrinos.

where $m_{Z_D}$ is the mass of the $Z_D$ boson, $g_D$ is the coupling in the dark sector, $e$ is the electromagnetic coupling and $\frac{g}{c_w}$ is the $Z$ coupling in the SM. $\epsilon, \epsilon'$ characterise the kinetic and mass mixing respectively, and $J_\mu^{\text{em}}$ and $J_\mu^Z$ denote the electromagnetic and Z currents, respectively. The mixing between $Z$ and $Z_D$ is considered to be negligible for simplicity.

In the proposed dark neutrino model, the mass of the dark neutrino $m_{N_D}$ is postulated to be larger than the mass of the dark sector boson $m_{Z_D}$, allowing the dark neutrino to decay into $Z_D$ "on-shell". To explain the MiniBooNE LEE anomaly, the mass of $Z_D$ is further assumed to be smaller than the mass of two muons, $2m_\mu$, so that $Z_D$ can only decay into electrons. The decay width of $N_D \to Z_D + \nu_i$ can be written as

$$\Gamma_{N_D \to Z_D + \nu_i} = \frac{\alpha_D}{e}|U_{D4}|^2(1-|U_{D4}|^2)\frac{m_{N_D}^3}{m_{Z_D}^2}(1-\frac{m_{Z_D}^2}{m_{N_D}^2})(1+\frac{m_{Z_D}^2}{m_{N_D}^2}-2\frac{m_{Z_D}^4}{m_{N_D}^4}). \tag{2.23}$$

The decay width of $Z_D$ into an $e^+e^-$ pair can be described as

$$\Gamma_{Z_D \to e^+e^-} \approx \frac{\alpha\epsilon^2}{3} m_{Z_D}. \tag{2.24}$$

For simplicity, the model considers the case where $|U_{e4}|^2$, $|U_{\tau 4}|^2 \ll |U_{\mu 4}|^2$, and assumes the energies of the dark neutrino $E_{N_D}$ and the dark sector boson $E_{Z_D}$ are around 1 GeV. Then the lifetime of the dark neutrino becomes:

$$\gamma c \tau_{N_D} \approx 4 \times 10^{-8} m_{Z_D}^2 [\text{MeV}] \frac{1}{(m_{N_D}^4 [\text{MeV}^4] \alpha_D |U_{\mu 4}|^2)} \text{ cm}. \tag{2.25}$$

Similarly, the lifetime of dark-sector boson can be estimated as

$$\gamma c\tau_{Z_D} \approx \frac{6 \times 10^{-8}}{m^2_{Z_D}[\mathrm{MeV}^2]\alpha\epsilon^2} \text{ cm}. \tag{2.26}$$

Assuming $\alpha_D \approx 0.25$, $\alpha\epsilon^2 \approx 2 \times 10^{-10}$, $|U_{\mu 4}|^2 \approx 10^{-8}$, and 5 MeV $< m_{Z_D} < m_{N_D}$, both the dark neutrino and the dark sector boson will decay promptly. This model, in which both particles decay promptly, is considered the baseline model for comparison with the MiniBooNE data described in the following section. Moreover, the dark neutrino model has been expanded to include various scenarios. The analyses described in Chapter 10 will use the expanded models.

### 2.4.2 Model Predictions Compared with MiniBooNE Data

A few additional assumptions are needed to make predictions for comparison with the MiniBooNE results using the dark neutrino model. Firstly, the MiniBooNE detector was filled with mineral oil ($CH_2$). If the dark neutrino is light enough, the cross-section for neutrino upscattering can be enhanced by considering coherent scattering. Moreover, the high intensity of the neutrino beams also contributes to a significant production rate of dark neutrinos.

Secondly, MiniBooNE would interpret the $Z_D \rightarrow e^+e^-$ signature as electron-like events. Consequently, this signature would lead to an incorrect reconstruction of the neutrino energy using the approximate charged-current quasi-elastic (CCQE) formula as follows [107]:

$$E_\nu^{\text{reco}} \approx \frac{m_p E_{Z_D}}{m_p - E_{Z_D}(1 - \cos\theta_{Z_D})}, \tag{2.27}$$

where $m_p$ is the proton mass, $E_{Z_D}$ and $\theta_{Z_D}$ are the dark sector boson energy and its direction with respect to the beam line.

Figure 2.16 shows the reconstructed neutrino energy in both neutrino and anti-neutrino modes, as well as the angle distribution in the neutrino mode. For all plots, the SM background predictions and the data measurements reported by MiniBooNE are shown. The dark neutrino model introduces additional events in the lower energy and higher angle regions. Compared with the data, the dark neutrino model predictions are in good agreement with the experimental data, performing better than the sterile neutrino oscillation model reported by MiniBooNE, as shown in Figure 2.11.

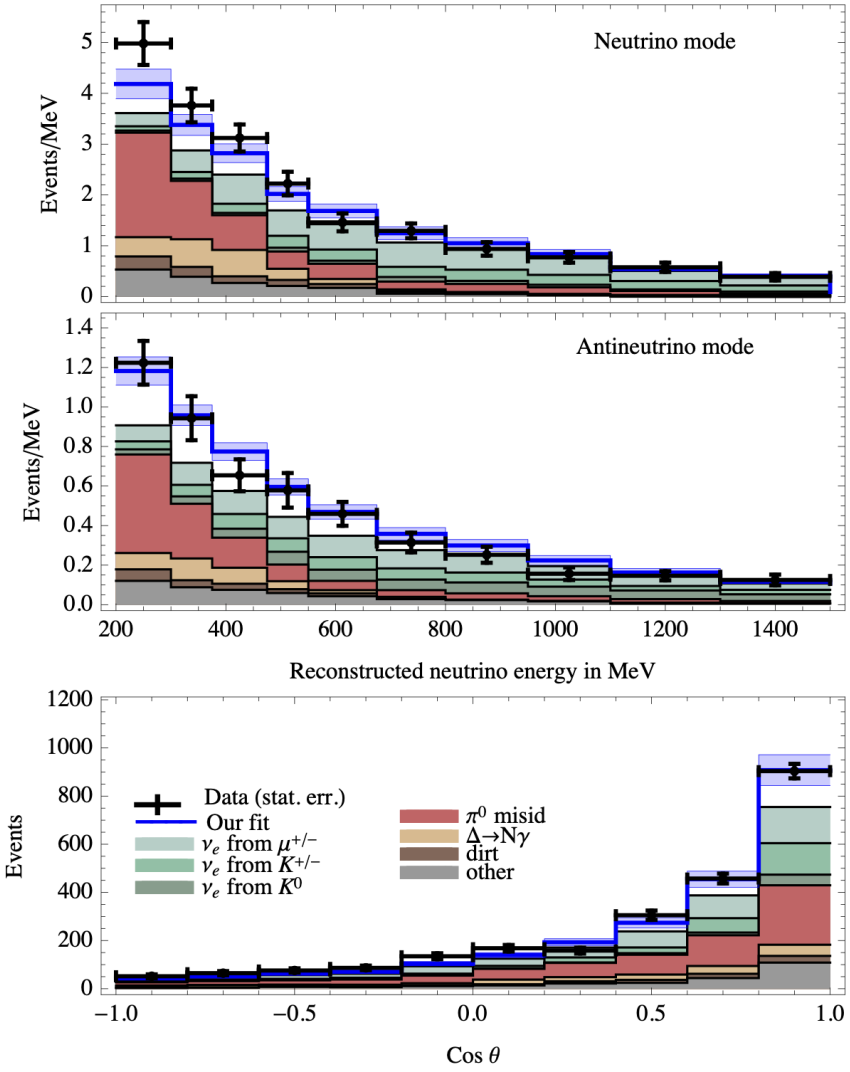


**Figure 2.16** Top (middle) panel: Reconstructed neutrino energy in neutrino (anti-neutrino) modes. Bottom panel: Reconstructed angle verses the beam line for the neutrino case. For all panels, the dark neutrino model predictions are shown as blue histograms, compared with MiniBooNE data represented by black data points. Figures from Reference [106].

The benchmark point for this dark neutrino model assumes $m_{N_D} = 420$ MeV, $m_{Z_D} = 30$ MeV, $|U_{\mu 4}|^2 = 9 \times 10^{-7}$, $\alpha_D = 0.25$, and $\alpha\epsilon^2 = 2 \times 10^{-10}$. The dark neutrino model provides a best fit with $\chi^2/\text{dof} = 33.2/36$, while the standard model background yields $\chi^2_{\text{bkg}}/\text{dof} = 63.8/38$. Thus, a $5.2\sigma$ preference can be set for the dark neutrino model [106].

### 2.4.3 Experimental Constraints

The dark neutrino model is relatively new, and direct experimental constraints have not been published yet as this thesis is written. Provided how the dark neutrino model might manifest, one can reinterpret constraints for other models with similar topologies [106].

Constraints on the mass and kinematic mixing of dark-sector bosons can be informed by results from dark photon studies [108], as dark-sector bosons predominantly decay into charged fermions. For a mass range of 20 to 60 MeV, constraints from beam dump experiments and NA48/2 [109, 110] provide useful estimates. The constraints for dark neutrinos are expected to be similar to those for heavy sterile neutrinos [109, 110]. However, experimental limits from fixed-target experiments [107, 111–114] are not applicable to the dark neutrino model, as this model assumes prompt decay.

Figure 2.17 illustrates the MiniBooNE allowed region in the $m_{N_D}$ versus $|U_{\mu 4}|^2$ parameter space, spanning from $1\sigma$ to $5\sigma$ confidence levels (C.L.). The plot is based on the assumptions $m_{Z_D} = 30$ MeV, $\alpha_D = 0.25$, and $\alpha\epsilon^2 = 2 \times 10^{-10}$. Additionally, it includes the reinterpreted experimentally excluded regions for heavy sterile neutrinos from meson decays, the muon decay Michel spectrum, and lepton universality constraints. The area above the red curve is excluded at 99% C.L.

## 2.5 Beyond Dark Neutrinos: Model-independent Searches

The dark neutrino model from the dark sector offers a potential explanation for the MiniBooNE LEE. Over the past decade, numerous BSM physics models, including dark neutrinos in the MeV-GeV range, have been proposed to address the MiniBooNE LEE anomaly and other outstanding questions in particle physics, such as the origin of neutrino mass, dark matter, and the muon anomalous magnetic moment [115, 116]. So far, searches for BSM physics have traditionally relied heavily on predictions from specific models, which can limit the scope and flexibility of new physics searches. Since many BSM models, such as heavy neutral leptons [117], axion-like particles [118, 119], and Higgs portal scalars [120], can predict the same final state (e.g., an $e^+e^-$ pair), a more flexible theoretical framework for model-independent searches has been proposed [121]. This framework aims to unify BSM searches regardless of specific theoretical models.

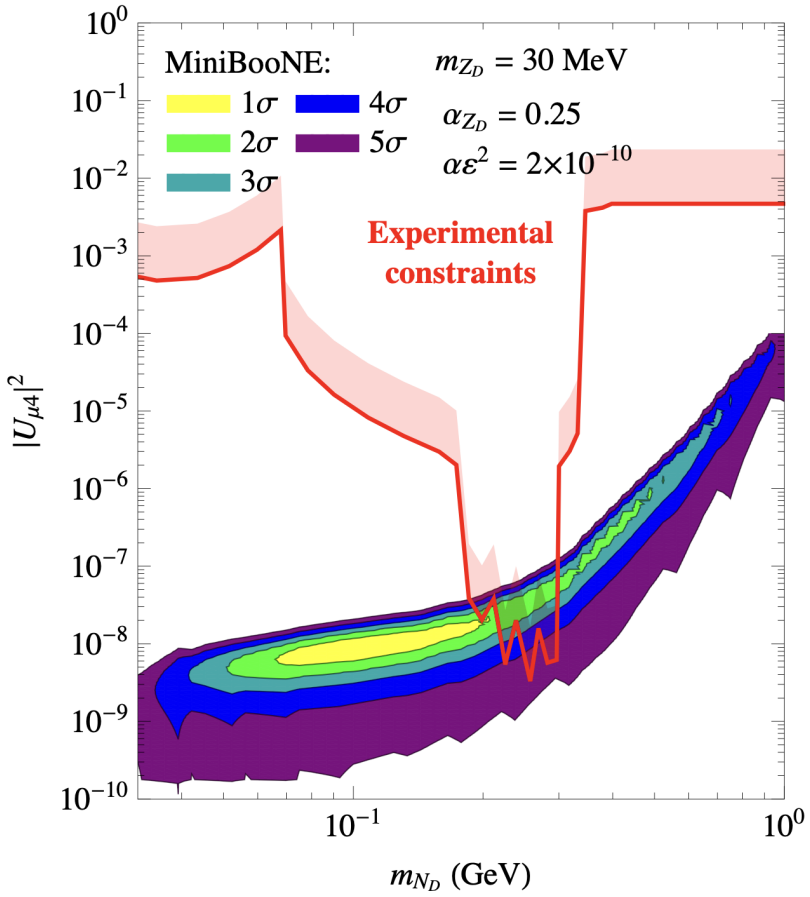


**Figure 2.17** The MiniBooNE allowed region in the $m_{N_D}$ versus $|U_{\mu 4}|^2$ parameter space from $1\sigma$ to $5\sigma$ C.L. The experimental constraints interpreted from other models are also shown here, and the region above the red curve is excluded at 99% C.L. Figures from Reference [106].

In parallel, accelerator-based neutrino beam experiments offer a unified approach to produce BSM particles, as they can be abundantly generated in the intense proton collisions with a fixed target. This strengthens the potential for model-independent searches. Theoretically, BSM particles can be produced alongside SM particles or via interactions with SM particles. In the model-independent framework, a generic long-lived particle (LLP) $X$ is proposed as a representative of all BSM particles. Although the dark neutrino model was initially proposed to decay promptly to explain the MiniBooNE LEE, different parameters within the model can be redefined. By adjusting these parameters according to Equation 2.25, the dark neutrino lifetime can be extended to a long-lived scenario. With the framework introduced in the next section, the results from dark neutrino searches can be expanded to a model-independent search. A model-independent search will be further discussed in Chapter 11.

The model-independent approach serves as a bridge between model-specific studies and various other models, maximising the potential of the detector by broadening the scope of discovery. By extending the framework to a model-independent search, it allows for the identification of potential new physics in unexpected areas or through novel signatures that may not be predicted by any particular model. If such a model-independent search uncovers anomalies or unexplained phenomena, it can be used as a base to guide the development of new BSM theories.

### 2.5.1 Model Description

In the proposed framework in [121], the production process involves a SM meson $\mathfrak{M}$, which is generated from proton collisions with a target, generating a LLP $X$ through interaction or decay. The $X$ particle subsequently decays into one or more SM final states $F$ via $X \to F$. The final state $F$ is typically assumed to be distinct from SM backgrounds, such as those from cosmic rays and neutrino interactions. To perform a model-independent search, the key step is to define what quantities are relevant and can directly determine the signal rates and kinematics of final stets. The extracted quantities from the signal rate calculation are:

- **Br($\mathfrak{M} \to X$)**: The branching ratio represents the probability of an SM meson $\mathfrak{M}$ decaying into the LLP $X$.
- **The signal of interest** $F$: Whether $F$ is a fully-visible final state for the detector or if particles like neutrinos are present in the final state, making $F$ partially visible. The branching ratio Br($X \to F$) represents the probability of the $X$ particle decaying into a fully-visible final state $F$ and is relevant for the signal rate calculation.
- $m_X$: The mass of the $X$ particle. Both the boost $\gamma_X$ and the spectrum of $X$ particle from $\mathfrak{M} \to X$ can be influenced by the mass.
- $c\tau_x$: The lifetime of $X$ particle.

The quantities mentioned above can be translated into experimental observables. Considering the final state is an $e^+e^-$ pair, the invariant mass $m_{e^+e^-}$ can be used to estimate the parent mass $m_X$. In both fully visible and partially visible cases, $m_{e^+e^-}$ is expected to be smaller than $m_X$. The energy distribution $E_{e^+e^-}$ is related to the lifetime $c\tau_X$ of the $X$ particle, making it useful for measurement. A short- or long-lived $X$ particle will tend to favour a larger or smaller $E_{e^+e^-}$, respectively, which helps determine whether the $X$ particle can travel to and decay within the detector.

Additionally, the opening angle between the final state particles depends on whether the decay is fully or partially visible. Therefore, this angle provides insights into different hypotheses, allowing for model discrimination and aiding in determining the correct branching ratio $\mathrm{Br}(X \to F)$.

A model-independent search can serve as a bridge to connect results from model-specific studies to different models. Using the simplified long-lived neutral scalar $S$ as an example, if one considers the $K$-meson as a source to produce the $X$ particle that then decays into an $e^+e^-$ pair, the Lagrangian of scalar $S$ describing both production and decay can be expressed as [121]:

$$\begin{aligned}\mathcal{L} \supset & -\frac{1}{2}m_s^2 S^2 - g_{k\pi} S \pi^- K^+ + h.c \\ & - g_e S \bar{e} e - g_\chi S \overline{\chi} \chi,\end{aligned} \tag{2.28}$$

where $g_{k\pi}$ and $g_e$ are the effective couplings for the kaon decay into $S$ and for $S$ decaying into an $e^+e^-$ pair, respectively. The last term, related to $g_\chi$, describes the decay of $S$ into dark matter pairs if kinematically allowed. Parameters, such as $g_{k\pi}$ and $g_e$, in the Lagrangian can be mapped onto parameters specific to other models. The Lagrangian of a generalised fermion model can be constructed similarly.

By using a simplified Lagrangian as a bridge, parameters in Equation 2.28 can be mapped onto specific model parameters and vice versa, facilitating straightforward interpretation of results across different models and model-independent studies. This approach is useful for consolidating constraints from various models into a unified framework and for assessing whether new results from emerging models are consistent with well-studied minimal models, such as heavy neutral leptons and Higgs portal scalars.

### 2.5.2 Experimental Constraints

Model-independent constraints and sensitivities can be reinterpreted from existing results using the simplified framework. For instance, considering the $K$-meson as a source that produces the $X$ particle, which then decays into an $e^+e^-$ pair, constraints from Higgs portal scalars as observed in MicroBooNE [122] and from heavy neutral leptons as observed in T2K [123] can be applied to this framework for constraint calculations. Similarly, sensitivity projections for future experiments, such as the DUNE near detector, can also be estimated using these models.

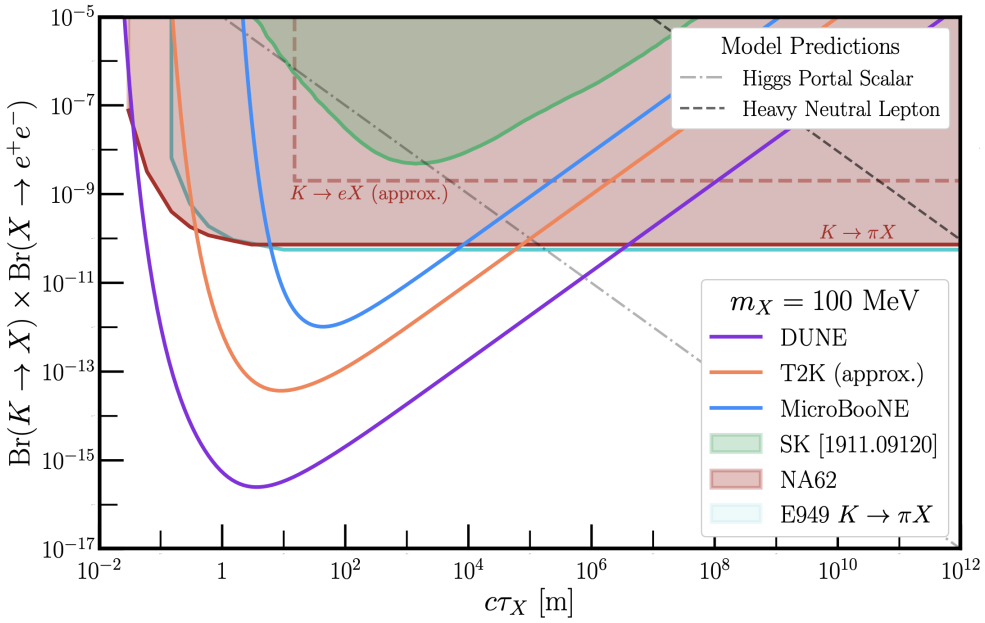


**Figure 2.18** Constraints and sensitivity in LLP lifetime $c\tau_X$ and the product of branching ratios $\mathrm{Br}(\mathfrak{M} \to X) \times \mathrm{Br}(X \to F)$ phase space, calculated from the model-independent framework for T2K, MicroBooNE and DUNE near detector, compared with the existing results. Dashed black and dot-dashed grey lines indicate the predictions from heavy neutral leptons and Higgs portal scalars models. Figures are from Reference [121].

The constraints and sensitivities can be mapped as functions of the LLP lifetime $c\tau_X$ and the product of branching ratios $\mathrm{Br}(\mathfrak{M} \to X) \times \mathrm{Br}(X \to F)$. Figure 2.18 shows the reinterpreted constraints from MicroBooNE and T2K, along with the DUNE sensitivity for a chosen $X$ mass of 100 MeV; results for other mass assumptions can be found in [121]. These constraints and sensitivities are compared with existing results from Super-Kamiokande [124], E949 [125, 126], and NA62 [127–129]. Additionally, predictions from generic heavy neutral lepton and Higgs portal scalar models are illustrated as dashed black and dot-dashed grey lines, respectively.

Looking ahead, neutrino beam experiments are strong candidates for exploring the potential of using the simplified framework for BSM searches with current and upcoming data. This approach enables us to search for new physics in a broad manner. Generic long-lived particle searches with neutrino beam experiments can potentially enhance our chances of discovering new physics.

## 2.6 Summary

Neutrinos are particle that have a very interesting history with many challenges along the way, from the the discovery of the particle, three light active flavours, and oscillations. Several outstanding problems related to neutrinos are still present in modern physics. Motivated by the short-baseline anomalies observed in the LSND and MiniBooNE experiments have led to the birth of many new models of BSM physics including the dark neutrino model was proposed, and the underlying framework of this model was discussed. The dark neutrino model provides a compelling explanation for the MiniBooNE LEE observation. Building on this, the search for specific models can be extended to a model-independent approach, which allows experiments to explore a wide variety of different BSM models that predict similar SM signatures in accelerator-based neutrino beam experiments. This approach maximises the potential of the detector for BSM searches and can also serve as a bridge to connect results from model-specific studies to different models.

# 3

# Particle Interactions in Scintillators

Scintillators are some of the most widely used ionising radiation detectors, converting deposited energy into scintillation light which can be registered with optical detectors. Both polystyrene and liquid argon are examples of scintillators and are commonly employed for this purpose. Polystyrene is used as a scintillator in the detector setup for the work and analyses conducted by the author, as detailed in Chapter 8, Chapter 9, Chapter 10, and Chapter 11. Nowadays, liquid argon is commonly chosen for neutrino detection, and the Liquid Argon Time Projection Chamber (LArTPC) is the technology employed for the analysis in Chapter 6. Moreover, in liquid argon, a drift electric field can be applied allowing a portion of the deposited energy to produce ionised electrons, providing an additional signal for detection.

This chapter will first provide an overview of energy deposition in scintillators, highlighting differences in energy deposition with various particles. Then, the chapter will describe the production of scintillation light in both polystyrene and liquid argon, along with associated effects affecting its propagation. It will then explore the production and propagation of ionised electrons in liquid argon in the presence of a drift electric field.

## 3.1 Energy Deposition in Scintillators

Scintillators, as absorbing materials, convert the energy of an incident charged particle or energetic photon (UV, X-ray and gamma-ray) into a number of photons with much lower energy, usually in (or near) the visible spectrum. The scintillation photons can then be detected by photomultipliers, or other optical detectors. Therefore, scintillation materials such as Polystyrene and liquid argon are widely employed in particle detection. Different types of particles interact with scintillation media in different ways. Charged particles deposit energy by directly interacting with electrons of the scintillator medium through Coulomb interactions. Neutral particles can only be detected when they directly interact with a nucleus and produce daughter charged particles. By reconstructing all daughter particles, a neutral particle can often be identified.

The mean energy deposition of a charged particle per unit travel distance ($dE/dx$) is well described by the Bethe-Bloch formula [38]:

$$-<\frac{dE}{dx}>=Kz^2\frac{Z}{A}\rho\frac{nz^2}{\beta^2}\left(\frac{1}{2}\ln\frac{2m_ec^2\beta^2\gamma^2W_{\max}}{I^2}-\beta^2-\frac{\delta(\beta\gamma)}{2}\right), \tag{3.1}$$

where $K=4\pi N_A r_e^2 m_e c^2$ is a numerical conversion factor and has a value of 0.307075 $\mathrm{MeVg}^{-1}cm^2$, here $N_A$ is Avogadro's number and $r_e$ is the classical electron radius. $z$ is the charge of the incident particle, $Z$, $A$, and $\rho$ are the atomic number, charge number and density of the medium, $\beta=v/c$ of the incident particle, $\gamma$ is the Lorentz factor ($\gamma=1/\sqrt{1-\beta^2}$), $m_e$ is the electron mass, $I$ is the mean excitation energy, and $\delta(\beta\gamma)$ is the correction for density effects on the energy loss, $W_{max}$ is the maximum kinetic energy transfer in a single collision and can be expressed by:

$$W_{max}=\frac{2m_ev^2}{1+2\gamma m_e/M+(m_e/M)^2}. \tag{3.2}$$

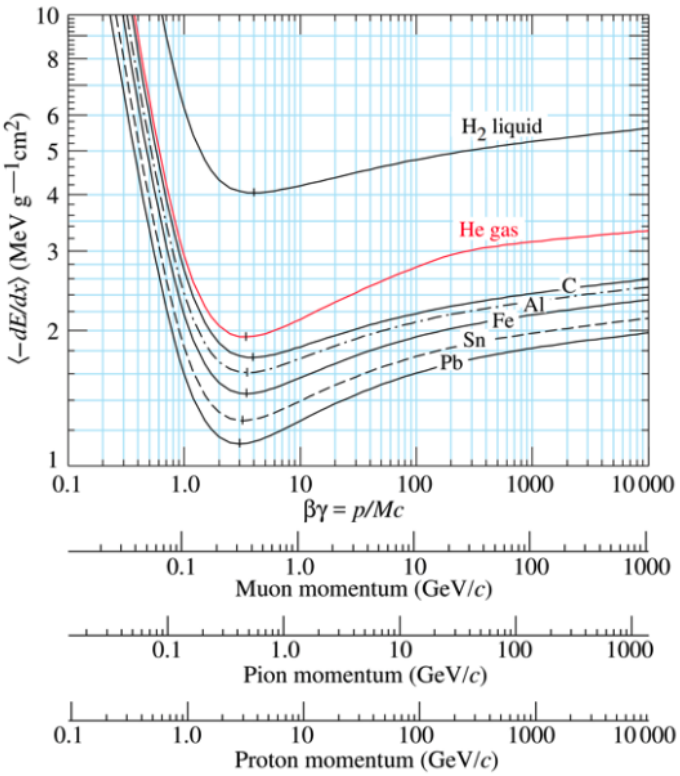


**Figure 3.1** Bethe-Bloch curves illustrating the mean energy deposited, $\frac{dE}{dx}$, by charged particles, such as muons, pions, and protons, as a function of their momentum. Black dots represent the data from proton candidates. Figure from Reference [48]

Figure 3.1 demonstrates Bethe-Bloch curves for muons, pions, and protons in different media. The $x$-axes indicate the corresponding momentum range for each particle. In the moderate $\beta\gamma$ region, the average energy loss reaches a minimum, and particles in this region are referred to as Minimally Ionising Particles (MIPs). It is noteworthy that the mean energy loss for different particles in the MIP region is the same in the same medium. At lower $\beta\gamma$ values, the mean energy loss increases rapidly. Therefore, as a particle travels and deposits energy, its energy decreases towards the low-energy region. With increasing deceleration, the particle eventually experiences a sudden stop, resulting in a significant amount of energy deposition, towards the end, usually called the Bragg peak.

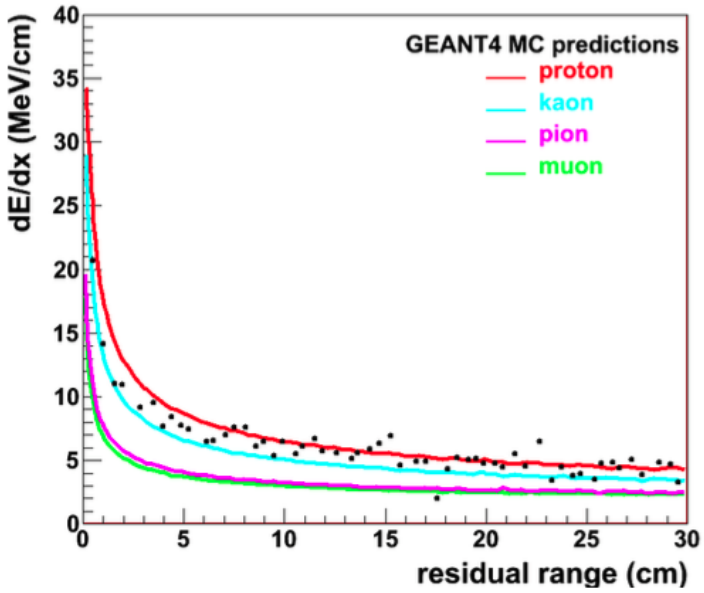


**Figure 3.2** Energy loss as a function of residual range in liquid argon, for muons, pions, kaons and protons. Figure from Reference [130].

In the energy region of a few hundred MeV, as shown in Figure 3.1, muons and pions are predominantly produced in the MIP region, while protons are in the steeply rising part of the curve. This indicates that protons will deposit more energy than MIPs in this energy region. Because of this, the particles of deposited energy can be utilised for particle identification. Figure 3.2 provides an example of using energy loss as a function of the residual range—the distance to the end of particle propagation—in liquid argon to identify different particles.

## 3.2 Scintillation Light

For particle detection, it is crucial to understand the efficiency of scintillation light, its emission wavelength, and the factors that can affect its propagation. This section will discuss these aspects for both polystyrene-based scintillators and liquid argon.

### 3.2.1 Scintillation light in Plastic scintillators

The development of plastic scintillator detectors dates back to the early 1950s [131]. Today, these detectors are widely used in high-energy physics, particularly for particle tracking [132, 133]. Plastic scintillators are composed of hydrocarbon-based molecules and can emit scintillation light in the visible wavelength range with high efficiency. Although plastic scintillators are not fully transparent to their own scintillation light, the prompt production of scintillation light allows for sub-nanosecond measurements of particle interactions with the detector.

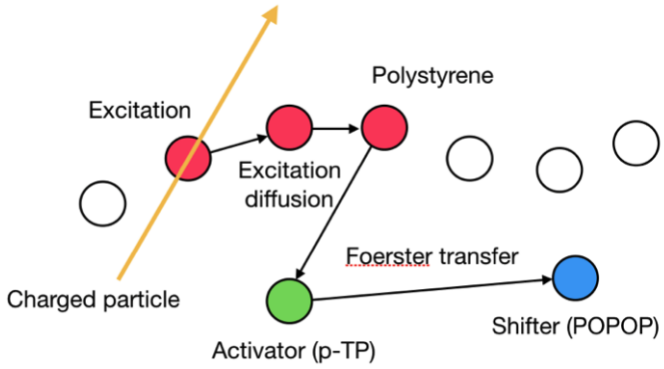


**Figure 3.3** Schematic representation of energy transfer in plastic scintillator. Figure from Reference [134]

Figure 3.3 schematically illustrates the mechanism of transferring deposited energy to scintillation material and producing scintillation light in plastic scintillator. This process occurs in several steps. First, an energetic charged particle interacts with the plastic scintillator, and the deposited energy excites the polymer matrix molecules. This energy is then transferred to the activator through a resonant dipole-dipole interaction known as the Förster mechanism. This mechanism creates a strong bond between the polymer base and the activator, enhancing the light yield of the plastic scintillator and reducing the delay of light emission. The scintillation light emission spectrum is defined by the non-radiative collection ability of the polymer-based excitation energy. The WLS, acting as the second dopant, further shifts the wavelength of the emitted scintillation light to maximise the material's transparency to the emitted light.

Polystyrene is one of the typical materials used for plastic scintillators. For the past 50 years, a well-defined composition has involved introducing an activator molecule, such as Diphenylbenzene (PTP), into the polymer at a concentration of approximately 2% by weight [134]. Additionally, a wavelength shifter (WLS) material, such as Bis(5-phenyl-2-oxazolyl)benzene (POPOP), is typically added at around 0.04% in polystyrene-based scintillators to shift the wavelength of the light emitted by PTP to a range where normal photon detectors are more sensitive [133]. The scintillation light emission spectrum is measured to peak at 430 nm with 1.5% PTP as the activator and 0.04% POPOP as the WLS dopant in polystyrene-based scintillator [133].

For scintillators, a crucial optical parameter is the Bulk Attenuation Length (BAL), which measures the transparency of the scintillator material to its own emitted light. The BAL for a polystyrene-based scintillator with 1.5% PTP as the activator and 0.04% POPOP as the WLS dopant is measured to be 7.5 cm [133]. If polystyrene is used in a detector where a large transportation length of the scintillation light is expected, additional WLS may be necessary to enhance the light transmission.

#### Quenching in Plastic Scintillator

For low densities of energy loss, the scintillation yield (the amount of scintillation light produced) is linearly proportional to the deposited energy. However, as the density of energy loss increases, various processes hinder the production of scintillation light, leading to a non-linear response to the deposited energy. The scintillation yield per unit of distance travelled can be expressed as [135]:

$$\frac{dL}{dx} = \epsilon \cdot S \cdot Q(\epsilon), \tag{3.3}$$

where $\epsilon$ denotes energy lost by a particle per unit of distance $dE/dx$, $S$ represents the linear proportionality between light yield and energy deposition at high energy, measured in units of photons per unit energy, and $Q(\epsilon)$ is defined as a unitless quenching function, which approaches unity at small $\epsilon$.

Birks developed the first model to explain the ionisation quenching in the early 1950s, the quenching function can be expressed as [136]:

$$Q_{\text{Birks}}(\epsilon) = 1/(1 + kB\epsilon), \tag{3.4}$$

where $kB$ is a numerical parameter commonly referred to as Birks' coefficient. Several other models have been proposed as extensions to Birks' model. Chou et al. considered secondary effects in their model [137]. Wright et al. introduced a phenomenological quenching function [138], and Voltz et al. developed a model that distinguishes between primary and secondary ionisation [139].

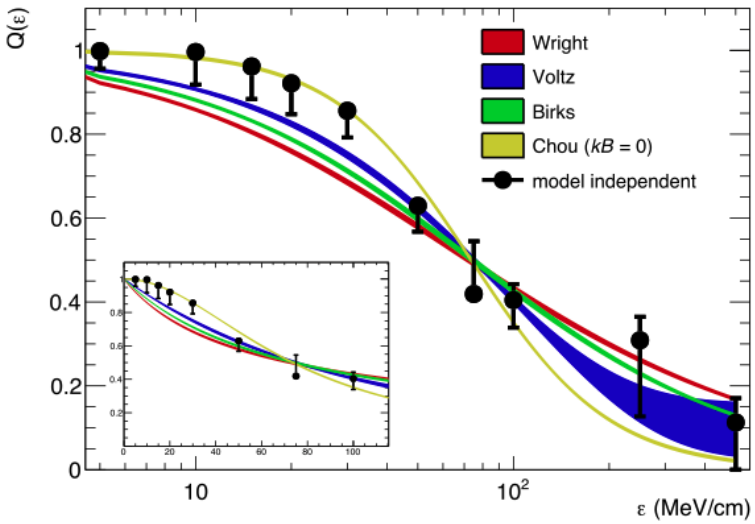


**Figure 3.4** Quenching as a function of deposited energy $\epsilon$ for a plastic scintillator material of SCSF-78, which is a polystyrene-based material. Figure from Reference [135].

Figure 3.4 shows predictions of the quenching function from different models, compared with data in a polystyrene-based material. The quenching function causes the amount of scintillation light to decrease as the deposited energy increases.

### 3.2.2 Scintillation Light in Liquid Argon

Liquid argon is an excellent scintillator since it produces around 40,000 photons per MeV. In liquid argon, as depicted in Figure 3.5, deposited energy can lead to the formation of an argon dimer, $Ar_2^*$, through excitation, or ionisation followed by electron recombination. When the argon dimer de-excites, it will revert back to separate argon atoms while simultaneously emitting scintillation light. The photons are emitted in the Vacuum Ultra-Violet (VUV) range, peaking at about 128 nm with a width of approximately 10 nm [140, 141].

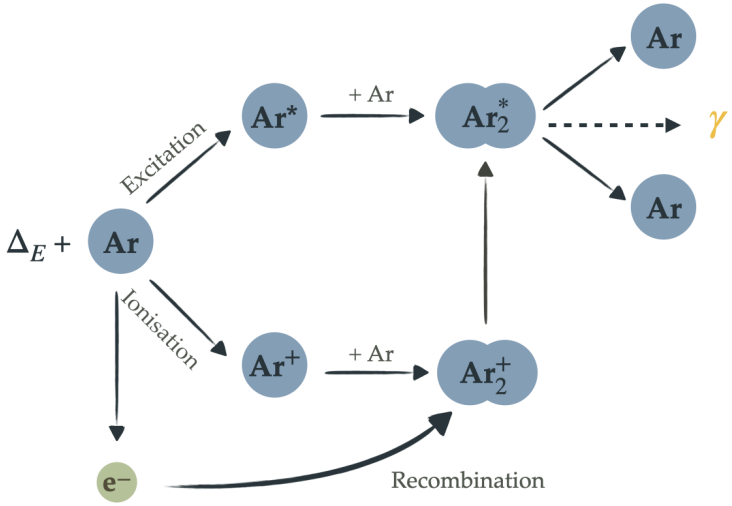


**Figure 3.5** Schematic representation of ionisation and excitation process in liquid argon.

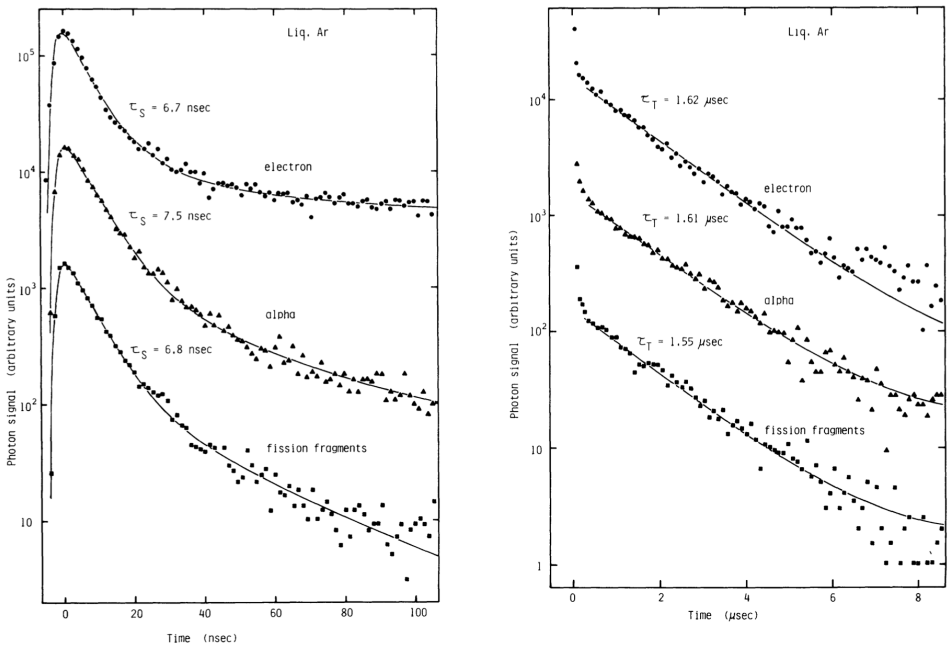


**Figure 3.6** De-excitation time distribution of the scintillation light from the singlet (left) and triplet (right) excited states of argon dimer. Cases from different particles are presented. Figure taken from Reference [142].

There are two excited states for the excited argon dimer, referred to as a singlet state ${}^1\Sigma_u^+$ and a triplet state ${}^3\Sigma_u^+$. These two states are different due to the coupling between the spin of the electron and argon dimer in the Rydberg atom [143]. Figure 3.6 shows the time distribution of emitted simulation light for both states. The decay time of the singlet and triplet states is measured to be $\tau_1 \approx 6$ ns and $\tau_3 \approx$ 1,000 - 1,700 ns [142]. These are normally referred to as fast (prompt) and slow (late) components of scintillation light.

Ionising quenching due to high ionisation density also occurs in liquid argon [144]. Consequently, the scintillation yield varies for different particles. The ratio between the fast and slow components of scintillation light also depends on ionisation density, making it a useful method for particle discrimination at low energies corresponding to dark matter searche [145].

### Rayleigh Scattering

Liquid argon is transparent to its own scintillation light, allowing scintillation photons to travel long distances until they are either absorbed or detected by a photon detector. The mean free path of these photons is primarily influenced by Rayleigh scattering. Rayleigh scattering occurs when the wavelength of the photon is much larger than the particle size of the medium. This scattering process does not change the number of propagating photons but alters their paths. Consequently, compared to a photon that takes a direct path, a scattered photon experiences a delay in arrival time. Additionally, depending on the emission position within the detector, Rayleigh scattering can either increase or decrease the probability of light reaching the photon detectors.

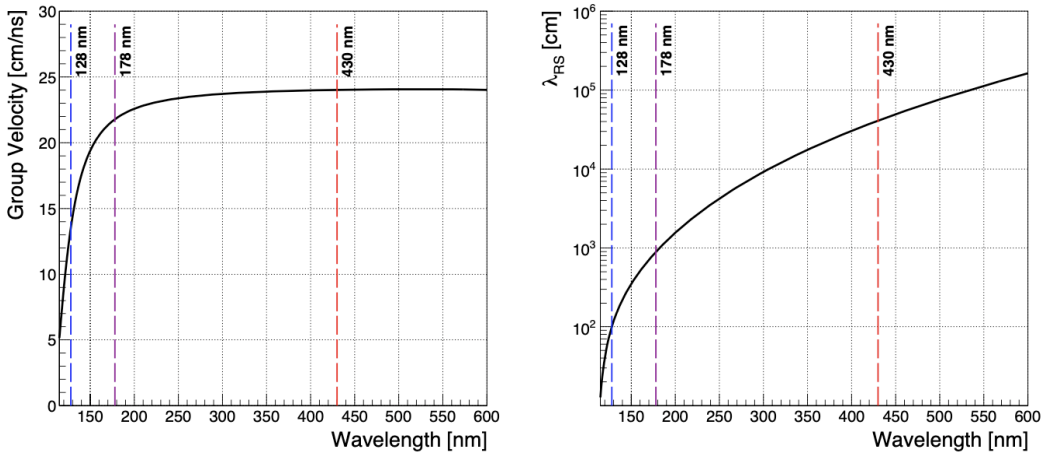


**Figure 3.7** Group velocity (left) and Rayleigh scattering length $\lambda_{RS}$ (right) as a function of the photon wavelength. The lines at 128 nm, 178 nm, and 430 nm corresponds to scintillation light in argon, liquid xenon and visible light. Figure from Reference [146].

Several measurements and theoretical predictions have reported the Rayleigh scattering length in liquid argon $\lambda_{RS}$ with values ranging from 50 cm [147, 148] to 110 cm [149]. The most recent measurement reports a value of 99.1 $\pm$ 2.3 cm for 128 nm scintillation light [150]. Figure 3.7 shows the group velocity and Rayleigh scattering length as a function of the photon wavelength in liquid argon. The group velocity of argon scintillation light is approximately half as fast as that of visible light. The Rayleigh scattering length for argon scintillation light is much shorter than that for xenon scintillation light and visible light. Therefore, for detectors using liquid argon as the medium, the effect of Rayleigh scattering becomes more significant as the size of the detector increases, since photons will need to travel distances on the order of $\lambda_{RS}$, leading to non-negligible effects.

#### Light Quenching and Absorption due to Impurities

Argon is transparent to its own scintillation light because the emitted photons are not energetic enough to re-excite the argon bulk. However, if impurities such as nitrogen and oxygen are present in liquid argon, the scintillation yield can be affected through absorption and quenching. The primary physical process to consider for quenching involves two-body collisions between impurities and the $Ar_2^*$ dimer excited states. Using nitrogen as an example [151]:

$$Ar_2^* + N_2 \rightarrow 2Ar + N_2. \tag{3.5}$$

Non-radical collisions disrupt the de-excitation process that emits scintillation photons. The slow component of scintillation light is more affected by impurities than the fast component because there is more time available for collisions to occur. Figure 3.8 demonstrates this effect with varying levels of nitrogen contamination. As the level of nitrogen contamination increases, the time constant of the slow component significantly decreases.

Absorption, on the other hand, refers to the process in which produced scintillation light is absorbed by impurities during propagation. Measurement of the absorption of nitrogen impurities in LArTPC shows that the absorption effect is relatively weak compared to other processes [153]. The quenching effect, however, becomes significant when the nitrogen concentration exceeds $\mathcal{O}(1$ parts per million (ppm)) and $\mathcal{O}(0.1$ ppm) for oxygen [154].

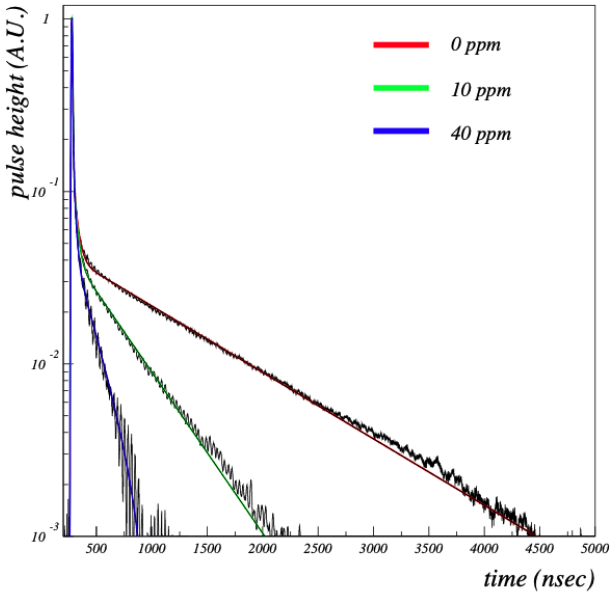


**Figure 3.8** Signal pulse of scintillation light at different levels of nitrogen contamination. Figure from Reference [152].

## 3.3 Ionisation Signal in Liquid Argon

As shown in Figure 3.5, during the ionisation process that produces scintillation light, an ionisation pair consisting of $e^-$ and $Ar^+$ is generated. In liquid argon, the energy required to produce an ionisation pair is 23.6 eV [155, 156]. Therefore, approximately 40,000 ionisation pairs can be produced per MeV of deposited energy. The electron and $Ar^+$ can recombine to form the argon dimer, resulting in the production of scintillation light. If a uniform electric field is applied, a fraction of the ionisation pairs can escape recombination. The electron will drift away from the $Ar^+$ along the field direction and can be detected by electron-sensitive detectors.

### 3.3.1 Recombination Effect

The recombination process affects the number of detected electrons and is highly dependent on both the strength of the external electric field [157] and the ionisation density [158]. Figure 3.9 shows the ionisation charge detected per unit length ($dQ/dx$) as a function of deposited energy per unit length ($dE/dx$) under different electric field strengths. As the electric field strength increases, the recombination effect decreases because a stronger field more effectively separates electrons from ions, allowing more electrons to be detected.

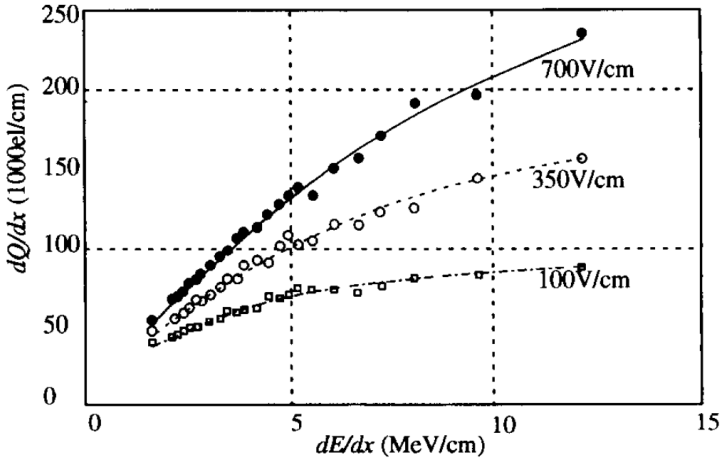


**Figure 3.9** Ionisation charge detected per unit length ($dQ/dx$) as a function of the deposited energy per unit length ($dE/dx$), with different electric field strengths applied. Figure from Reference [159].

Conversely, for a given electric field, particles with higher ionisation densities, such as protons, experience increased recombination because the higher ionisation density reduces the distance between electrons and ions. Despite the increased recombination, the detected ionisation charge can still be significant due to the larger production of ionisation charge associated with higher energy deposition. As illustrated in Figure 3.9, a non-linear relationship between $dQ/dx$ and $dE/dx$ is observed for a given electric field. This is the result of the combined effects of recombination and large energy deposition.

The relationship between $dQ/dx$ and $dE/dx$ with the recombination effect can be described using either the semi-empirical Birks' model [136] or the modified Box model [158, 160].

#### Charge-light Anti-correlations

The recombination effect also influences the production of scintillation light because both scintillation light and ionisation charge are produced by the deposited energy, with recombination playing a significant role. For a given charged particle traversing liquid argon with a fixed amount of deposited energy, a stronger electric field increases the amount of ionisation charge ($Q$) while decreasing the scintillation light ($L$). This anti-correlation relationship is illustrated in Figure 3.10 for three different noble gases—argon, xenon, and krypton [143]. By carefully selecting the electric field strength, the ratio of ionisation charge to scintillation light ($Q/L$) can be optimally tailored for a detector.

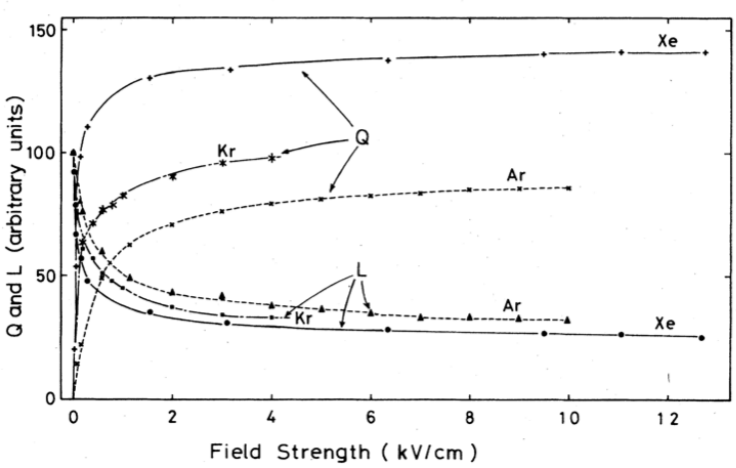


**Figure 3.10** Anti-correlation relation between charge yield (Q) and light yield (L) for argon, xenon and krypton as a function of applied electric filed. Figure from Reference [143].

### 3.3.2 Diffusion

While propagating through the liquid argon, the distribution of ionised electrons can spread out from a point source, as shown in Figure 3.11. This diffusion is not isotropic due to the presence of the electric field and is typically characterised by two components: **transverse diffusion**, which is perpendicular to the drift direction, and **longitudinal diffusion**, which is parallel to the drift direction.

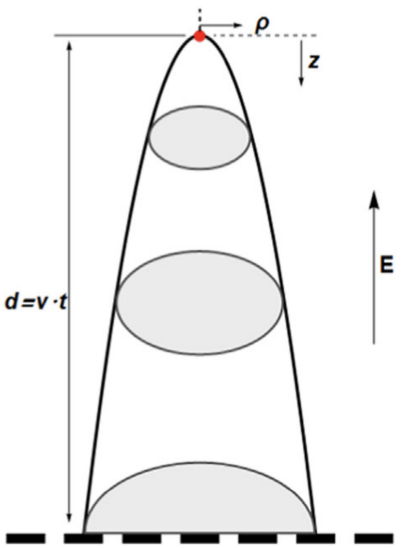


**Figure 3.11** A schematic diagram of the diffusion process from a point source to the detection plane, as indicated by dashed lines. Figure from Reference [161].

The longitudinal diffusion is characterised by a constant $D_L$, and the width of a signal

pulse $\sigma_t(t)$ at a given time $t$ can be expressed by [161, 162]:

$$\sigma_t^2(t) \simeq \sigma_t^2(0) + \left(\frac{2D_L}{v_d^2}\right) t, \tag{3.6}$$

where $v_d$ is the drift velocity, and $\sigma_t^2(0) \sim 1.96\ \mu s^2$ is the minimum width for the pulses. Based on Equation 3.6, ionised electrons far from the detectors are most affected since they have to travel longer distances. The longitudinal diffusion results in the spreading of the signal in time upon detection.

The transverse diffusion is characterised by the transverse diffusion constant, $D_T$, expressed using the Atrazhev and Timoshikin model as [163]:

$$D_T = \frac{\mu \epsilon_L}{e}, \tag{3.7}$$

where $\mu$ is the electron mobility, $e$ is the electron charge, and $\epsilon_L$ is the energy of the electron. The transverse diffusion causes the point charge to spread out perpendicularly to the drift direction.

### 3.3.3 Space Charge Effect

As the electrons drift towards the detector, the ions move simultaneously in the opposite direction but at a much slower speed (approximately 4 mm/s [164], compared to an electron drift velocity of around 1.1 mm/$\mu$s [165]). Due to thermal flows in the detector, which have very similar velocities, these slowly drifting $Ar^+$ ions can accumulate in the detector, resulting in a non-negligible distortion of the electric field. This distortion is commonly referred to as the Space Charge Effect (SCE). Correcting for this distortion is essential for accurately reconstructing the initial positions of the ionised electrons.

Figure 3.12 illustrates the impact of the SCE on the reconstruction of the start and end positions (blue dots) for cosmic muons compared to the detector boundaries (black dashed line). As shown in the left plot, the electric field distortion caused by the SCE leads to deviations in the reconstructed positions from the actual detector boundaries. Fortunately, the SCE can be corrected for. As shown in the right plot, the reconstructed start and end positions of the tracks align with the detector boundaries once the SCE correction is applied.

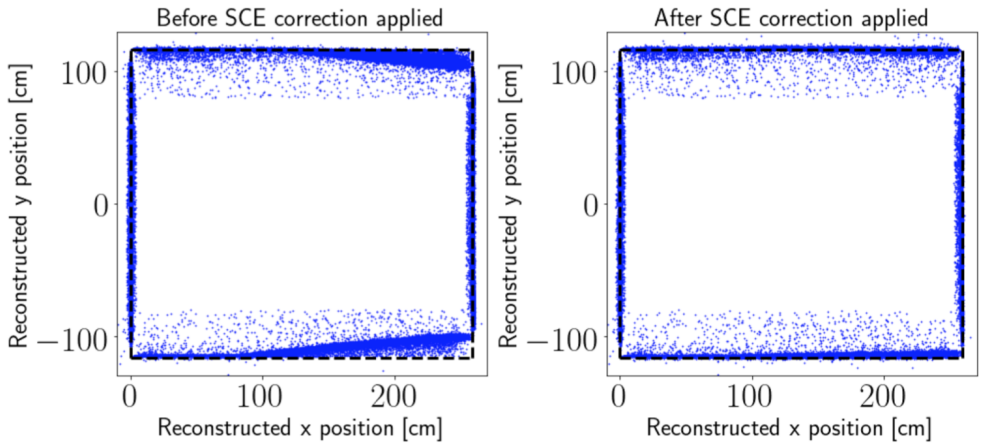


**Figure 3.12** Reconstructed start and end positions (blue dots) of cosmic muons before (left) and after (right) SCE correction. Left: the SCE introduces a bias in the reconstruction, causing the start and end positions to deviate from the detector boundaries, as indicated by the black dashed line. Right: after SCE correction, the start and end positions are aligned with the detector boundaries. Figure from Reference [166].

### 3.3.4 Impurities in Liquid Argon

In reality, impurities such as oxygen and water are commonly found in liquid argon. When electrons drift under an electric field, they can attach to these impurities, thereby reducing the number of electrons detected [167, 168]. This attachment impacts particle reconstruction in detectors which rely on ionised electrons. The strength of this effect can be modelled as an exponential suppression, known as the **electron lifetime**.

Currently, for detectors using liquid argon, the purity of the argon is monitored using electron lifetime as a key metric. Additionally, detectors are generally equipped with sophisticated argon purification systems to control the level of impurities. The purity of argon is typically maintained at levels in the parts per trillion (ppt) range, which ensures that the electron lifetime is usually on the order of a few milliseconds.

## 3.4 Summary

This chapter introduced two commonly used scintillator materials in particle physics detectors: polystyrene and liquid argon. Both materials detect particles based on the energy deposited as the particles traverse the scintillator. This chapter discussed the physical processes that influence scintillation light propagation, such as quenching and Rayleigh scattering. Additionally, in liquid argon, the application of an external electric field converts a portion of the deposited energy into ionised electrons, providing a secondary signal alongside the scintillation light. Physical processes which can affect the propagation of ionised electrons were also addressed in this chapter.

# 4

# The Short-Baseline Neutrino Program and Selected LArTPC Detectors

The Short-Baseline Neutrino (SBN) program at Fermilab aims to address the long-standing question of the potential existence of sterile neutrinos with a mass scale around 1 eV, as suggested by phenomena such as the MiniBooNE low-energy excess. The program consists of three LArTPC detectors: the Short-Baseline Near Detector (SBND), the intermediate detector: MicroBooNE, and the far detector: ICARUS T600.

This chapter will first introduce the SBN program and its associated neutrino beam, the Booster Neutrino Beam (BNB). It will then discuss the LArTPC technology chosen for the program with a focus on the two experiments relevant to this thesis: MicroBooNE and SBND.

## 4.1 The Short-Baseline Neutrino Program at Fermilab

Three detectors in the SBN program, SBND, MicroBooNE, and ICARUS, are positioned along the BNB line with baselines of 110 m, 470 m, and 600 m, respectively, as illustrated in Figure 4.1. Together, these experiments will measure neutrino oscillations with the goal of searching for short-baseline oscillations, which could be caused by sterile neutrinos. Evidence for sterile neutrinos would be indicated by observing $\nu_e$ appearance correlated with $\nu_\mu$ disappearance in a $\nu_\mu$-dominated beam.

The SBN program is designed to investigate both channels and aims to definitively address the short-baseline neutrino anomalies, described in Chapter 2.3.4. By using the same neutrino beam and detector technology across all three experiments, the SBN program can effectively minimise systematic uncertainties reaching the needed sensitivity.

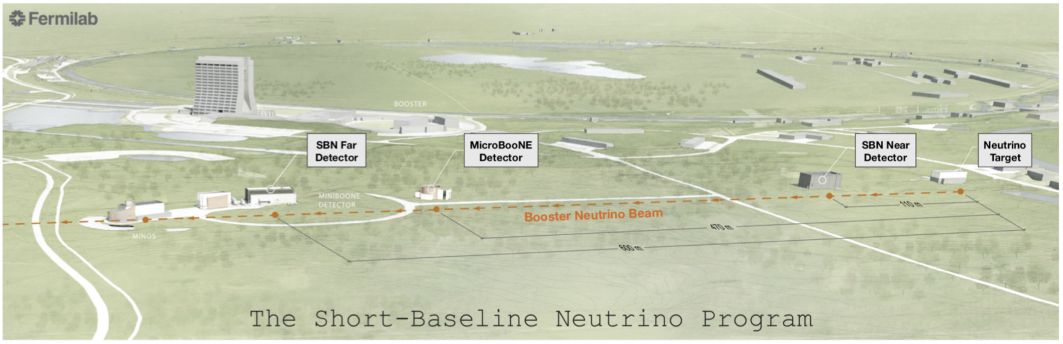


**Figure 4.1** The bird's-eye view of the Short-Baseline Neutrino program at the Fermilab campus. From right to left, the three LArTPC detectors are: the near detector SBND, the intermediate detector MicroBooNE, and the far detector ICARUS, positioned at distances of 110 m, 470 m, and 600 m from the neutrino beam, respectively. Figure from Reference [169]

The MicroBooNE detector, the first to be constructed as part of the SBN program, collected neutrino data from 2015 to 2020. As of this writing, MicroBooNE has collected the world's largest dataset of neutrino interactions on argon. The detector was positioned at roughly the same distance as the MiniBooNE detector to investigate the nature of MiniBooNE LEE observation. In recent years, MicroBooNE has published a series of results concerning the LEE search, finding no evidence for $\nu_e$-like excess, single photons with multi channels, or sterile neutrinos [96–100, 105]. Further details on the latest findings from MicroBooNE are provided in Section 2.3.4.

To fully exclude the presence of eV-scale sterile neutrinos, the SBND and ICARUS detectors are designed to maximise the precision of neutrino oscillation measurements. The far detector, ICARUS began its commissioning phase in 2020 and has been collecting data since then. The near detector, SBND, is situated just 110 meters from the neutrino source. Its proximity allows SBND to collect unoscillated neutrino data, providing a precise constraint on the neutrino flux and interaction models. As of the time of writing this chapter, SBND has become fully operational, and data collection commenced in July 2024.

## 4.2 The Booster Neutrino Beam

The SBN program detects neutrinos produced by the BNB [170]. The BNB was first utilised by the MiniBooNE experiment to study the neutrino anomaly observed by the LSND. As shown in Figure 4.2, 8 GeV protons from the booster synchrotron are extracted and delivered in a 1.6 $\mu$s spill at a rate up to 5 Hz. In each spill, around 5 $\times$ $10^{12}$ protons are injected in 81 bunches. Each bunch is approximately 1.3 ns wide, with a 19 ns gap between bunches [170].

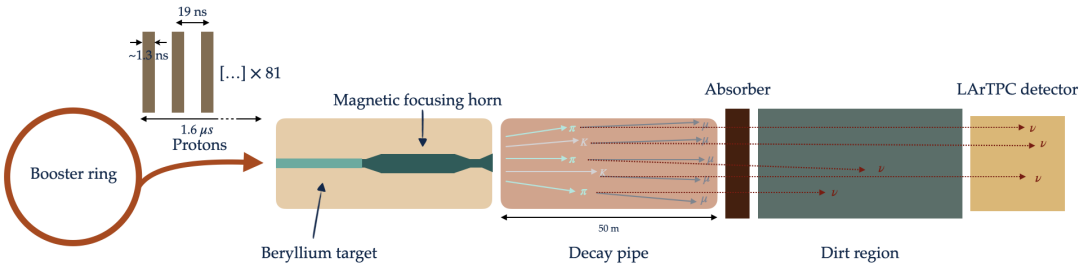


**Figure 4.2** A schematic diagram of BNB production. Protons from the Booster Ring interact with a Beryllium target to produce hadrons, which propagate through a magnetic focusing horn and decay pipe to produce neutrinos. Remaining mesons are removed by an absorber.

These protons hit the Beryllium target, producing secondary hadrons, predominantly pions and kaons. These secondary hadrons are generated in all directions and are then focused by a 174 kA magnetic focusing horn. The polarity of the magnetic horn can be adjusted to focus particles with either positive or negative electric charges, enabling operation in "neutrino" or "anti-neutrino" mode. The focused secondary hadrons then travel through a 50 m decay pipe, where most pions decay and produce muon neutrinos via $\pi^{\pm} \rightarrow \mu^{\pm} + \nu_{\mu}/\overline{\nu}_{\mu}$. When running in neutrino mode, the beam is predominantly composed of $\nu_{\mu}$, with smaller fractions of $\overline{\nu}_{\mu}$, $\nu_e$, and $\overline{\nu}_e$ produced by secondary pion decays, kaon decays, and secondary muon decays [171]. The average neutrino energy is approximately 800 MeV. The produced neutrinos then propagate along the beam direction and can be detected when interacting with detector nuclei. Neutrinos can also interact with the material situated between the decay pipe and the detector, known as the *dirt* region. Meanwhile, as neutrinos continue travelling along the beamline, all remaining hadrons are removed by the absorber at the end of the decay pipe.

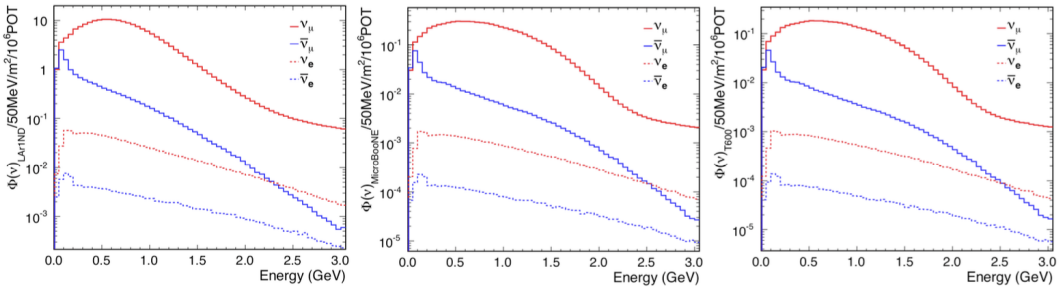


**Figure 4.3** The BNB flux spectra as a function of neutrino energy in the SBN program. From left to right: SBND, MicroBooNE and ICARUS. Figure from Reference [172].

The BNB fluxes have been extensively modelled by the MiniBooNE experiment [170] and tuned with hadron data collected by the Hadron Production (HARP) Experiment at CERN [173]. Utilising the GEANT 4 simulation toolkit, the beam profiles have been simulated for each experiment within the SBN program. Figure 4.3 illustrates the BNB flux spectra for the SBND (left), MicroBooNE (middle), and ICARUS (right) detectors, respectively. In each case, the neutrino beam consists of neutrinos and antineutrinos of electron and muon flavours. While the composition of the flux varies with energy, it is notably dominated by $\nu_\mu$ across different energy ranges and different experiments.

A flux of neutrons can also be produced by primary interactions in the BNB target, which can scatter into the atmosphere at high angles and diffuse back to the detector. This phenomenon, commonly referred to as the *neutron skyshine*, contributes to background radiation outside the immediate beamline region [174, 175]. The SciBooNE experiment observed an increased rate of hits at the top of the detector during the beam spill [176], attributed to this effect. The neutron skyshine is needed to be carefully accounted for to mitigate its impact on physics analyses.

## 4.3 Liquid Argon Time Projection Chambers

The LArTPC has been selected as the core technology for the SBN program and will be employed in next-generation large neutrino experiments at Fermilab due to its advantageous properties. Liquid argon is chemically inert, an excellent scintillator, and transparent to its own scintillation light. When an electric drift field is applied, ionisation electrons, produced in charged particle interactions, can drift over several metres if the purity of the liquid is maintained at a high level. The high density of liquid argon (1.41 g/cm$^3$) and its substantial atomic mass enhance the likelihood of neutrino interactions with the nuclei of argon atoms. Additionally, liquid argon is relatively inexpensive. Being the most abundant noble gas, it can be liquefied using liquid nitrogen, making it a practical choice for large-scale neutrino detectors.

The idea of LArTPC was originally proposed in 1977 by Rubbia [177]. It is an evolution of the original gas-filled time projection chamber idea from Nygren [178, 179], adapted to use liquid argon as the medium [180]. Figure 4.4 shows a cartoon of the operational principle of a LArTPC. An incoming neutrino interacts with an argon nucleus and produces secondary charged particles. These secondary particles will ionise and excite the liquid argon, producing ionisation electrons and scintillation light. Electrons are drifted under an applied electric field towards the charge readout sensors located at the anode.

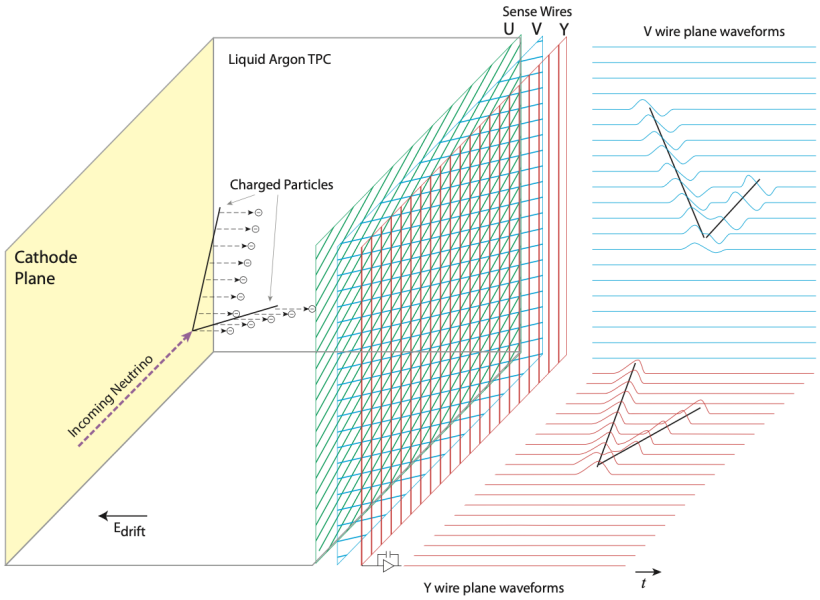


**Figure 4.4** LArTPC operational principle diagram. Figure from Reference [181].

### 4.3.1 Detection of Ionisation Electrons

A typical charge readout for a LArTPC detector consists of planes of sense wires with different orientations. Each wire plane provides two-dimensional projections of ionised charge in space and time. When ionisation electrons pass by a sense wire plane, they induce a bipolar signal, as shown in the top panel of Figure 4.5. Therefore, this plane is commonly referred to as the induction plane. The sense wire plane where electrons are collected is known as the collection plane, where the detection signal is a unipolar signal, as depicted in the bottom panel of Figure 4.5.

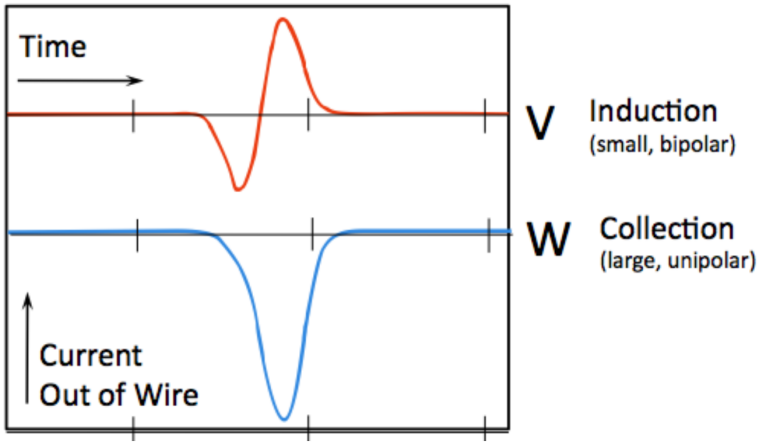


**Figure 4.5** Charge signals on the induction (top) and collection (bottom) plane. The induction plane sees a bipolar signal shape while the collection plane sees a unipolar signal shape. Figure from Reference [130].

To construct photographic-like three-dimensional images of particle interactions, at least two sense wire planes are required. Modern LArTPC detectors typically employ three wire planes (two induction planes and one collection plane) to enhance the accuracy of 3D reconstruction, particularly in situations where the interacting particle travels along the direction of the wires in one of the planes [80, 181–183]. The LArTPC reconstruction chain has been shown to achieve a precision down to the scale of millimetres.

The amount of charge induced or collected on the wires is related to the deposited energy inside the detector. Therefore, calorimetric information can be reconstructed from the ionisation signals, provided that losses or distortions in charge collection due to propagation effects are carefully calibrated. Details on this calibration can be found in Section 5.4.1. These propagation effects that occur during the drift time of electrons ($\mathcal{O}(ms)$) include impacts from impurities, diffusion, and the space charge effect, as described in Section 3.3.

### 4.3.2 Detection of Scintillation Light

Since the propagation time of photons, $\mathcal{O}(ns)$, is much shorter than the drift time of electrons, the scintillation light is typically used for triggering purposes and can provide $ns$-resolution timing in LArTPC detectors [184]. The scintillation light produced by the excited argon propagates isotropically across the volume of the detector and can be detected by photon detectors, such as photomultiplier tubes (PMTs), typically positioned behind the charge readout planes. The propagation of scintillation light can be influenced by Rayleigh scattering, quenching, and absorption by impurities, as described in Section 3.2.2.

Scintillation photons are emitted at 128 nm, which lies in the VUV region and is not detectable by standard light detectors directly. To address this, wavelength shifter (WLS) materials are often used to coat the light detection system. The WLS material absorbs VUV photons and re-emits them in a region where the detector has a high efficiency. The original VUV photons and the re-emitted photons are typically referred to as the two components of scintillation light.

## 4.4 The MicroBooNE Detector

The MicroBooNE detector is an 87-tonne LArTPC detector, serving as the intermediate detector in the SBN programme. Located 470 m from the neutrino target along the BNB, the detector comprises two main systems: the Time Projection Chamber (TPC), which collects the ionised electrons, and the Photon Detection System (PDS), which collects the scintillation light. This section will introduce the design of both systems in MicroBooNE.

### 4.4.1 The MicroBooNE TPC

The box-shaped MicroBooNE TPC is positioned inside a cylindrical cryostat containing a total mass of 170 tonnes of liquid argon, as shown in Figure 4.6. The TPC consists of three main components: a cathode, a field cage, and an anode. The active volume of the TPC, defined by the field cage, contains 87 tonnes of liquid argon and measures 10.36 m along the neutrino beam direction, 2.33 m vertically, and 2.56 m horizontally. Inside the cryostat, MicroBooNE operates at a temperature of 87 K and a pressure of 1.24 bar [181].

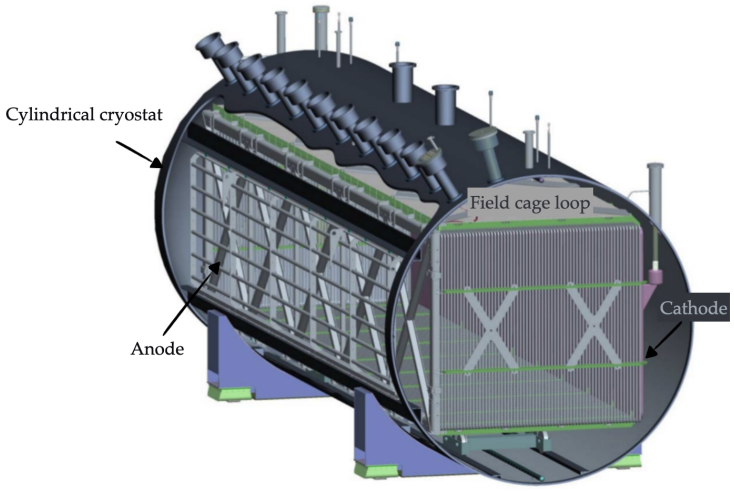


**Figure 4.6** A schematic diagram of the MicroBooNE TPC inside of a cylindrical cryostat. Figure adapted from Reference [181]

A voltage of -73 kV is applied at the cathode to achieve an electric field strength of 273.9 V/cm, resulting in a dirft time from cathode to anode of 2.3 $ms$. Due to concerns about possible electrical breakdown at higher electric fields, the operational electric field is lower than the designed value of 500 V/cm for MicroBooNE. The field cage is designed to maintain a uniform electric field across the entire active volume. It consists of 64 stainless steel tubes shaped into a rectangular loop, with each tube electrically connected to its neighbouring tubes using 250 MΩ resistors. These resistors are used to gradually step down the voltage from the cathode across the field cage to the anode.

The anode plane of MicroBooNE consists of three wire planes. Each plane comprises very thin wires (approximately 150 $\mu m$) of distances with a wire pitch of 3 mm. The first two planes, known as the ”U” and ”V” induction planes, are positioned at $\pm$ 60° with respect to the vertical direction and have 2,400 wires each. The third plane, referred to as the ”Y” collection plane, is vertically oriented and contains 3,456 wires. The spacing between each plane is also 3 mm. The PDS is located behind the anode. To shield against field distortions and surviving electrons from the collection plane, a grounded mesh is placed between the anode and the PDS.

Signals registered on the wire planes undergo initial processing by a set of cold electronics installed within the cryostat, followed by a subsequent set of warm electronic outside the cryostat. Cryogenic low-noise front-end Application Specific Integrated Circuits (ASICs) preamplify and shape the signals. These processed signals are then transmitted outside the cryostat to the data acquisition (DAQ) system, where they are converted from analogue to digital format. This facilitates the collection of ionisation electron data.

### The Coordinate System

MicroBooNE uses a right-handed Cartesian coordinate system in which $x, y$ and $z$ denote the drift, vertical and beam-aligned direction. The origin is defined to be located centred in the vertical direction, on the first induction plane near the anode, and on the upstream face of the LArTPC [181]. Figure 4.7 shows the coordinate system and boundaries of MicroBooNE with a cartoon.

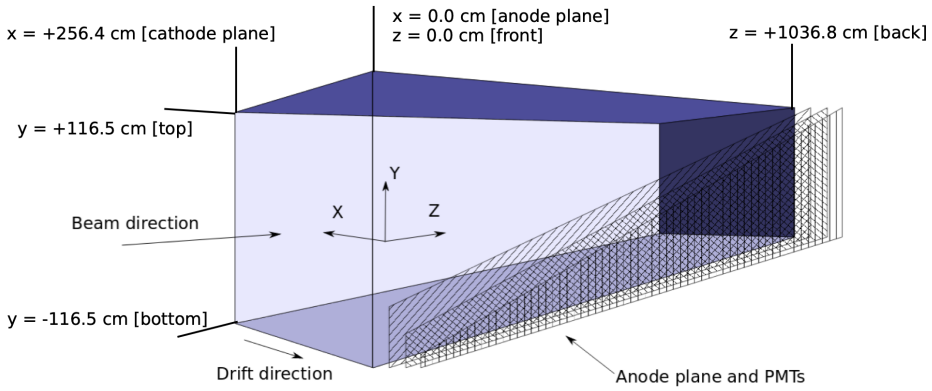


**Figure 4.7** A depiction of the coordinate system for MicroBooNE. Figure from Reference [185].

### TPC Unresponsive Wire Regions

In the MicroBooNE detector, a fraction of the wires are unresponsive. Most of these unresponsive channels are due to short circuits caused by touching wires. Additionally, mis-connected or malfunctioning ASICs can also result in unresponsive wires [186]. Cross-connected wires between the "U" and "V" planes can lead to some of the charges being collected by the wires in the "U" or "V" planes, causing a reduction in the charge observed by the collection plane. This effect can be addressed and corrected through calibrations [187].

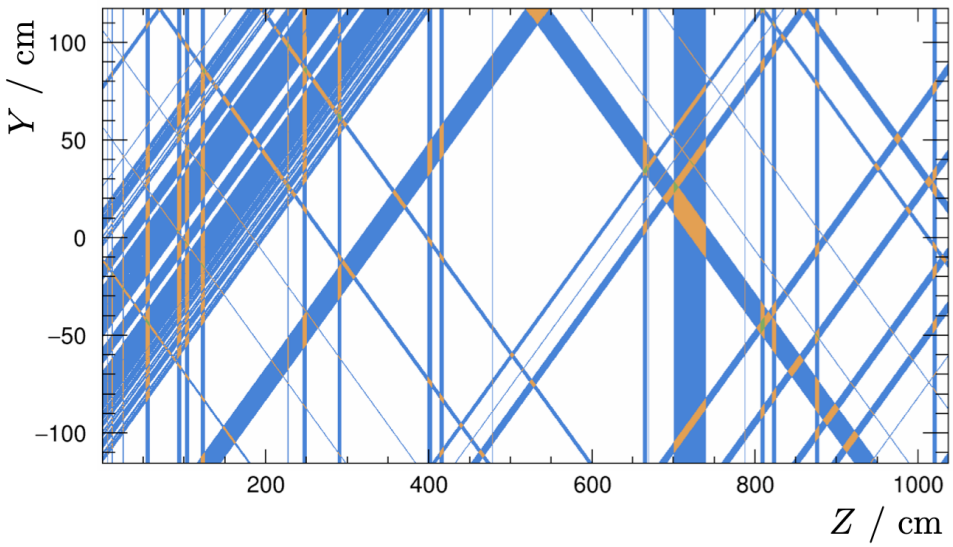


**Figure 4.8** Unresponsive TPC regions in MicroBooNE. White, blue, orange, and green represent 0, 1, 2, 3 unresponsive wire planes, respectively. Figure from Reference [188].

All dead channels in the MicroBooNE detector are identified and their locations are recorded in a database for use in physics simulations and reconstruction. As shown in Figure 4.8, approximately 17% of the channels are unresponsive in the "U" plane, about 5% in the "V" plane, and around 10% in the collection plane. Consequently, roughly 30% of the detector volume is not visible in at least one plane. However, when requiring at least two planes for 3D track reconstruction, only about 2.5% of the detector is unresponsive. Furthermore, the unresponsive volume is reduced to approximately 0.04% if all three planes are required [188].

### 4.4.2 The MicroBooNE PDS

The PDS in the MicroBooNE detector consists of 32 optical units, each equipped with an 8-inch diameter Hamamatsu R5912-02mod cryogenic PMT. These PMTs are designed to operate at cryogenic temperatures and are positioned behind the anode wire planes. Figure 4.9 shows the placement of the PMTs in the detector.

In MicroBooNE, these PMTs are capable of providing timing accuracy to the nanosecond level [184]. Although the argon medium itself is transparent to its own scintillation light, the glass of the PMTs absorbs the argon scintillation light at a wavelength of 128 nm, as depicted by the solid black glass transmittance curve in Figure 4.10. To mitigate this issue, Tetraphenyl Butadiene (TPB) is employed as the WLS material. TPB is coated on acrylic plates placed in front of the PMTs, as shown in the right plot of Figure 4.9. TPB absorbs the argon emission light at 128 nm and re-emits it in the visible range, peaking at 425 nm, which aligns with the sensitive detection range of the PMTs. This process is illustrated by the dashed green curve in Figure 4.10.

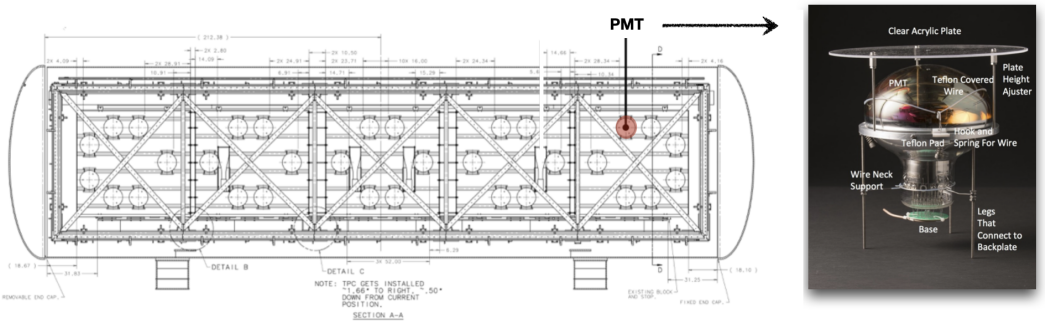


**Figure 4.9** Left: the MicroBooNE light collection system, which consists primarily of PMTs behind the anode wire planes. Right: a picture of a PMT behind an acrylic plate. The plate was not coated with TPB when picture was taken but during the operation of the detector, the acrylic plate was coated with TPB. Figure adapted from [181].

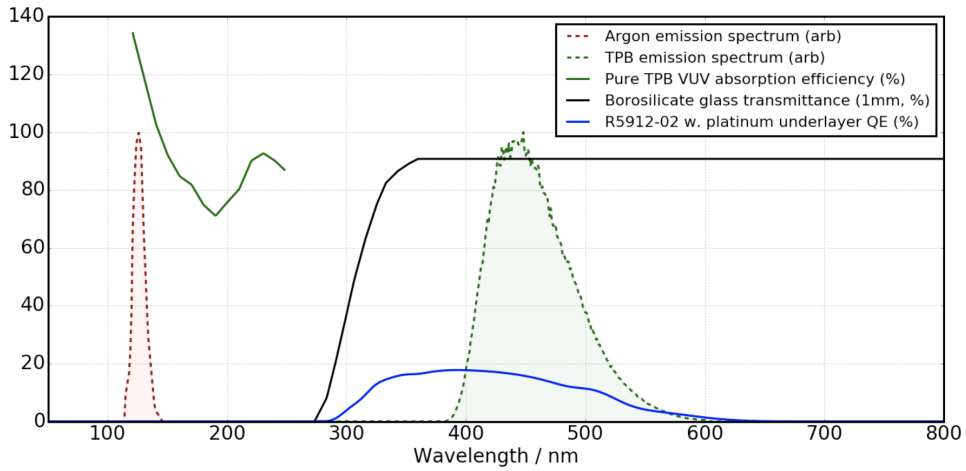


**Figure 4.10** Scintillation light emission spectrum in liquid argon (dashed red) and TPB re-emission light spectrum (dashed green), the graph is in arbitrary units. TPB absorption efficiency (solid green), borosilicate glass transmission efficiency (solid black), and quantum efficiency of an R5912-02mod cryogenic PMT (solid blue) in %. Figure from Reference [181].

The coverage of the PMT array in the MicroBooNE detector is estimated to be around 0.9%, which is relatively small. However, this limited coverage is adequate for the primary role of the PDS in triggering events. So far, particle reconstruction and calorimetry in LArTPC detectors are mainly achieved using ionisation electron signals. Recent studies have shown that scintillation light, which contains at least half of the deposited energy in LArTPC detectors, significantly enhances energy reconstruction resolution for low-energy events [189]. Consequently, more recent LArTPC detectors, such as SBND, have incorporated PDS designs with larger coverage to fully explore the capability of scintillation light. Details on the SBND PDS can be found in Section 4.5.2.

In MicroBooNE, the PMTs are positioned behind the anode plane, which leads to a dependence of light yield on the position of scintillation event. Much higher light yield is observed when the light is produced closer to the PMTs compared to when it is produced farther away. Chapter 6 will describe a novel method for measuring position-dependent light yield.

The analogue signals from each PMT are pre-amplified and shaped into a unipolar signal with a 60 ns rise time. These signals are then digitised at a rate of 64 MHz using a 16-bit ADC, with the 60 ns rise time allowing several samples to be captured on the rising edge, thereby ensuring precise determination of the initial interaction time.

Operating at approximately 1300 V, the cryogenic PMTs require recalibration of their gain, measured as the charge recorded per photoelectron, each time the PMT system is restarted, with minor adjustments to the high voltage [190]. These gain values are stored in a database for simulation and reconstruction.

Additionally, during the summer accelerator shutdown period following Run 2, the PDS encountered an issue where one PMT failed due to a faulty connection and it has been off since then [190].

#### Non-linearity of the PMT Response

The non-linearity of the PMT response at high light intensities was measured in MicroBooNE using a test stand at Fermilab [191]. As shown in Figure 4.11, the PMT initially responds linearly to the amount of light. However, in the higher intensity region, the response deviates and cannot be described by a linear superposition of single photoelectron (PE) responses.

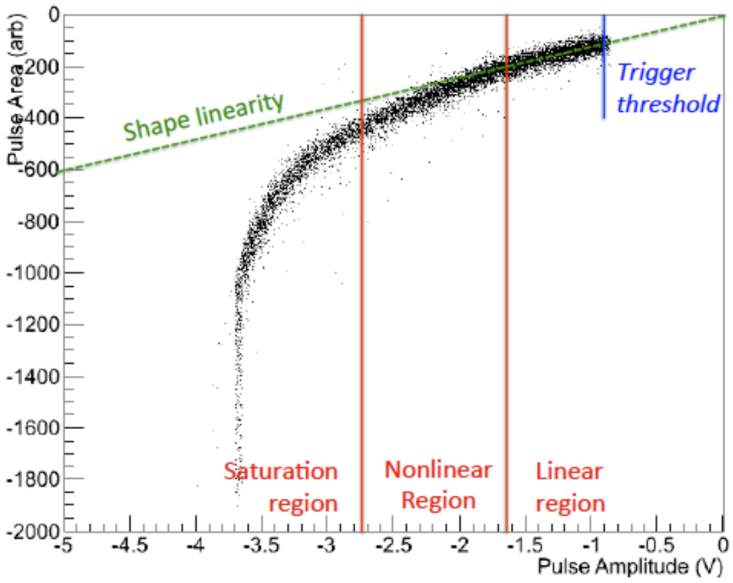


**Figure 4.11** The measured non-linearity response for the MicroBooNE PMT in the teststand. Figure from Reference [181].

### 4.4.3 The MicroBooNE Readout and Trigger System

In MicroBooNE, continuously recording every event associated with a beam spill is impractical due to the enormous data volume it would require and the relatively rare fraction of neutrino interaction within the beam spill. To manage data volume effectively, MicroBooNE employs several triggering schemes designed to accurately identify beam neutrino and cosmic interaction candidates. These schemes often use light signals from the PMTs to determine whether an event is of interest.

MicroBooNE operates in two trigger modes: **beam-on** mode and **beam-off** mode. In **beam-on** mode, events are recorded when the beam is active, with triggers based on PMT signals. In **beam-off** mode, events are recorded when the beam is inactive, also using PMT signals for triggering. While most trigger schemes require a specific trigger signal to record an event, MicroBooNE also employs a "random trigger" in the beam-off mode without a specific trigger requirement. The various triggering schemes employed in MicroBooNE are detailed in the following sections.

### Readout system

The MicroBooNE readout system comprises two components: a continuous readout of 6.4 ms (4 frames) for the PMT system and a continuous readout of 4.8 ms (3 frames) for the TPC system. A frame is defined as a time interval of 1.6 ms for both PMT and TPC readout. This frame duration was initially designed for an electric field of 500 V/cm. However, the detector operates with an actual electric field of 273.9 V/cm, resulting in an electron drift time of 2.3 ms. To ensure a proper readout of neutrino interactions, three TPC readout frames are opened: one before the beam gate and two after, as shown in Figure 4.12. Additionally, to reduce the size of PMT data, only PMT waveforms with a signal exceeding a specified number of PEs are recorded.

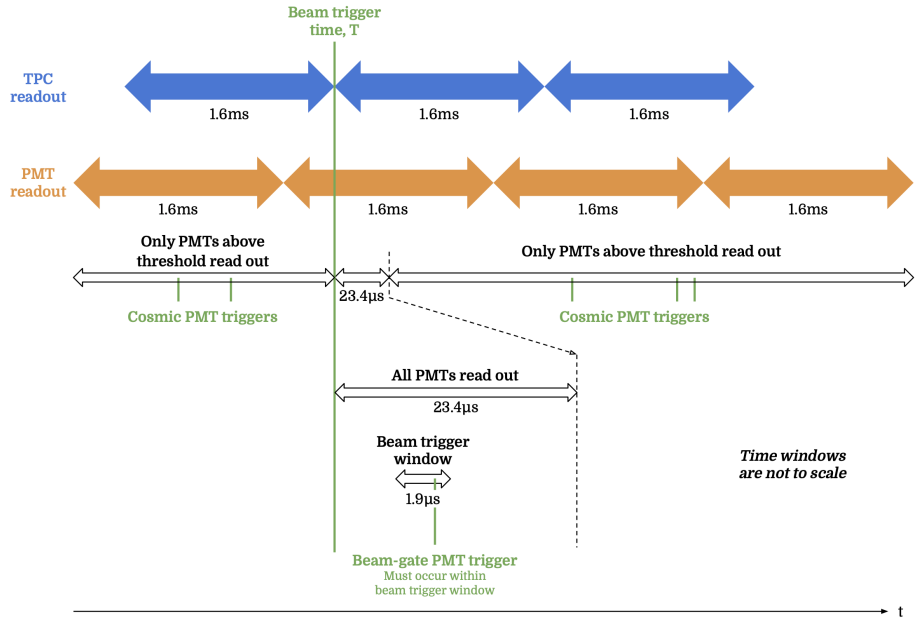


**Figure 4.12** The timing structure of neutrino readout stream with regard to the BNB beam gate in MicroBooNE. Figure from Reference [188].

### Hardware Trigger

The neutrino beam is managed by the Fermilab Accelerator Division, which generates signals when protons collide with the target to produce neutrinos. These signals are used as the hardware trigger for MicroBooNE. Upon detecting a hardware trigger, an unbiased readout window of 23.4 $\mu$s is opened, without requiring scintillation light.

### Software Trigger

The software trigger determines whether to record data. In MicroBooNE, neutrinos are expected to interact with argon nuclei occasionally during beam spills. To efficiently manage the vast amount of data and identify potential neutrino interactions, the software trigger, or PMT trigger, is employed. This system relies on detecting scintillation light measured by the PMT arrays during the beam spill.

The **online trigger** is set to capture events with a minimum of 5 PEs in total detected by the 32 PMTs within any 100 ns time window during the beam spill. Events satisfying this criterion are considered candidates for neutrino interactions and are saved to tape. However, not all events that pass the online trigger are further processed.

To further select events of interest, the **offline trigger** is defined, requiring at least 20 PEs in total from all of the PMTs. This threshold ensures that only events with sufficient light intensity are forwarded for detailed reconstruction and analysis. The threshold for the offline trigger is carefully defined to maximise data processing efficiency without compromising the detection of low-energy neutrino interactions.

### External and Unbiased Trigger

For beam spills without neutrino interactions, cosmic ray activity passing through the detector can produce sufficient scintillation light to meet the software trigger condition. To account for these interactions, MicroBooNE employs a pulse generator to trigger the readout window when the beam is off and record the events where the online trigger condition is satisified. Additionally, a portion of events that do not meet the software trigger criteria are still recorded. These events, which are not influenced by timing or light intensity, are referred to as unbiased events.

## 4.5 The Short-Baseline Near Detector

SBND is the last detector in the SBN to come online. As the near detector of the SBN program, SBND is located just 110 m from the BNB target. Due to this proximity, SBND will experience a very high number of neutrino interactions. With such high statistics, SBND will be able to perform precision measurements of cross-sections, including multidimensional cross-sections and rare channel searches. Additionally, SBND will be capable of conducting searches beyond the Standard Model of particle physics. In the flagship short-baseline oscillation searches, SBND, as the near detector, will collect unoscillated neutrino data to constrain the neutrino flux. Furthermore, SBND will contribute to the development of LArTPC technology towards the DUNE experiments.

SBND is positioned at the Earth's surface, making it susceptible to cosmic ray particles, with muons being the most prevalent. These cosmic-ray muons can be mistaken for $\nu_\mu$-like interactions within the detector. Additionally, $\delta$-rays generated by cosmic muons may produce photons via bremsstrahlung, which can mimic $\nu_e$-like interactions through Compton scattering or pair production. To address these issues, the Cosmic Ray Tagger (CRT) system is implemented to identify and mitigate cosmic-ray activities. Details about the CRT system will be detailed in Chapter 7. Similar to the MicroBooNE detector, SBND features both a TPC and a PDS, which will be discussed in this section.

### 4.5.1 The SBND TPC

The SBND TPC is placed inside a membrane cryostat, which is a novel design for physics and commonly used in industry to carry liquefied gases. The membrane cryostat was first used in the DUNE 35-ton prototype detector and will be used for DUNE detectors in the future [192].

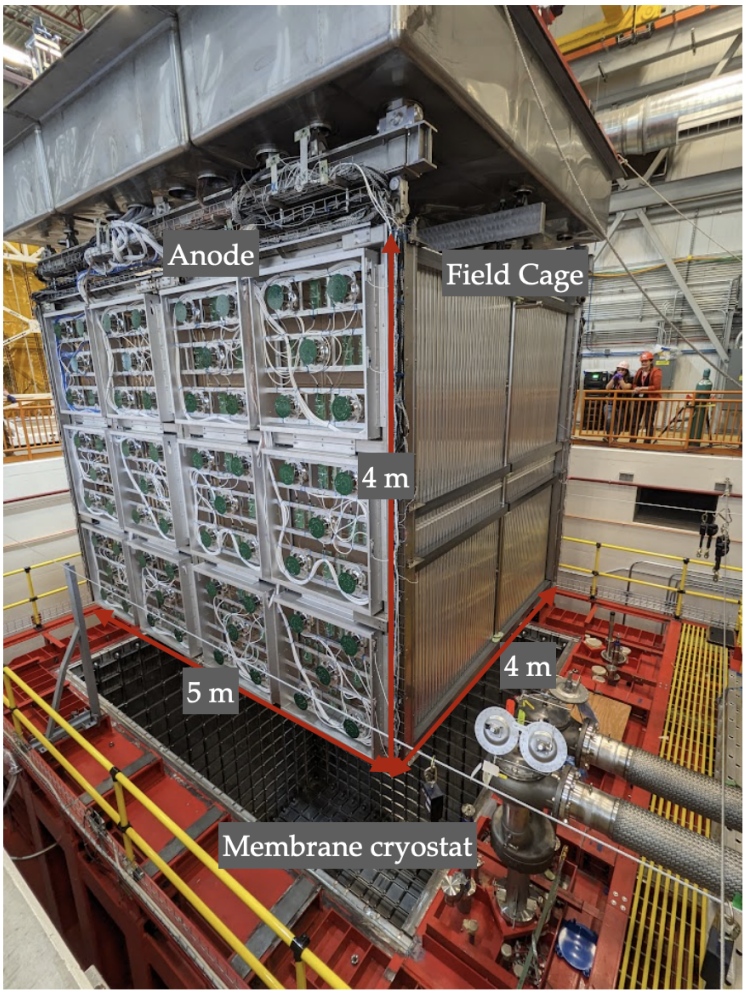


**Figure 4.13** The SBND TPC during the installation into the membrane cryostat. Image courtesy of the SBND collaboration, with minor modifications.

Figure 4.13 shows the day when the SBND TPC was installed into the membrane cryostat. The active volume of the detector defined by the field cage contains 112 tons of liquid argon. The detector features two independent TPC volumes, separated by the cathode plane. Each TPC has dimensions of 2 m in the drift direction, 4 m in the vertical direction, and 5 m in the beam direction. The electric field is designed to be 500 V/cm, drifting the ionisation electrons towards the anode planes inside each TPC. Similar to the wire plane design in MicroBooNE, the anode planes in SBND are composed of three planes of sense wires: two induction planes (”U” and ”V” planes) oriented at $\pm$ 60° to the vertical direction, and one collection plane (”Y” plane) oriented along the vertical direction. The wire pitch is 3 mm, and the spacing between the subsequent planes is also 3 mm.

### 4.5.2 The SBND PDS

The PDS in the SBND is also positioned behind the wire planes and comprises three main components: the cathode, a primary PDS consisting of PMTs, and a secondary PDS incorporating X-ARAPUCAS modules.

The SBND cathode is coated with TPB, the same choice used in MicroBooNE for wavelength shifting. TPB converts scintillation light from the VUV region to a wavelength where photon detectors exhibit optimal efficiency. The coating on the cathode enhances the uniformity of detected light across the entire drift volume [193]. Additionally, the cathode is opaque to prevent scintillation light from crossing between the two TPCs, minimising cross-talk and ensuring the containment of light in each TPC.

The primary PDS in SBND includes 120 Hamamatsu R5912-MOD PMTs. Of these, 96 PMTs are coated with TPB, which makes them sensitive to both the argon VUV scintillation light and visible light. The remaining 24 PMTs are uncoated and thus sensitive only to visible light. Complementing these PMTs, the secondary PDS consists of 192 X-ARAPUCAS light trap modules [194, 195], which are novel photon detectors proposed for the DUNE PDS. SBND will test this technology in a neutrino beam and develop it for DUNE. The X-ARAPUCAS modules are divided into two groups: one half is sensitive to VUV light, and the other half is sensitive only to visible light.

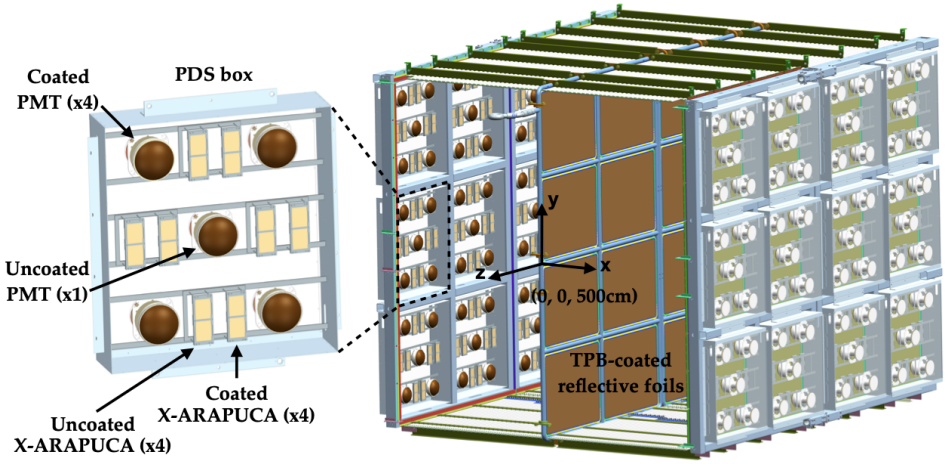


**Figure 4.14** Left: a zoomed-in view of the SBND PDS box. Right: The photon detection system in SBND. Figure from Reference [193].

The PDS system is installed behind the wire planes and is subdivided into twelve PDS boxes for each TPC, as illustrated in Figure 4.14. Each PDS box contains four TPB-coated PMTs at its corners, one uncoated PMT in the centre, and four pairs of coated and uncoated X-ARAPUCAS modules.

The photon detector coverage in SBND is approximately 40%, making it the highest among all LArTPC detectors. This extensive coverage significantly enhances SBND's sensitivity to scintillation light. With its unique detector design, SBND is well-positioned to explore various applications of scintillation light in LArTPC detectors. These applications include position reconstruction based solely on light information by analysing the ratio of visible light to VUV light, and reconstructing the BNB proton time structure [193]. Such advancements can be leveraged to improve signal detection and enhance physics analyses.

## 4.6 Summary

This chapter introduced the fundamental principles of LArTPCs and the detection of both ionisation electrons and scintillation light. It explained the production and composition of the BNB beam used in the SBN program. The chapter also introduced the two detectors in the SBN program: MicroBooNE and SBND. Data collected from the MicroBooNE detector will be used for the analysis detailed in Chapter 6. The external design of SBND, the CRT system, will be introduced in Chapter 7.

# 5

# Event Simulation and Reconstruction in LArTPCs

The Liquid Argon Software (LArSoft) framework is commonly used by LArTPC detectors [196]. It is a C++ based software suite built on top of the **art** particle physics event processing framework [197] and the ROOT data processing toolkit [198]. LArSoft provides the structure to handle both simulation and reconstruction with numerous algorithms and tools. Additionally, it provides interfaces with various particle physics simulation packages, including the GENIE [199] and CORSIKA [200] event generators, and the GEANT 4 particle propagation simulation toolkit [201].

This chapter provides an overview of simulation and reconstruction in LArTPC detectors, with an emphasis on the MicroBooNE detector, which will be used for the analysis in Chapter 6. The chapter is structured according to the LArSoft workflow: event generation, particle propagation, the production and propagation of ionised signals and scintillation light, the detector response simulation, and finally reconstruction.

## 5.1 Overview of Simulations in LArTPC

To simulate a Monte Carlo (MC) event, as shown in Figure 5.1, the first stage involves generating primary particle interactions to determine the vertices and kinematics of the secondary particles. Various event generators are employed for different physics processes. Using the kinematic inputs from these generators, the particles propagate inside the detector using the GEANT 4 toolkit, which accurately simulates physics processes in transport. Ionised electrons and scintillation photons are also produced and propagated using GEANT 4. The detector response for both signals is further simulated, resulting in a simulated event that can be fed into the reconstruction chain in the same way as real data. Detailed explanations for each stage are covered in the following sections.

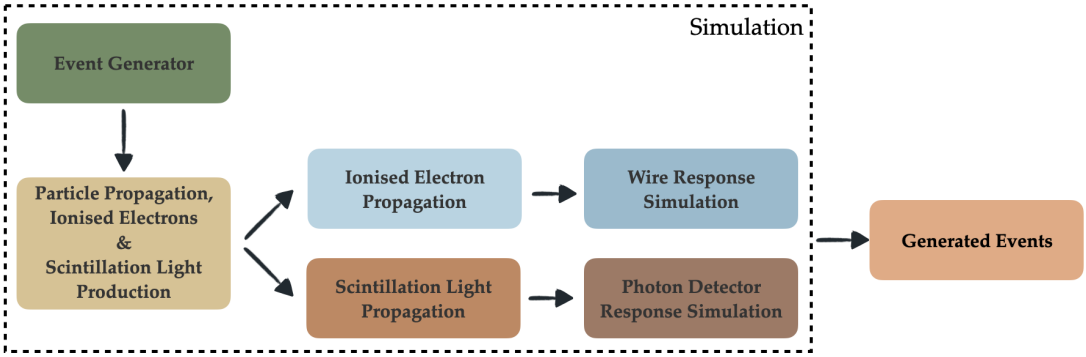


**Figure 5.1** Simulation workflow in LArSoft to generate events.

### 5.1.1 Geometry Models Used in Simulation

One of the fundamental requirements for accurate simulations that represent real data collected by the detector is a **precise geometry**. In LArSoft, the geometry for simulations is typically defined using the Geometry Description Markup Language (GDML) [202]. For the analysis detailed in Chapter 6, the default MicroBooNE geometry file, `microboonev12.gdml`, was used. For the BSM searches involving CRT-beam telescope data, the geometry was modified based on the SBND standard geometry file, `sbnd_v02_00.gdml`. More details regarding the geometry modifications for the CRT Beam Telescope will be discussed in Chapter 9.

## 5.2 Event Generation

The event generation is performed using software libraries provided by different event generators. These libraries are either directly integrated within the LArSoft suite or used externally, with their results subsequently fed into LArSoft using a common input file. The kinematics of the resulting particles are determined, establishing the initial conditions for the subsequent simulation. This section will introduce several event generators that are relevant to the analyses presented in this thesis.

### 5.2.1 Simulation of Cosmic Rays in SBND and MicroBooNE

Both SBND and MicroBooNE are surface detectors and are therefore exposed to a significant flux of charged particles from cosmic-ray interactions in the atmosphere. The simulation employs the CORSIKA software package, which models detailed air showers generated by high-energy cosmic-ray particles such as protons, light nuclei (up to iron), photons. These particles interact in the atmosphere, primarily producing showers dominated by pions, which decay to muons. These muons can travel large distances into the detector, producing signals in the liquid argon. Due to the computational complexity of simulating the high number of particles produced by cosmic-rays, a pre-generated CORSIKA library is used. This database contains kinematic information, such as energy, particle types, and directions. For each simulation, events are randomly sampled from this database. The performance of the CORSIKA simulation has been verified with data in studies conducted by MicroBooNE, as detailed in Reference [203].

SBND uses CORSIKA for cosmic-ray simulation. There are two databases available for SBND: `sbnd_corsika_cmc`, which contains data generated from a mix of primary particles, and `sbnd_corsika_p`, which is generated from proton primaries. SBND has chosen to use the latter as the default, as it provides a more accurate cosmic-ray rate compared to the former from MicroBooNE experiment.

An alternative way to account for cosmic-ray backgrounds utilising a data-driven technique was developed by MicroBooNE. Cosmic-ray data from the external unbiased trigger stream was recorded and is used to overlay with simulated events. This approach helps to mitigate uncertainties related to both CORSIKA modeling and detector-specific effects. This technique serves as an alternative method for cosmic simulation and has been commonly used in MicroBooNE simulations. SBND may adopt the overlay technique in the future. The overlay technique is used for the cosmic simulation in the analysis detailed in Chapter 6.

### 5.2.2 Isolated Proton Event Generation in MicroBooNE

The isolated proton events analysed in Chapter 6 are generated within the active volume using a particle gun simulation. The positions and kinematics are specifically defined to align with the analysis requirements, which are derived from the data sample after applying relevant selections. The analysis focuses on relatively short-length (ideally point-like) isolated protons, which are isotropically distributed across the detector. The initial parameters of these generated isolated protons are summarised in Table 5.1.

| parameter | Value |
|---|---|
| $x$ [cm] | $127.5 \pm 117.5$ |
| $y$ [cm] | $0 \pm 105.0$ |
| $z$ [cm] | $518.5 \pm 518.5$ |
| $\theta_{xz}$ [°] | $0 \pm 180$ |
| $\theta_{yz}$ [°] | $0 \pm 90$ |
| $P$ [GeV/c] | $0.59 \pm 0.20$ |

**Table 5.1** Initial parameters for the generation of isolated proton events in MicroBooNE. The $x$, $y$, and $z$ coordinates represent the positions in the drift, vertical, and beam directions, respectively. The angle $\theta_{xz}$ is the azimuthal angle in the $x-z$ plane, while $\theta_{yz}$ is the complementary zenith angle relative to the $x-z$ plane.

### 5.2.3 Simulation of BNB Beam in the SBND

SBND utilises the GENIE neutrino generator [199, 204], which is integrated into LArSoft, to simulate the interactions of beam neutrinos within and around the detector. Other widely used generators include GiBUU [205], NEUT [206], and NuWro [207].

The GENIE generator combines theoretical and empirical models by tuning its predictions to experimental data, and it covers an energy range from around 100 MeV to a few hundred GeV [204]. The generator samples the neutrino flux profile to determine the rate of neutrino interactions, accounting for the cross-sections of the different materials present. Once an interaction occurs on a target, GENIE simulates the neutrino interaction using a combination of nuclear physics, cross-section models, hadronisation models and hadron transport, as shown in Figure 5.2. The combined configuration is tuned by GENIE based on real data. The configuration of the default tune `AR23_20i_00_000` is selected by the SBN and DUNE programmes and can be found in Table I of the reference [208].

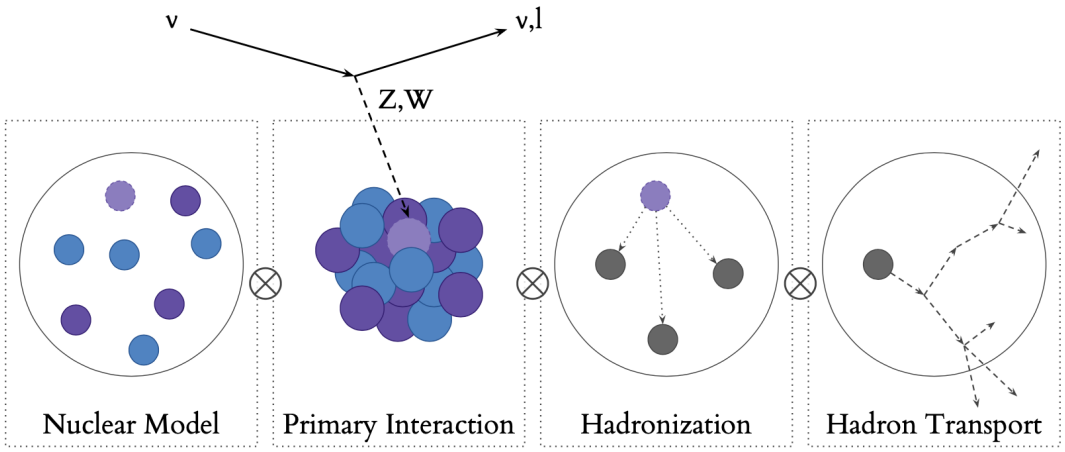


**Figure 5.2** A schematic diagram illustrating an example of neutrino interaction simulation with the GENIE generator. The process is divided into nuclear model, primary neutrino interaction, hadronisation, and hadron transport. Figure from Reference [209].

Since the beam neutrinos interact with nucleons bound within the nucleus, the simulation starts by selecting a nuclear model to describe the momentum and potential energy of the nucleons. The version of GENIE used by SBND employs the local Fermi gas model [210] as its nuclear model.

Next, a cross-section model is selected to describe how neutrinos interact, based on their energy. For example, the Quasi-Elastic (QE) interactions are characterised by the Valencia model [211], while Baryon Resonance Scattering (RES) is described by the Berger-Sehgal model [212]. Deep Inelastic Scattering (DIS) interactions are represented by the Bodek-Yang model [213]. The interaction type is chosen according to the neutrino energy to provide an accurate description of the interaction processes.

The hadronisation process refers to the production of hadrons when a neutrino interacts with a quark within the nucleus, which is particularly important in the Deep Inelastic Scattering (DIS) regime. In GENIE, this process is described using the Andreopoulos-Gallagher-Kehayias-Yang model [214], which interfaces with `PYTHIA` [215] for detailed hadronisation simulation. Following hadronisation, the transport of hadrons within the nucleus can further introduce secondary hadrons through re-scattering. These Final State Interactions (FSI) are modelled using a data-driven cascade model in GENIE [204]. The GENIE FSI model includes pions, kaons, protons, and neutrons.

In addition to interacting with the medium inside the detector, neutrinos can also interact with surrounding materials. The neutrinos created in these interactions, commonly referred to as **dirt** neutrinos, generate a substantial number of beam-induced particles that can pass through the detector, creating a significant background for the analysis described in Chapter 10 and Chapter 11. To ensure that all potential events are accounted for, the dirt simulation is performed within a large "world" volume defined in the geometry GDML file. This "world" volume is the largest in the geometry, designed to encompass all relevant physics components and interactions of interest.

### 5.2.4 Simulation of Dark Neutrinos in SBND Beam Telescope

BSM event generators are typically not integrated directly into LArSoft. Instead, custom generators developed externally by phenomenologists specialising in specific models are more commonly used. The custom generators provide the rates, positions, and kinematics of BSM particles, along with their subsequent interactions or decays. These parameters are then provided as input to the later stages of the LArSoft simulation. This approach is used for the dark neutrino generations for the analysis in this thesis.

As discussed in Section 2.4, dark neutrinos can be produced through the up-scattering of SM beam neutrinos with nuclei. Subsequently, the dark neutrinos propagate along the beam-line and decay into a SM neutrino and a dark gauge boson ($Z_D$), with the latter further decaying into a charged-lepton pair. Depending on where the dark neutrino decays, the detector can be sensitive to two types: short-lived dark neutrinos, which decay before reaching the upstream CRT panel, and long-lived dark neutrinos, which decay between two CRT panels. For the short-lived dark neutrino case, a di-muon pair is chosen for the study, while a di-electron pair is chosen for the long-lived dark neutrino case. For the analysis, the mass of the dark neutrino is assumed to be sub-GeV, while the mass of the dark gauge boson is fixed at 1.25 GeV, making dark neutrino decay off-shell into a SM neutrino and a lepton pair.

The SM beam neutrinos are predominantly produced by the two-body decays in flight of charged pions. Therefore, due to kinematic considerations, as one moves away from the beam axis, the observed neutrino energy spectrum narrows and peaks at lower energy. This effect is commonly referred to as the **off-axis** effect, as shown in the left plot in Figure 5.3. Since the dark neutrino is produced via SM neutrino scattering, its production must account for the **off-axis** effect. To address this, six annuli around the beam axis are selected to simulate the off-axis energy dependency. The neutrino spectrum for each annulus is then used as input for event generation. The right plot of Figure 5.3 shows the decay vertices of dark neutrinos, clearly illustrating the beam structure. The production of dark neutrino signal is simulated using DarkNews [216].

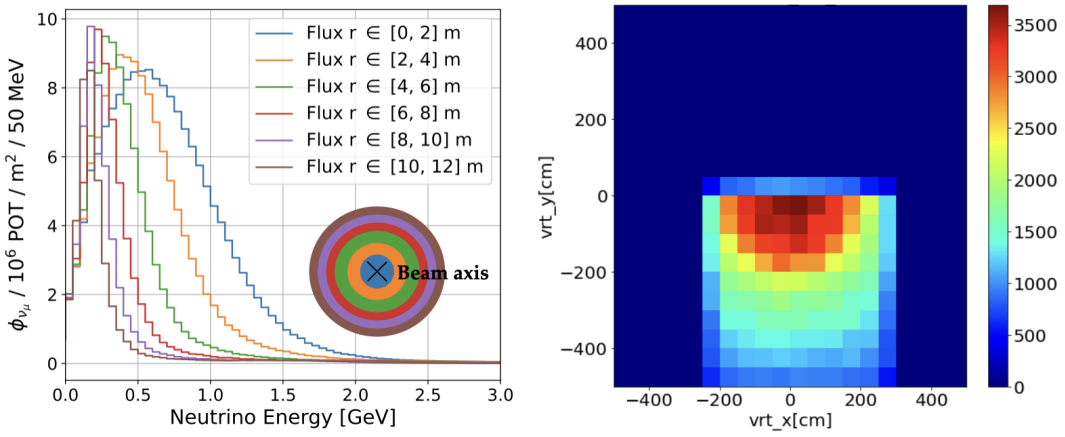


**Figure 5.3** Left: The neutrino energy spectrum for six annuli around the beam axis [217]. Right: The decay vertices of dark neutrinos in the $x$-$y$ plane of the CRT Beam Telescope detector, where a beam structure is visible.

## 5.3 Particle Propagation, Charge and Light Simulation

### 5.3.1 Particle Propagation

Once the particles have been generated, their propagation within the detector is simulated using GEANT 4, which is integrated into LArSoft. Each particle is independently stepped along its trajectory, and at each step, the probabilities of various physics processes, such as scattering, interactions with argon or other materials, and decay processes, are evaluated. The deposited energy and the particle's trajectory are determined at each step. This process continues until the particle's energy falls below a detection threshold, typically around 10-100 keV. At this low energy, the deposited energies from these particles are not detectable in a LArTPC and are therefore considered negligible. All secondary particles produced during propagation are saved and simulated in the same way, with a connection to their parent particles being saved.

In GEANT 4, a **physics list** is a collection of physical process and models used to simulate interaction of particle with matter. The physics list `QGSP_BERT` is commonly used in LArTPC detectors. The `QGSP_BERT` list includes standard electromagnetic processes, the Bertini Cascade model (BERT) [218] for hadrons at low energies ($< 10$ GeV), the Low Energy Parametrization model (LEP) [219] for intermediate energies, and the Quark Gluon String model (QGS) [220] for high energies ($> 20$ GeV). The physics list `QGSP_BERT_HP` is similar to `QGSP_BERT`, but it includes a high-precision neutron model. A comparison of these two physics lists with data will be presented in Section 9.3.1.

During the propagation, the energy deposited during each step along the simulated particle trajectory is used to calculate the amounts of ionisation charge and scintillation light produced. This calculation takes into account the charge-light anti-correlation, which varies with the electric field, as described in Section 3.3.1.

### 5.3.2 Charge Simulation

The simulated ionised electrons generated by the deposited energy inside of the LArTPC are grouped into clouds and directed towards the anode plane. The simulation takes into account electron lifetime, as well as the effects of transverse and longitudinal diffusion, and distortions in the electric field caused by space charge. Figure 5.4 depicts the electron drift paths as they approach the sense wire planes. The figure shows three wire planes: two induction planes and a collection plane, with points representing individual wires in each plane. The drifted electrons pass through the shield plane, move between the wires in the two induction planes, and are finally collected on the collection plane. The field response function describing the induced current on wires due to moving charge, is modelled by the 2D Garfield program [221].

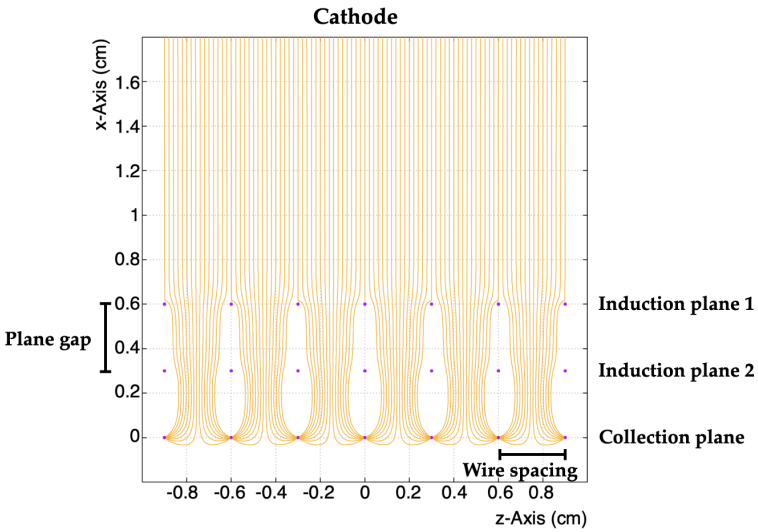


**Figure 5.4** A schematic diagram illustrates the electron drift paths inside the detector. It includes four three planes: two induction planes and a collection plane. The points represent the individual wires in each plane. Figure adapted from Reference [222]

Once the number of electrons per readout channel is calculated, the wire response function is used to model the electronic response of each channel separately. This response is measured in data by injecting a signal into each channel. Electronic noise from components is subsequently incorporated into the simulation. The noise model is data-driven and based on the wire response when the drift field is inactive. Validation of the simulation has been performed using cosmic-ray data in MicroBooNE experiment [223]. As a result, the simulated waveform in ADCs closely mirrors real data and will serve as input for the reconstruction process.

### 5.3.3 Light Simulation

Scintillation photons, along with ionised electrons, are generated by the deposited energy in GEANT 4. Unlike ionised electrons, which propagate along the drift field, scintillation photons can follow a much more complex path to reach the photon detectors due to reflections and processes such as Rayleigh scattering, detailed in Section 3.2.2. The propagation of photons can be accurately modelled using GEANT 4, where each photon's trajectory is simulated individually until it reaches the detectors. This approach, known as the **full optical simulation**, predicts both the quantity of photons detected at each photon detector and their arrival times.

However, due to the substantial scintillation yield of liquid argon (∼20,000 photons per MeV at standard LArTPC operational voltage) and the high energies (GeV) involved in neutrino interactions, performing a full optical simulation becomes impractical due to its time-consuming nature. To mitigate this challenge, methods for **fast optical simulation** are designed as a replacement. These methods are typically trained using full optical simulation and then subsequently used in place of it. In this case, the computationally challenging full optical simulation only needs to be performed once.

#### The Photon Library Method

A common approach for the fast optical simulation is the optical look-up table, also known as the photon library. This method is the default for the MicroBooNE light simulation. The concept involves dividing the LArTPC volume into many small cubes, referred to as voxels (an analogy to pixels in two dimensions), as illustrated in Figure 5.5. For each voxel, a large number of isotropic photons (300,000 in the case of MicroBooNE) are generated and simulated using the full optical simulation. By comparing the produced photons with those detected by an optical detector, a parameter called the visibility of a given optical detector from the respective voxel is calculated. These visibilities are then stored in a look-up table and used in the standard simulation chain as a substitute for the full optical simulation.

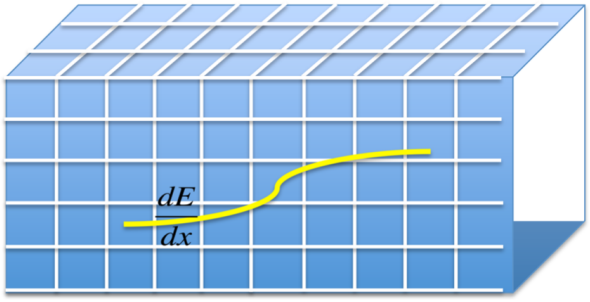


**Figure 5.5** Illustration of the photon library approach. The detector is voxelised and the visibility of each photon detector from each voxel is calculated from full optical simulation and stored in a look-up table. Figure from [146].

The performance and resolution of the photon library method depends on the size of the voxels chosen. In parallel, the size of the library scales with both the detector's size and the number of photon detectors. The photon library method is effective for smaller LArTPC detectors, such as MicroBooNE, where the voxel size is typically set to approximately 5 m in the $x$ direction, and 5 m and 3 m in the $y$ and $z$ directions, respectively. However, for larger detectors like the DUNE far detector, or detectors with a higher number of photon detectors like SBND, the photon library method becomes highly memory-intensive in simulation if reasonable performance is required.

### The Semi-analytical Model

To address the limitations of the photon library method, an alternative approach called the semi-analytical model [224] has been developed. This model was first employed in the SBND and DUNE experiments. It combines geometric predictions with a set of parameters for corrective factors, allowing it to scale effectively to large detectors and those with a large number of photon detectors without encountering memory-related issues.

The initial geometric predictions of the number of photons detected by a specific optical detector are made using the solid angle from the scintillation point to that detector. This can be described by:

$$N_\Omega = e^{-\frac{d}{\lambda_{abs}}} \Delta_E \cdot S_\gamma(\mathcal{E}) \frac{\Omega}{4\pi}, \tag{5.1}$$

where $\lambda_{abs}$ is the absorption length, $d$ is the distance from the scintillation point to the photon detector, $\Delta_E$ is the deposited energy, $S(\mathcal{E})$ is the scintillation yield of liquid argon for a given electrical field $\mathcal{E}$, $\Omega$ is the solid angle.

Additionally, to account for other effects such as Rayleigh scattering, correction factors must be applied to the geometric predictions. By comparing the photons detected using a full optical simulation with the geometric predictions, correction curves are subsequently obtained. These correction curves are parameterised as a function of $(d, \theta)$, where $d$ and $\theta$ are defined as the distance and the offset angle from a scintillation point to a photon detector, as shown in Figure 5.6.

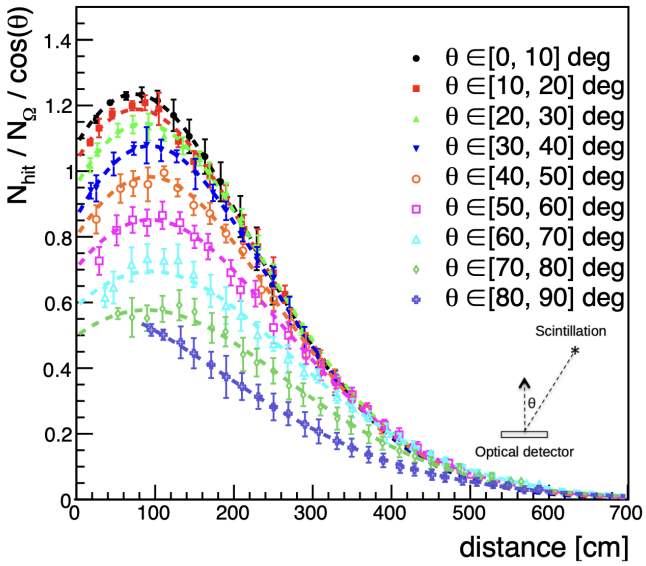


**Figure 5.6** Correction curves of the semi-analytical model for MicroBooNE geometry, generated with Rayleigh scattering length of 66 cm. The error bar in each bin represents the RMS of the distribution of the ratio between the number of hits generated by GEANT 4 and those predicted by the geometry calculation, corrected by the offset angle. The different colour lines are separated with 10° in the angle $\theta$.

The ratios at different angles and distances can be accurately described by the Gaisser-Hillas distribution [225]. Therefore, this distribution is used to fit these ratio curves and obtain the corresponding parameterisation. The Gaisser-Hillas function is defined as follows [225]:

$$GH(d) = N_{max}\left(\frac{d - d_0}{d_{max} - d_0}\right)^{\frac{d_{max}-d_0}{\Lambda}} e^{\frac{d_{max}-d}{\Lambda}}, \tag{5.2}$$

where $N_{max}$ is the maximum of the function, $d_{max}$ is the distance at which the function reaches $N_{max}$. The remaining two parameters, $d_0$ and $\Lambda$, are parameters describing the width of the distribution.

Border effects resulting from the real life-size of the detector are also accounted for in the correction curves. By generating correction curves for different radial distances from the photon detector centre, the relationship between this distance and the parameters defining the Gaisser-Hillas function ($N_{max}$, $d_{max}$, and $\Lambda$) are also parameterised to account for border effects [224].

The semi-analytical approach was adapted by the author for use in the MicroBooNE experiment, with two Rayleigh scattering length (RSL) assumptions: 66 cm and 100 cm. Both the semi-analytical model with these two RSL values and the default photon library method with RSL of 66 cm are employed as simulation approaches for the analysis in Chapter 6.

**Comparison with Full Optical Simulation** The semi-analytical predictions are compared with the full optical simulation results to assess their accuracy. Figure 5.7 shows that across the entire drift distance, the semi-analytical model demonstrates good agreement with the full optical simulation, with deviations calculated as the RMS values of the fractional difference between the predicted number of photons from the semi-analytical model and those propagated by GEANT 4. The results show that the RMS for all bins is less than 10%. In comparison, the photon-library method exhibits a similar bias but with a higher RMS.

### The Hybrid Model

Due to the geometric approach employed by the semi-analytical model, the model is limited to simulating scintillation light emitted directly in front of the photon detectors within the TPC. However, outside the TPC, the absence of an electric field results in brighter scintillation in the surrounding argon, possibly causing the scintillation light to be non-negligible. Consequently, modelling scintillation light outside the TPC becomes necessary. This necessity prompted the development of a combined approach known as **the Hybrid Model**. Initially implemented in SBND, this hybrid method integrates the semi-analytical model for the active volume and incorporates a photon library for areas outside the TPC. This approach was later adapted for use in DUNE by the author.

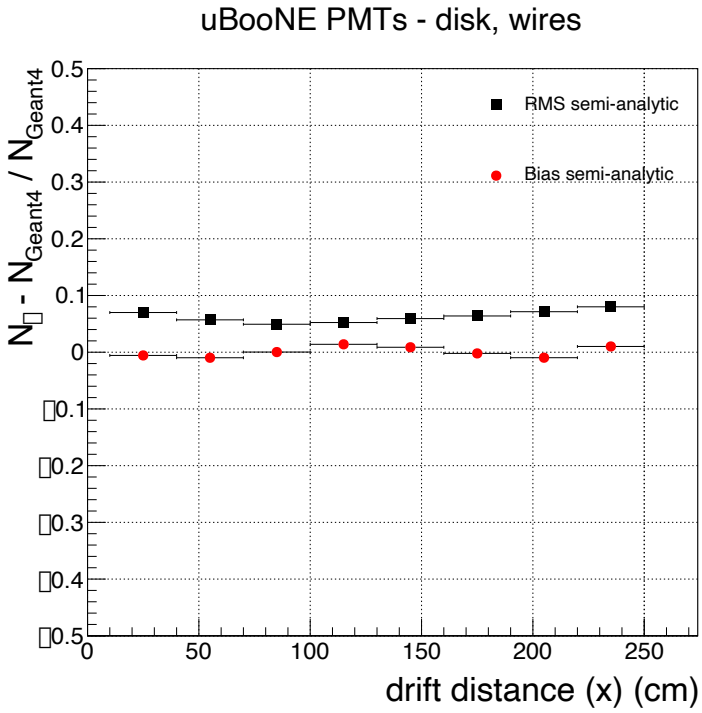


**Figure 5.7** The number of photons generated from the semi-analytical model is compared with the GEANT 4 full optical simulation across varying drift distances. The bias is defined as the mean value of the fractional difference between the number of photons predicted by the semi-analytical model and those propagated by GEANT 4. The RMS represents the standard deviation of this fractional difference.

### Detector Simulation

Once the number of photons on each photon detector is established, the response of the photon detector is simulated. This includes using the single electron response (SER) function to simulate each incoming photon. Different experiments have different SER functions based on the detector design. An example of the SER function in SBND is shown in Figure 5.8. Additional effects, such as fluctuations in the gain of PMTs converting photons to electrons, as well as the expected level of noise, are also incorporated into the simulation.

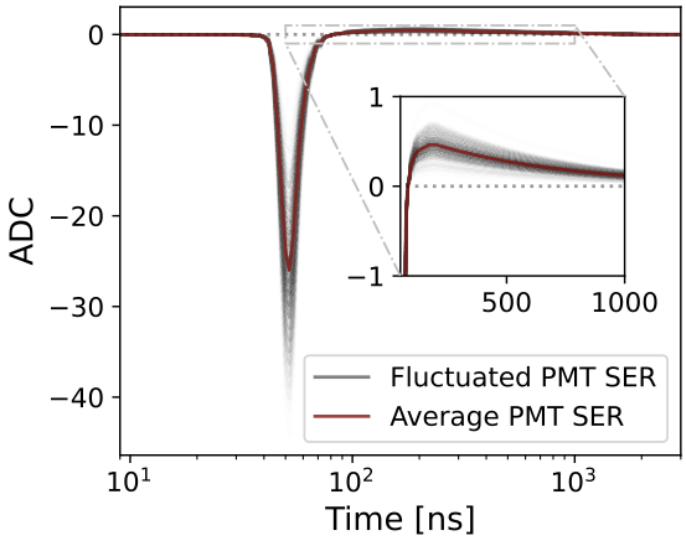


**Figure 5.8** Measured single electron response for the PMT in the SBND. Figure from Reference [193].

## 5.4 Reconstruction in MicroBooNE

The reconstruction in LArTPCs is performed using the LArSoft suite, which provides a robust framework with minor variations across different LArTPC experiments. This section will describe the reconstruction method for both electron and light signals, focusing on the MicroBooNE detector. The outputs of the reconstruction are used in the analysis detailed in Chapter 6.

### 5.4.1 Charge reconstruction

After the detector simulation stage, the simulated raw wire waveforms have an identical format to the recorded data. The ultimate purpose of reconstruction is to extract the information about the particle interactions from the raw detector data. To achieve this, the TPC signal undergoes both **low-level** and **high-level** reconstruction.

The **low-level** reconstruction refers to the processing stage where detector effects such as noise, field response, and electronics response are mitigated to recover the number of ionised electrons passing by or being collected by each wire. The results from the **low-level** reconstruction serve as the input for higher-level frameworks, such as Pandora [226], which are used to identify and reconstruct patterns created by particle interactions.

### Signal processing

In MicroBooNE, removing detector effects from the raw TPC signals involves performing deconvolution using the Fourier transform. Additionally, a filter is applied to mitigate high-frequency noise. MicroBooNE employs an updated deconvolution technique that considers the response on each wire separately and also takes into account the response of neighbouring wires. This approach introduces a second dimension for signal processing, hence it is commonly referred to as 2D deconvolution. The traditional method, which considers only the response on a single wire, is called 1D deconvolution.

Deconvolution is crucial for the induction planes as it converts bipolar signals into unipolar signals, simplifying the subsequent hit-finding and calorimetric reconstruction processes. Examples of unipolar and bipolar signal shapes are shown in Figure 4.5. This simplification allows the same algorithms to be used across all three wire planes. After deconvolution, a region of interest (ROI) finding process is performed to locate signals that exceed a predefined threshold.

### Hit Finding

After the ROI have been located, the hit finding is performed. Within each ROI region, the deconvolued waveform is fitted with one or a series of Gaussian distributions. Each Gaussian fitted waveform is reconstructed as a **hit**. The peak time represents the time that electrons arrive at the wires, which can be used to determine the drift position of the hit and the coincidence between different planes. The integral of each hit is used to reconstruct the amount of charge deposited on wire. These parameters associated to the hit are extracted and serve as the input for the **high-level** reconstruction.

### Pandora Multi-Algorithm Pattern Recognition Framework

The analysis in MicroBooNE described in Chapter 6 uses the Pandora [226, 227] multi-algorithm pattern recognition framework for the high-level reconstruction. The framework initially clusters the TPC hits based on proximity within each plane to reconstruct 2D images. Using the peak time of the TPC hits, the drift position for each cluster is determined, and coincidences are sought between clusters across planes to perform 3D reconstruction.

Due to the nature of MicroBooNE being an on-surface detector, neutrino interactions can coincide with cosmic-ray activities. Pandora utilises hundreds of algorithms to identify these interactions, categorising them into two passes, **PandoraCosmic** and **PandoraNu**:

- **PandoraCosmic**: The reconstruction algorithms in this path are strongly track-oriented to reconstruct primary particles such as cosmic muons and their $\delta$-rays. The starting point for object reconstruction is selected based on high $y$ values in the TPC. All hits produced from the low-level reconstruction are first processed through the PandoraCosmic path to identify candidate cosmic-ray particles. Hits associated with the identified candidates are subsequently removed before processing with PandoraNu.
- **PandoraNu**: All remaining hits are then input into the PandoraNu algorithms. These hits are clustered into topologically associated objects, known as "slices," based on their proximity and direction.

The reconstruction is handled with PandoraCosmic and PandoraNu streams separately to isolate possible neutrino interactions from cosmic-ray activities. The output of the Pandora reconstruction is a slice containing a collection of reconstructed objects known as Particle Flow Particles (PFParticles). Each PFParticle is assigned a score ranging from 0 to 1 to indicate whether it is track-like (score of 1) or shower-like (score of 0), with the classification boundary set at a score of 0.5.

#### Charge and Energy Calibrations

LArTPCs can provide excellent calorimetry information, which is needed to construct particle identification (PID), proper calibration of the detector's calorimetric response is necessary for the accurate PID. In MicroBooNE, the measured deposited charge per unit length $\langle dQ/dx \rangle$, measured in ADC/cm, is first calibrated to convert it into the deposited energy per unit length $\langle dE/dx \rangle$.

The detector effects, such as the space charge effect, unresponsive wire regions, both transverse and longitudinal diffusion, and quenching due to impurities, introduce discrepancies between the amount of charge produced and detected. The calibration for $\langle dQ/dx \rangle$ aims to mitigate these effects and ensure uniform detector response across the entire volume. Cosmic muons are chosen as the calibration sample because they span the entire detector volume. MicroBooNE stores correction maps that account for all detector effects in a database, which are used for calibrations on an event-by-event basis.

The absolute energy loss per unit length $\langle dE/dx \rangle$ can be calculated from the calibrated $\langle dQ/dx \rangle$ using the modified box recombination model [187]:

$$\langle \frac{dE}{dx} \rangle = \frac{\rho\xi}{\beta' W_{ion}} [exp(\frac{< dQ/dx >_{calibrated}}{C_{cal}} \frac{\beta'}{\rho E} - \alpha)], \tag{5.3}$$

where $C_{cal}$ is a calibration constant to convert ADC to electrons, $W_{ion}$ is the work function of argon euqals to 23.6 $\times 10^{-6}$ MeV/electron, $\xi = 0.273$ kV/cm is the MicroBooNE drift field, $\rho = 1.38$ g/cm$^3$ is the density of liquid argon at pressure of 123.106 kPa. $\alpha, \beta'$ are parameters of the model measured to be 0.212 (kV/cm)(g/cm$^2$)(MeV$^{-1}$) and 0.93 [158].

Calibration for $\langle dE/dx \rangle$ is performed using a sample of TPC-contained muons from neutrino interactions. This sample is chosen because it is MIP-like, with $\langle dE/dx \rangle$ being theoretically well understood [187], and because forward-going muons provide plenty of hits on the collection wires. The calibration constant $C_{cal}$ is determined by comparing the most probable value (MPV) obtained from $\langle dE/dx \rangle$ measurements with predictions derived from the Landau-Vavilov function [228].

Once the calibration is completed, the energy for tracks can be calculated from $\langle dE/dx \rangle$ and the track length. For the proton used in the analysis in Chapter 6, the energy resolution is estimated to be around 1-2% [229].

### 5.4.2 Light Signal Reconstruction

Similar to TPC signals, light reconstruction begins with the raw waveforms collected from individual PMTs. First, the baseline of the raw waveform is calculated and subtracted. Then, optical hits are reconstructed from the processed waveforms. By clustering these optical hits in time, optical flashes are reconstructed. These flashes represent optical activity across different PMTs associated with either neutrino or cosmic interactions.

### Baseline Calculation

For waveforms outside the beam-spill window, the baseline is simply taken as the first recorded ADC value. However, for waveforms within the beam-spill window, where the baseline is not uniform, a local estimation algorithm is employed. The algorithm is designed as follows: the waveform ADC values are looped through and subdivided into small groups. The standard deviation (STD) of the ADC values within each group is then calculated. A low STD indicates the absence of optical activity in the region, thus establishing the baseline as the mean ADC value of the group. In the region which has a high STD, the baseline is estimated through a linear interpolation between the two neighbouring regions with low STD. Figure 5.9 illustrates an example of the estimated baseline using this algorithm.

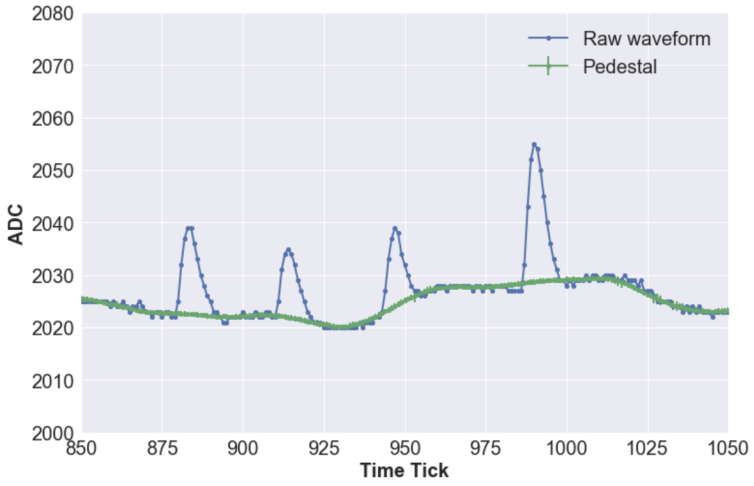


**Figure 5.9** The PMT waveform after the shaper in the late light region. The green line shows the estimated Pedestal with the looping algorithm. Figure from Reference [230].

### Optical Pulse/Hit Reconstruction

Once the baseline of the raw waveform has been established, the ROI is determined by identifying the area where the waveform exceeds a certain threshold. The threshold is set at the area of 10 ADC, which is approximately 0.5 reconstructed PE. Signals within this region are reconstructed as optical hits, also known as pulses. The rising edge time of the pulse is recorded, and the integrated area of the pulse is converted to photon-electrons (PEs) using the SER function.

### Flash Reconstruction

The flash reconstruction algorithm clusters reconstructed pulses from individual PMTs if they occur within a close time window (100 ns), as illustrated in Figure 5.10. Once coincident pulses are identified, an integration window of 8 $\mu$s is applied to capture the late light component. Additionally, an 8 $\mu$s dead time window is used to prevent another flash from overlapping with the late light pulse. If two candidate flashes are reconstructed within this 8 $\mu$s window, the one with the higher PE deposition is retained. The amount of PE, flash time, centre, and width of the flash in the $y$ and $z$ directions are saved for the reconstructed flash object.

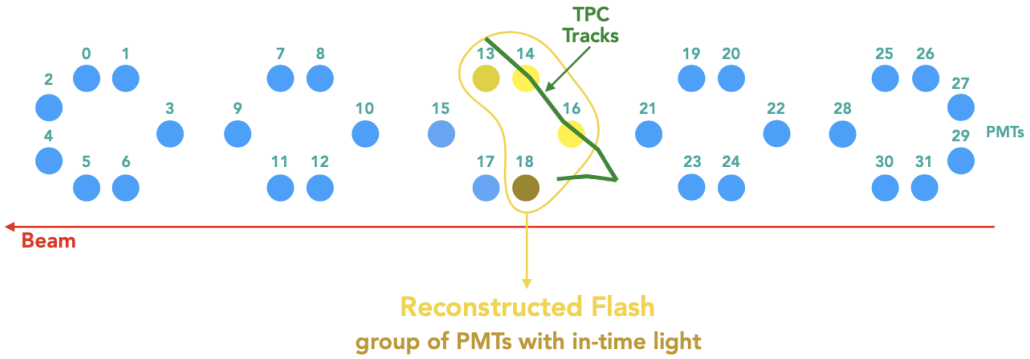


**Figure 5.10** The schematic diagram illustrates the flash reconstruction, with the blue circles representing untriggered PMTs and the yellow circles representing PMTs that detect the light. Figure from Reference [230].

### Light Reconstruction Performance

The fractional difference used to test the light reconstruction performance is defined as:

$$\text{Fractional Difference} = \frac{PE_{true} - PE_{reco}}{(PE_{true} + PE_{reco})/2} \tag{5.4}$$

where $PE_{true}$ is the number of PEs simulated and $PE_{reco}$ is the number of PEs reconstructed. The performance of the light reconstruction in MicroBooNE is shown in Figure 5.11. For all 32 PMTs, a good reconstruction resolution was observed, although PMT 29 exhibited an unusual reconstruction resolution, and the reason for it remains unknown.

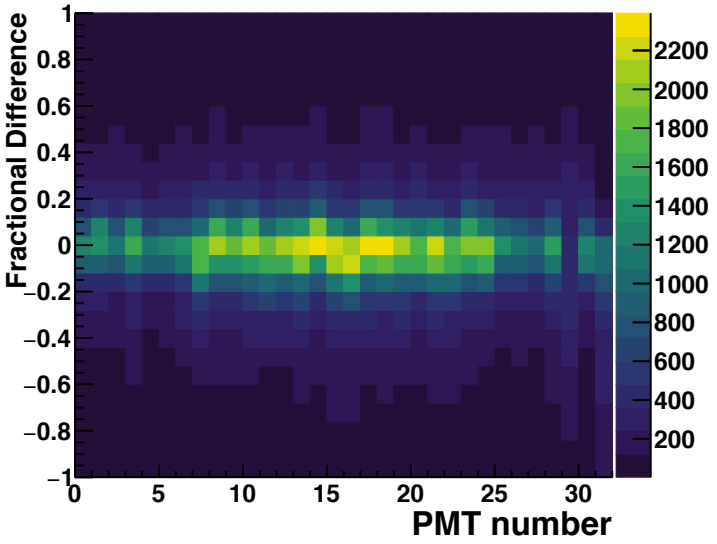


**Figure 5.11** Fractional difference between the simulated and reconstructed PE per MicroBooNE PMT.

### 5.4.3 Flash-matching to the Pandora-reconstructed Neutrino Interaction

The reconstructed optical and TPC activities are matched within a single triggered event, ensuring that information from both systems are available for analysis. In MicroBooNE, the probability of more than one neutrino interaction occurring within the beam window is negligible, so the primary goal is to correctly match the flash with the Pandora-reconstructed neutrino interaction. As illustrated in Figure 5.12, the process begins with the reconstructed TPC candidates. The number of photons incident on each photon detector is predicted using the fast optical simulation, forming light hypotheses. By comparing these hypotheses with the actual measurements, the flash and neutrino interactions are connected. The flash with the best matching hypothesis is used to provide the timing of the neutrino interaction.

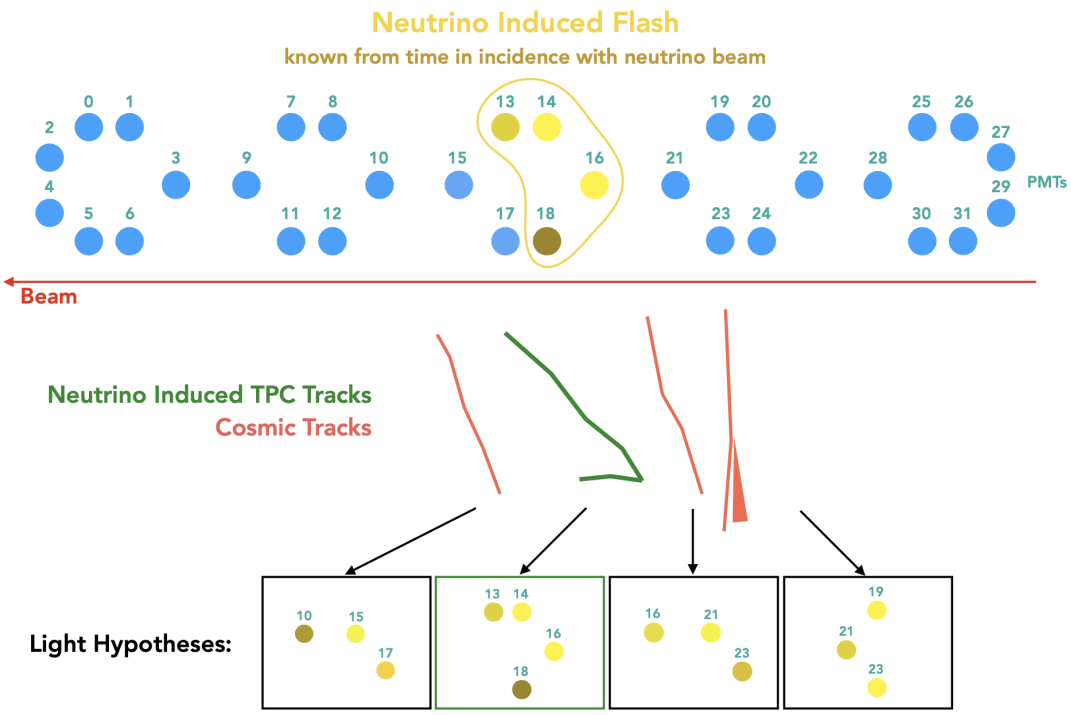


**Figure 5.12** The schematic diagram demonstrates the flash matching algorithm. The PMTs are represented by circles, with the colour of each circle indicating the number of detected photons. Yellow indicates the brightest PMT, while blue indicates the darkest. The neutrino interaction is labelled in green, while the cosmic is in red. The light hypothesis is matched with the PMT measurements. Figure from Reference [230].

### 5.4.4 Particle Identification

The mean energy loss per unit travel distance, $\langle dE/dx \rangle$, varies for different particles, as discussed in Section 3.1. In MicroBooNE, $\langle dE/dx \rangle$ is utilised for particle identification (PID). This is achieved by comparing the measured $\langle dE/dx \rangle$ from a reconstructed track, especially close to its end, to the predicted values for various particle types. Therefore, high-ionising protons can be distinguished from less-ionising muons and pions. However, separating muons from pions based solely on $\langle dE/dx \rangle$ is extremely challenging. Figure 5.13 illustrates a tool developed by MicroBooNE based on $\langle dE/dx \rangle$, demonstrating the PID separation capability for the MicroBooNE detector.

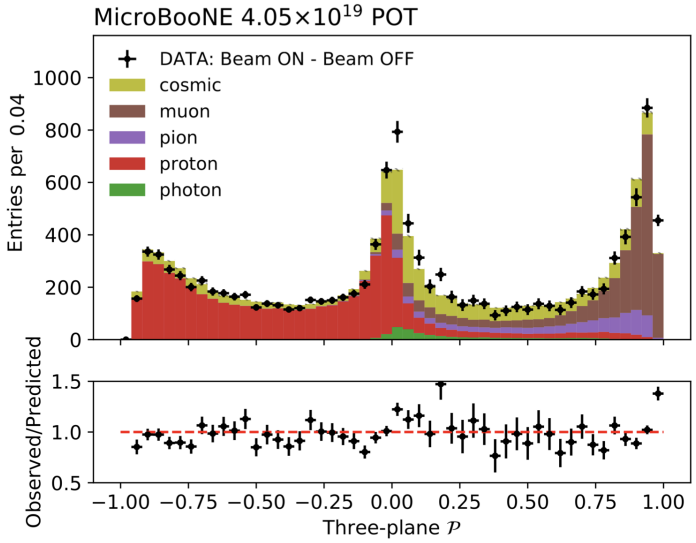


**Figure 5.13** Distribution of PID score $\mathcal{P}$ for neutrino-induced tracks. Figure from Reference [231].

## 5.5 Summary

This chapter provided an overview of the simulation and reconstruction processes for both the MicroBooNE and SBND detectors using the common suite LArSoft. The simulation process was divided into several stages: event generation, particle propagation, charge and light simulation, and detector simulation. The chapter highlighted various methods of fast light simulation, which serve as essential background knowledge for the light yield measurements described in Chapter 6.

The reconstruction process was primarily oriented towards the MicroBooNE detector. It encompassed both charge signal reconstruction from ionised electrons and light signal reconstruction from scintillation light. Charge reconstruction was divided into two parts: low-level reconstruction and high-level reconstruction, with the Pandora framework introduced for the latter. The chapter also covered the calibration of charge signals. Furthermore, the flash-matching algorithm, which combines the reconstructed charge and light signals, is needed to match the light and charge signals. The PID tool developed by MicroBooNE was also introduced in this Chapter.

# 6

# Light Yield Measurement with Isolated Protons in the MicroBooNE Detector

This chapter describes a novel method for measuring the efficiency of light collection in a LArTPC using the MicroBooNE detector. By utilising cosmic-induced isolated protons, the light yield—calculated as the number of photon electrons per unit of deposited energy—can be studied across the entire detector, enabling a position-dependent light yield measurement. Two considerations of Rayleigh scattering length (RSL) are simulated: one with 66 cm, which is the default setting for MicroBooNE light simulation, and one with 100 cm, which is the most recent measurement, commonly adopted by newer LArTPC experiments. In the future, this method can be used to calibrate the light response in large-scale LArTPC detectors and to test assumptions used in simulating scintillation light.

## 6.1 Previous Light Yield Decline Results from Anode/Cathode Piercing Muons

The light yield was previously studied in MicroBooNE with anode- and cathode-piercing cosmic muon rays. As shown in Figure 6.1, a significant decline in light yield during the Run 2 period was observed, ranging from 25-45%. Additionally, a difference in light yield between the anode and cathode planes was present after the decline.

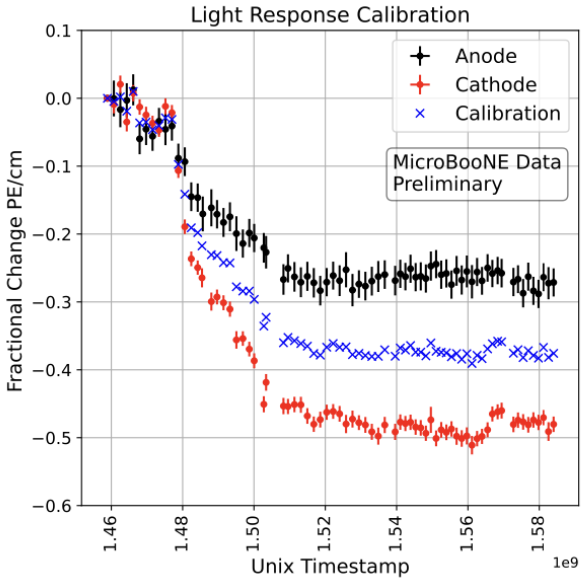


**Figure 6.1** The measured light yield over time for anode- and cathode-piercing muon tracks is shown as black and red points, respectively. The calibration data points, shown in blue, represent the average between the two results. Figure from Reference [232].

The differences between the cathode and anode are challenging to quantify precisely with muon tracks due to their diffuse nature as light sources. Therefore, "point-like" sources are needed as they would be better suited for mapping the light yield at various positions across the detector. Moreover, a better performance is expected when comparing these results with simulations that use specific scintillation points. This analysis uses isolated protons as such "point-like" sources for the first time.

## 6.2 Analysis Dataset

### 6.2.1 Data Sample

A sample of cosmic-ray isolated protons was acquired by identifying events from MicroBooNE off-beam cosmic data with interactions in the TPC that are in-time with the unbiased PMT readout window. The Pandora pattern-recognition reconstruction framework was employed to identify isolated interactions in each event. MicroBooNE's flash-matching algorithms were further applied to isolate interactions that are in-time with the unbiased PMT readout window. The entirety of MicroBooNE's off-beam dataset from the first three years of data-taking was utilised for the analysis.

MicroBooNE's particle identification (PID) tools were used for the pre-selection of isolated protons. Figure 6.2 shows the contribution from off-beam data specifically in the range [-1, 0], which is dominated by proton-like tracks. For this off-beam sample, a clear peak of proton-like events is observed, indicating the presence of many proton-like tracks in the off-beam data that can be leveraged for the analysis. After a simple preselection, an example of PMT waveforms after the shaper from a proton candidate is shown in Figure 6.3.

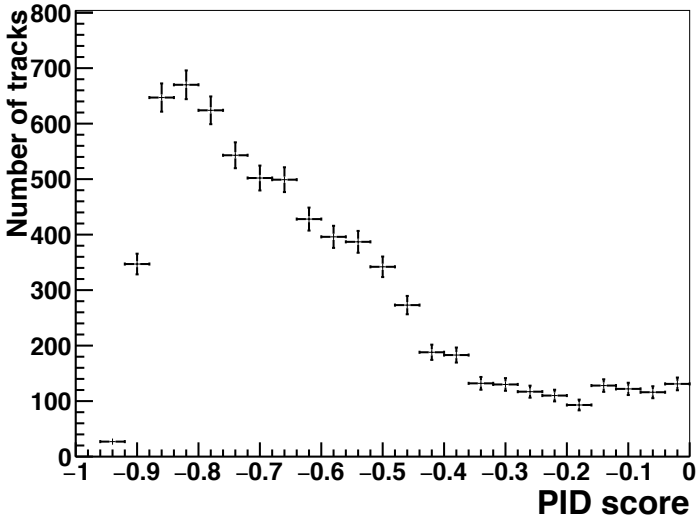


**Figure 6.2** The distribution of the PID score for track-like particles in the MicroBooNE off-beam data.

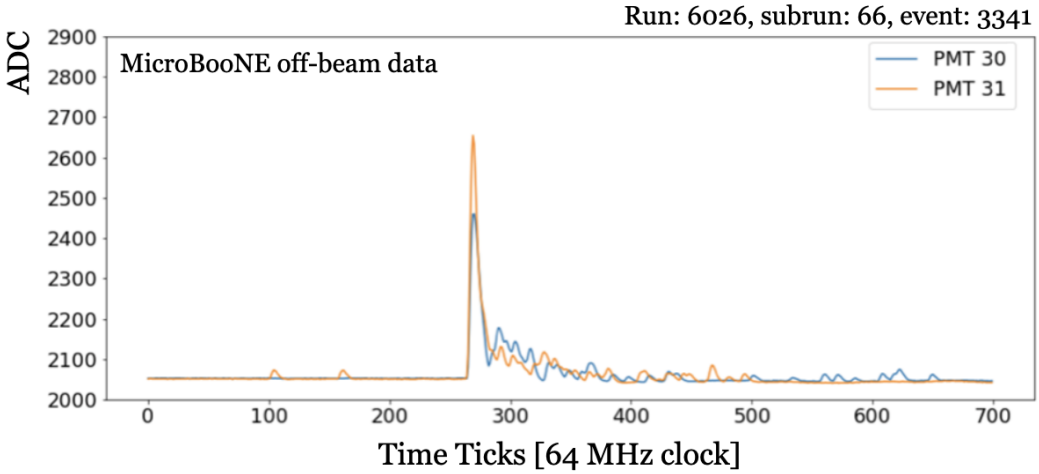


**Figure 6.3** An example of PMT waveforms after the shaper from a proton candidate in the MicroBooNE off-beam data.

### 6.2.2 Monte Carlo Samples

The Monte Carlo (MC) samples were generated with a single particle gun to produce isolated protons and overlaid with cosmic rays from data to accurately reproduce MicroBooNE's busy cosmic environment. Protons were generated isotropically within the detector volume, with kinetic energies ranging from a few MeV to 500 MeV, ensuring their track lengths are short enough to be considered "point-like." The parameters used for the MC simulation were chosen based on the data sample and are listed in Section 5.2.2. A filter module was implemented to select proton tracks fully contained within the detector, ensuring they meet the requirements for track length and drift direction. This was done to retain tracks more likely to pass the selections described in the next section and to improve the efficiency of sample production. The filter module was applied after the GEANT 4 stage. The simulation followed the standard MicroBooNE simulation chain, incorporating detector simulation and reconstruction effects, enabling comparisons between data and MC. Three fast optical simulation methods, including the MicroBooNE default photon library with RSL 66 cm and the semi-analytical model with RSL of 66 cm and 100 cm, were used to generate the MC samples. For Run 1, samples of $\mathcal{O}$(60k) protons were generated, while for Run 3, samples of $\mathcal{O}$(140k) protons were produced.

## 6.3 Event Selection

This section describes the selection process designed to identify point-like isolated protons from MicroBooNE off-beam data for the light yield measurement. The selection process is broken down into four stages, as shown in Figure 6.4. At each stage, a cut-based selection is utilised. The selections include:

- **Pre-selection**: An initial filter to reduce the dataset.
- **Fiducial volume selection**: Ensures that the proton sample is contained within the TPC.
- **Track topology selection**: A series of cuts to refine the sample and isolate the desired proton events.
- **Flash-matching quality**: Ensures the quality and integrity of the selected sample.

The performance of the selections at each stage is summarised in Table 6.1 for Run 1 and Table 6.2 for Run 3. It is worth noting that the MC samples have better selection efficiencies because the simulation only included protons with tailored parameters, whereas this is not the case for the data.


**Figure 6.4** A schematic diagram showing the event selections.

| | Data | MC photon library (RSL 66 cm) | MC semi-analytical model (RSL 66 cm) | MC semi-analytical model (RSL 100 cm) |
|---|---|---|---|---|
| **Reconstructed tracks** | 840435 (100.000 %) | 59832 (100.000 %) | 56998 (100.000 %) | 60901 (100.000 %) |
| **Pre-selection** | 1550 (0.184 %) | 18414 (30.776 %) | 17773 (31.182 %) | 18816 (30.896 %) |
| **Fiducial volume selection** | 1106 (0.132 %) | 18035 (30.143 %) | 17346 (30.433 %) | 18382 (30.183 %) |
| **Track topology selection** | 611 (0.073 %) | 13172 (22.015 %) | 12604 (22.113 %) | 13441 (22.070 %) |
| **Flash-matching quality** | 595 (0.071 %) | 12786 (21.370 %) | 12218 (21.436 %) | 13059 (21.443 %) |

**Table 6.1** A summary of the number of **Run 1** selected events (efficiency) per stage of the selection for data, MC using photon library, MC using Semi-analytical model with RSL assumption of 66 cm, MC using Semi-analytical model with RSL assumption of 66 cm.

| | Data | MC photon library (RSL 66 cm) | MC semi-analytical model (RSL 66 cm) | MC semi-analytical model (RSL 100 cm) |
|---|---|---|---|---|
| **Reconstructed tracks** | $2.27\times10^6$ (100.000 %) | 136079 (100.000 %) | 136197 (100.000 %) | 130438 (100.000 %) |
| **Pre-selection** | 4754 (0.210 %) | 42444 (31.191 %) | 42364 (31.105 %) | 41363 (31.711 %) |
| **Fiducial volume selection** | 3484 (0.154 %) | 41611 (30.579 %) | 41512 (30.479 %) | 40544 (31.083 %) |
| **Track topology selection** | 1975 (0.087 %) | 30332 (22.290 %) | 30263 (22.220 %) | 29603 (22.695 %) |
| **Flash-matching quality** | 1858 (0.082 %) | 29530 (21.701 %) | 29466 (21.635 %) | 28872 (22.135 %) |

**Table 6.2** A summary of the number of **Run 3** selected events (efficiency) per stage of the selection for data, MC using photon library, MC using Semi-analytical model with RSL assumption of 66 cm, MC using Semi-analytical model with RSL assumption of 66 cm.

### 6.3.1 Pre-selection

The first stage of the selection process utilises the Pandora reconstruction framework [226] to identify isolated proton tracks in a MicroBooNE readout event. The pre-selection aims to remove tracks that are definitely not protons and to identify isolated tracks for subsequent selection stages. The tracks after pre-selection will be referred to as *candidates* in the following sections. The pre-selection criteria are:

- **One in-time track**: One Pandora-identified interaction ("slice") matching an in-time PMT scintillation flash is required. Additionally, only **one** reconstructed track in the slice is identified.

- **PID score cut**: The PID score for the pre-selected reconstructed track must be below -0.3. The PID score is used to classify particles, with scores closer to -1 indicating the track is more proton-like and scores closer to +1 indicating the track is more muon-like.

### Event Handscans

After pre-selection, a subset of events was visually scanned to verify if these events represent truly isolated protons. The results indicate that the majority of event displays are indeed isolated protons. An ideal candidate of reconstructed proton track is illustrated on the left side of Figure 6.5. However, there are still some events where either the track is across the detector boundary or long, as shown separately in the middle and right panels of Figure 6.5. These types of events will not be useful for the final analysis and therefore need to be excluded.

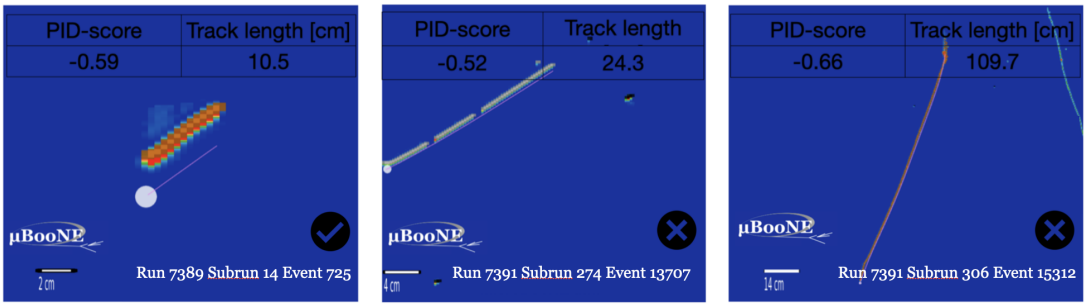


**Figure 6.5** Three event displays of candidate tracks after preselection. On the left is a good candidate for this analysis. The middle display shows a candidate that should be rejected due to its penetration of the detector border. The right display depicts a candidate track that needs to be rejected because of its excessive length.

### 6.3.2 Fiducial Volume Selection

Event hand-scans have shown that some tracks penetrate the border of the detector, making these tracks incomplete and potentially leading to misidentification as proton-like tracks, as shown in the middle of Figure 6.5. To reject these events, the reconstructed vertex and endpoint positions associated with candidates are required to lie within the fiducial volume of the detector. Additionally, since the photon library voxelises the detector, precautions are taken to ensure that the cut does not intersect a voxel boundary. Therefore, the vertex and endpoint positions are required to be at least 12.375 cm away from the border of the active volume in the $x$-axis, 10.49 cm in the $y$-axis, and 11.5941 cm in the $z$-axis, with the values stemming from the voxel size.

### 6.3.3 Track Topology Selection

The track topology selection involves a series of cuts aimed at selecting point-like proton candidates for the light yield calculation. The first criterion is to exclude candidates with very long track lengths. Figure 6.6 illustrates the distribution of track lengths for the proton candidates, which, while predominantly short, can extend up to 100 cm in maximum length. However, since these lengths exceed typical proton track lengths and point-like sources are targeted to avoid diffuse sources like muons, we define our "point-like" tracks as having a track length below 30 cm. Additionally, given the expected strong variation in light yield with drift distances, the projection of the track length in the drift direction is limited to less than 10 cm.

Furthermore, the chosen bin size for plotting is 30 cm along the drift distance to match the track length ranges of proton tracks under investigation. To maintain the integrity of our analysis and prevent photon tracks from spanning multiple bins, we impose an additional criterion: the tracks we consider must remain confined within a single bin, which has a width of 30 cm.

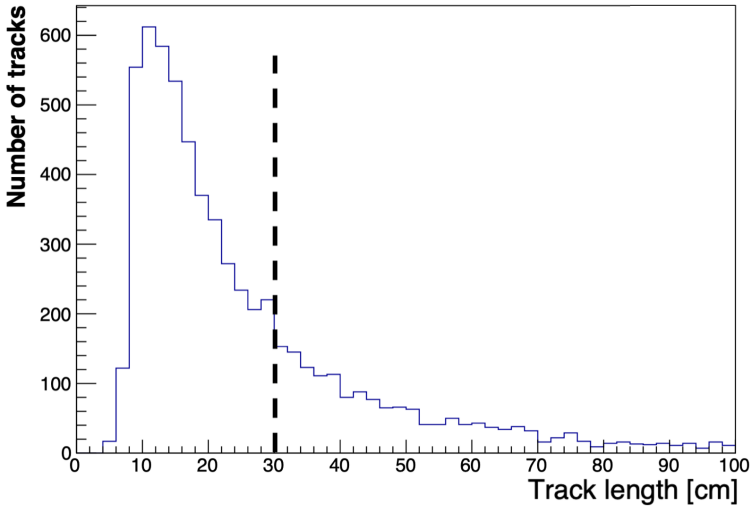


**Figure 6.6** The distribution of track lengths of proton candidates in MicroBooNE off-beam data. The dashed line demonstrates the chosen selection.

### 6.3.4 Flash-Matching Quality

A combination of TPC and light information in the detector is used to assess the flash-matching quality. This selection calculates the distance between the reconstructed light flash centre and the midpoint of tracks reconstructed by Pandora. The distance is required to be smaller than the flash width in the beam direction to confirm that photons are generated from the reconstructed track. Due to the limited number of rows in PMT layouts, as shown in Figure 4.9, a similar cut is not applied in the vertical direction.

Additionally, outlier events for calculated light yield are observed in the data and could potentially be related to mismatched events. To understand the outliers, the distance between the midpoint of tracks and the flash centre is calculated in the $y$-$z$ plane. Mismatched tracks will have larger distances between the TPC and the flash position, subsequently becoming outliers in the PE distribution. As shown in Figure 6.7, the majority of the outliers are mismatched events. Therefore, a distance requirement of 160 cm is applied to remove these mismatched events.

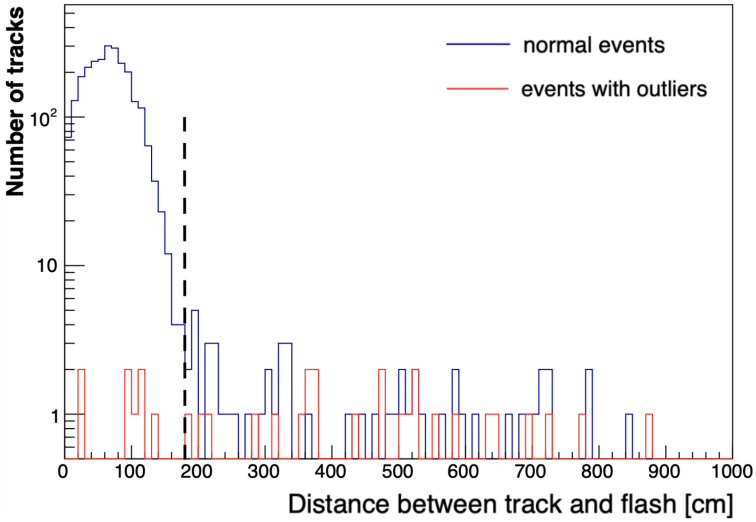


**Figure 6.7** The distributions of the distance between the midpoint of the TPC track and the flash centre in the y-z plane for normal tracks and outlier tracks. The dashed line represents the chosen selection.

## 6.4 Samples after Selection

The overall performance of the selections is shown in Table 6.1 for Run 1 and Table 6.2 for Run 3. In the data, **595** events are selected in Run 1 and **1,858** events in Run 3, which are sufficient for our further measurement of the light yield. Figure 6.8 shows the distributions of midpoints in the $x$, $y$, and $z$ directions for selected proton candidate tracks in the MicroBooNE off-beam data. As expected, the proton candidates cover the entire range along the $x$-direction, with a higher distribution in the upper $y$-range because our sample comes from cosmic rays. For all three directions, the decreases in the first and last bins were due to the fiducial volume cut. The dips at small $z$ values and around 700 cm are due to the difficulty in reconstructing "point-like" tracks in regions of the collection plane with unresponsive wires, as described in Section 4.4.1. For the selected proton candidates, the reconstructed kinetic energies in the data sample are shown in Figure 6.9, with the majority of proton candidates having kinetic energies around 100 to 150 MeV.

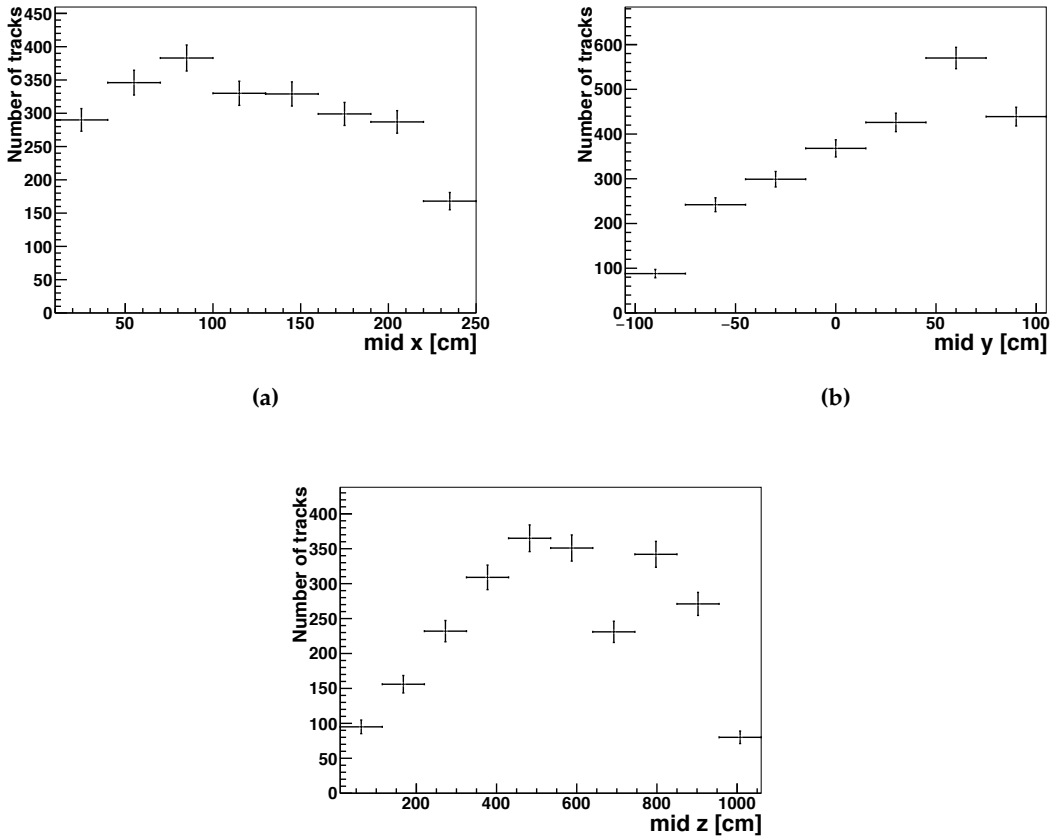


**Figure 6.8** The distributions of proton candidate midpoints in (a) $x$-direction, (b) $y$-direction, and (c) $z$-direction in the MicroBooNE Run 1 and Run 3 off-beam data.

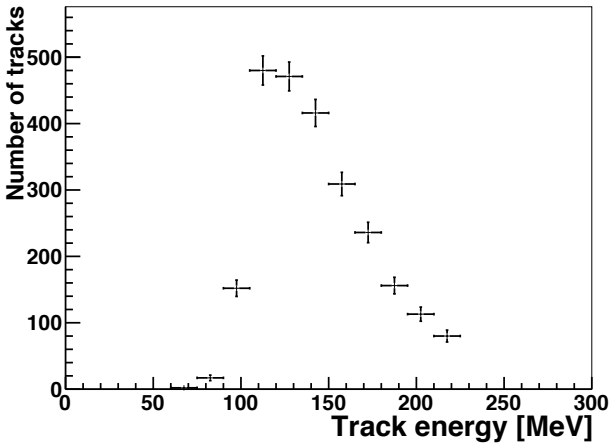


**Figure 6.9** The distribution of the proton reconstructed kinetic energy in the MicroBooNE off-beam data.

## 6.5 Note on the Choice for the Statistical Uncertainty

In this analysis, we aim to measure the light yield across the detector as a function of position. For the statistical uncertainty, two options could be considered: the standard deviation and the standard error. The standard deviation is typically used to describe the dispersion within a dataset and helps understand the variation of the sample. The standard error, on the other hand, measures the precision of the sample's mean estimation. For this analysis, the **standard error** has been used as the statistical uncertainty, as the objective is to measure the light yield at a given position, focusing on the mean value and the accuracy of the mean value.

## 6.6 Total Light Yield Measurement (Statistical-only Uncertainty)

With the selected proton candidates, a position-dependent light yield measurement can be performed. In this section, we introduce the total light yield as a function of drift position. The total light yield is calculated as the number of reconstructed flash PEs from all PMTs divided by the energy deposited by the protons. The total light yield was determined in the same way for both data and MC samples, and the results were compared to assess the agreement.

For this analysis, both Run 1 and Run 3 data were used. Three simulation approaches for the light simulation were used for comparison with the data: the default photon library with an RSL assumption of 66 cm, and the semi-analytical model developed by the author with two different RSL assumptions: 66 cm and 100 cm.

For the reconstructed flash PE, MicroBooNE employs a series of calibrations. The first is the PMT gain calibration, as each PMT has a different gain value during operation, while the reconstruction assumes a fixed value. The second calibration addresses the light-yield decline, using the average values between the anode and cathode results from cosmic muons, as indicated by the blue points in Figure 6.1. For this analysis, reconstructed PEs both before and after the light-yield decline calibration were used to independetly verify the effect of the calibration.

In this section, we first discuss the total light yield in an ideal detector where the photon detectors are evenly distributed, with results presented in Section 6.6.1. Then, the total light yield results from data using the actual MicroBooNE detector setup are compared with all three MC samples for both Run 1 (see Section 6.6.2) and Run 3 (see Section 6.6.2). Finally, the measured total light yield for the MicroBooNE detector from Run 1 and Run 3 data will be compared to previous results obtained using cosmic muons, as shown in Section 6.6.3.

### 6.6.1 Total Light Yield along the Drift Direction in an Ideal Detector

The coverage for the photon detectors in MicroBooNE is calculated to be around 0.9%, and the sparse distribution of the PMTs can cause large fluctuations. To address this, we aim to measure the light yield under the ideal assumption of a uniform distribution of the photon detectors. Thus, a series of total light yield plots in the $y$-$z$ plane, varying with different drift positions, were generated to understand the non-uniformity of the light yield caused by the positioning of the photon detectors. The top left plot of Figure 6.10, focusing on the range 10 cm $< x <$ 40 cm, demonstrates that the total light yield varies significantly depending on the relative position to the photon detectors. Therefore, a hexagonal cut, as illustrated in the top right plot of Figure 6.10, is applied to select the brighter region and construct an ideal scenario data sample with a uniform distribution of the light yield. As one moves away from the detectors in the drift direction, specifically when $x > 100$ cm, the light yield becomes approximately uniform in the $x$-$y$ plane. Therefore, the hexagonal cut is only applied up to a drift position of $x = 100$ cm. Appendix A presents additional total light yield maps across varying drift distances.

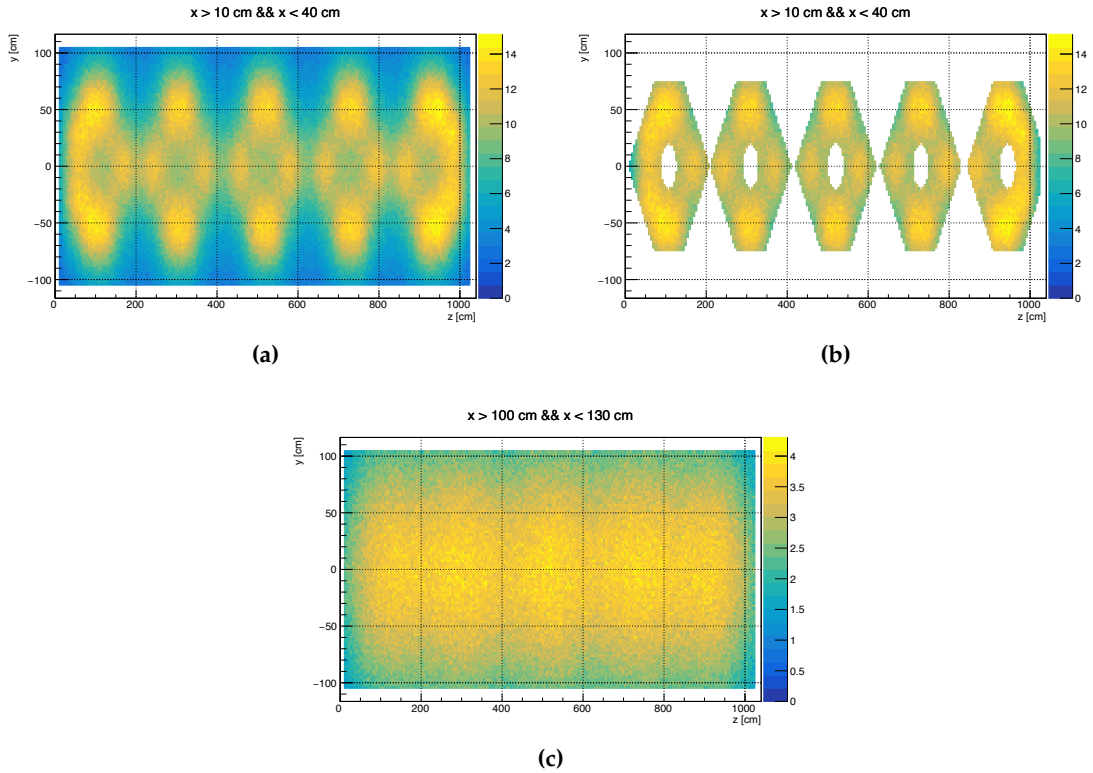


**Figure 6.10** (a) the total light-yield map in the $y$-$z$ plane for 10 cm $< x <$ 40 cm, showing drastic variations in light yield based on the relative position to the PMTs. (b) the brighter region is selected to form the uniformity of the light yield. (c) the total light-yield map in the $y$-$z$ plane for 100 cm $< x <$ 130 cm, where the light yield is approximately uniform.

After applying hexagonal cuts, an "ideal" detector setup with reasonably uniform light-yield distribution is achieved. Due to the loss of a PMT in Run 3, only Run 1 data are used for this study. The total light yield is measured as a function of drift distance. As shown in Figure 6.11, there is a strong position dependence of light yield across the drift distance. The results demonstrate that, for all three simulation approaches, the MC simulations generally align well with the data across the entire drift direction. Both the photon library and the semi-analytical model, under the same RSL assumption, yield similar results. For larger drift distances ($x > 160$ cm), an RSL of 100 cm shows slightly better agreement with the data.

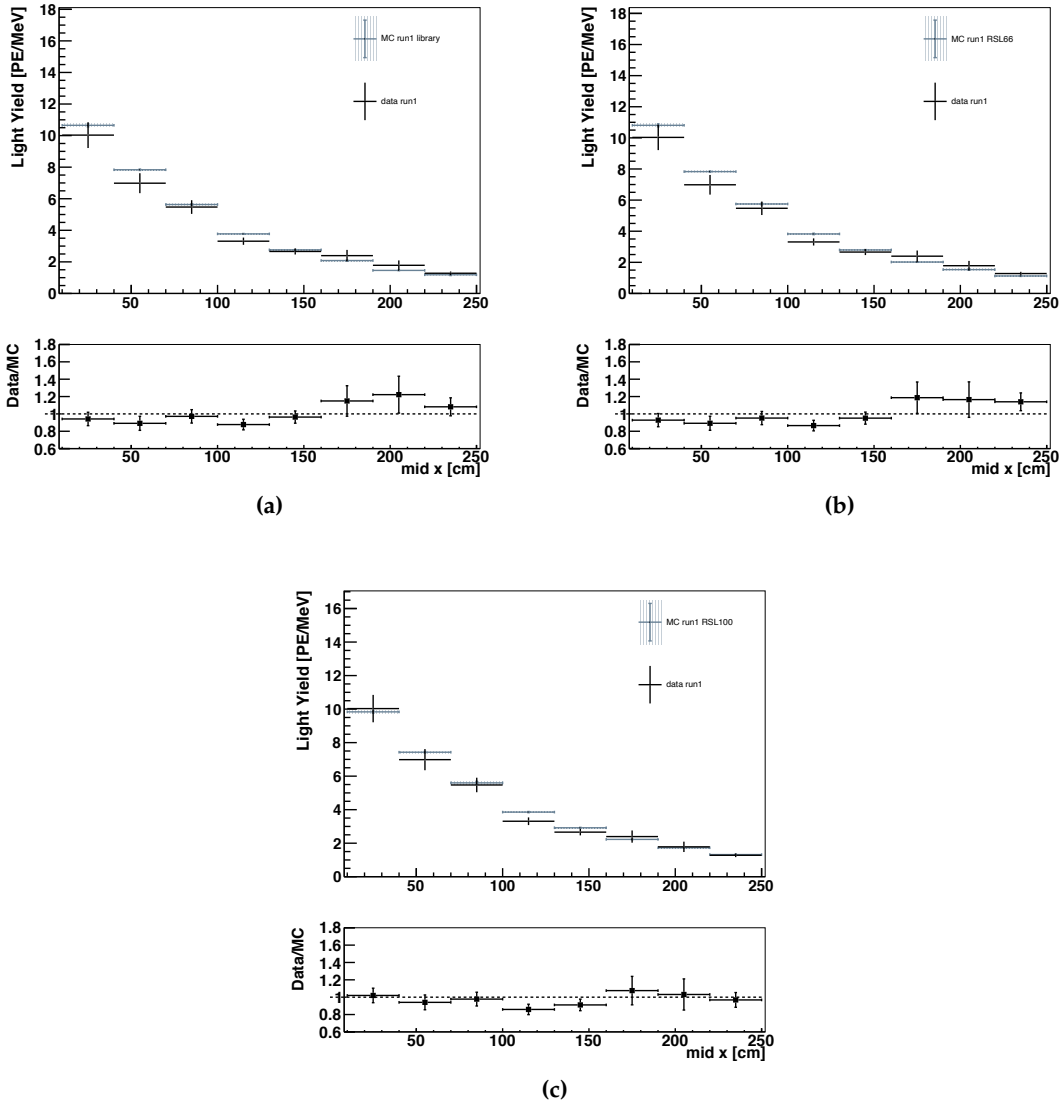


**Figure 6.11** Total light yield as a function of different positions along the drift direction, for (a) photon library, (b) semi-analytical model with 66 cm RSL, and (c) semi-analytical model with 100 cm RSL in an ideal detector.

### 6.6.2 Total Light Yield along the Drift Direction in MicroBooNE

The previous section presented the hexagonal cut used to select a region with a uniform light yield, creating an "ideal" detector setup. However, in reality, to measure the light yield in the MicroBooNE detector, this hexagonal cut needs to be removed.

#### Run 1

The measured light yield from Run 1 is compared with three different MC samples, and the results are shown in Figure 6.12. The photon library and the semi-analytical model display similar light yield predictions in the MC assuming the same RSL. The MC exhibits good agreement with the data, except for the first bin when the scintillation points are closest to the PMTs in the drift direction. This discrepancy arises due to the challenges in modeling the large offset angle and the drastic change in light yield for smaller drift distances, as discussed in Section 6.6.1. The data to MC comparison returns to around 1 once the scintillation points in line with the PMTs are selected, as shown in Figure 6.11. Notably, for larger drift distances, a RSL of 100 cm demonstrates slightly better agreement with the data, similar to what was found in the ideal detector case.

#### Run 3

For Run 3, the light yield decline for both data and simulation is removed by calibration. The results from the data are again compared with three different MC samples, as shown in Figure 6.13. The photon library and the semi-analytical model with the same RSL assumption continue to produce similar results. For shorter drift distances, all three simulation methods predict light yield results that in a good agreement with the data. For larger drift distances ($x > 130$ cm), the 100 cm RSL shows significantly better agreement with the data. It is worth noting that overall, the MC sample with 100 cm RSL has a very good agreement with data across the whole drift direction.

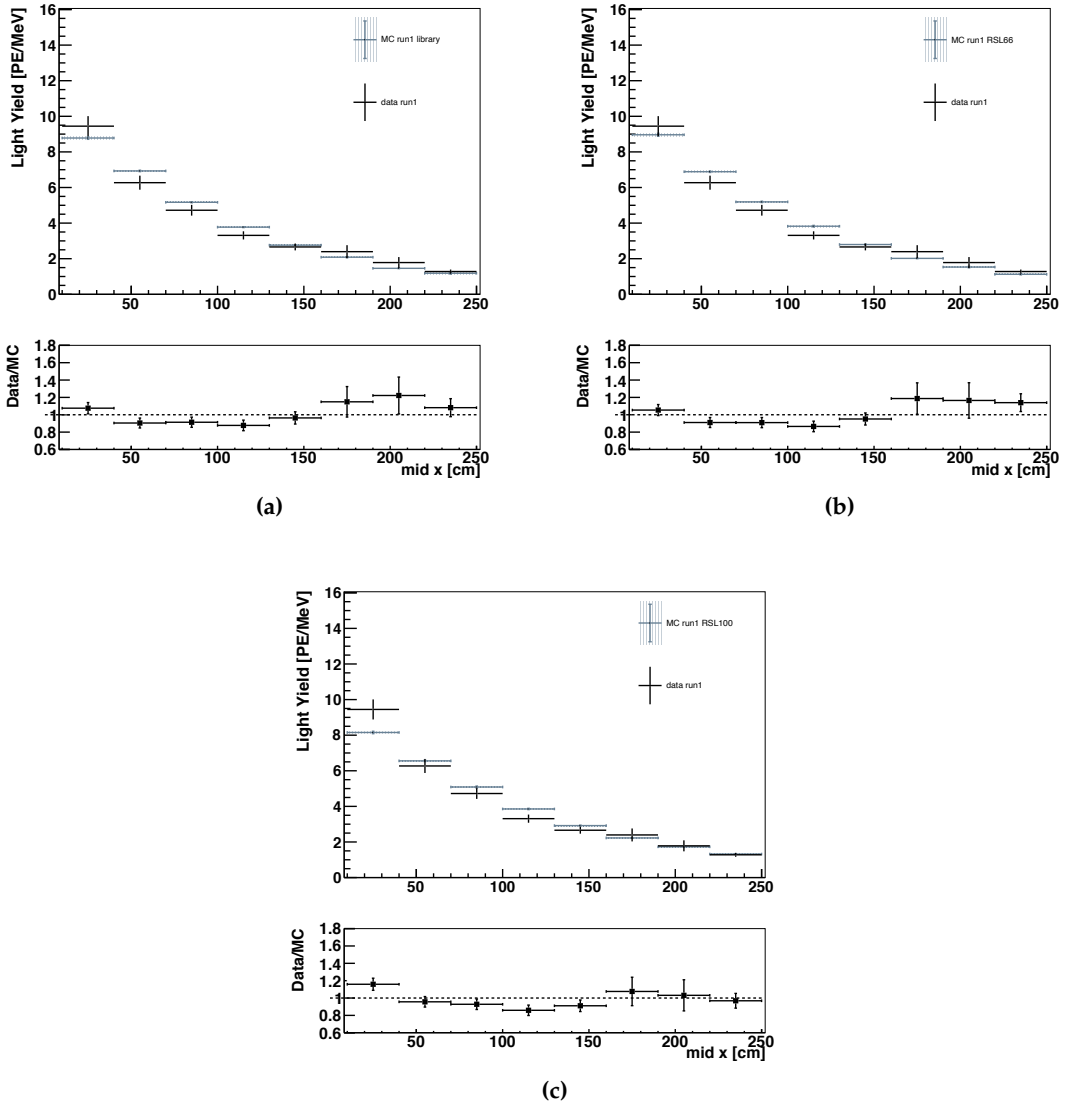


**Figure 6.12** The Run 1 measured total light yield as a function of the drift position compared with (a) photon library, (b) semi-analytical model with 66 cm RSL, (c) semi-analytical model with 100 cm RSL.

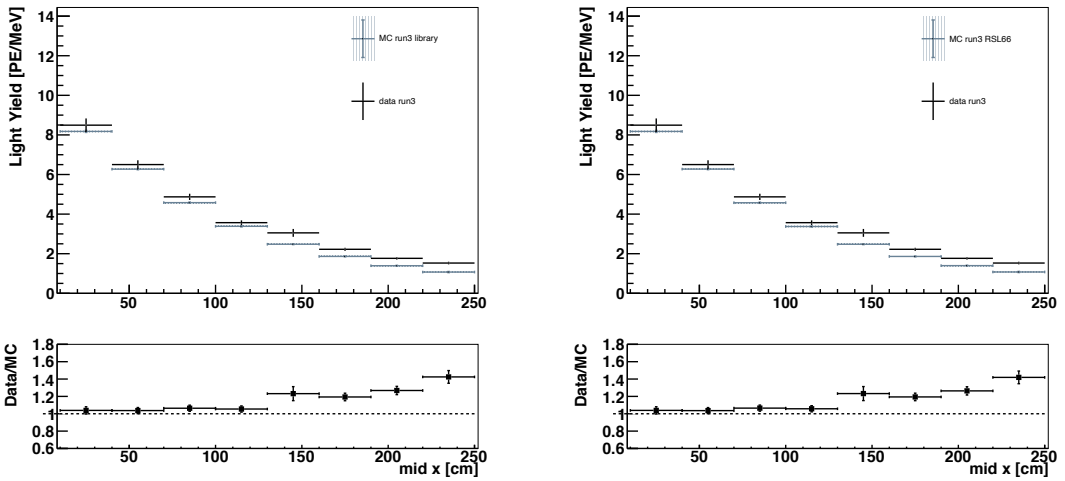


(a)




(b)

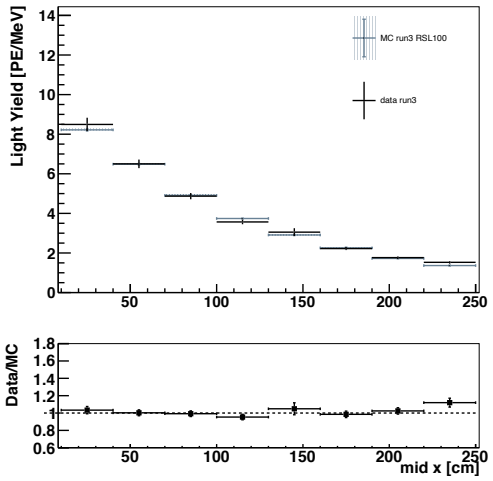


(c)

**Figure 6.13** The Run 3 measured total light yield as a function of the drift position compared with (a) photon library, (b) semi-analytical model with 66 cm RSL, (c) semi-analytical model with 100 cm RSL.

### 6.6.3 Total Light Yield Decline and its Calibration in MicroBooNE

The total light yield is measured using both Run 1 and Run 3 off-beam data. As illustrated in the left panel of Figure 6.14, a decline in light yield from Run 1 to Run 3 is observed, consistent with results obtained from cosmic muons. The ratio of this decline, depicted in the bottom panel of the left Figure 6.14, remains relatively constant ($\sim$ 0.6) across the entire drift distance. Unlike the results from the cosmic muon sample, the isolated proton sample shows no significant position dependence of this decline. However, the constant ratio is similar to the calibration value used in MicroBooNE, as shown in Figure 6.1.

The total light yield from Run 3 after calibration is compared with that from Run 1. As shown on the right of Figure 6.14, the calibration effectively cancels the light yield decline, equalising the total light yield ratio between Run 1 and Run 3 to approximately 1. The first bin highlights the challenges of reconstructing the non-linear response region with high light intensities in Run 1, which leads to over-reconstruction of light. Conversely, in the last bin, where the proton candidates are further from the detector, the results demonstrate less agreement, could be related to the challenges of reconstructing light at low intensities.

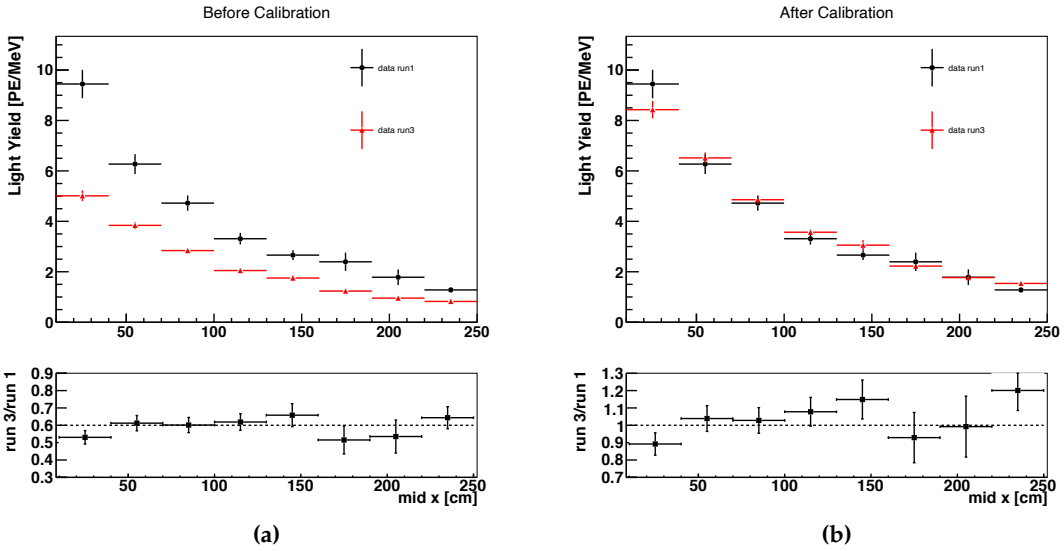


**Figure 6.14** (a) Measured total light yield as a function of the drift position, for Run 1 (in black) and Run 3 (in red), respectively. (b) The measured total light yield in Run 1 (in black) and the total light yield in Run 3 (in red) after calibration.

## 6.7 PMT-by-PMT Measurement (Statistical-only Uncertainty)

In the previous sections, we presented the total light yield results as a function of drift distance. A non-uniformity in the light yield is observed as one moves away from the PMTs. The drift distance, being a one-dimensional projection of the absolute distance from the scintillation point to the PMTs, can result in a variety of event configurations with significantly different light yields for the same projected distance. For example, events close to the PMTs with a small offset angle and events further away with a large offset angle can both have similar drift distances, but very different light yields making the light yield predictions difficult. To study the distance dependency more accurately, we introduce the absolute distance as a new variable in the analysis. To facilitate this, the reconstructed flash PEs are allocated to individual PMTs, allowing for PMT-by-PMT measurements. This method not only identifies the contributions from each PMT but also significantly increases the number of measurements, thereby enhancing the statistical robustness of the dataset.

For the PMT-by-PMT measurement, the light yield results are calculated for each individual PMT, and the correlation as a function of absolute distance is studied. These results, derived from Run 1 and Run 3 data, are compared separately with three MC samples: the photon library and the semi-analytical models with RSL assumptions of 66 cm and 100 cm. Detailed comparisons between the data and the MC samples are presented in Section 6.7.1 and Section 6.7.1.

### 6.7.1 Light Yield as a Function of Distance in MicroBooNE

#### Run 1

The light yield for each PMT at a given distance is calculated using data from selected proton candidates in Run 1. As expected, the light yield decreases significantly with increasing distance. The comparisons between the data and MC simulations are depicted in Figure 6.15. Both the photon library and the semi-analytical model, employing the same RSL assumptions, yield similar results. At shorter distances, the MC simulations generally align well with the data. However, for absolute distances greater than 240 cm, the semi-analytical model with an RSL of 100 cm exhibits a better agreement with the data.

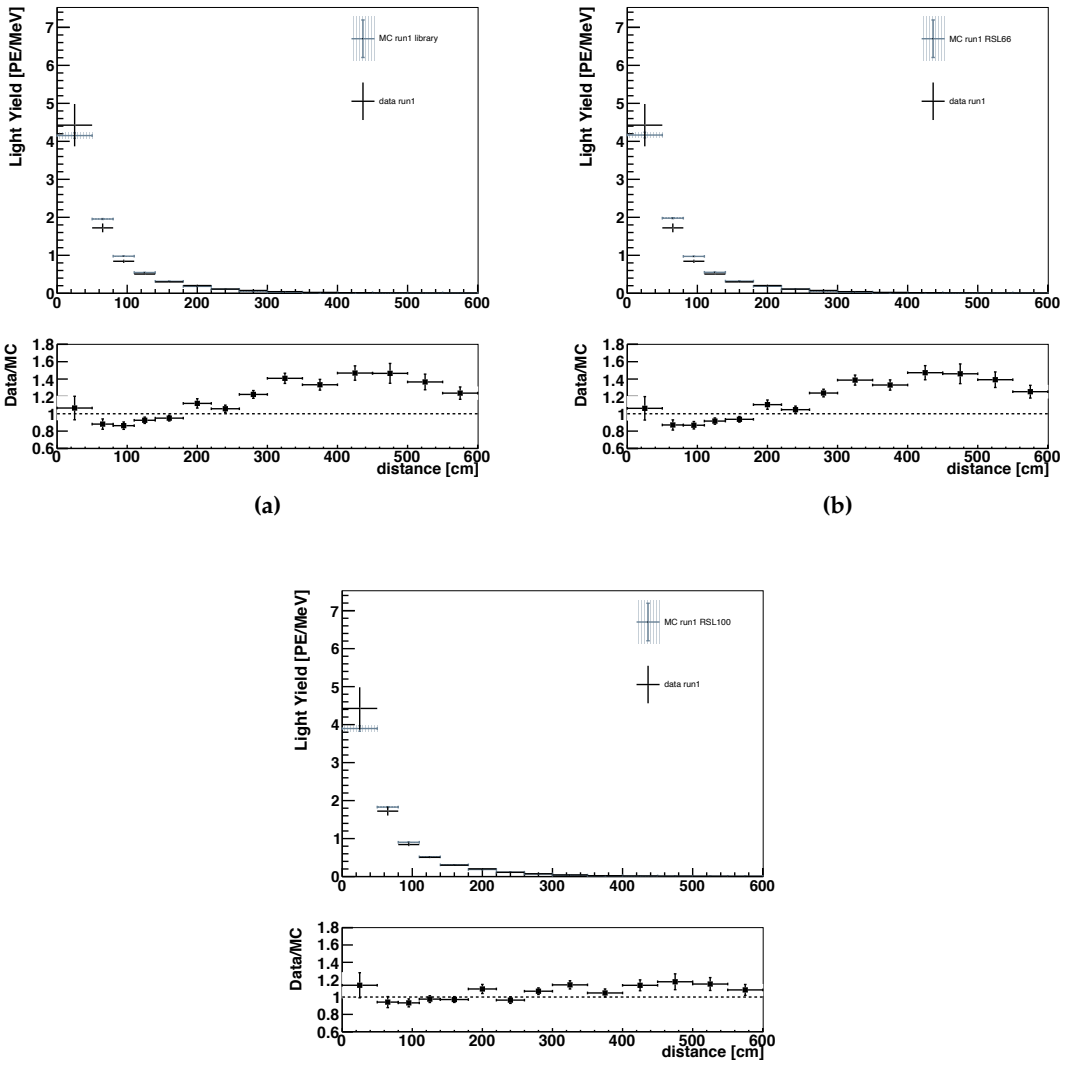


**Figure 6.15** Light yield as a function of the drift distance for Run 1 data, comparing with (a) photon library, (b) semi-analytical model with 66 cm RSL, and (c) semi-analytical model with 100 cm RSL.

### Run 3

Similarly, the individual light yield from Run 3 data is measured and compared with the three MC samples. All three MC samples yield predictions similar to the data at shorter distances ($< 130$ cm). Conversely, only the MC sample using a 100 cm RSL assumption shows good agreement with the Run 3 data across larger distances to the PMTs. However, similar to Run 1, a slight excess was also observed at large distances in the MC sample with 100 cm RSL, though it was much smaller than in the 66 cm RSL case. Therefore, testing a slightly larger RSL assumption in the future could potentially help achieve better agreement with the data.

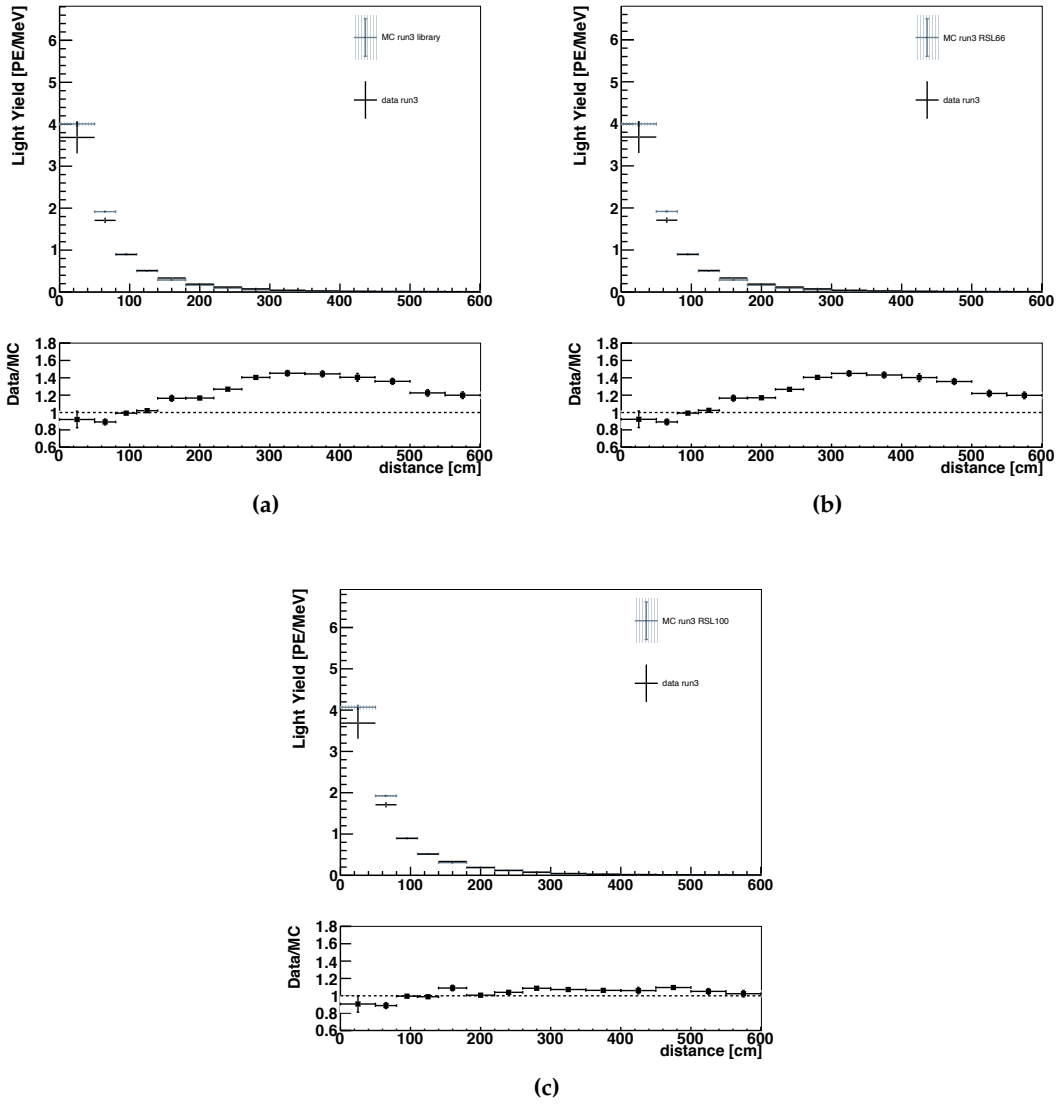


**Figure 6.16** Light yield as a function of the drift distance for Run 3 data, comparing with (a) photon library, (b) semi-analytical model with 66 cm RSL, and (c) semi-analytical model with 100 cm RSL.

## 6.8 Systematic Uncertainties

Up to now, only statistical errors have been considered. To calculate the systematic errors, we first employ the baseline simulation, also referred to as the Central Value (CV) sample, which represents the simulation using nominal parameter values. For the systematic error calculations, the MC sample with the 100 cm RSL assumption has been chosen as the CV sample for this analysis. The systematic uncertainties for the other two MC samples are expected to yield similar results for the systematic uncertainty sources considered in this analysis, therefore we apply calculations only once.

The systematic uncertainties are calculated using the **unisim** technique, which involves modifying the input assumptions of the simulation one by one and observing how these variations affect the results. This evaluation is carried out through a method known as **sample re-simulation**. In this approach, the nominal value of a parameter is varied by $\pm 1\sigma$, and the modified parameter is used to generate a new MC sample. The effect of this variation is measured by the fractional difference, and the systematic uncertainties are then determined by summing these differences in quadrature. The formula for calculating the systematic uncertainty is defined as:

$$\sigma_{\text{syst.}} = \sqrt{\sum_{n}^{\text{params}} \left( \frac{LY_i^n - LY_i^{CV}}{LY_i^{CV}} \right)^2}, \tag{6.1}$$

where $LY_i^n$ is the light yield value of the $i$th bin for each detector variation samples, and $LY_i^{CV}$ is the light yield value of the $i$th bin calculated with the CV sample.

Uncertainties in modelling the detector response are considered the systematic uncertainties for this analysis. Specifically, all TPC-related detector variations related to the space charge effect, recombination, and wire response simulation are considered. For all variations, samples with 10 times larger statistics were generated for the evaluation of systematic uncertainties.

### 6.8.1 Space Charge Effect

The space charge effect (SCE) results from distortions in the electric field due to the accumulation of $Ar^+$ ions, as described in Section 3.3.3. For this analysis, the SCE could potentially impact the energy and position reconstruction of protons.

In MicroBooNE, the SCE is modelled using distortion and correction displacement maps derived from through-going cosmic rays [165]. Additionally, displacement maps are generated with the laser calibration system in MicroBooNE [233]. Since the trajectory of the laser is precisely known, corrections for each point along the trajectory can be applied, allowing for accurate calculation of displacement maps.

Laser calibration data is used to estimate the residual uncertainty in the SCE modelling. By comparing displacement maps obtained from laser calibration data (a combination of cosmic and laser data) with those derived solely from cosmics, the bias can be evaluated. This bias is taken as an estimate of the uncertainty in the SCE modelling. The detector variation sample is produced using displacement maps where the laser track trajectory is unbiased.

### 6.8.2 Recombination

As described in Section 5.4.1, MicroBooNE uses the modified box recombination model to estimate the energy loss per unit length $dE/dx$ from the charge deposition per unit length $dQ/dx$. The modified box recombination model is expressed in Equation 5.3. For the parameters $\alpha$ and $\beta'$, the baseline simulation uses values derived by the Argon Neutrino Teststand (ArgoNeuT) experiment [158]. MicroBooNE also fit the model using a sample of protons from beam-on data [187]. Differences in the parameters used for the box recombination model can impact the accuracy of the recombination effect calibration, thereby affecting the energy reconstruction for this analysis. To assess the uncertainties due to different assumptions of the model parameters, a detector variation sample is produced using the parameters obtained from this fit.

### 6.8.3 Wire Modifications

Differences in modelling the wire response can affect both energy and position reconstruction in this analysis. The wire response to the ionised charge depends on various effects modelled in the simulation, such as recombination, diffusion, and non-responsive wires. To estimate the uncertainties in the simulated wire response, a data-driven approach is used, leveraging MicroBooNE beam-off data and the cosmic simulation sample generated by CORSIKA [223]. The differences in wire waveforms between the data and the simulation (data/MC ratios) are derived, and the dependence of these differences on the position $X, YZ$ and the direction $\theta_{XZ}, \theta_{XY}$ of the reconstructed hits is measured. Here, $X$ represents the drift position, $YZ$ represents the 2D coordinate in the plane perpendicular to the drift direction, and $\theta_{XZ}$ and $\theta_{XY}$ are the angles of the reconstructed direction with respect to the drift and wire directions, respectively [234]. The detector variation sample is then produced by modifying the wire response waveforms based on these ratios as a function of these relevant variables.

### 6.8.4 Results

Systematic uncertainties are calculated for both the total light yield versus drift distance and the light yield versus absolute distance. Figures 6.17 and 6.18 provide breakdowns of the fractional detector variation uncertainties for light yield measurements from Run 1 and Run 3, respectively. By using Equation 6.1, the overall systematic uncertainties for both analyses are derived. In general, the systematic uncertainties are found to be small, less than 3% in both cases.

## 6.9 Final Light Yield Results

### 6.9.1 Total Light Yield Results

Systematic and statistical uncertainties are combined in quadrature to obtain the total uncertainty. Figures 6.19 and 6.20 present the total light yield results with combined uncertainties across different drift distances for Run 1 and Run 3, respectively. In this analysis, since the systematic uncertainties are calculated to be within 3%, the error bars do not significantly change when combined with statistical uncertainties. For both Run 1 and Run 3 data, the MC results with a RSL of 100 cm consistently show better agreement with the data.

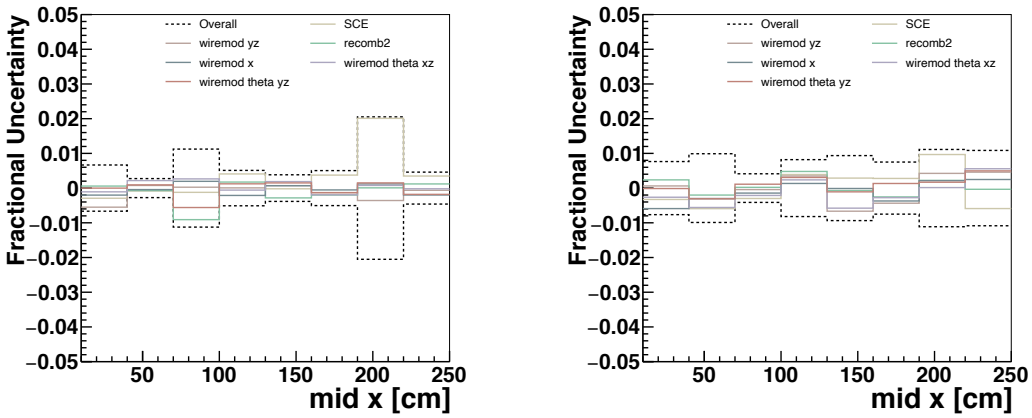


(a) (b)

**Figure 6.17** Breakdown of fractional difference for detector variation uncertainties for total light yield against drift distance for (a) Run 1 and (b) Run 3. The jump around 200 cm in (a) is currently under investigation.

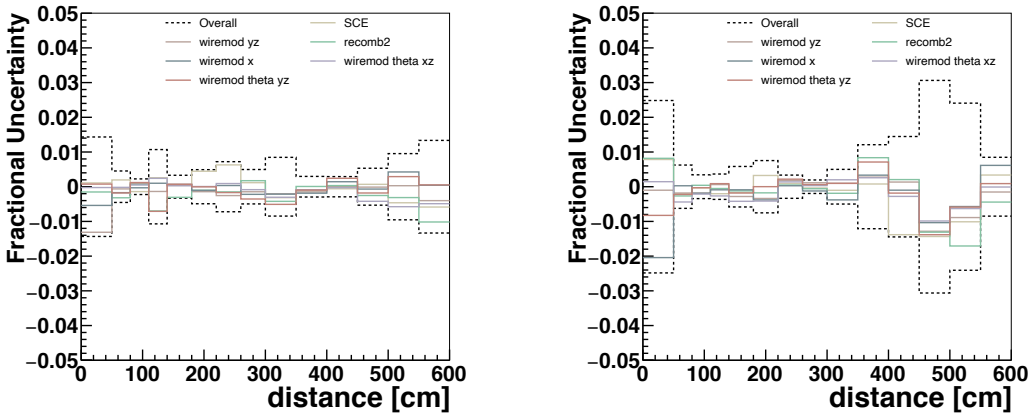


(a) (b)

**Figure 6.18** Breakdown of fractional difference for detector variation uncertainties for individual light yield against distance for (a) Run 1 and (b) Run 3.

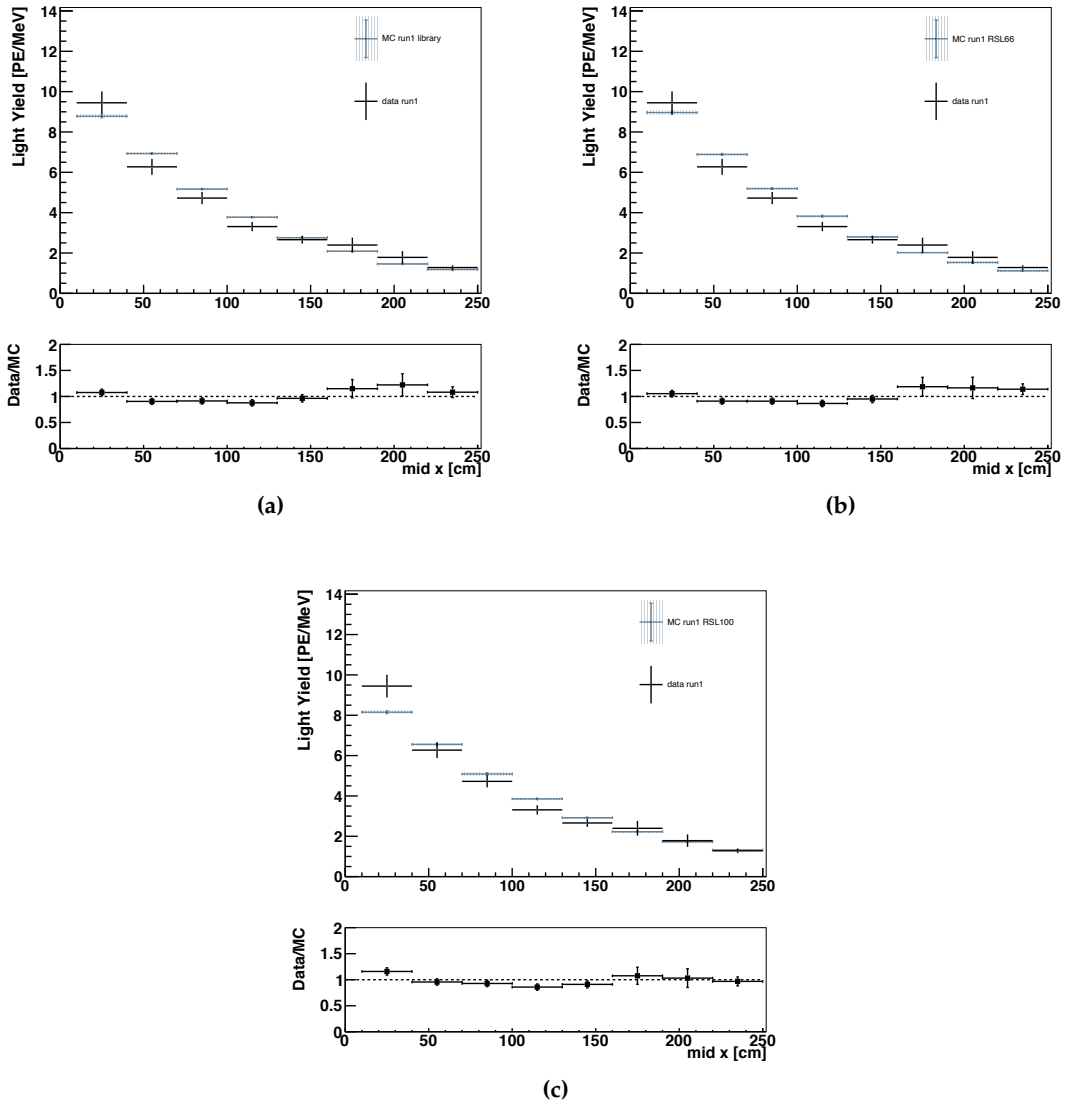


**Figure 6.19** Run 1: Total light yield as a function of the drift distance for (a) photon library, (b) semi-analytical model with 66 cm RSL, and (c) semi-analytical model with 100 cm RSL, combined statistical and systematic errors are shown in these plots.

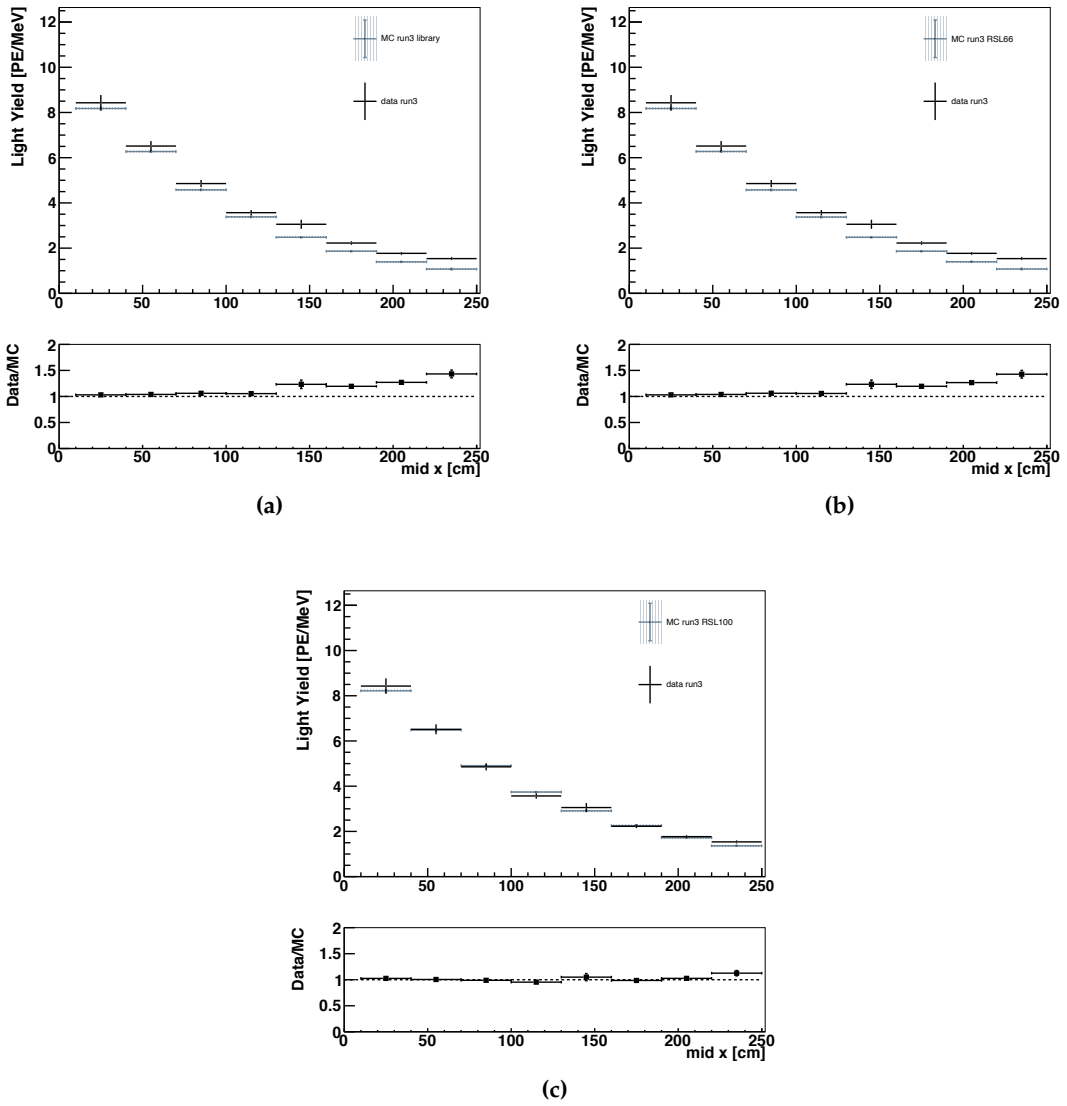


**Figure 6.20** Run 3: Total light yield as a function of the drift distance for (a) photon library, (b) semi-analytical model with 66 cm RSL, and (c) semi-analytical model with 100 cm RSL, combined statistical and systematic errors are shown in these plots.

### 6.9.2 PMT-by-PMT Measurement Results

Similar to with the total light yield results, the overall uncertainties are calculated by combining statistical and systematic uncertainties in quadrature. Figures 6.21 and 6.22 present the individual light yield results as a function of absolute distance with combined uncertainties for Run 1 and Run 3, respectively. For larger distances, the larger uncertainties arise from error propagation, as the mean values are very small (close to zero). Overall, across both datasets, simulations implementing a RSL of 100 cm consistently show better agreement with the observed data.

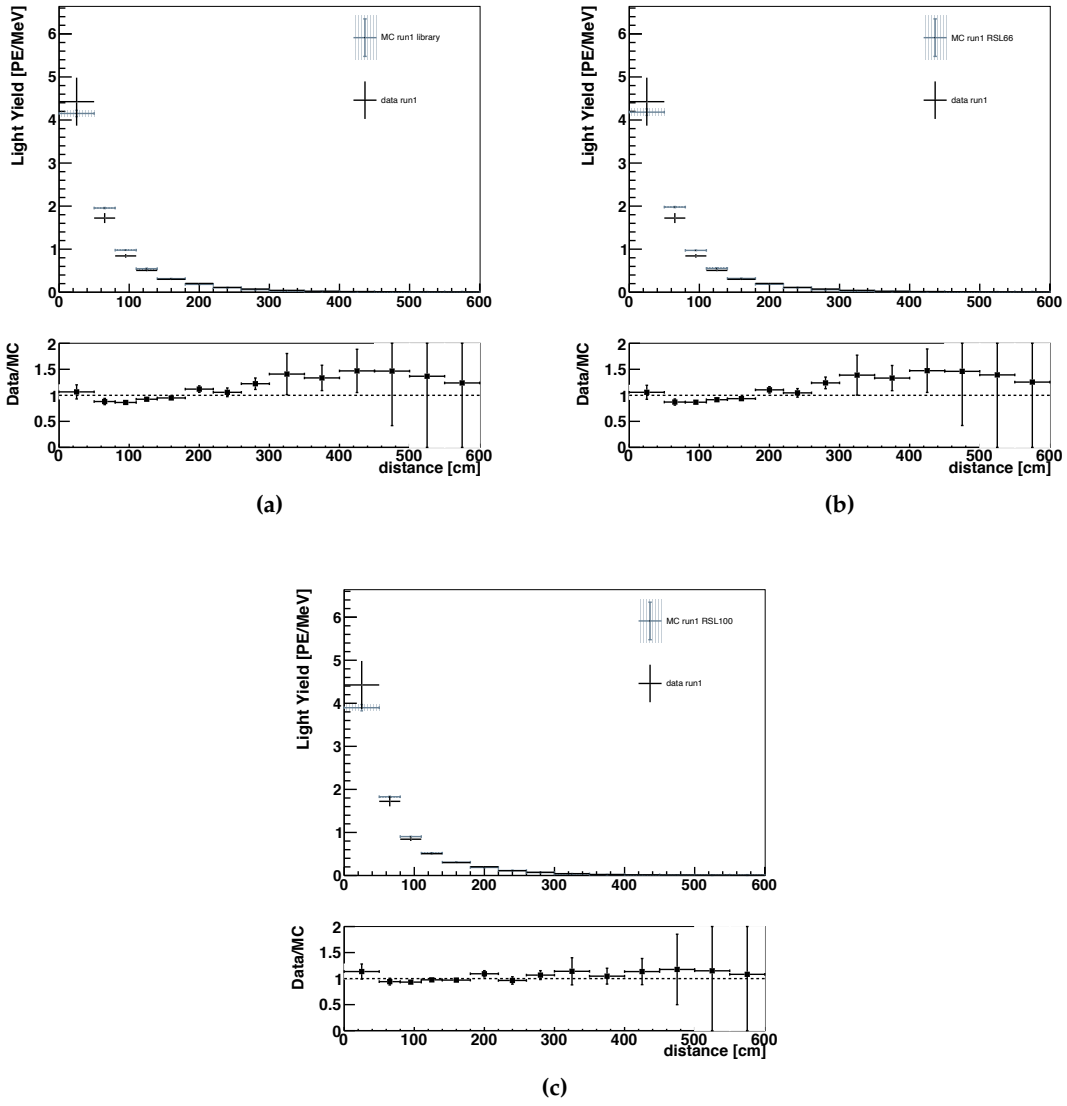


**Figure 6.21** Run 1: Individual light yield per PMT as a function of the distance for (a) photon library, (b) semi-analytical model with 66 cm RSL, and (c) semi-analytical model with 100 cm RSL, combined statistical and systematic errors are shown in these plots.

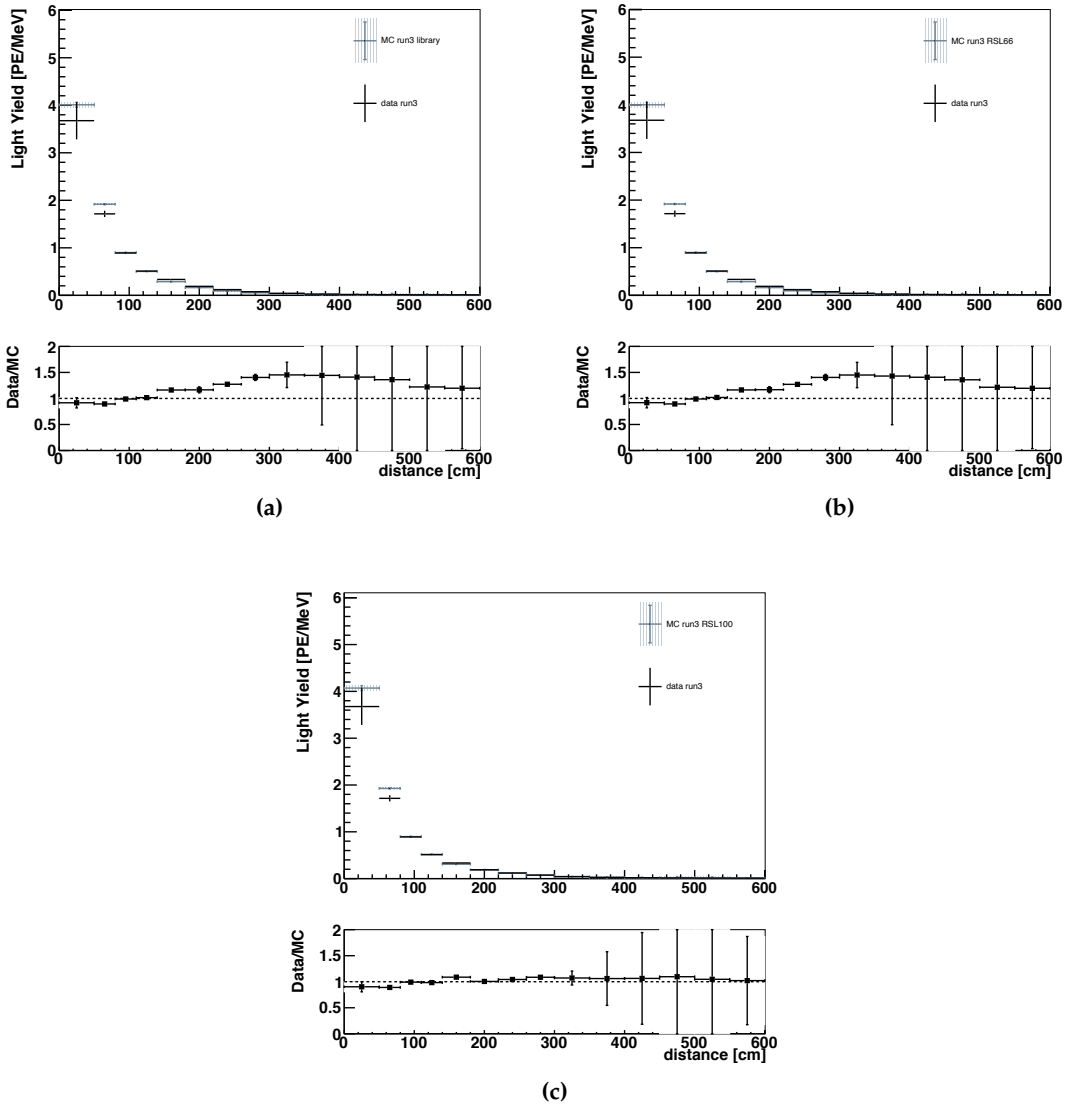


**Figure 6.22** Run 3: Individual light yield per PMT as a function of the distance for (a) photon library, (b) semi-analytical model with 66 cm RSL, and (c) semi-analytical model with 100 cm RSL, combined statistical and systematic errors are shown in these plots.

## 6.10 Statistical Test for the Different RSL Assumptions

As discussed in Section 3.2.2, the measured and theoretically predicted RSLs range from 50 cm [147, 148] to 110 cm [149]. MicroBooNE uses 66 cm as the default. The most recent measurement reports a value of 99.1 $\pm$ 2.3 cm for argon scintillation light, leading to 100 cm being commonly adopted by other LArTPC detectors. Therefore, for this measurement, both assumptions are used for simulation. By comparing the simulated light yield results to the measured light yield, we can attempt to determine a preferred Rayleigh scattering length for MicroBooNE. So far, the 100 cm RSL shows better agreement when comparing data to the MC. To quantify the preference properly, a Chi-square test is chosen using the ratio plot (data/MC).

### 6.10.1 Definition of Hypotheses

To perform the Chi-square test, it is essential to establish a **null hypothesis**. In this analysis, where we are comparing the ratio of experimental data to MC simulations, the null hypothesis is that the **ratio = 1** for the different bins in the PMT-by-PMT measurements. This hypothesis assumes that there is no significant difference between the observed data and the MC predictions, implying that any deviations observed are due to random fluctuations rather than systematic discrepancies.

### 6.10.2 Chi-square Goodness-of-Fit Test and p-value Calculation

The Chi-square is calculated to quantify the discrepancy between the measurement and the hypothesis to test the goodness-of-fit. The Chi-square for this analysis is defined as:

$$\chi^2 = \sum_{i=1}^{n} \frac{(1 - r_i)^2}{\sigma_i^2}, \tag{6.2}$$

where $r_i$ is the calculated ratio in each bin, $\sigma_i$ is the propagated error for each bin, 1 is the hypothetical ratio value. The number of degrees of freedom is calculated as the number of bins minus 1. With the calculated Chi-square value and degrees of freedom, the p-value representing the probability to observe the computed Chi-square value can be determined based on the Chi-square distribution. The predefined threshold value $\alpha$ for the p-value test is set to be 0.05.

### 6.10.3 Results

The individual light yield per PMT as a function of the absolute distance has been selected for the statistical test, as this distance provides the highest accuracy. Both Run 1 and Run 3 data are used to determine the RSL preference in the MicroBooNE detector. The results of the statistical tests are presented in Table 6.3.

| | MC sample | $\chi^2/d.o.f$ | p-value |
|---|---|---|---|
| Run 1 | Photon library, RSL 66 cm | 2.55 | 1.6e-3 |
| | Semi-analytical model, RSL 66 cm | 2.68 | 8.8e-4 |
| | **Semi-analytical model, RSL 100cm** | **0.68** | **0.78** |
| Run 3 | Photon library, RSL 66 cm | 9.00 | 8.0e-19 |
| | Semi-analytical model, RSL 66 cm | 9.03 | 6.7e-19 |
| | **Semi-analytical model, RSL 100cm** | **1.88** | **0.03** |

**Table 6.3** Statistical test results for Run 1 and Run 3 using individual light yield results. The best goodness-of-fit result is highlighted in the bold font.

For Run 1, the statistical test results show that the semi-analytical model with a 100 cm RSL assumption yields the lowest $\chi^2$ value and a p-value greater than 0.05. This suggests that the null hypothesis cannot be excluded and that the 100 cm RSL model aligns well with the data. In Run 3, the semi-analytical model with a 100 cm RSL also has the lowest $\chi^2$ value, but its p-value is less than 0.05, indicating some discrepancy between the simulation and the data. Nevertheless, among the three simulation scenarios, the 100 cm RSL consistently provides the best fit, as evidenced by its lowest $\chi^2$ values. For future work, different RSL values, potentially longer ones, could be evaluated to determine which provides the best fit to the data.

## 6.11 Summary and Outlook

Scintillation light provides both trigger and timing for neutrino interactions in the LArTPC detector. Therefore, understanding the detector response to the light signal is crucial. This chapter introduces a position-dependent light yield measurement using point-like isolated protons. The cosmic-induced proton sample maps the entire detector volume, with the point-like topology allowing precise quantification of the detector response within the detector.

In this analysis, we tested two different fast optical simulation methods: the photon library and the semi-analytical model. Due to the size of the detector and the number of photon detectors in MicroBooNE, both methods produced consistent results under the same physics assumptions. We also tested two Rayleigh scattering lengths: 66 cm, the default value for MicroBooNE, and 100 cm, the most recent measurement. Results demonstrate that a 100 cm Rayleigh scattering length provides a better agreement with the data for the MicroBooNE detector.

This analysis can be extended to other LArTPC detectors, such as SBND and DUNE. For underground detectors, the sample can be switched to beam-induced protons produced by neutral current interactions. Moreover, by comparing simulations with different combinations of physics parameters, such as Rayleigh scattering length and absorption length, preferences for these values can be established. This method can also be employed to test simulation performance. A paper detailing this method is currently in preparation.

# 7

# The SBND Cosmic Ray Tagger System and the SBND CRT Beam Telescope Detector Setup

To effectively address the cosmic background, the CRT system has been specifically designed as an auxiliary detector element of SBND to identify and mitigate cosmic muon backgrounds, thereby facilitating the detection of neutrino interactions within the TPC. This chapter will describe the design of the CRT system and the hardware setup for the CRT system. In addition, a special, CRT-only setup, the SBND CRT Beam Telescope, will be introduced, together with the details about its data collection.

## 7.1 Cosmic Ray Tagger Design

As shown in Figure 7.1, seven CRT planes are designed to surround the detector, providing approximately $4\pi$ coverage. Since cosmic rays entering from above are significantly more abundant than those entering from any other side of the detector, the pair of walls on the top are placed to maximise the coincidence of the top-down cosmic rays and form a telescope setup to maximally mitigate them.

This section will describe the design of the CRT system, beginning with the most basic unit, the scintillating strips, progressing to the scintillating plane, and finally detailing the designed coincidences to tag cosmic activities.

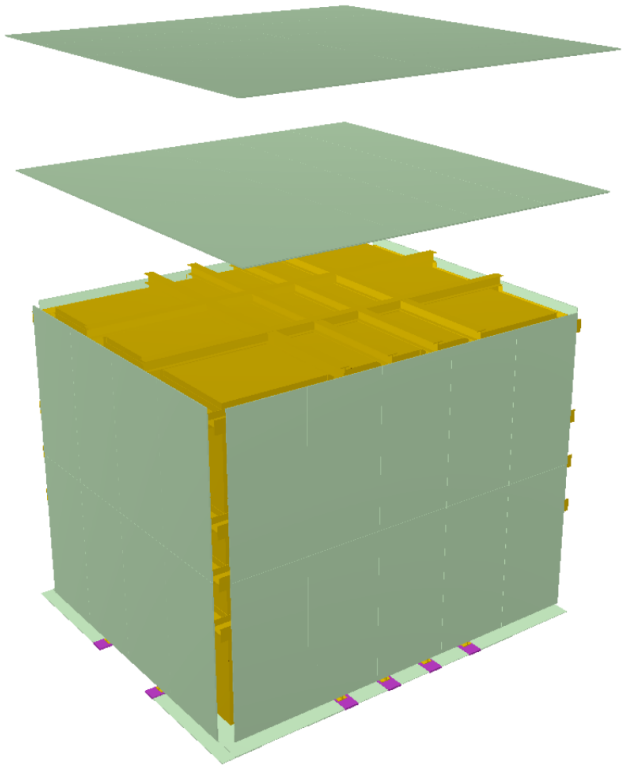

**Figure 7.1** The arrangement of the 7 Cosmic Ray Tagger (CRT) planes, depicted in light green, is shown surrounding the SBND cryostat, which is illustrated in dark yellow.

### 7.1.1 Scintillator Strip

The basic unit of the CRT system is the scintillating strip, made from a polystyrene-based material called USMS-03, with a mixture of 1.5% diphenylbenzene (PTP) as the activator molecule. The wavelength shifter material (WLS) used is bis(5-phenyl-2-oxazolyl)benzene (POPOP), added at a 0.04% level. This composition formula has been well-established for plastic scintillators over the past 50 years.

The scintillator emits photons up to a wavelength of 430 nm, and the bulk attenuation length is measured to be longer than 7.5 cm [133]. In order to achieve effective and uniform collection, WLS fibres (Kuraray Y11(200)M, 1 mm diameter [235]) are used to guide the scintillation light to photosensors and are glued into grooves along the long edge of the scintillator strips, as shown in Figure 7.2. The absorption peak of the WLS fibres is located at 430 nm and the emission peak is at 476 nm. To trap the scintillation photons within the strips, the surface of the scintillator strip is coated with a highly reflective white layer. Additionally, reflective aluminised Mylar tape is used to cover the WLS fibres to reduce photon losses and provide the mechanical protection for the fibres.

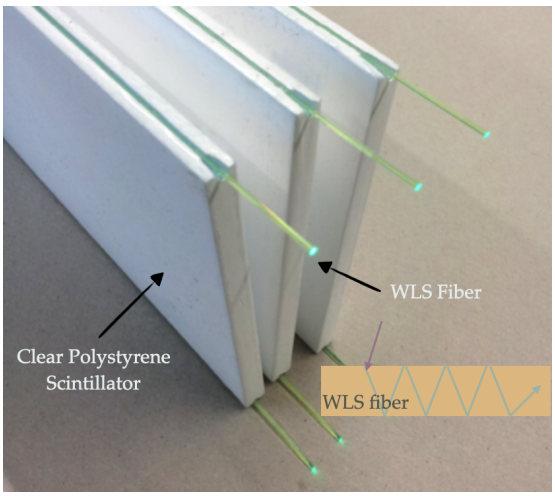


**Figure 7.2** The scintillation strips with the wavelength shifter fibres glued along the long edges. The wavelength shifter fibre is used to guide the light transportation to the detector. Figure adapted from Reference [133].

Hamamatsu S12825-050P [236] silicon photomultipliers (SiPMs) were chosen to detect the scintillation light, with a peak sensitivity wavelength at 450 nm. Compared to commonly used PMTs, SiPMs are more compact, have higher detection efficiency, and require significantly lower operating voltages (typically tens of volts compared to hundreds of volts for PMTs). However, SiPMs suffer from a high rate of spontaneous discharge ("dark noise") when operating above cryogenic temperatures. The scintillator strip is designed to have one SiPM per WLS fibre (two SiPMs per strip). By requiring the coincidence between two SiPM, the intrinsic dark noise from SiPMs can be mitigated.

### 7.1.2 Scintillator Module and X-Y Coincidence

As illustrated in Figure 7.3, a group of 16 scintillator strips are mechanically bonded to form the scintillator module using a 0.1 mm thick double-sided adhesive layer. The strips are arranged side by side with a gap of less than 0.2 mm, all enclosed within a protective aluminium case. The case has a thickness of 2 mm and ensures the required mechanical stability of the modules.

The scintillator modules are further arranged in two layers oriented orthogonally to form the CRT walls, as shown in Figure 7.4. The coincidence between these two orthogonal layers is normally referred to as the $X - Y$ coincidence. In this configuration, a charged particle will deposit energy and trigger at least one strip per module, allowing the 2D position of the interaction to be reconstructed using the $X - Y$ coincidence.

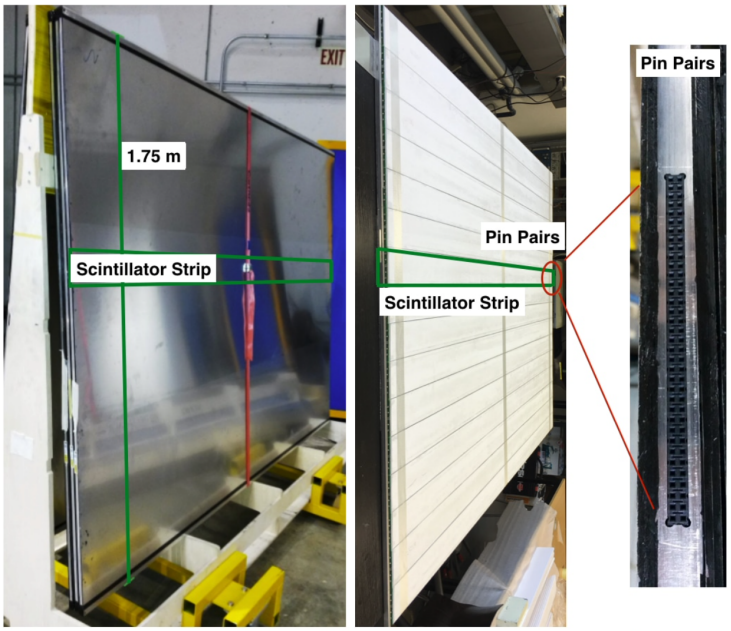


(a) CRT module. (b) Pin pairs.

**Figure 7.3** (a) Left: CRT modules with a protective aluminium case. Right: Inside the aluminium case, 16 scintillating strips are assembled together (b) with 32 pin pairs for readout electronics and SiPM connections from the module to readout electronic, along with four spare pin pairs. Figures from Reference [237].

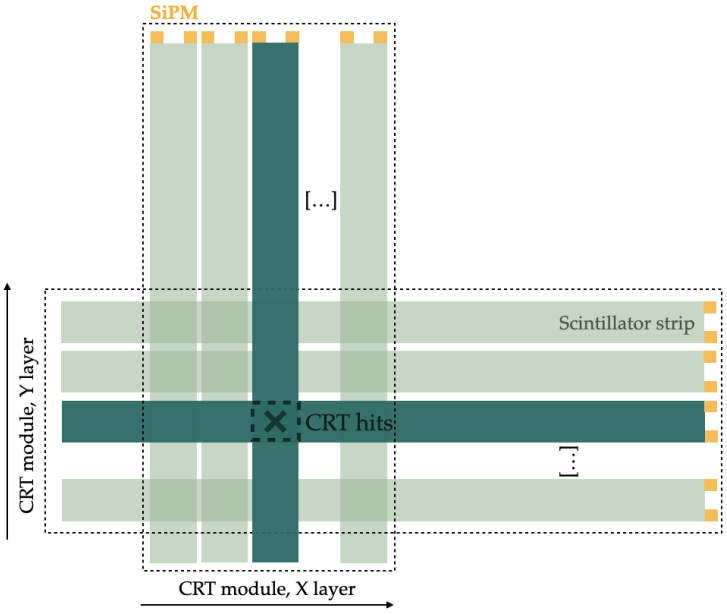


**Figure 7.4** Two orthogonal layers of CRT modules for $X - Y$ coincidence.

## 7.2 Front-End Electronics

The Front-End Board (FEB) is a multi-functional electronics module specifically designed as the readout for one scintillating CRT module (16 scintillating strips). The functionalities implemented in the FEB are summarised below [238]:

- Provides individual bias adjustment for each of the 32 SiPMs in the range of 40–90 V (extendable to 20-90 V).
- Amplifies and shapes the output signals of the photosensors, and digitises the signal amplitudes for each of the 32 channels.
- Performs signal discrimination of shaped signals at an adjustable level from 0 to 50 photoelectrons.
- Provides coincidence of signals from each pair of adjacent channels to form a two-SiPM coincidence (optional).
- Generates a primary trigger for all 32 channels in one module.
- Generates an event trigger with external signals from another module to when the $X - Y$ coincidence is satisfied.
- Produces a timestamp relative to the input reference pulse with a precision of 1.3 ns.
- Offers built-in data buffering.
- Enables efficient back-end communication using the 100 Mbps Ethernet standard.
- Enables firmware upgrades through the back-end Ethernet link.

The basic design of the FEB is shown in Figure 7.5. The top side of the board includes a 32-pin SiPM connector (between module and FEB), while the bottom side contains a power connector, two Ethernet ports, and four LEMO connectors for reference and control signals. A CITIROC 32-channel ASIC chip [239] amplifies and shapes analogue signals from the SiPMs. The FPGA chip establishes the basic input coincidence and event triggering logic. The CPU is used to initiate the readout cycle and send reset signals.

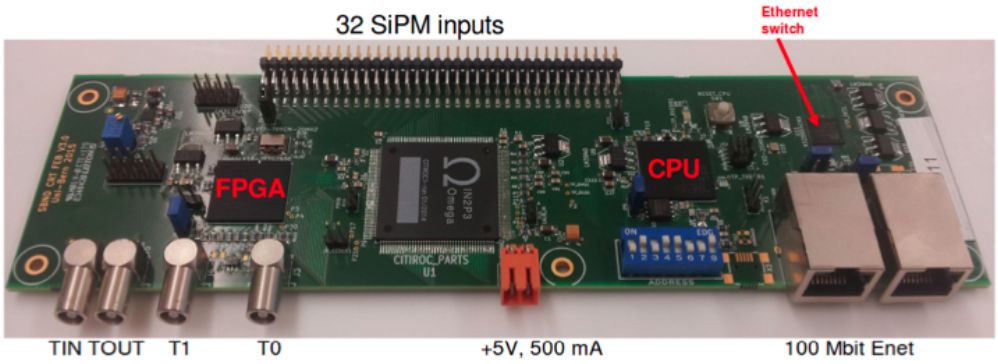


**Figure 7.5** General design of the Front-End Board [238]. T1 and T0 are two independent timing reference input. TIN is a validation pulse input. TOUT is a trigger output.

Analogue signals from 32 SiPMs are first processed by the CITIROC chip. Within the CITIROC chip, each channel passes through a charge amplifier with a configurable gain value and a dynamic range of 1 to 2000 photoelectrons. The CITIROC chip provides two shaper modes:

- **Fast shaper mode**: This mode has a peaking time of 15 ns and is used to determine the primary trigger.
- **Slow shaper mode**: This mode has a configurable peaking time between 12.5 ns and 87.5 ns, and is used for the proper readout during analogue output generation and processing.

### 7.2.1 Trigger Design

The fast-shaped signals from the 32 channels are routed to the XILINX Spartan-6 FPGA chip [240], which handles the coincidence and triggering logic. Each pair of SiPMs from the same strip is processed using an **AND** logic gate to form the two-SiPM coincidence signal. This signal is then subjected to an **OR** logic gate, which combines the results from 16 strip signals. Specifically, for the two-SiPM coincidence, the FPGA first checks if the amplitude of the input pulse from one SiPM exceeds a predefined threshold. If this condition is met, the FPGA then looks for a simultaneous signal from the adjacent SiPM. If the adjacent SiPM does not detect a signal, the FEB does not generate a primary trigger, as illustrated in the first event of Figure 7.6. Conversely, if the coincidence condition is satisfied, meaning both SiPMs in the pair detect signals within the specified time frame, the FEB will generate a primary trigger. This trigger initiates the process by sending a HOLD signal to the ASIC Sample-and-Hold (S/H) circuit to capture and hold the signal for further processing.

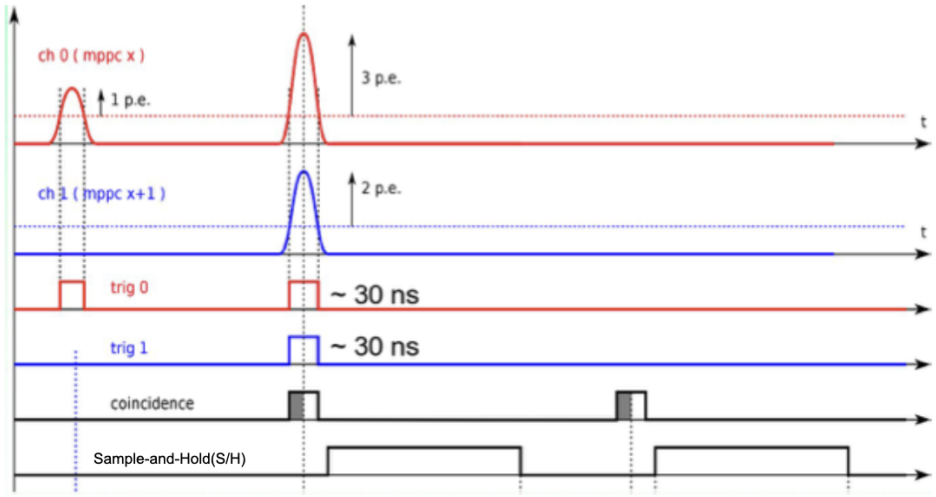


**Figure 7.6** Timing diagram for the trigger circuit. The lack of coincidence in the first event fails to produce a trigger and therefore no signal is sent to the Sample-and-Hold (S/H) circuit. The second event creates a trigger because of the coincidence between ch0 (red) and ch1 (blue). Once a trigger is formed, a HOLD signal will be sent to the S/H circuit. Figure adapted from Reference [238].

The primary trigger signal is sent out by the CPU through the "TOUT" LEMO connector to communicate with other FEBs to form the higher-level trigger. The "TIN" and "TOUT" connectors are designed to receive and deliver trigger signal for the $X - Y$ coincidence. The HOLD signal is retained in the S/H circuit for at least 150 ns to allow for the $X - Y$ coincidence window. If, during this period, the "TIN" port on the same FEB receives any signal from "TOUT" output from other FEBs, the $X - Y$ coincidence will be achieved, and an event trigger will be generated by the CRT readout. If no signal is received from the "TIN" connector during the 150 ns coincidence window, the HOLD signal will be reset by the FPGA, and the event will be discarded. The "TOUT" signal is also reset each time after the coincidence window ends.

### 7.2.2 Analogue Signal Readout

The CPU initiates the readout cycle for the FEB when a primary trigger is produced. The readout begins with signal shaping, where the signal is shaped using the slow shaper mode with a configurable peaking time. This peaking time is adjusted so that the readout (R/O) window for the HOLD signal starts approximately when the signal reaches its peak. As shown in Figure 7.7, the solid lines represent the shaper signal. When the readout cycle is initiated, only the **amplitude** instances of the 32 shaper signals are captured, as indicated by the dotted lines, and stored in the event buffer at the S/H circuit. If an event trigger is formed, the data in the event buffer will be saved. The amplitudes are routed to an analogue multiplexer by the CPU, which digitises the 32 channels using a 12-bit single-line ADC format. Once the digitisation process is complete, the CPU issues a reset signal to the FPGA, marking the end of the readout cycle.

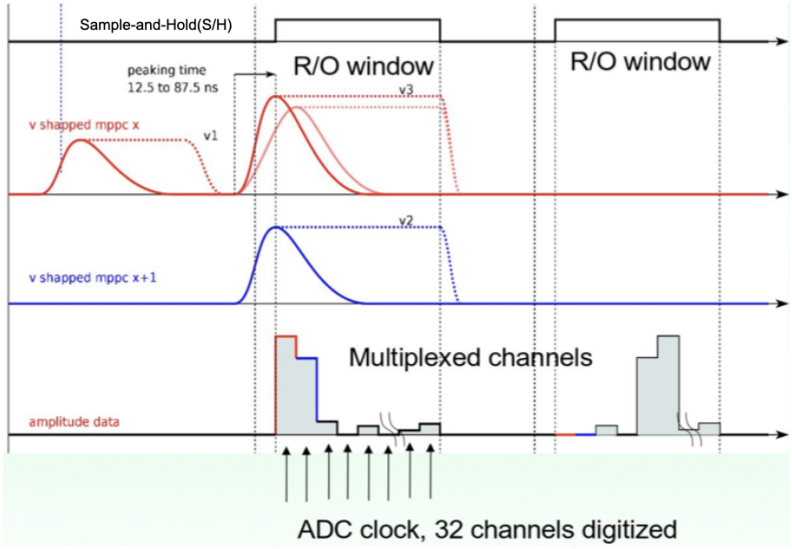


**Figure 7.7** Timing diagram for the analogue signal readout circuit. The second event produces a primary trigger through the two-SiPM coincidence. With this primary trigger, the readout begins from the signal shaper. The shaper outputs are represented as solid lines, while the outputs of the S/H circuits are shown as dotted lines, indicating the signal peak instances. The peak instances of all channels are stored, multiplexed to a common analogue output, and digitised within the readout (R/O) window. For simplicity, only 8 channels are shown. Figure adapted from Reference [238].

#### Effective Gain

The charge response (in ADC) per photoelectron is commonly referred to as the effective gain. This effective gain can be adjusted by the bias voltage applied to the FEB. The bias voltage is generated by a stabilised power supply circuit, which

is common to all 32 SiPMs connected to the hardware input from the FEB. Each of the 32 channels can have its bias voltage individually adjusted by an 8-bit Digital-to-Analog Converter (DAC) within the CITIROC chip. The positive output levels from the DAC are supplied as DC offsets to the signals, meaning that an increase in the DAC value results in a reduction of the bias voltage for individual SiPMs. The DAC setting is often referred to as the bias setting. The conversion between the DAC value and the bias voltage is given by:

$$V_{\text{bias}} = V_{\text{common}} - \frac{\text{DAC}_{\text{max}} - \text{DAC}}{\text{DAC}_{\text{max}}} \times V_{\text{range}}, \tag{7.1}$$

where $V_{\text{common}} = 68.1$ V is the offset voltage set for the SBND CRT hardware, $\text{DAC}_{\text{max}} = 255$ is the maximum value that the DAC can take, and $V_{\text{range}}$ is the adjustable range (4 V) for the bias voltage, spanning from 0.5 V to 4.5 V [238].

### 7.2.3 Time Stamp Generation

The timestamp is generated alongside the primary trigger within the FPGA, which operates at a clock frequency of 250 MHz. As shown in Figure 7.8, the event time stamping is generated with a 1.3 ns accuracy. Two independent timestamps can be recorded relative to two reference signals, named ”T1” and ”T0”. ”T1” corresponds to the timing relative to the early beam signal, which is sent out when the neutrino beam is produced. ”T0” is referenced from a high-stability GPS-disciplined pulse-per-second generator. Once the timestamp is registered with an event, the CPU initiates the data transmission from the FPGA to the event buffer. Subsequently, the data can be transmitted via Ethernet port if the global trigger condition, potentially involving other subsystems such as the TPC and PDS system, is satisfied.

## 7.3 SBND CRT-Only Detector Setup: CRT Beam Telescope

In 2017, a few of the SBND bottom CRT modules were installed in the SBND pit, where the SBND cryostat is now located. These modules collected data from the BNB beam. This early installation enabled the testing of the CRT modules, validation of the SBND timing system, identification of any related issues, and basic characterisation of the beam profile with appropriate simulations.

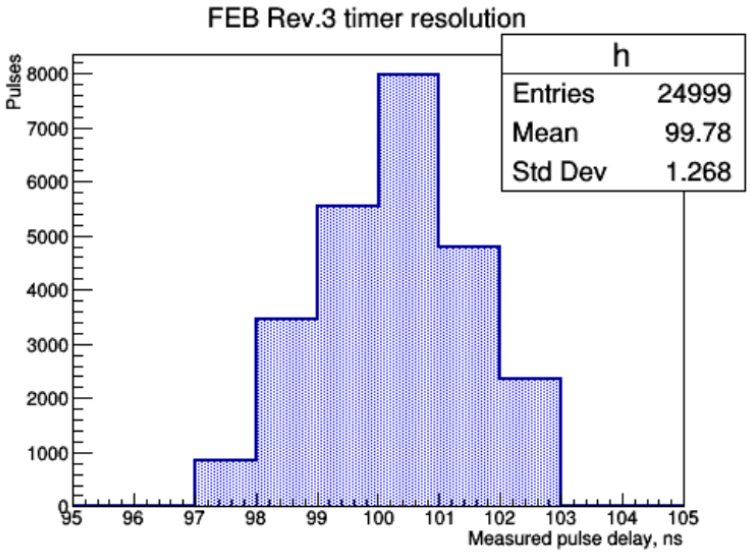


**Figure 7.8** Resolution of the time-stamp generator in FEB. Events are delayed by 100 ns regarding the reference signal. Figure from Reference [238].

### 7.3.1 Detector Design

The detector, also referred to as the CRT Beam Telescope, is composed of twenty-four CRT modules with dimensions of 272 cm (length) $\times$ 96 cm (width) $\times$ 2 cm (thickness). As shown in Figure 7.9 (a), the beam telescope consists of upstream and downstream panels. The distance along the beam direction between the two panels is measured to be 926.0 cm.

For the downstream panel, as shown in Figure 7.9 (b), three modules are arranged horizontally and three modules are installed vertically to form the X-Y coincidence. The upstream panel has the same design but is composed of three such sections. Each CRT module weighs 56 kg, and therefore, the modules are mounted on Unistrut frames, which are fixed to the floor and the walls of the SBND pit. All vertical modules are oriented with the readout end upwards, while the horizontal modules are oriented with the readout end towards the left along the beam direction.

### 7.3.2 Data Acquisition

The data collection was handled by a standalone Data Acquisition (DAQ) system. Each run lasted 4 hours, with a new run starting automatically every 4 hours. The data transmission was daisy-chained within the upstream and downstream panels separately, and the data was recorded separately for each panel.

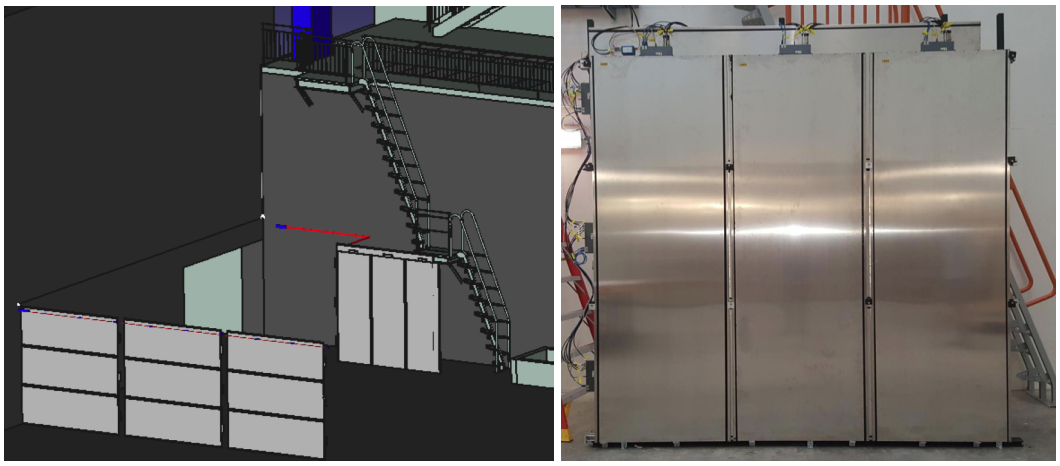

(a) (b)

**Figure 7.9** (a) A cartoon demonstrating the CRT Beam Telescope geometry. (b) The actual installation for the bottom panel in the SBND CRT Beam Telescope. Figures from Reference [241].

Both the distribution of time reference signals and the trigger circuit for $X - Y$ coincidence were designed to loop within each $3 \times 3$ module set, as the downstream panel. As shown in Figure 7.10 (a), both the "T0" (GPS pulse per second) reference signal and the "T1" (beam warning) reference signal are distributed across different FEBs with daisy-chains. The chain was terminated with 50 Ω at the last FEB to avoid signal reflections. The cable delay was measured and is presented in Figure 7.10, and measurements were saved in a database for later corrections. Figure 7.10 (b) shows the design of the circuit performing the X-Y coincidence to locate the energy deposition. Two loops connect the "TOUT" and "TIN" from the vertical and horizontal modules, allowing triggers from charged particles to come from both directions. The signal from each loop is a 150 ns-long pulse for the event trigger to be formed.

### 7.3.3 File Processing

The output data format from the standalone DAQ is binary, which differs from the data collected using the *artdaq* framework [242]. Typically used for LArTPC experiments, *artdaq* files are optimised for input into downstream reconstruction and analysis. To facilitate this, a specific workflow has been designed to convert the data format, as illustrated in Figure 7.11.

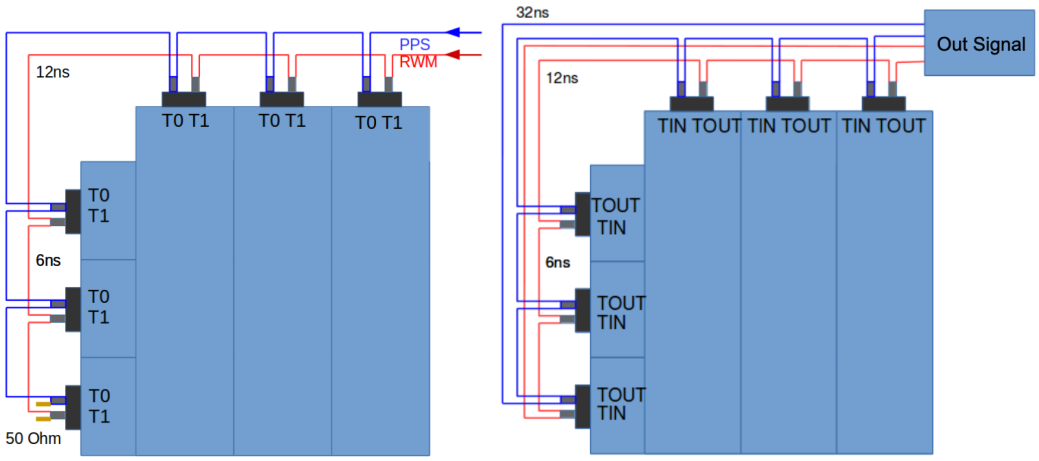


**Figure 7.10** (a) A cartoon demonstrates the distribution of time reference. (b) A schematic design of local $X - Y$ coincidence loops. Figures from Reference [241].

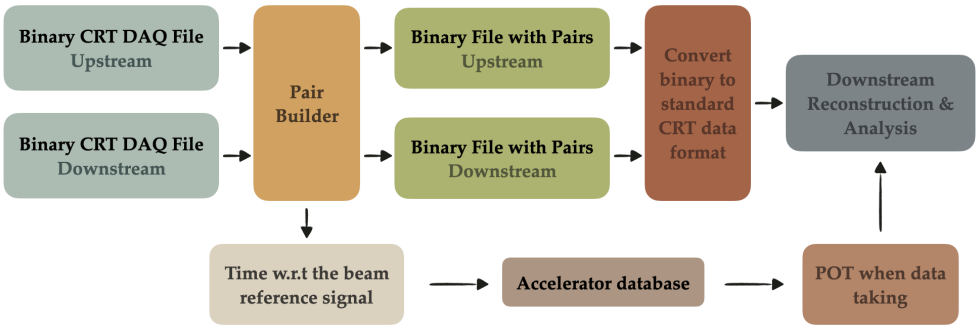


**Figure 7.11** A schematic diagram to show the file processing to convert the recorded binary data format to standard CRT format for further reconstruction and analysis.

The binary data files were recorded separately for downstream and upstream. In both files, the data is organised by individual SiPM, so a pair builder was first employed to replicate the 2-SiPM coincidence. Once paired, a macro is executed to convert the binary data into the standard CRT data format produced by the *artdaq* framework, which includes timing, ADC values, FEB number, and flags to indicate the validity of the data.

### 7.3.4 Collected Dataset

The protons-on-target (POT) represent the number of protons delivered to the target, measuring the intensity of the neutrino beam. Since the POT information was not stored during data collection, it can only be retrieved from the accelerator database using the time when the event is registered with respect to the beam reference signal.

The data collection spanned from July 2017 to June 2018, with a total collected POT of 2.95 $\times 10^{20}$. Figure 7.12 shows the accumulated POT over time for the data collected with CRT Beam Telescope.

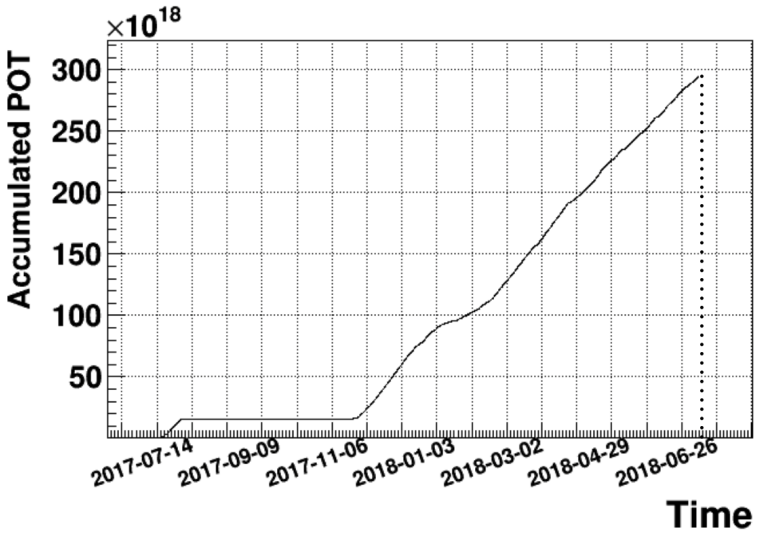


**Figure 7.12** Accumulated POT for collected dataset with the CRT Beam Telescope.

## 7.4 Summary

This chapter provided an overview of the CRT system in SBND, detailing the hardware design of the modules and readout electronics. It explained the process of trigger formation within the CRT and the logistics of the readout in CRT. Additionally, the chapter introduced the CRT-only setup in SBND, known as the CRT Beam Telescope detector. The dataset collected in 2017 from the Beam Telescope will be used in the analyses described in Chapter 10 and Chapter 11.

# 8

# Calibration and Commissioning of the SBND CRT system

SBND entered the commissioning stage while the author was at Fermilab. During this time, the author joined the CRT commissioning team and actively participated in the CRT commissioning. The author gained extensive experience with CRT hardware, the DAQ system, and the trigger system. This chapter will highlight one of the tasks the author was responsible for: determining the single PE response as a function of bias voltage per SiPM channel. The commissioning work was carried out with a test stand prior to installation. Additionally, the author designed an automation system for data collection with different configurations and a user-friendly automated analysis tool to produce results.

## 8.1 Detector and Readout Setup

The goal of the CRT commissioning was to test all the modules before installation. The commissioning work was conducted using the so-called A-frame test stand, a wooden frame where the CRT modules were placed during their delivery from Bern to Fermilab. In collaboration with other members of the experiment, we designed a comprehensive procedure for module testing, which included light leak tests, timing-related tests, FEB readout electronics tests, single PE response measurements with various bias voltages, and the equalisation of the Analog-to-Digital (ADC) response.

Overall, the SBND DAQ system integrates various components into one triggered event for further analysis. For the CRT commissioning data collection, we aimed to maintain the structure of the DAQ system but used a simplified version. As shown in Figure 8.1, a dedicated trigger and readout system was designed.

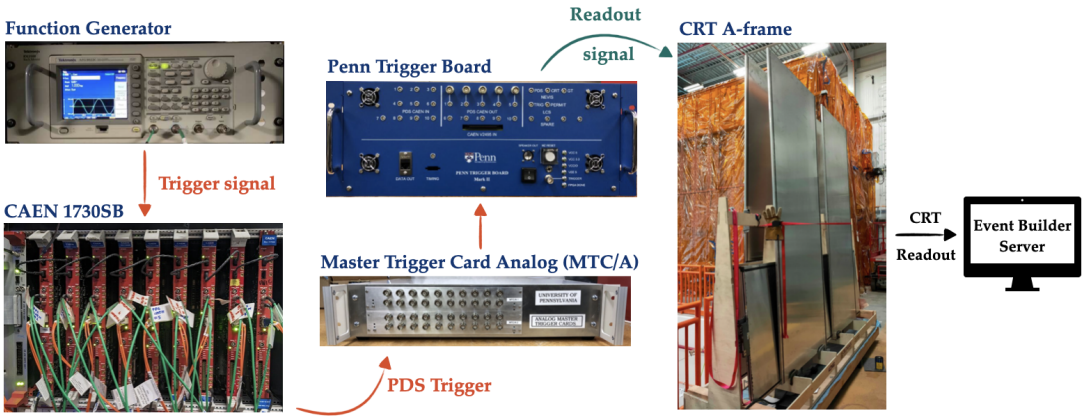


**Figure 8.1** The CRT commissioning data collection design. The function generator sends a signal to trigger the CAEN digitiser, which then sends a signal to the Master Trigger Card Analog (MTC/A) and then Penn trigger board to initiate the readout for the CRT module. The CRT data is then sent to the event builder server.

A function generator sends out a signal around 1 Hz to trigger a CAEN V1730 digitiser board [243]. The CAEN board, used in SBND for the PDS readout, sends a trigger signal once the trigger condition is satisfied. For the standard SBND trigger design, this condition is a certain number of PMTs above a threshold. For the A-frame data collection, the trigger condition is the 1 Hz signal.

Triggered by the function generator, the CAEN board sends a trigger signal to the Master Trigger Card Analog (MTC/A) [244], which sums all the signals and compares them to three individually programmed thresholds to define the signal as high, medium, or low. This signal is then passed to the Penn trigger board [245], which creates the final trigger decision to initiate the readout cycle to different subsystems, in this case, the CRT modules on the A-frame. Additional inputs, such as the beam signal and CRT trigger, can be combined within the Penn trigger board in the standard SBND trigger design. The CRT readout data is sent to the event builder server to build the event and store the data.

## 8.2 Measurement of CRT-Module SiPM Response

One of the primary objectives of CRT commissioning was to equalise the charge response (in ADC) for all the strips in the CRT modules. SBND employed cosmic muon data to develop the tools for this equalisation. To optimise the design of these tools, it is useful to consider the different components the CRT response can be factorised into:

- The number of photons generated by the deposited energy from charged particles, $\text{Photon}_{\text{gen}}$.
- The photon propagation efficiency of the CRT strip, $\epsilon_{\text{strip}}$.
- The efficiency of the coupling between strips and SiPMs, $\epsilon_{\text{coupling}}$.
- The detection response of the SiPMs, $\text{Response}_{\text{SiPM}}$.

In summary, this CRT response can be expressed as:

$$\text{Response}_{\text{CRT}} = \text{Photon}_{\text{gen}} \times \epsilon_{\text{strip}} \times \epsilon_{\text{coupling}} \times \text{Response}_{\text{SiPM}} \tag{8.1}$$

Assuming $\text{Photon}_{\text{gen}}$, $\epsilon_{\text{strip}}$ and $\epsilon_{\text{coupling}}$, the SiPM response, $\text{Response}_{\text{SiPM}}$, can be used as a baseline to guide the equalisation of the CRT charge response for cosmic muons. Depending on the calibration goals, some experiments, such as ICARUS, have calibrated their CRT modules using the SiPM response. SBND has expanded this method to include trigger efficiency for the CRT module calibration, characterising the SiPM response remains crucial and beneficial. In addition, it provides information on converting the ADC response to the number of PEs, which will be stored in the database for high-level CRT reconstruction. During my stay at Fermilab, I was primarily responsible for understanding and characterising the SiPM response.

### 8.2.1 Methodology

The measurement aims to establish the relationship between the single PE response (ADC response per PE) and the bias voltage applied to the SiPM. This section will outline the methodology developed for this measurement.

### Source

The rate of cosmic muons in the SBND detector building is significantly lower than the rate of beta and gamma photons from ambient radioactivity, mainly due to $^{40}$K contained in the concrete. These radiation processes yield charged particles that can trigger the CRT strips, making them suitable sources for measurements. It is worth noting that the charged particles produced by gamma photons from the radiogenic background typically have relatively low energy, making it challenging for them to traverse two modules and generate an X-Y coincidence. Therefore, during data collection, the X-Y coincidence was disabled by disconnecting the "TIN" and "TOUT" ports from the FEB. However, the two-fold SiPM coincidence was still maintained while collecting data.

### Determining the Single PE Response

For a given bias voltage, our goal is to quantify the SiPM response for a single PE. The SiPM response (in ADC) depends on the number of detected PEs. Figure 8.2 illustrates analogue SiPM readout waveforms for one PE and two PEs. Since the CRT readout is designed to save only the peak value rather than the entire waveform, $ADC_1$ and $ADC_2$ represent the respective charge readout responses.

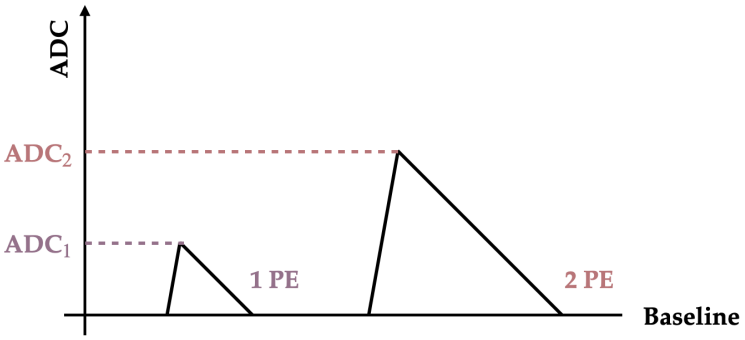


**Figure 8.2** A schematic diagram illustrates the analogue SiPM waveforms for one PE and two PEs, with the peak values $ADC_1$ and $ADC_2$ saved correspondingly.

The first step to establish the single PE response involves reproducing the distinct peaks in the ADC response of the triggered channel, which correspond to different PE levels, as illustrated in Figure 8.3. The ADC distribution of the SiPM is characterised by these distinct peaks, with each peak representing the detection of a specific number of photons. This distribution, commonly referred to as the "finger" plot for SiPM, provides insight into the single PE response, which effectively converts the detected PE into an ADC value.

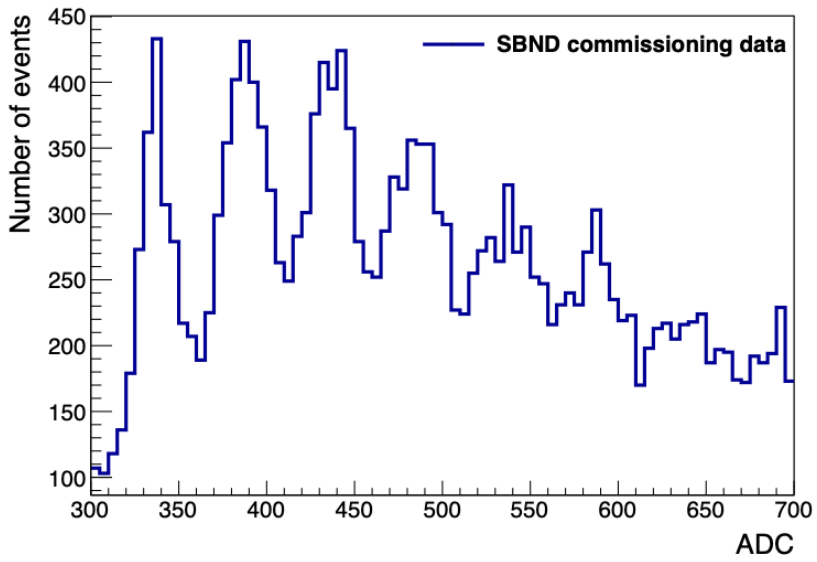


**Figure 8.3** ADC distribution for one SiPM, the values of each peak of ADC corresponds to a subsequent number of PEs.

To reproduce these distinct ADC peaks, the amplifier settings for CRT channels need to be adjusted, which helps to separate the ADC peaks from one another. This is done by modifying the configuration files used during data collection. Specifically, an array can be modified to fine-tune the configuration on a channel-by-channel basis. Additionally, this array can be used to adjust the bias voltage applied to each channel. More details about the array and its configuration are provided in Appendix B.

To ensure sufficient statistics, data collection with the adjusted amplifier lasted for two hours. Once the finger plots were obtained, peak values were determined by fitting multiple Gaussian curves to the peaks. The ADC response per PE was established by calculating the difference between two adjacent peaks. The single PE response, defined as the slope of a linear fit representing the ADC response correlation, is illustrated in Figure 8.4.

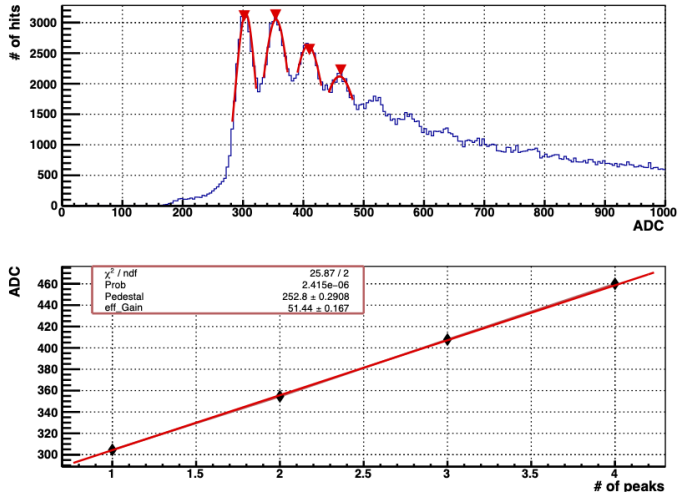


**Figure 8.4** Upper: the ADC distribution fitted with multiple Gaussian curves. Bottom: the fitted peak values of the individual ADC peaks as a function of the number of peaks. The linear fit is used to extract the single PE response (the slope) and the pedestal (the y intercept)

### Bias Voltage Scanning

To characterise the correlation between single PE response and applied bias voltage, a total of five different bias voltages were tested. By repeating the aforementioned procedure, single PE responses corresponding to each bias voltage were calculated, as shown in Figure 8.5. Applying a linear fit to these data points allows us to derive a parameterisation that characterises this relationship. The linear fit is defined as:

$$\mathrm{SPR} = p1 * V_{\mathrm{bias}} + p0, \tag{8.2}$$

where SPR is the single photon response, $V_{\mathrm{bias}}$ is the voltage applied to the SiPM, $p_1$ is the slope of the linear fit, and $p_0$ is the intercept of the SPR when $V_{\mathrm{bias}} = 0$. This parameterisation allows for the calculation of the single PE response for a specific bias voltage, and vice versa. Once the appropriate bias voltage is determined for CRT operation, the corresponding single PE response will be stored in the database and used for reconstruction.

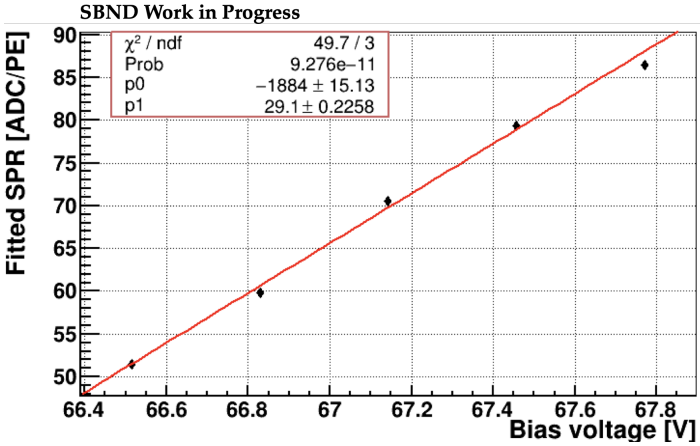


**Figure 8.5** The fitted single PE response values with different bias voltages for a selected SBND SiPM. The linear fit is applied to the data points, and the parameterisation that characterises this relation is shown as p0 and p1 in the legend.

## 8.3 The Automated Analysis Box Design

The SBND CRT system consists of seven walls, each comprising at least 16 modules, with each module containing 32 SiPMs. Conducting measurements manually for all SiPMs at five different bias voltages would therefore be highly impractical. Given that the procedure to obtain the single PE response for each SiPM is consistent and must be repeated for each channel at each bias voltage, an automated analysis tool, referred to as the ”analysis box” was developed to streamline this process as much as possible.

The analysis box plots the ADC distribution for each SiPM for each given bias voltage and automatically identifies the peaks using the TSpectrum [246] algorithm. It is worth noting that this algorithm may encounter challenges such as failing to locate the peak or identifying the incorrect peak. Additionally, small peaks near the pedestal level may appear in some noisy channels, potentially influencing the results if not addressed properly. To mitigate these issues, the code incorporates examination mechanisms to correct false or missed peaks, as well as peaks near the pedestal level. This enhances the accuracy and reliability of the analysis. Once the peaks are identified, multiple Gaussian curves are used to fit the peaks locally to extract the single PE response per SiPM for the given bias voltage. A separate analysis macro links all bias settings together and derives the single PE response with respect to the bias voltages for each SiPM.

The analysis box is designed to operate on raw data files, requiring minimal user input while offering a high degree of flexibility and thoroughness. The code preserves results from each step of the data analysis process, including the ADC distribution before fitting, the fitted ADC distribution, and the resulting fit outcomes. The unfitted ADC distribution is saved to allow for manual fitting of specific channels if the automated fitting fails.

The code can automatically detect the FEB number from the raw data but also provides the option for users to input this information manually if needed. Moreover, a predefined fit range for the ADC distribution concerning single PE peaks is available, yet the code also allows users to manually fine-tune this fit range as required. All these settings are configurable parameters, enabling users to freely modify the values as needed. The analysis box automatically produces a summary with all fitting plots across different stages for the users, as shown in Figure 8.6 with an example.

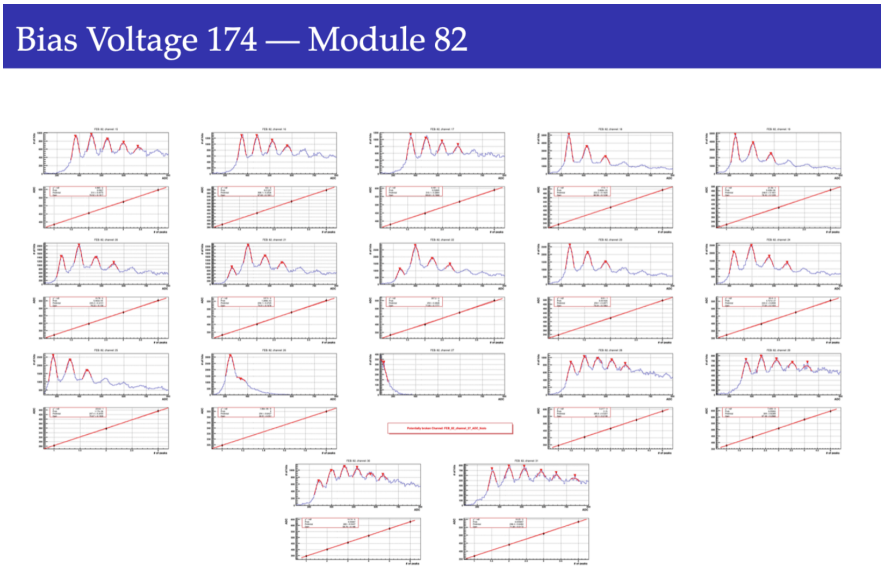


**Figure 8.6** An example of the summary of produced results for a FEB with a given bias voltage, with a potential broken channel identified from the analysis box.

There are some additional features of the analysis box worth mentioning. It produces a summary plot for single PE responses for one FEB, as shown in Figure 8.7. For a given bias voltage, an expected range of the single PE response can be estimated and plotted as a purple band, serving as a reference for the user. This plot is useful for identifying any channels exhibiting unusual behaviour.

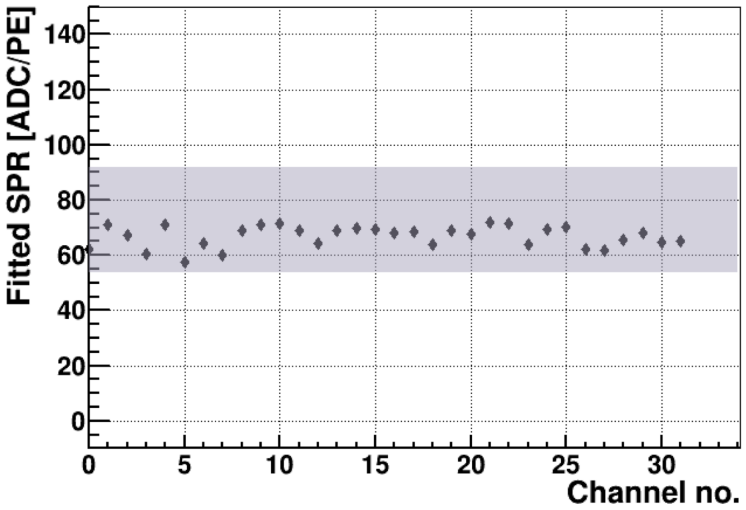


**Figure 8.7** The summary plot of single PE response across 32 channels of a CRT module. The purple band represents the expected range for the single PE response and serves as a reference.

The analysis box can also detect dead channels, which are reported at the end of the analysis run and also shown in the summary results, as shown in Figure 8.6. As a final output, the parameterisation describing the correlation between the single PE response and the bias settings is calculated and saved as text files. These files can later be stored in the SBND database to be used in the high-level reconstruction.

## 8.4 Results from the CRT North Wall Commissioning

The infrastructure described in the previous sections for commissioning CRT modules was initially tested using A-frames prior to the installation of the CRT North (downstream) wall in April 2023, over a two-week period. Despite the short timeline, the data collection with the automated script and overall procedure for CRT module test were successful, with no light leaks identified in any of the modules. All channels demonstrated reasonable responses, with only two dead channels detected, indicating overall good performance among the modules. Following the test, all modules were installed as a CRT wall and positioned downstream of the SBND detector, as shown in Figure 8.8.

**Figure 8.8** Pictures of CRT north wall installation.

The results from measuring the SiPM response indicated a reasonable shape for a given bias voltage. Additionally, the fitted single PE response increased as expected with higher bias voltages, as illustrated in Figure 8.9. The relationship between the single PE response and the bias voltage was characterised, with the slope ($\epsilon$) from the linear fit shown in Figure 8.10. All channels exhibited a similar response within the range of 20 to 35. The data point around 0 is attributed to the presence of a dead channel in the modules.

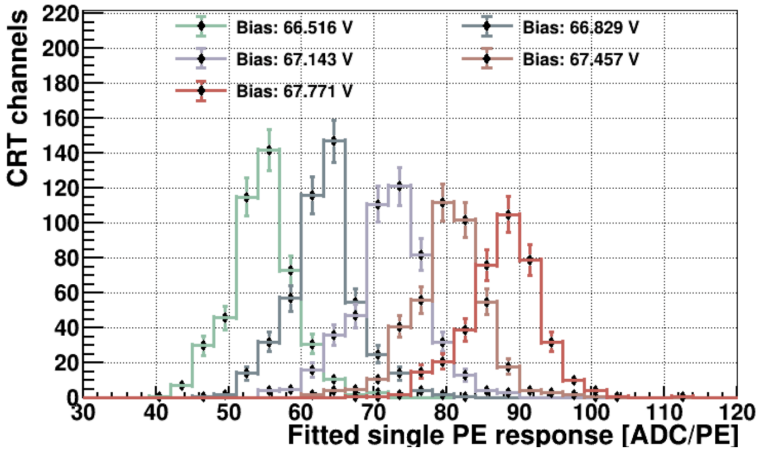


**Figure 8.9** The fitted single PE response with 5 different bias voltages for all channels for CRT north wall channels.

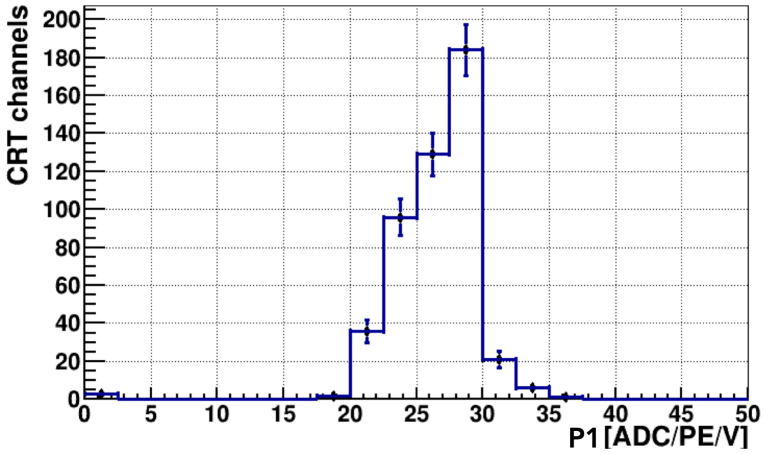


**Figure 8.10** The distribution of the slope ($\epsilon$) extracted from the linear fit from the relationship between the single PE response and the bias voltage.

## 8.5 Summary and Outlook

This chapter presented the commissioning work designed and tested for the SBND CRT system and its application on the modules installed in SBND's North wall. The dedicated readout and trigger system facilitated smooth data collection within a short timeline. The test for the CRT North wall modules was successful, with results showing that most channels, except for two, were functional and demonstrated reasonable responses.

Specifically, we outlined the methodology for characterising the SiPM response at a given bias voltage. The parameterisation derived from this characterisation will be saved in the SBND database to aid in converting the ADC response to the number of PEs for high-level reconstruction. The automated analysis box proved significantly useful during the commissioning period. After the author left Fermilab, the methodologies and automated scripts developed for the North wall commissioning were reused for the commissioning of other walls without any major difficulties. All modules from the remaining walls were tested in the summer of 2023. As of the time of writing this thesis, SBND has installed all CRT walls.

# 9

# Simulation and Reconstruction of the CRT Beam Telescope

Similar to the TPC and PDS systems in LArTPC experiments, the simulation and reconstruction algorithms for the auxiliary CRT system are also implemented within the LArSoft framework and follow the same workflow, as described in Chapter 5. This chapter provides a specific overview of the simulation and reconstruction processes for the CRT-only setup, the CRT Beam Telescope detector, described in Chapter 7. It will detail both the simulation and reconstruction of charge and timing signals, as well as the trigger simulation. Additionally, it will describe reconstruction algorithms and the calibration including these tailored for the analysis outlined in Chapter 10 and Chapter 11.

The simulation and reconstruction work, which had significant contributions from the author, laid the foundation for the analyses described in Chapter 10 and Chapter 11.

## 9.1 CRT Simulation

The CRT simulation for the CRT Beam Telescope includes the detector geometry setup and a simulation workflow, including event generation through different generators and particle propagation in GEANT 4, which is shared with the TPC and PDS system simulations.

The CRT simulation uses the GEANT 4 deposited energy from charged particles within each CRT scintillator strip as input. This energy is then divided between two fibres on either side of the strip based on the lateral position of the energy deposition. The attenuation of light and time delay are simulated based on the longitudinal distance from the deposition to the readout, using phenomenological models. The model for light attenuation is derived from the CRT Beam Telescope data, while the model for the time delay is based on the CRT "Module-0" test stand results at Bern in July-August 2015. The CRT "Module-0" test stand, shown in Figure 9.1, was set up with a full-size CRT module and employed a pulsed laser with $\lambda = 400$ nm to measure these parameters. The fitted data provided a set of parameters used for simulation and further reconstruction. Additionally, the electronic response at the front-end board (FEB) and the trigger for reading out a single ADC value from all 32 channels were also simulated.

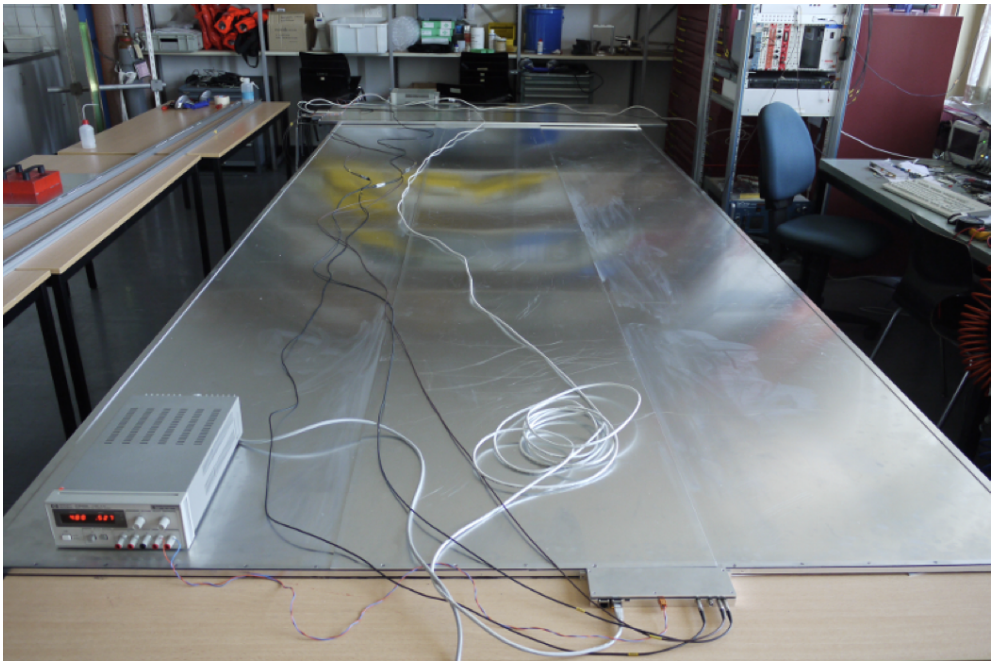

**Figure 9.1** The Module0 with attached FEB under test procedure at the University of Bern. Figure from Reference [247].

The simulated events, after the procedure described above, will be in the same format as raw data from the CRT. From this point onwards, reconstruction to extract high-level information for further analysis should be applied to both data and MC simulations in the same way.

### 9.1.1 Geometry

As mentioned in Section 5.1.1, a precise geometry is necessary for an accurate simulation of the data. The CRT Beam Telescope was set up in the SBND building and in the pit where the current detector is located. Therefore, the geometry was obtained by modifying the standard SBND geometry file using GDML, specifically `sbnd_v02_00.gdml`. Since the modules from the Beam Telescope are from the bottom panel of the SBND CRT system, these modules from the geometry file were reused and placed in the position and orientation where the Beam Telescope was set up. Additionally, since LArSoft will fail if the LArTPC is completely removed from the geometry file during simulation, the entire SBND cryostat was modelled as floating above the building around 30 m, as shown in Figure 9.2. This geometry will be referred to as the "floating" SBND geometry from now on.

The cryostat is chosen to be floating in the air in the simulation to prevent any interactions with the beam simulation. For the cosmic simulation, CORSIKA simulates cosmic events originating from a surface at the roof of the cryostat, extended by 10 m in each direction, and propagates them backwards to a higher surface approximately 20 m above. After modifying the geometry, the surface has been adjusted to be the roof of the CRT panels, with the simulated particles still propagating backwards to a higher surface but below the floating cryostat. Therefore, the cosmic simulation for the CRT modules in the Beam Telescope should not be affected by the floating cryostat.

### 9.1.2 Charge Response Simulation

In the GEANT 4 simulation, the basic unit is the scintillation strip. Moreover, very limited tracking information for scintillation photons is available in individual CRT strips, and thus the energy deposition is assumed to be point-like. The true interaction point is estimated to be the centroid of the entry and exit points.

The data collected with the CRT Beam Telescope can be used to model the number of PEs detected as the distance to the readout increased; the results are shown in

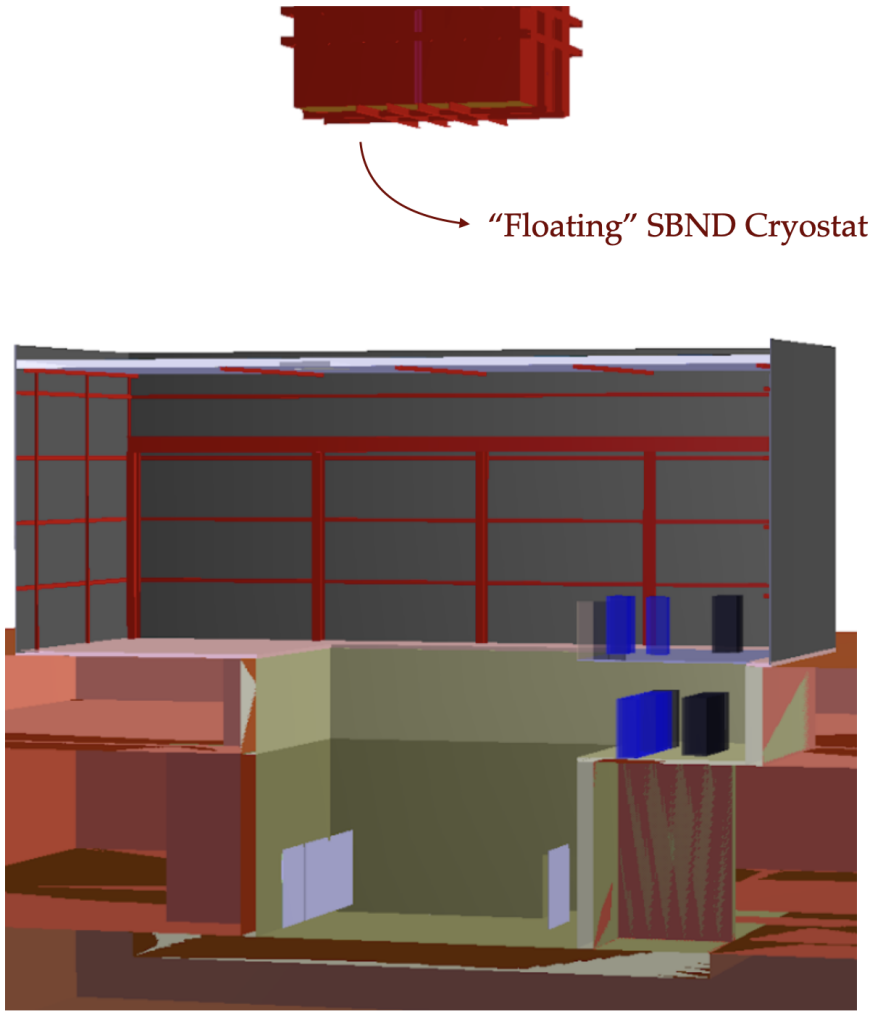


**Figure 9.2** The "floating" SBND geometry represents the CRT Beam Telescope detector setup.

Figure 9.3. The attenuation can be modelled by a $1/r^2$ dependence, where $r$ is the distance to the readout. The number of detected scintillation photons is modelled as

$$N_{\mathrm{PE}} = \frac{A}{(r-B)^2} \times \frac{Q}{Q^0}, \tag{9.1}$$

where $A = 1.39 \times 10^8$ cm$^2$ and $B = -1133.15$ cm are both extracted from the fitting. $Q$ is the GEANT 4 deposited energy, and $Q^0$ is the most probable value (MPV) for minimum ionising particles (MIPs). $Q^0$ is calculated by simulating MIP muons with momenta of 500 MeV/c to estimate the deposited energy spectrum, as shown in Figure 9.4. A Landau-Gaussian convolution function is used to extract the MPV, resulting in $Q^0 = 1.68$ MeV.

Subsequently, the number of PE produced before accounting for the attenuation effect

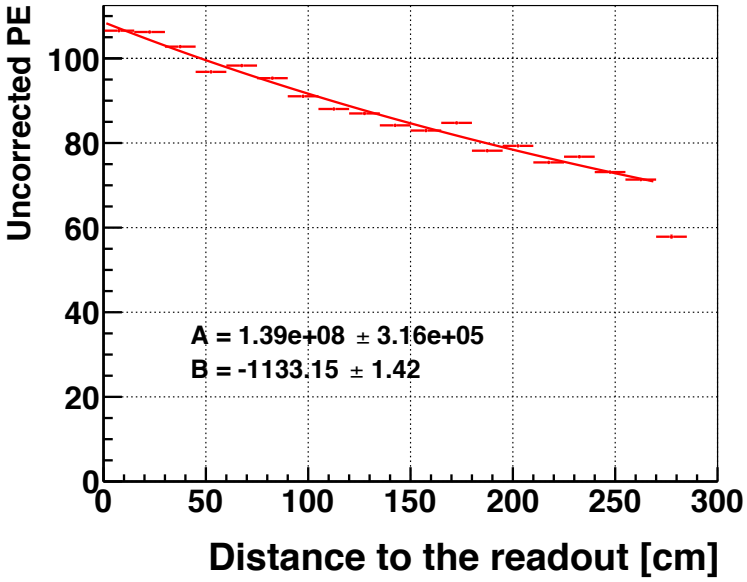


**Figure 9.3** The number of PEs as a function of distance to the readout from CRT Beam Telescope data.

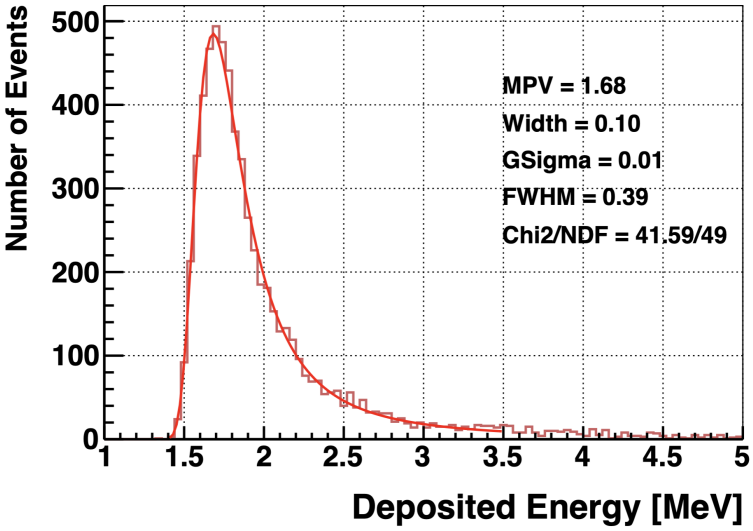


**Figure 9.4** Deposited energy for MIP muons with momenta of 500 MeV/c, fitted with a Landau-Gaussian convolution function. The fit results are shown in the figure.

can be estimated as:

$$N_{\text{PE, produced}} = \frac{A}{B^2} \times \frac{Q}{Q^0}. \tag{9.2}$$

Each strip has two optical fibres to transport photons to the optical detectors (SiPMs). Once the scintillation photons are produced, they propagate laterally into the two fibres, as shown in Figure 9.5. The attenuated $N_{\text{PE}}$ is partitioned between the two


**Figure 9.5** A schematic diagram illustrating the scintillation photon propagation to two optical fibres.

fibres according to an exponential absorption model described as

$$N_{\mathrm{PE},i} = \frac{e^{-d_{L,i}/\tau}}{e^{-d_{L,0}/\tau} + e^{-d_{L,1}/\tau}}, \tag{9.3}$$

where $i = 0, 1$, $d_L$ is the lateral distance from the scintillation point to the fibre, and $\tau = 8.5$ cm [248]. The simulated number of photons as a function of the lateral position is shown in Figure 9.6.

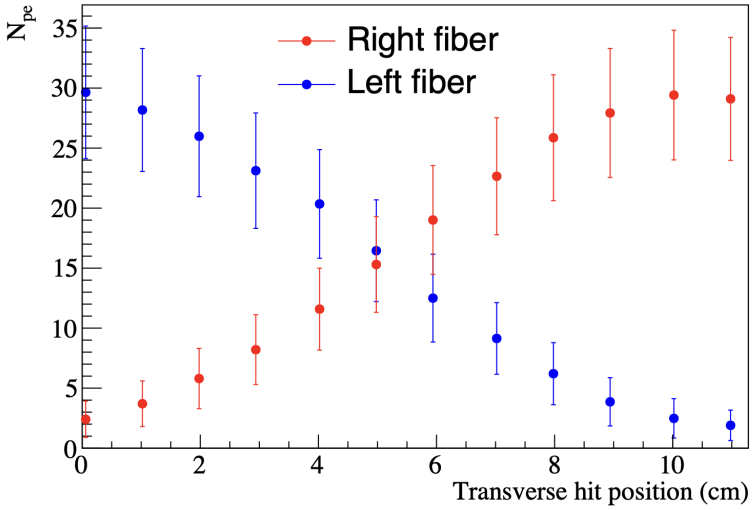


**Figure 9.6** Number of PE per fibre as a function of the lateral (transverse) distance from the left edge of the strip. Figure from Reference [248].

The simulated number of expected PE per SiPM is smeared by a Poisson distribution. The final step of the charge response simulation is to model the response of the SiPMs. The conversion from the number of PEs per fibre to a 12-bit ADC count is given by

$$ADC_i = N_{\mathrm{PE},i} \cdot Q_{\mathrm{slope}} + Q_{\mathrm{pedestal}}, \tag{9.4}$$

where $Q_{\mathrm{slope}}$ is the SiPM response that converts PE to ADC values, and $Q_{\mathrm{pedestal}}$ is the pedestal value of the SiPM. In the simulation, $Q_{\mathrm{slope}}$ is assumed to be 40 ADC/PE across all channels, and $Q_{\mathrm{pedestal}} = 0$ for simplicity. The saturation at 4095 ADC is also simulated.

### 9.1.3 Timing Response Simulation

The timing response of the CRT module is also simulated. Starting from the GEANT 4 true time $t_{\text{true}}$, two delay effects are considered in the simulation. The first-order effect is the light propagation time $t_{\text{prop}}$. The second timing delay $t_{\text{TWE}}$ arises from the CRT hardware's "time walk" effect, as shown in Figure 9.7. The hit timing is recorded once the amplitude of the ADC count exceeds the threshold. Since the rising time in the CRT hardware is fixed, a larger pulse, having a steeper rising slope, will be registered earlier. In hardware, an interpolator [249] is installed on the FEB electronics to correct for the time walk effect, but it does not completely eliminate it. Therefore, the time walk effect still needs to be modelled and simulated.

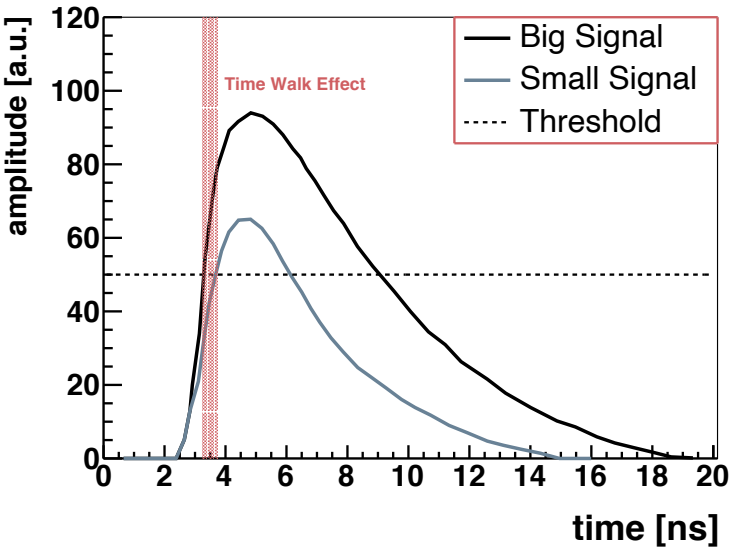


**Figure 9.7** The time walk effect arises from using a fixed threshold to register signals, causing a larger pulse to appear earlier than a smaller pulse, even if they start simultaneously.

Both the propagation delay and the time walk effect were measured with the test stand "Module-0" at Bern. Figure 9.8 shows the trigger delay time and uncertainty as a function of signal amplitude (number of PEs), measured by a laser positioned 25 cm and 375 cm from the readout edge.

The light propagation time was measured to be $6.1 \pm 0.7$ ns/m. Therefore, the simulation for the light propagation time is estimated by taking the mean value and its uncertainty as a Gaussian distribution, and then multiplying this by the distance from the scintillation point to the readout.

The time walk effect is simulated using a phenomenological model based on the fit

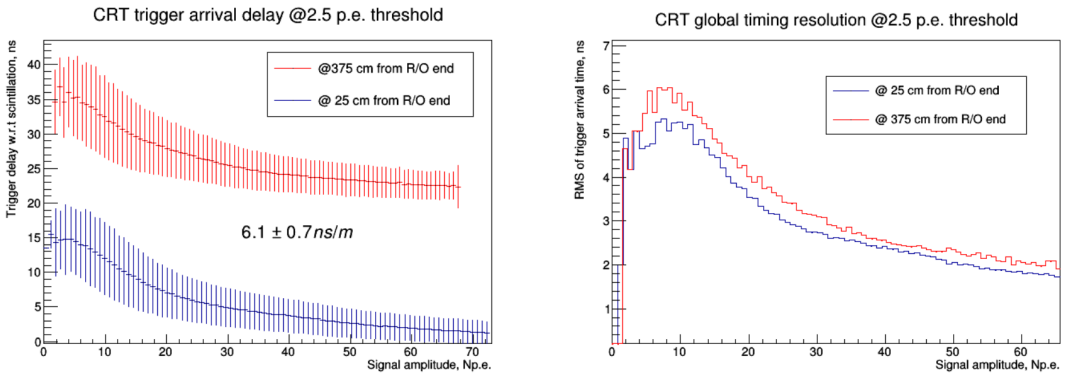


**Figure 9.8** Trigger delay time (left) and uncertainty (right) as a function of the number of photons in the scintillator strip. Figure from Reference [247].

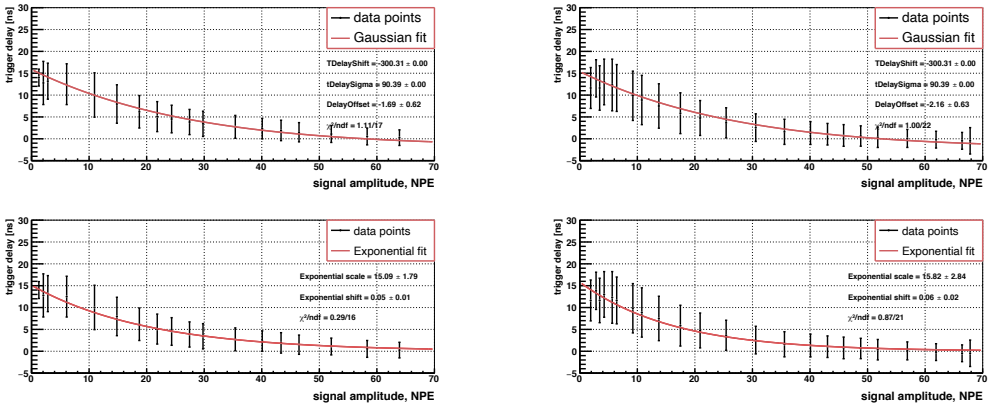


**(a)** **(b)**

**Figure 9.9** Trigger delay time as a function of the number of photons in the scintillator strip, fitting with a Gaussian function (top) and an exponential function (bottom), for distance to the readout of (a) 25 cm and (b) 375 cm.

results from the "Module-0" test. First, the mean value of the trigger delay time is corrected for the light propagation effect. Parameterisations are then extracted from the corrected results and used for the simulation. Initially, the mean value of the trigger delay time was modelled with a Gaussian function, as shown in both top plots of Figure 9.9. However, the original Gaussian fit function with an offset can result in negative values when the number of PE exceeds 60. To avoid these unphysical values, an exponential function is used to model the trigger delay time as a function of PE $N_{\mathrm{PE}}$, as follows:

$$t_{\mathrm{TWE,\,mean}} = a \cdot e^{-b \cdot N_{\mathrm{PE}}}, \tag{9.5}$$

where $a = 15.455$ is the scaling factor extracted from the average value of fitting results at 25 cm and 375 cm, and $b = 0.055$ is the exponential decay scale factor.

The uncertainty for the delay can also be modelled as a function of the number of

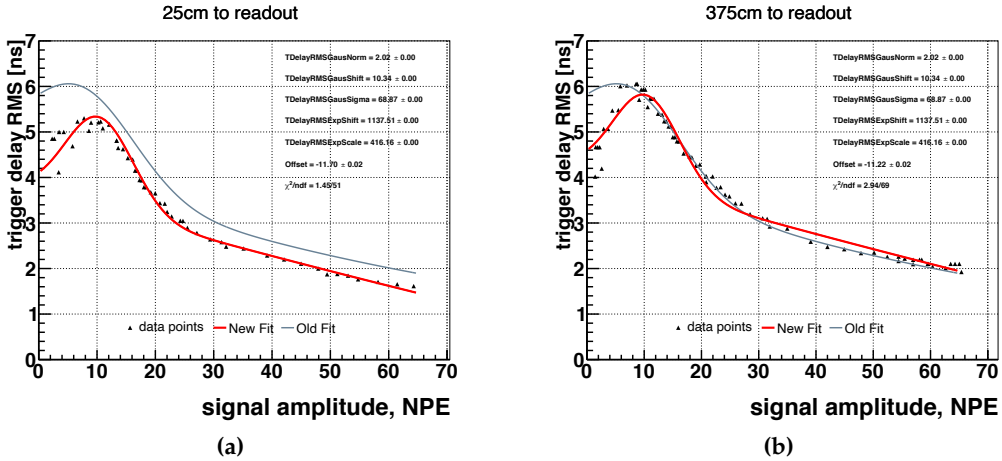


**Figure 9.10** Uncertainties of the trigger delay time as a function of the number of PEs for distances to the readout of (a) 25 cm and (b) 375 cm. For both cases, the new fit (red curves) and the old fit (light blue curves) are shown alongside the data points.

PEs $N_{\mathrm{PE}}$ using a combination of a Gaussian function and an exponential function. The uncertainties are expected to increase with the distance to the readout, $r$, as shown in Figure 9.8 (b). However, the initial fitting model does not account for this dependence. Additionally, as shown in Figure 9.10, the old parameterisations do not accurately describe the data for the readout distance of 25 cm. While the old parameters offer a slightly better fit for the 375 cm readout distance when the number of PEs exceeds 10, the overall agreement is still improved with the new fit function. Therefore, a new Gaussian plus exponential model is used, described as

$$t_{\mathrm{TWE,\,RMS}} = \eta \cdot e^{-\frac{(N_{\mathrm{PE}}-\lambda_1)^2}{\sigma}} + e^{-\frac{N_{\mathrm{PE}}-\lambda_2}{\tau}} + \alpha \cdot r + \beta. \tag{9.6}$$

A linear relation $\alpha \cdot r + \beta$ is considered for the distance dependence. The obtained fitting parameters are listed as follows:

- $\eta = 2.02$ is the Gaussian scaling factor,
- $\lambda_1 = 10.34$ is the Gaussian shift,
- $\sigma = 68.87$ is the sigma in the Gaussian function,
- $\lambda_2 = 1137.51$ is the exponential shift,
- $\tau = 416.16$ is the exponential scaling factor,
- $\alpha = 1.37 \times 10^{-3}$ is the slope of the linear relation,
- $\beta = -11.74$ is the offset of the linear relation.

After determining $t_{\text{TWE, mean}}$ and $t_{\text{TWE, RMS}}$ based on the number of PEs, $t_{\text{TWE}}$ is obtained by sampling from a Gaussian distribution with $t_{\text{TWE, mean}}$ as the mean and $t_{\text{TWE, RMS}}$ as the standard deviation. The time when the signal arrives at the SiPM can then be calculated as

$$t_{\text{arrived}} = t_{\text{true}} + t_{\text{prop}} + t_{\text{TWE}}. \tag{9.7}$$

### 9.1.4 Trigger Simulation

So far, both the charge signal and the timing of a signal arriving at the SiPM have been simulated. To replicate actual data taking, triggers need to be simulated as well. The first trigger is the two-SiPM trigger. In the simulation, a SiPM is labelled as triggered if the ADC value exceeds the threshold, which is set to 60. If a trigger is fired, the adjacent SiPM is checked to see whether it is also triggered within the coincidence window (100 ns). A strip is labelled as triggered if the two-SiPM coincidence is satisfied, and subsequently, the module is marked as triggered as well. The timing for all 32 signals is recorded with the earliest time from the SiPM.

Once a triggered module is identified, another coincidence window (150 ns) is opened for the $X - Y$ coincidence. All data from hits within this fixed coincidence window are saved. As in reality, after this window, a dead time (22 $\mu$s) is applied to the triggered module to prevent any additional triggers from being created within this period.

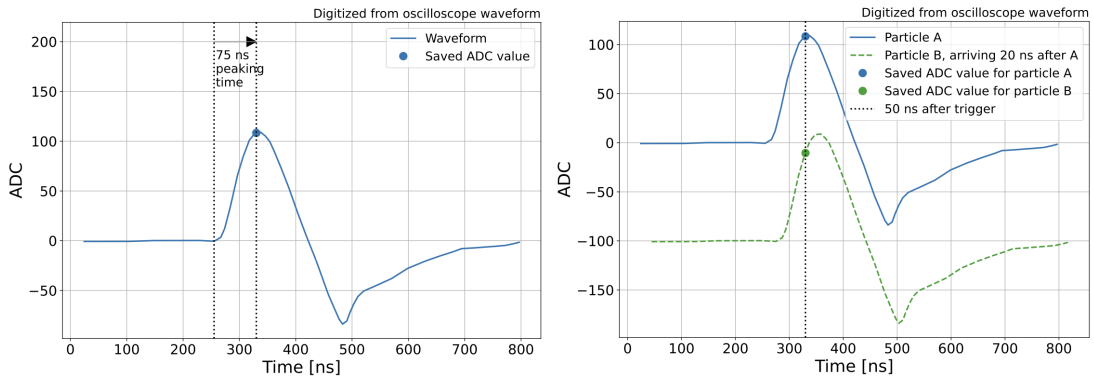


**Figure 9.11** (a) A SiPM waveform from real data. (b) An illustration of two particles crossing two strips in the same module with a 20 ns delay; the green dotted waveform is shifted for the visualisation purpose. Figures from Reference [248].

As for the charge signal of a triggered event, the FEB is configured to save the ADC value after a fixed time delay following the trigger. This delay is set to the shaping time when the waveform reaches its peak, as shown by the dot in Figure 9.11 (a).

However, if a second particle arrives in the same module with a delay $\Delta t$ but within the coincidence window, the value saved will not correspond to the peak of the waveform for this second particle, as demonstrated in Figure 9.11 (b). The reduced simulated ADC value for the second particle can be estimated by

$$\mathrm{ADC}_{\mathrm{reduced}} = \frac{wf(t_{\mathrm{peak}} - \Delta t)}{wf(t_{\mathrm{peak}})} \cdot \mathrm{ADC}_{\mathrm{peak}}, \tag{9.8}$$

where $wf$ is a function representing the waveform.

## 9.2 CRT Reconstruction

The CRT reconstruction process involves FEB readout data, including the time relative to the PPS ($t_0$), the time relative to the early beam warning signal ($t_1$), and 32 ADC values. As with PDS and TPC, a simpler hit-finding procedure is used to identify hits. The positions of these hits are reconstructed based on the $X - Y$ coincidence. Both timing signals are corrected for light propagation effects and time walk effects. The ADC values are corrected for attenuation and then converted to the number of PE for further analysis.

### 9.2.1 Strip Hit Reconstruction

The hit-finding algorithm selects strips of interest for each module by looking for concurrent pairs of channels with ADC values at least 60 counts above their pedestals. The lateral position within the selected strip is reconstructed as:

$$d = \frac{w}{2} \cdot (1 + \tanh(\log(\frac{\mathrm{ADC}_2}{\mathrm{ADC}_1}))), \tag{9.9}$$

where $w$ is the strip width, and $\mathrm{ADC}_1$ and $\mathrm{ADC}_2$ are the ADC counts for the two channels of the selected strip. The logarithmic ratio is used to represent the light distribution between the two channels, whereas the hyperbolic tangent function, with its range of (-1,1), ensures that the position is confined within the physical boundaries of the strip. Along with the reconstructed lateral position, the reconstructed object also includes ADC values and pedestal values for the two SiPMs, timing information, channel number, and FEB number. For data reconstruction, both timing information $t_0$ and $t_1$ are corrected for the cable delay using values saved in the database. All of this information is relevant for downstream reconstruction.

### 9.2.2 CRT Hit Reconstruction

The next stage of the reconstruction involves using $X - Y$ coincidence to reconstruct 3D CRT hits from strip hits. By combining strips from vertical and horizontal directions within a 20 ns coincidence window, a CRT hit can be identified, and its position can be determined based on the overlap with the reconstructed lateral position in the CRT strip hit.

As described in Section 7.3.1, the CRT Beam Telescope detector was set up as a 3×3 module set. In each set, all modules overlap with each other in both vertical and horizontal orientations. If more than one charged particle passes through a module set within the coincidence window, the reconstruction algorithm cannot determine the correct combinations for the $X - Y$ coincidence. For instance, if two particles arrive at a similar time, as shown in Figure 9.12, the algorithm is designed to save all possible combinations, resulting in four reconstructed CRT hits. Of these, two reconstructed hits will have real particles associated with them, while the other two will not and will be referred to as "fake hits" from now on.

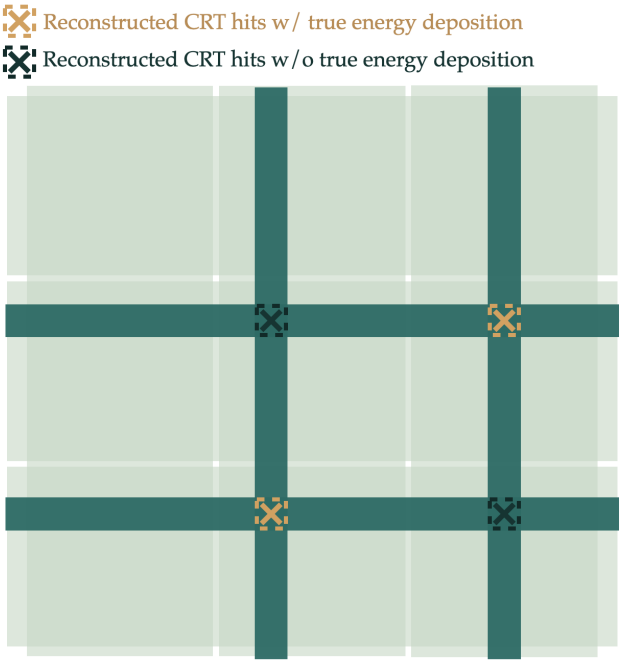


**Figure 9.12** A schematic diagram illustrating the CRT hit reconstruction for the scenario where two true particles pass through the CRT module set at similar times result in four reconstructed hits based on the algorithm, with only two hits correctly linked to real particles.

The reconstructed three-dimensional positions enable corrections to be applied to both timing and charge signals. The timing signal is corrected for both the

propagation effect $t_{\text{prop}}$ and the time walk effect $t_{\text{TWE}}$ with the same set of parameters used in simulation. Based on whether the channel is saturated or not, the number of PEs converted from the ADC count is corrected for the attenuation effect by

$$N_{\text{PE, corrected}} = \begin{cases} N_{\text{PE}} \cdot \frac{(r-B)^2}{B^2}, & \text{if ADC is unsaturated,} \\ N_{\text{PE}}, & \text{if ADC is saturated,} \end{cases} \tag{9.10}$$

where $r$ and $B$ are the same as in the Equation 9.1.

### Hit Reconstruction Performance

A "backtracking" algorithm was developed to identify the simulated energy depositions contributing to each reconstructed CRT hit, enabling the linking of truth particles with the reconstruction information. The algorithm also helps assess the accuracy of the CRT hit reconstruction. Figure 9.13 illustrates both the resolution of reconstructed position and timing for CRT hits. Results indicate a good reconstruction accuracy for both aspects.

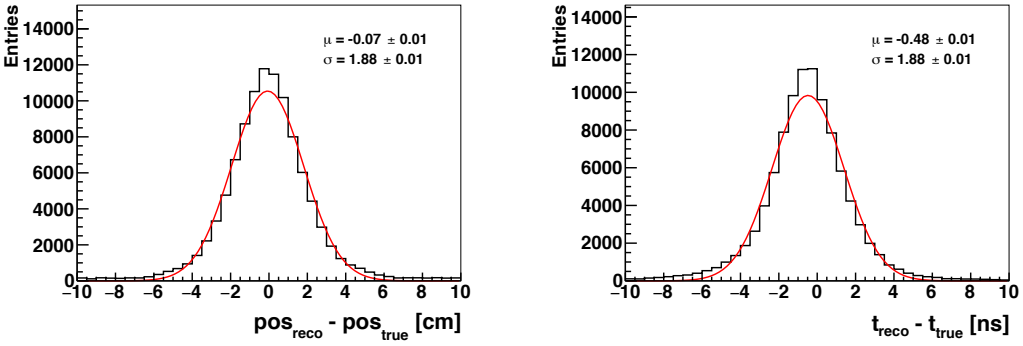


**Figure 9.13** Accuracy of (a) position reconstruction and (b) timing reconstruction for CRT hits.

The reconstruction algorithm is also applied to the CRT Beam Telescope data. Figure 9.14 (a) shows the number of PE after corrections as a function of distance to the readout. The observed non-uniformity in corrected PE across distances results from the presence of fake hits in the reconstruction. When only one hit is selected during reconstruction to avoid fake hits, the corrected PE remains consistent regardless of the distance to the readout, as shown in Figure 9.14 (b). Appendix C investigates whether CRT hits with real energy depositions influence the behaviour of the corrected number of PE. The results indicate that fake hits lead to an increase in the number of PE after attenuation corrections across different readout distances.

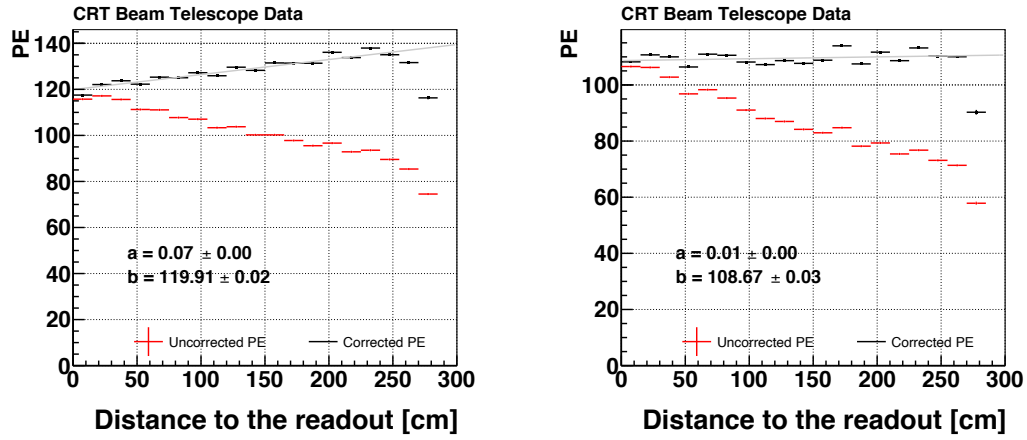


(a) (b)

**Figure 9.14** Corrected vs. uncorrected PE for events with (a) multiple hits and (b) only one hit in CRT Beam Telescope data.

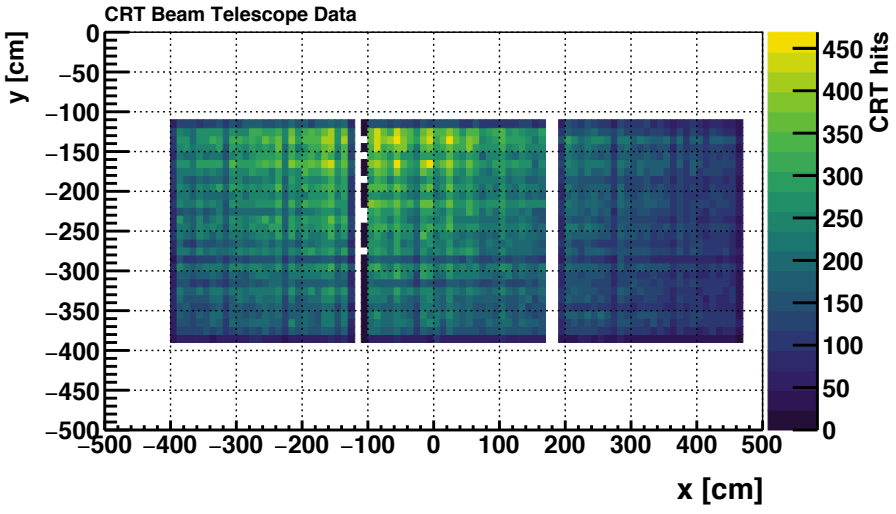


**Figure 9.15** The CRT hit position in the $X - Y$ plane for the CRT Beam Telescope upstream panel, showing a clear beam profile.

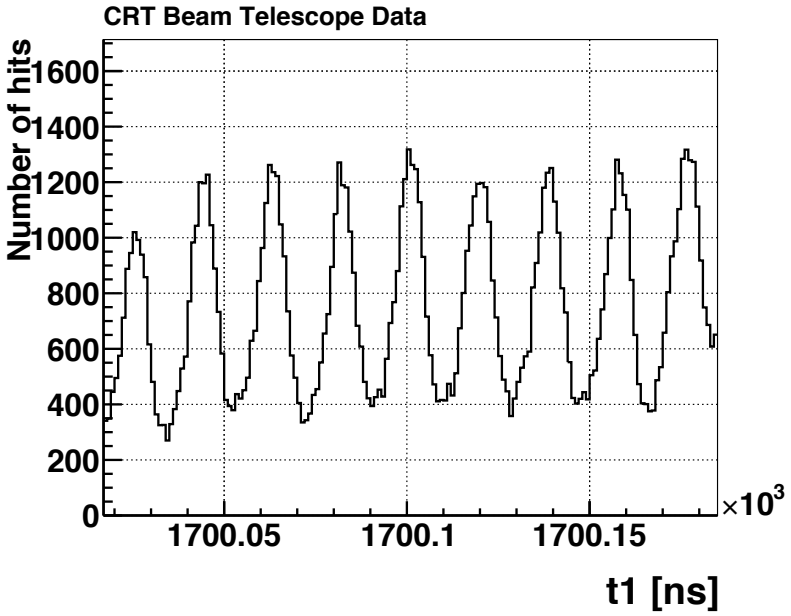


**Figure 9.16** The reconstructed timing relative to the early beam warning signal, with the beam bucket structure reconstructed in the CRT Beam Telescope data.

As previously introduced, SBND is situated just 110 metres from the beam source, allowing for a clear observation of the beam structure. Figure 9.15 illustrates the beam structure in the upstream panel of the CRT Beam Telescope detector. Section 4.2 describes the neutrino beam's delivery in proton bunches, and Figure 9.16 demonstrates this beam structure observed in the reconstructed CRT timing information.

### 9.2.3 CRT Track Reconstruction

The final stage of CRT reconstruction involves combining CRT hits from the upstream and downstream panels to form CRT tracks that represent the trajectory of a particle passing through the detector. As shown in Figure 9.17, two CRT hits can form a track if they are within 100 ns of each other. The start and end points of the track correspond to the positions of the two CRT hits. All possible combinations of CRT hits from the two panels are reconstructed into CRT tracks. It is important to note that while the CRT tracks are used for calibration, as explained in the next section, they were not used for the analysis detailed in Chapter 10 and Chapter 11.

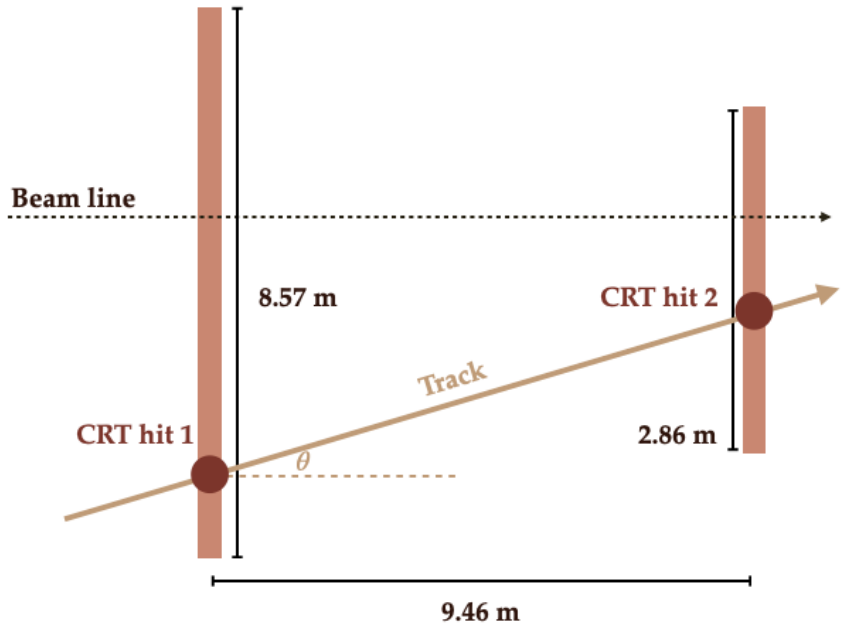


**Figure 9.17** A schematic diagram illustrating the CRT track reconstruction from two CRT hits from two panels.

## 9.3 Calibration of CRT Charge Signals

The charge signal in the CRT reconstruction is represented as the number of PE. The SiPM response $Q_{\text{slope}}$, which converts ADC counts to the number of PE, is expected to vary from strip to strip. However, this information is not recorded during data acquisition, and the current reconstruction uses a constant value across all channels. Additionally, in the actual detector setup, the CRT panels may not be installed vertically along the beam direction, leading to varying propagation lengths within the CRT module. Due to these factors, the number of PE for each panel can vary significantly, making it necessary to calibrate the number of PE. A data-driven calibration converting PE to deposited energy was performed for the charge signals in the CRT modules.

Using CRT tracks, the offset angles $\theta$ with respect to the beam-line, as shown in Figure 9.17, can be calculated. Combined with the thickness of the CRT modules (2 cm), the energy loss $dQ/dx$ can be calculated and plotted, as shown in Figure 9.18. The ADC counts are corrected for the attenuation effect using the correction factor described in Equation 9.10. The distribution of $dQ/dx$ can be well described by a Landau-Gaussian convoluted function, from which the most probable value,

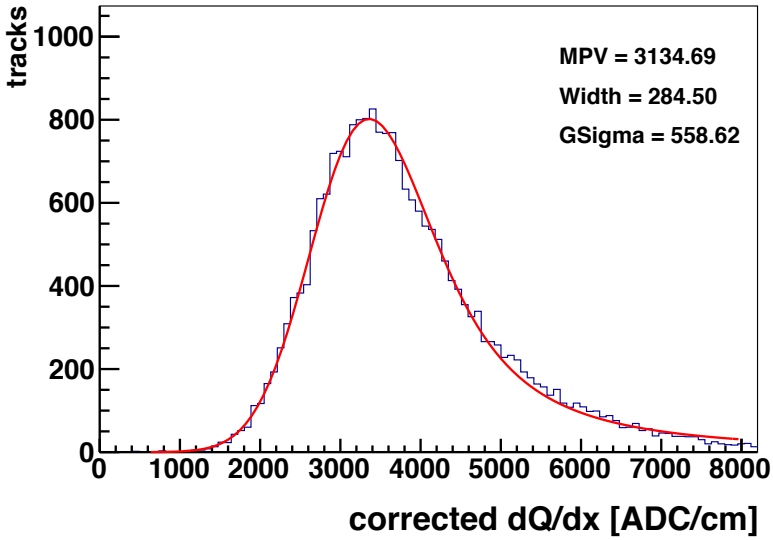


**Figure 9.18** The $dQ/dx$ distribution for the downstream panel in the simulation.

$(dQ/dx)_{\text{MPV}}$, can be extracted. The energy deposition can be reconstructed as

$$E_{\text{deposited, reco}} = N_{\text{PE, corrected}} \cdot \frac{Q^0}{(dQ/dx)_{\text{MPV}}/Q_{\text{slope}}}, \tag{9.11}$$

where $Q_{\text{slope}} = 40$ ADC/PE and $Q^0 = 1.68$ MeV is the MPV of energy deposition of MIP particles. The fitted $(dQ/dx)_{\text{MPV}}$ values for the upstream and downstream panels, for both data and simulation, are listed in Table 9.1.

| | Upstream [ADC/cm] | Downstream [ADC/cm] |
|---|---|---|
| Data | 2239.51 | 2475.66 |
| MC | 3139.33 | 3134.69 |

**Table 9.1** Extracted $(dQ/dx)_{\text{MPV}}$ for the upstream and downstream panels, for both data and simulation.

The reconstructed deposited energy for a CRT hit is compared with the true energy deposition to assess the resolution. As shown in Figure 9.19, the difference is centred around 0 with a reasonable distribution. Given that the true energy deposition is approximately 4 MeV, this results in an energy resolution of around 25%. This outcome is considered good, given both the calibration approach we have established and the fact that the CRT records only a single ADC count rather than the entire waveform for the charge signal.

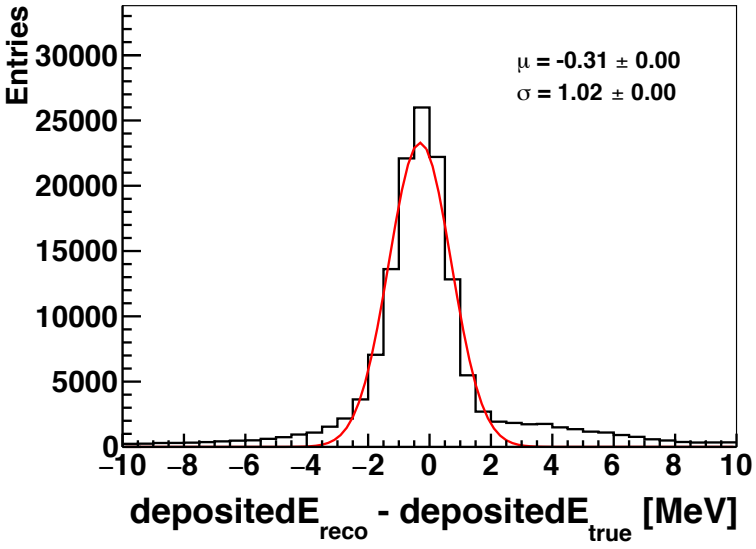


**Figure 9.19** Accuracy of reconstructed energy deposition for CRT hits.

### 9.3.1 Comparison of Simulation to Data

The reconstructed deposited energy from the MC samples is compared with the data. The simulation primarily consists of so-called dirt neutrinos, i.e., neutrino interactions occurring in the surrounding material. For data, events are first selected from within the beam window, and a time window of the same length outside the beam window is used to estimate the cosmic background. By subtracting the cosmic window histogram from the beam window histogram, a dirt-neutrino-dominant sample of data can be obtained.

As shown in Figure 9.20, this comparison uses CRT hits from the downstream panel; results for the upstream panel are presented in Appendix C. The simulation demonstrates contributions from various particle types, including muons, protons, pions, electrons, and fake hits. As expected, muons are the dominant particles produced from the dirt simulation. The fake hits arise from the CRT hit reconstruction process, as previously described. When comparing data to MC, a total fractional difference of -12.76% was observed, indicating that the simulation overestimated the deposited energy relative to the data. Although there is reasonable agreement around the peak region, the high-energy tail of the distribution shows a notable discrepancy.

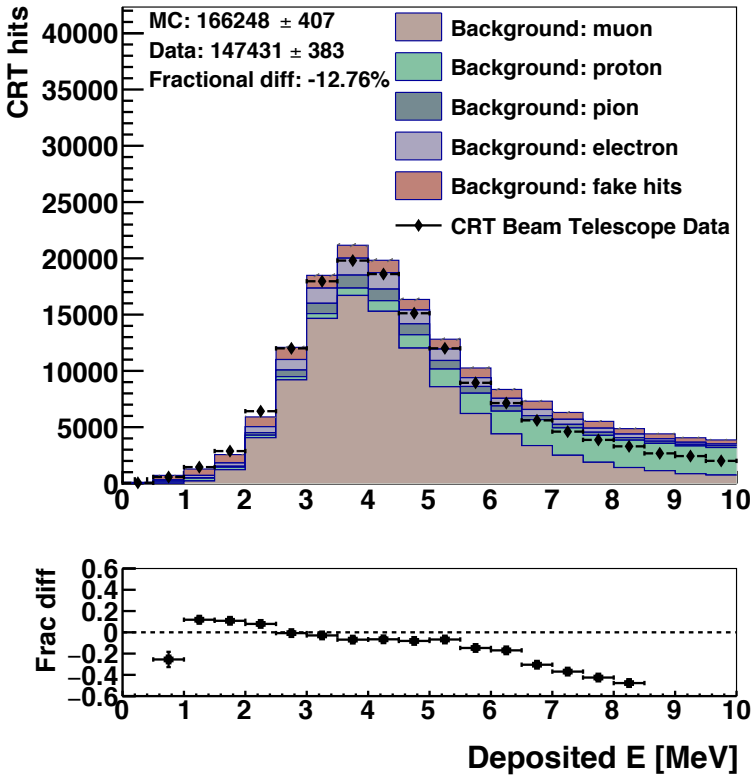


**Figure 9.20** The distribution of deposited energy for downstream panel from MC samples compared with CRT Beam Telescope data, broken down by particle type: muon, proton, pion, electron, and fake hits. Simulation with `QGSP_BERT` physics list.

### Simulation with an Alternative Physics List in GEANT 4

The tail region in Figure 9.20, where the largest discrepancy is observed, is dominated by protons. One possible explanation for this discrepancy could be an overestimation of proton production from neutron interactions in the GEANT 4 simulation. As explained in Section 5.3.1, GEANT 4 uses physics lists to simulate particle interactions with matter. The default physics list used by SBN experiments is `QGSP_BERT`. An alternative physics list is `QGSP_BERT_HP`, which includes a high-precision neutron model.

A different simulation using the high-precision list was produced and compared with the data, as illustrated in Figure 9.21. With the new physics list, contributions of high energies have been significantly reduced. Most importantly, the data and MC now demonstrate excellent agreement. Consequently, the `QGSP_BERT_HP` list has been selected as the default model for the beam telescope, and SBN currently uses it by default due to these improved results.

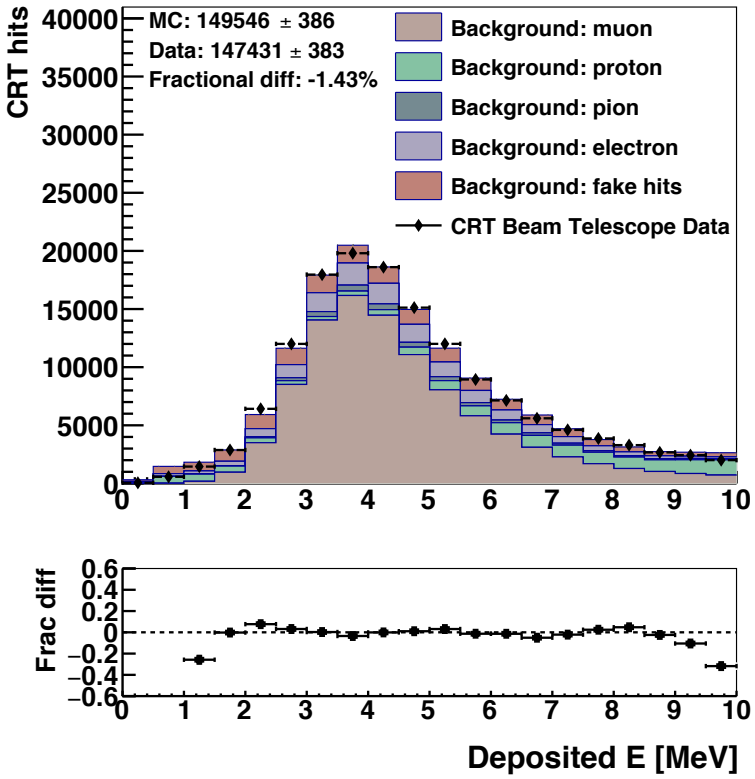


**Figure 9.21** The distribution of deposited energy for downstream panel from MC samples compared with CRT Beam Telescope data, broken down by particle type: muon, proton, pion, electron, and fake hits. Simulation with `QGSP_BERT_HP` physics list.

## 9.4 Summary

This chapter described the simulation and reconstruction processes for the CRT Beam Telescope. The simulations for charge signal, timing, and triggers are data-driven, relying on measurements from both the Beam Telescope and the Module-0 test at Bern. The CRT hit information obtained from the reconstruction discussed in this chapter will be used for the BSM searches in Chapter 10 and Chapter 11.

A calibration of the charge signal was performed. By comparing MC simulations to the collected dataset, it became evident that the high-precision physics list `QGSP_BERT_HP` provides a more accurate representation and must be incorporated correctly into our simulations. As a result, the `QGSP_BERT_HP` list has been selected as the default model for both the Beam Telescope detector and the broader SBN program.

# 10

# Long-lived Dark Neutrino Searches with the SBND CRT Beam Telescope

This chapter describes searches for dark neutrinos with masses of $\mathcal{O}(100)$ MeV using the SBND CRT Beam Telescope detector. Dark neutrinos are produced through neutrino up-scattering with nuclei, decaying with the signature $N_D \to \nu l^- l^+$ ($l = e, \mu$). The resulting lepton pairs from these decays can be detected within the CRT Beam Telescope detector. This chapter presents results from a search for long-lived dark neutrinos. The preliminary results for scenarios with a different lifetime will be presented in Appendix E.

Starting with the dark neutrino model and its simulation, this chapter will discuss the kinematic distributions at the truth level for the signals. The designed box selections will then be introduced, followed by the refinement of the selection process using a Boosted Decision Tree (BDT) to enhance signal significance. Additionally, the calculation of systematic uncertainties from various sources will be presented. Finally, with the calculated systematic uncertainties, the MC will be compared to the data to assess their agreement.

The searches presented in this chapter were conducted in collaboration with phenomenologists K. J. Kelly (Texas A&M University) and P. A. N. Machado (FNAL). The phenomenologists handled the theoretical aspects of the analysis, while the author focused on the experimental part.

## 10.1 Model and Simulation

Dark neutrinos, as introduced in Section 2.4, are produced by the BNB neutrino beam. For the study detailed in this chapter, the original model has been expanded. Firstly, the mass of the dark-sector boson $m_{Z_D}$ is assumed to be 1.25 GeV, with the masses of the dark neutrinos assumed to be sub-GeV. As a result, dark neutrinos decay "off-shell" into $\nu l^- l^+$ rather than undergoing a two-step decay into $Z_D \nu$ followed by $Z_D \to l^- l^+$. Secondly, the decay of dark neutrinos is no longer considered as prompt, allowing them to travel a certain distance after their production.

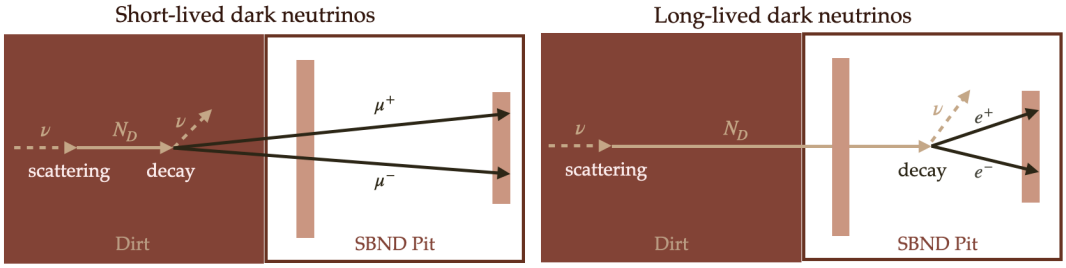


**Figure 10.1** A bird's-eye view schematic illustration of short-lived dark neutrino decays into a muon-antimuon pair (left) and long-lived dark neutrino decays into an electron-positron pair (right) in the SBND beam telescope geometry.

Depending on the decay position of the dark neutrinos, two separate cases are considered in the dark neutrino model. If dark neutrinos decay before reaching the Beam Telescope, they are classified as short-lived dark neutrinos. Conversely, if the dark neutrinos decay between the two panels within the detector, they are referred to as long-lived dark neutrinos, as illustrated in Figure 10.1. For the long-lived case, the lepton pair is selected to be $e^- e^+$ due to the initial interest in exploring the potential explanation of the MiniBooNE LEE with the $e^- e^+$ channel. In contrast, $\mu^- \mu^+$ pairs are chosen for the short-lived dark neutrinos, as $e^- e^+$ pairs tend to stop quickly once produced in the upstream surroundings, and so would not be detectable.

The generation of simulated dark neutrinos for both scenarios and their subsequent decays follows the method described in Section 5.2.4. To achieve high efficiency in signal production, a box volume is defined around the CRT Beam Telescope, extending three metres along both the vertical and horizontal directions of the CRT panel. Only dark neutrinos with decay positions within this defined volume are saved. Furthermore, instead of generating multiple events per kinematic case, a scaling factor, commonly referred to as a **weight**, is saved per event to represent the probability of that event occurring. The decay products are then used as input for simulation and reconstruction through the workflow chain outlined in Chapter 5 and Chapter 9.

| $m_{N_D}$ [MeV] | Number of Events |
|---|---|
| 140 | 180.08 |
| 400 | 2358.10 |

**Table 10.1** Details of the dark neutrino MC simulation samples generated for long-lived dark neutrinos are provided. In each mass, the number of events is not an integer due to the weight applied to each event.

Two mass assumptions are considered for the MC simulation samples of long-lived dark neutrinos. The samples are generated assuming $6.6 \times 10^{20}$ POT and are summarised in Table 10.1. The number of events is calculated as the sum of the weights per generated event.

For the background simulation, the SBND simulation of neutrinos from the BNB beam, as described in Section 5.2.3, was used during the development of the signal selections. A total of approximately 5,282,121 events were generated corresponding to $2.78 \times 10^{21}$ POT, which is 9.43 times the total POT of the CRT Beam Telescope data. Neutrino interactions are expected to be the primary background. However, cosmic ray activities can potentially contribute additional background, but they are expected to a sub-dominant background. To confirm this, an overlay sample combining cosmic and neutrino backgrounds was generated with $2.74 \times 10^{19}$ POT, allowing for confirmation of whether cosmic rays introduce significant background. Due to the high computational demands of simulating cosmic events, a larger sample has not yet been produced.

## 10.2 Signal Kinematics

The distribution of kinetic energy for electrons and positrons detected by the Beam Telescope is shown in Figure 10.2 for dark neutrino masses of 140 MeV and 400 MeV, respectively. The average kinetic energies for electrons and positrons are approximately 150 MeV for the 140 MeV dark neutrino mass and around 400 MeV for the 400 MeV dark neutrino mass.

The opening angle between electrons and positrons is presented in Figure 10.3 for both the 140 MeV and 400 MeV mass cases. For both masses, the electrons and positrons are not highly boosted, as indicated by the peak of the distribution being above 25°. This is because dark neutrinos decay off-shell, with a third particle, $\nu$, carrying away part of the energy. Comparing the distribution for the 400 MeV case to the 140 MeV case, we observe that lower masses result in greater boosting of the lepton pairs, leading to a relatively smaller opening angle.

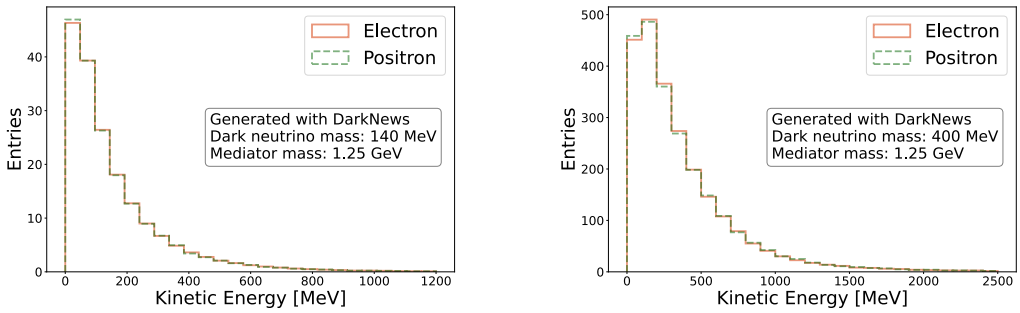


**(a)** **(b)**

**Figure 10.2** The kinetic energy distribution of electrons and positrons for dark neutrino masses of (a) 140 MeV and (b) 400 MeV.

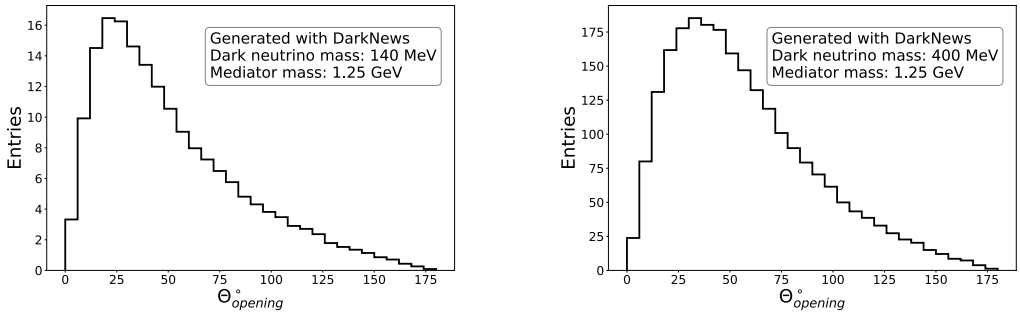


**(a)** **(b)**

**Figure 10.3** Opening angles between electrons and positrons for dark neutrino masses of (a) 140 MeV and (b) 400 MeV.

## 10.3 Event Selection

A series of selections has been applied to attempt to extract a clean sample of signal events. These selections were developed using the dark neutrino MC sample and 20% of the total neutrino MC background (referred to as the dirt sample from now on), while the remaining 80% of the dirt sample was reserved to test the effectiveness of the selections. Additionally, the cosmic overlay sample was used to evaluate whether cosmic ray activities would affect background rejection efficiency. The results presented in this section focus on dark neutrinos with a mass of 400 MeV, with equivalent results for dark neutrinos with a mass of 140 MeV provided in Appendix D.

### 10.3.1 Minimal Selections

The first stage of selections involves applying a set of basic requirements. First, events are required to interact with either of the CRT Beam Telescope panels during the beam spill. In addition, since long-lived dark neutrinos decay between the two CRT panels, the upstream panel is used as a veto to reject dirt events originating from the upstream direction along the beam. Given that the signal will appear as an $e^-e^+$ pair, the downstream panel is expected to register four reconstructed CRT hits due to the fake-hit creation, described in Section 9.2.2.

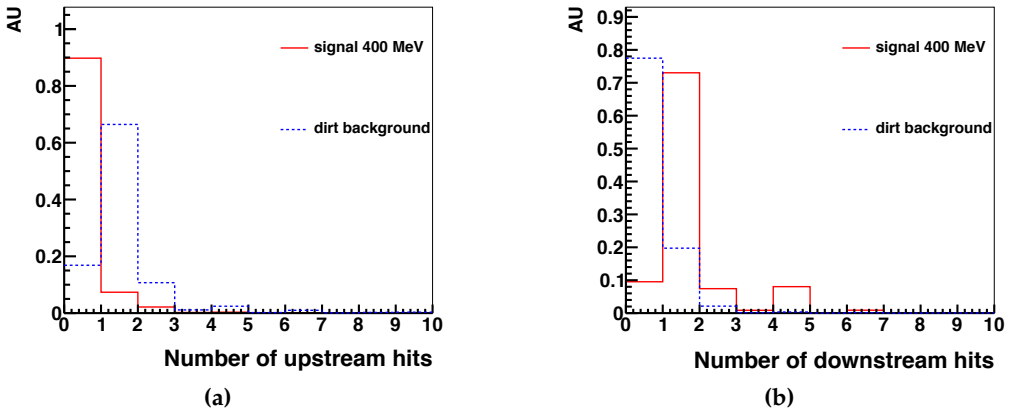


**Figure 10.4** Number of hits for the (a) upstream and (b) downstream panels, for dark neutrinos with a mass of 400 MeV, compared with the dirt neutrino background.

Figure 10.4 shows the number of hits for both the upstream and downstream panels for the signal and background. As expected, the signal predominantly shows zero hits in the upstream panel, with the non-zero-hit events attributed to electron/positron backscattering after production. By using the upstream panel as a veto, the majority of dirt background can be effectively rejected.

For the downstream panel, most events in the signal sample exhibit only one hit, indicating that only one particle interacts with the panel, as shown in the event display in Figure 10.5 (a). Several factors contribute to this outcome. Firstly, as shown in Figure 10.5 (b), the reconstructed beam centre is positioned significantly higher than the Beam Telescope. Since dark neutrinos are produced via neutrino up-scattering, even when the $e^-e^+$ pair travels towards the downstream panel, the particles are not highly boosted. As a result, capturing both particles on the relatively small downstream panel (2.7 m $\times$ 2.7 m) becomes unlikely. Even though the one-hit case is dominant in the signal sample, it is difficult to distinguish it from background events. Therefore, the selection criteria still require four hits to ensure a cleaner sample.

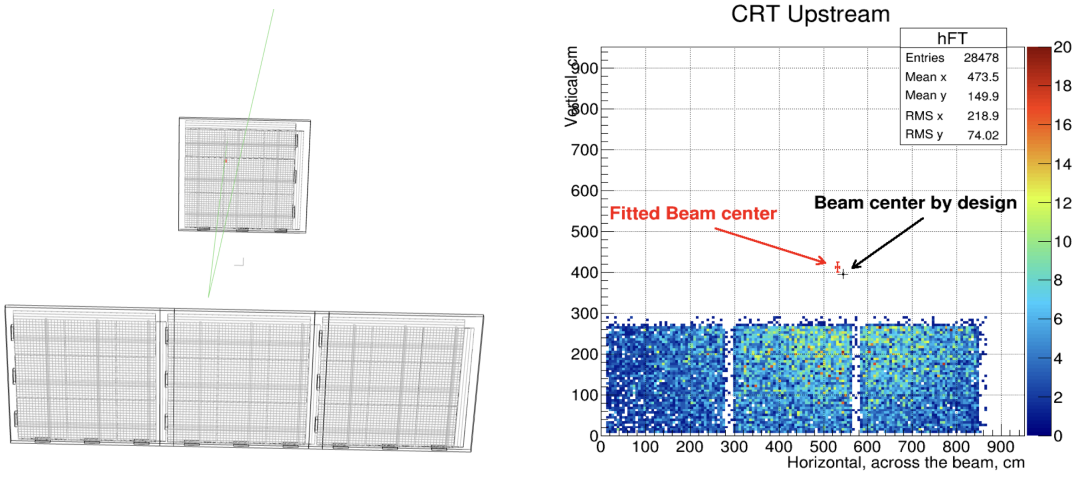


**Figure 10.5** (a) An event display with one hit in the downstream panel in the signal sample, where the green line represents true particle, red cubes represent reconstructed CRT hits. (b) Reconstructed neutrino beam centre as a reference of the upstream panel of the Beam Telescope [250].

Scanning through the dirt samples after applying the minimal selections, a set of events passes the four hits selection but shows a very different arrangement compared to the typical rectangle shape formed by two real energy depositions, as illustrated in Figure 10.6. To address this, a requirement was added on top of the four hits selection, ensuring that the selected hits form a rectangle shape.

**Selection Matrix** After the basic requirements, the selected candidates are positioned at the four corners of a rectangle. As a result, the two diagonal pairs are the potential candidates corresponding to the two real energy depositions. To identify the true diagonal pair with genuine energy depositions, a selection matrix was developed

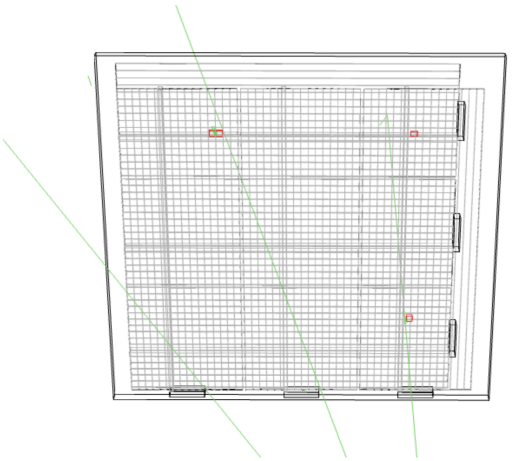

**Figure 10.6** An event display from the dirt sample shows four reconstructed hits that do not form a rectangle. This arrangement of CRT hits does not typically indicate two real energy depositions and hence rejected.

to choose the correct pair for further analysis. As shown in Figure 10.7, each CRT hit includes reconstructed timing and ADC information for both vertical and horizontal strips. For each CRT hit, the difference in timing and ADC values is calculated to aid in selecting the correct pair, the difference takes the form:

$$\begin{aligned} \Delta_{t_1} &= |t_{1,x} - t_{1,y}|, \\ \Delta_{\mathrm{ADC}} &= |\mathrm{ADC}_x - \mathrm{ADC}_y|, \end{aligned} \tag{10.1}$$

The true diagonal pair is expected to exhibit both a smaller $\Delta_{t_1}$ and $\Delta_{\mathrm{ADC}}$. Therefore, the selection matrix is designed as follows: first, the mean $\Delta_{t_1}$ value is calculated for both diagonal pairs. If one pair has a smaller value than the other, that pair is selected as the "real" diagonal pair. If the timing differences are equal, the selection is made by choosing the pair with the smaller $\Delta_{\mathrm{ADC}}$. The selection matrix results in around 60% accuracy of selecting the correct hit pair.

### 10.3.2 Distance between Hits

The distribution of the distance between hits within diagonal pairs is drawn for both signal and background, as shown in Figure 10.8. A peak is observed at shorter distances for the dirt background, while the signal exhibits a more uniform distribution.

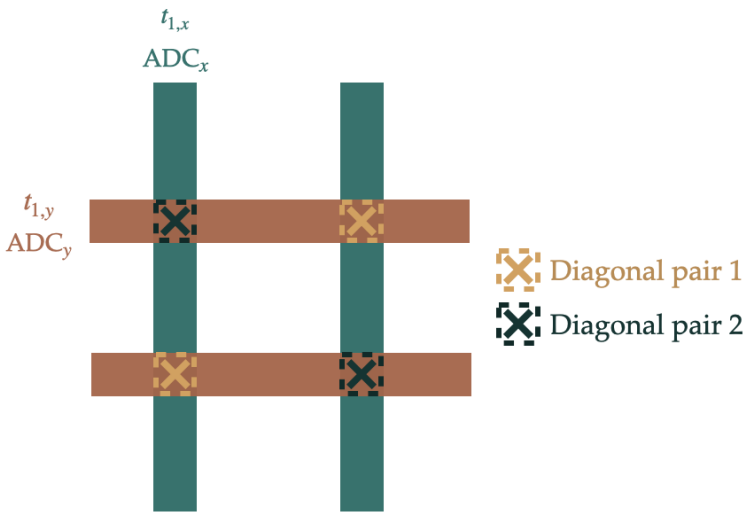


**Figure 10.7** A schematic diagram illustrating the two possible diagonal pairs for four reconstructed hits situation. $t_{1,x}$, $ADC_x$, $t_{1,y}$, $ADC_y$ are used for the selection matrix.

A two-dimensional range scanning algorithm was developed to determine the optimal selection range, combining different minimum and maximum values to calculate $S/\sqrt{BG}$, where $S$ is the number of signal events and $BG$ is the number of background events. The algorithm identified the region where $S/\sqrt{BG}$ is maximised, which in this case occurs at distances greater than 22 cm. The POT-normalised histogram was used as the input for the selection algorithm, but the same results were obtained from an area-normalised plot. Therefore, the area-normalised plot was chosen to show for visualisation purposes, as the signal is very small compared to the background, and this will be consistent for other handles.

The feature that many events in the dirt sample exhibit very small distances between hits in the diagonal pairs was unexpected. To investigate this, a truth-level study was conducted. As shown in Figure 10.9 (a), the dominant pairs are muon-proton pairs. When plotting the starting points of the muons and protons, the results indicate that the points of neutrino interactions are mostly within the downstream panel, as illustrated in Figure 10.9 (b).

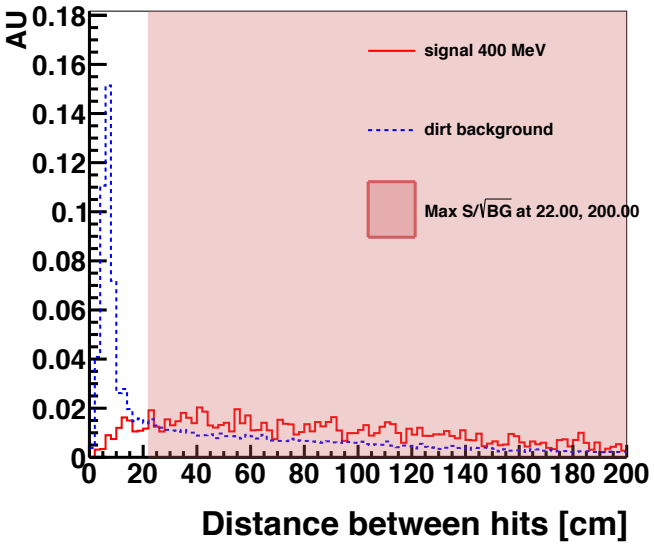


**Figure 10.8** The distance between two diagonal hits, for dark neutrinos with a mass of 400 MeV, compared with the dirt neutrino background.

### 10.3.3 Deposited Energy

Since dark neutrinos are expected to decay into electrons and positrons, which are typical minimum ionising particles (MIPs) in the scintillator, their behaviour contrasts with some background events. The opening angle of the electron-positron pairs for dark neutrinos with mass of 400 MeV peaks around 40°, whereas in the dirt sample, background events can involve low-momentum protons which are not MIPs or particles hitting the CRT panel at larger angles, leading to higher deposited energy than the signal, as shown in Figure 10.10. Again, the area-normalised plot was chosen for visualisation purposes. The selection algorithm identified a deposited energy range between 1.8 and 4.7 MeV as optimal for maximising $S/\sqrt{BG}$.

### 10.3.4 Timing Difference Selection

With the selected diagonal pair, the timing difference between the two CRT hits is used to further refine the signal selection. As shown in Figure 10.11, the signal and background exhibit similar timing distributions. This similarity is likely to arise from the time coincidence requirement when reconstructing CRT hits, meaning that having four CRT hits is more likely to result from the same neutrino interaction, making the background resemble the signal. To optimise the selection, the algorithm determined that a timing difference within 10 ns could further reduce the dirt background.

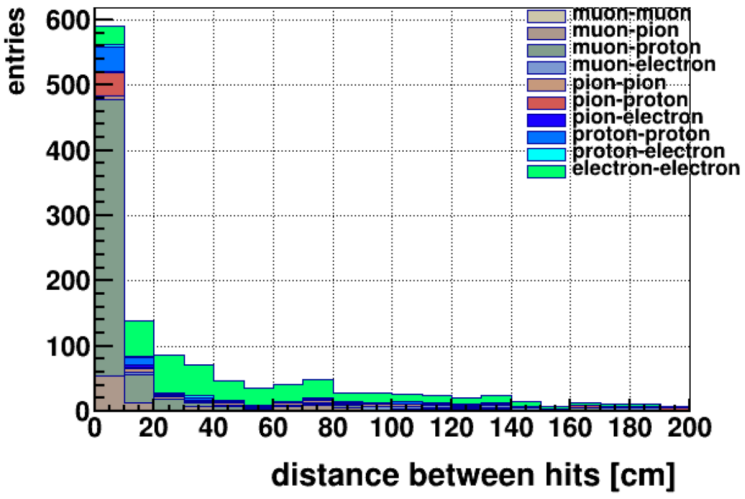


**(a)**

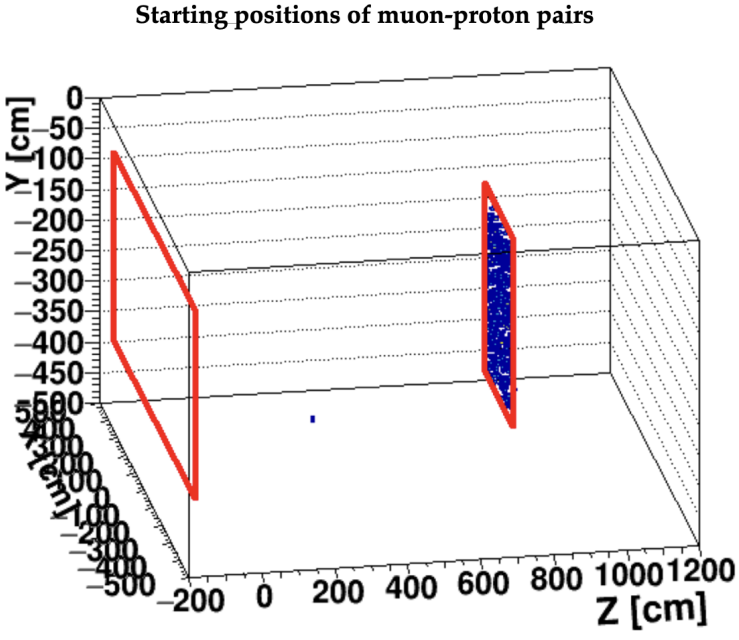


**(b)**

**Figure 10.9** (a) Distance between hits based on truth information. (b) The distribution of starting points for muon-proton pairs: blue dots represent the starting points of the pair, while the red rectangle represents the upstream and downstream panels.

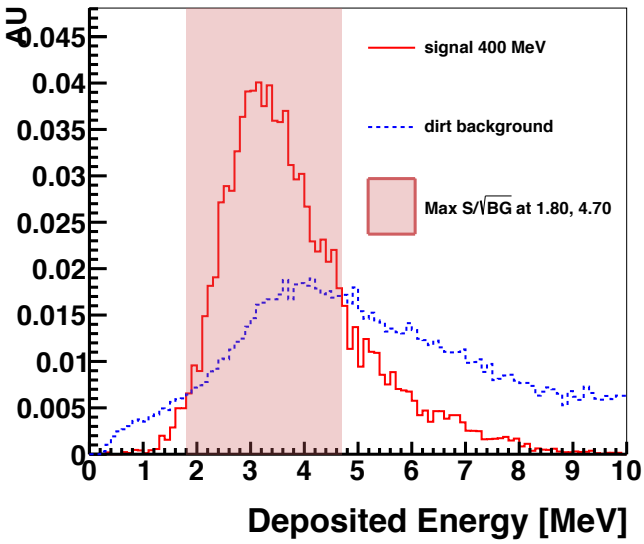


**Figure 10.10** The distribution of deposited energy for selected diagonal pair, for dark neutrinos with a mass of 400 MeV, compared with the dirt neutrino background.

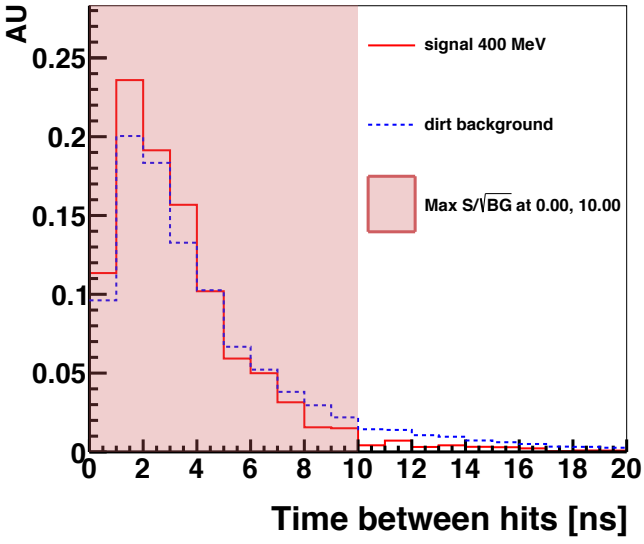


**Figure 10.11** The distribution of timing difference between two hits in the selected diagonal pair, for dark neutrinos with a mass of 400 MeV, compared with the dirt neutrino background.

### 10.3.5 Summary of Selection

A summary of the applied selections and their performance in terms of efficiency is presented in Table 10.2. Both the number of events and the efficiencies for signal selection and background rejection are provided. The selections were applied to two signal samples and background samples described in Section 10.1. For the background, the majority of events were successfully rejected by the selections. The overlay sample, which includes cosmic ray activities, was also tested, and no events from cosmic rays were observed after the application of these selections.

In both signal cases, a significant portion of events were lost when requiring four hits in the downstream panel. This loss is primarily due to the challenges posed by the detector's setup: its position is too low relative to the beam centre, and the downstream panel is not large enough to capture both hits.

| | **Dirt neutrino** | **Dark neutrino 400 MeV** | **Dark neutrino 140 MeV** |
|---|---|---|---|
| **Deposited energy in detector within beam spill** | 560272 (100.00 %) | 222.56 (100.00 %) | 18.35 (100.00 %) |
| **No hit in the upstream panel** | 94075 (16.79 %) | 199.78 (89.77 %) | 17.75 (96.73 %) |
| **Four hits in the downstream panel** | 1572 (0.28 %) | 17.9 (8.04 %) | 2.23 (12.15 %) |
| **Rectangle shape requirement** | 1469 (0.26 %) | 17.81 (8.00 %) | 2.22 (12.10 %) |
| **Distance between diagonal hits** | 767 (0.14 %) | 16.18 (7.27 %) | 1.99 (10.85 %) |
| **Deposited energy** | 180 (0.03 %) | 10.26 (4.61 %) | 1.31 (7.14 %) |
| **Timing diff between diagonal hits** | 171 (0.03 %) | 9.98 (4.48 %) | 1.27 (6.92 %) |

**Table 10.2** Numbers of events at each stage of the event selection for the long-lived dark neutrino case (normalised to $2.95 \times 10^{20}$ POT).

## 10.4 The Boosted Decision Tree Method

Based on the "box-cut" selection described above, the signal for a 400 MeV dark neutrino appears more promising compared to the 140 MeV case. However, the minimal selection criteria, particularly the four cuts on the downstream panels, result in the majority of signals being rejected. To optimise the significance ($S/\sqrt{BG}$), two possible approaches can be taken: one involves testing different combinations of values and the order of the selection criteria described in the previous section, while the other involves using a machine learning tool, such as the BDT method.

The BDT method is a powerful multivariate tool used for classification tasks, and it has been widely applied in high-energy physics [251]. BDT training involves a series of decision trees, also known as weak learners. Each decision tree is trained sequentially, with each subsequent tree focusing on correcting the errors made by the previous ones. The output of each tree is typically a weight proportional to its accuracy. The outputs of all the decision trees are then combined through a weighted sum, a process known as **boosting**. After training, the BDT assigns a score to each event in a sample, representing how signal-like it is.

The BDT was trained using the Toolkit for Multivariate Data Analysis (TMVA) package [252], a machine learning framework integrated into ROOT, specifically designed for the needs of high-energy physics. TMVA supports multiple machine-learning classifiers, including BDT, Neural Networks, Fisher discriminants, and likelihood methods. All these classifiers were tested for signal and background separation, and BDT demonstrated the best performance for the simulated samples. Hence, BDT was chosen as the selection tool to maximise the significance.

### 10.4.1 BDT Variables

A few variables used in the box selection can be directly applied in the BDT, such as the number of hits in the upstream, the number of hits in the downstream, whether the reconstructed hits in the downstream panel form a rectangle, the distance between the diagonal hits, and the timing difference between the selected diagonal pairs.

A few variables, such as deposited energy, are two-dimensional because, for each selected diagonal pair, the information from both hits was used in the box selection. Since the BDT can only accept one-dimensional variables, different parameters are introduced to represent the statistical distribution. Firstly, the mean value of the deposited energy for the selected pair is calculated and used as an input variable. The ratio between the two deposited energies from the selected diagonal pair is also included, as signals are expected to have a ratio closer to 1. Additionally, a variable is constructed to represent the deviation of deposited energy among all four hits, calculated as the sample deviation:

$$\text{std} = \sqrt{\frac{\sum_i (E_{\text{deposited},i} - E_{\text{deposited},CV})^2}{n-1}}, \tag{10.2}$$

where $E_{\text{deposited},i}$ represents the deposited energy for each of the four hits, $E_{\text{deposited},CV}$ is the average deposited energy, and $n = 4$. The sample deviation, rather than the standard deviation, is chosen because it is calculated per event, which represents a subset of the entire population. In addition to the distance between the diagonal pairs, the width of the rectangle (defined in the horizontal direction) is also used as a BDT variable to represent the shape of the two particles interacting with the downstream panel. This variable is correlated with the combination of the opening angle and the propagation length. Figure 10.12 shows the four additional variables introduced as BDT handles for training. Table 10.3 lists all the variables used in the BDT training.

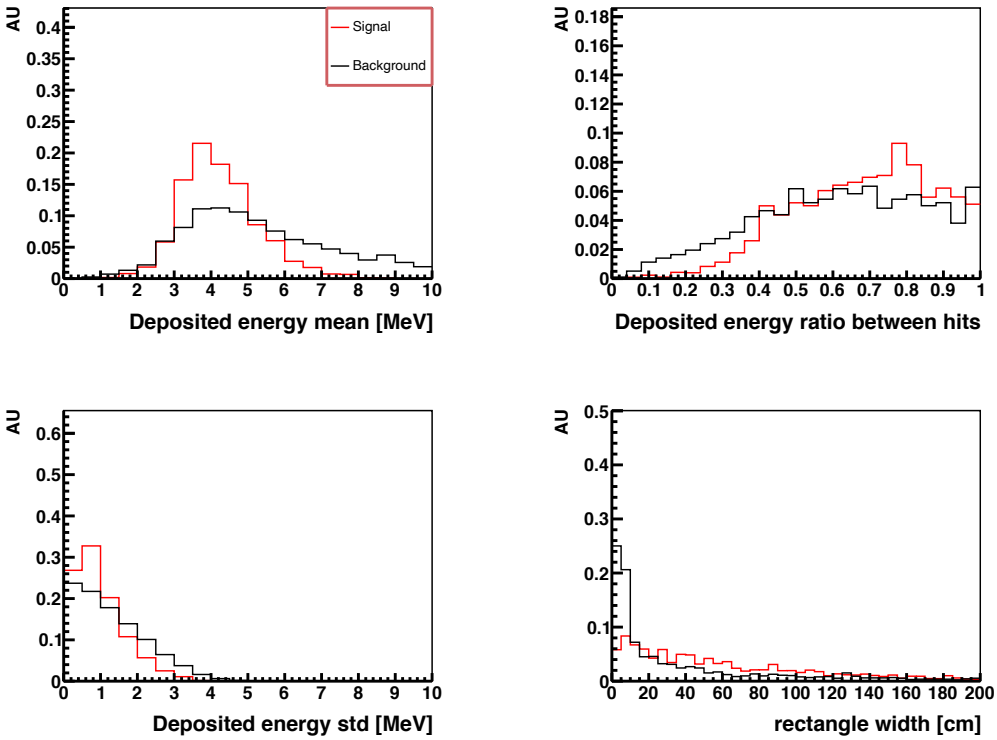


**Figure 10.12** Distributions of BDT variables for the signal and the dirt background: (top left) mean deposited energy between the selected diagonal pair, (top right) ratio of the two deposited energies, (bottom left) sample deviation of deposited energy from the four reconstructed hits, (bottom right) the width (defined in the horizontal direction) of the formed rectangle.

| Variable | Description |
|---|---|
| n_hits_upstream | Number of hits in the CRT upstream panel. |
| n_hits_downstream | Number of hits in the CRT downstream panel. |
| CanFormARectangle | A boolean variable indicating whether the arrangement of the CRT hits forms a rectangle. |
| Distance between hits | The distance between diagonal hits. |
| Rectangle width | The width in the horizontal direction to indicate the shape of the rectangle, with a value set to -1 if it is not a rectangular shape. |
| Deposited energy mean | The mean value of the deposited energy within the selected diagonal hits. |
| Deposited energy std | The sample deviation of the deposited energy across all CRT hits. |
| Deposited energy ratio between hits | The ratio of the deposited energy between the selected diagonal hits. |
| t1 diff between hits | The timing difference between the selected diagonal hits. |

**Table 10.3** The variables used in the training of the BDT models.

### 10.4.2 BDT Training and Overtraining Checks

The BDT was trained using the same dirt background and 400 MeV dark neutrino sample that were used for developing the selections in Section 10.3. Prior to training, a minimal requirement was applied: the number of hits in the downstream region had to be greater than two. This condition was necessary because many of the BDT variables, such as the distance and deposited energy ratio, require at least two hits to be present for accurate evaluation.

A BDT model can become overtrained if it picks up features that are only present in the training sample but not in a broader dataset. Overtraining may occur when the training sample is too small or if too many iterations are performed during training. To check for overtraining, the sample is typically split into test and training sets. TMVA provides this functionality by default, and the results from both samples are shown in Figure 10.13. For both the test and training samples, the BDT score distributions are quite similar, indicating that overtraining has not occurred. Therefore, the BDT model was confirmed as reliable for further selections.

### 10.4.3 Overlapping Region

A significant overlapping region in the BDT score distribution between signal and background was observed. To investigate the underlying cause, the BDT variables were plotted for both signal and background within this overlapping region, as shown in Figure 10.14. The majority of events in this region have two hits in the downstream panel, with only a few having four hits.

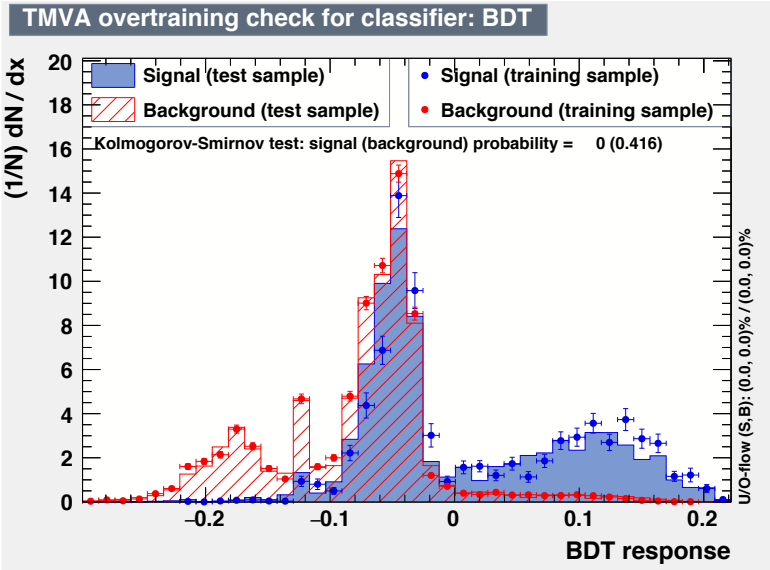


**Figure 10.13** Trained BDT scores for both the dirt background and the 400 MeV signal, with the BDT scores from both the training and test samples.

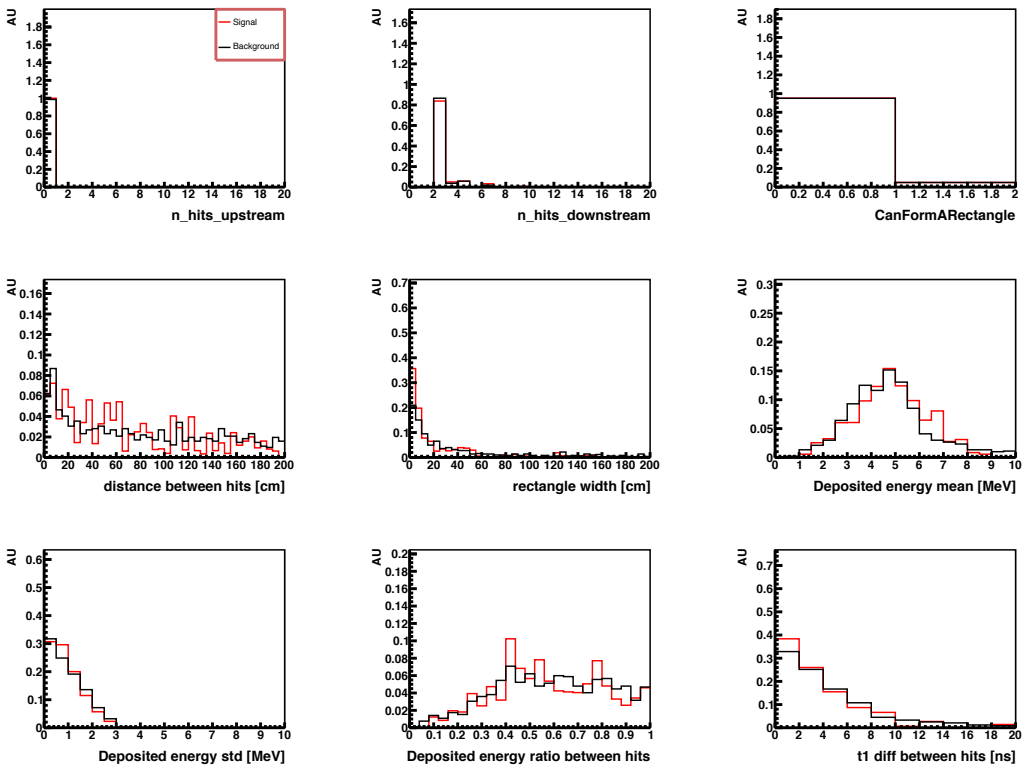


**Figure 10.14** Distributions of all BDT variables for the signal and the dirt background in the overlapping region of the BDT score.

To further understand the cause, event hand-scans were carried out. Figure 10.15 presents several event displays to illustrate the topology behind the events in the overlapping region. The majority of events in the overlapping region involve only one true particle propagating through the panel. However, this particle may propagate between two strips, or a secondary particle, such as a Compton photon with sufficient energy to trigger just one strip, could introduce an extra hit during the reconstruction, as shown in Figures 10.15 (a) and (b).

Additionally, two real particles can pass through a single strip if the decay position is very close to the panel. This can lead to only two hits being reconstructed, as illustrated in Figure 10.15 (c). In cases where four hits are recorded, if the opening angle is large, it could result in higher deposited energy and lead to misclassification as background events, as shown in Figure 10.15 (d).

### 10.4.4 BDT Performance and Selection

A Receiver Operating Characteristic (ROC) curve is typically used to describe the true positive rate versus the false positive rate for a given classifier. The ROC curve is generated by scanning through the signal selection efficiency and the background rejection efficiency. The area under the curve (AUC) is commonly used as a metric to evaluate the performance of a BDT model. A perfect classifier would completely separate the signal from the background, yielding an AUC of 1. A random classifier (the baseline) would not distinguish between signal and background, resulting in an AUC of 0.5.

Figure 10.16 shows the ROC curve for the trained BDT model, with a dashed line indicating the baseline. The AUC is calculated to be 0.826, demonstrating that the BDT is a reasonably effective classifier.

The BDT distribution for both signal and background is normalised to 2.95 $\times 10^{20}$ POT to observe the actual distribution, as shown in the left panel of Figure 10.17. Since the signal is very small, it is scaled up 100 times for comparison with the dirt background. The selection is performed by scanning through the modified significance, defined as $S/\sqrt{S+BG}$, to find its maximum, as shown on the right panel of Figure 10.17. The maximum occurs at a BDT score of 0.188, where 0 background events remain, with 0.88 signal events. Since the number of signals is less than one, this point is discarded.

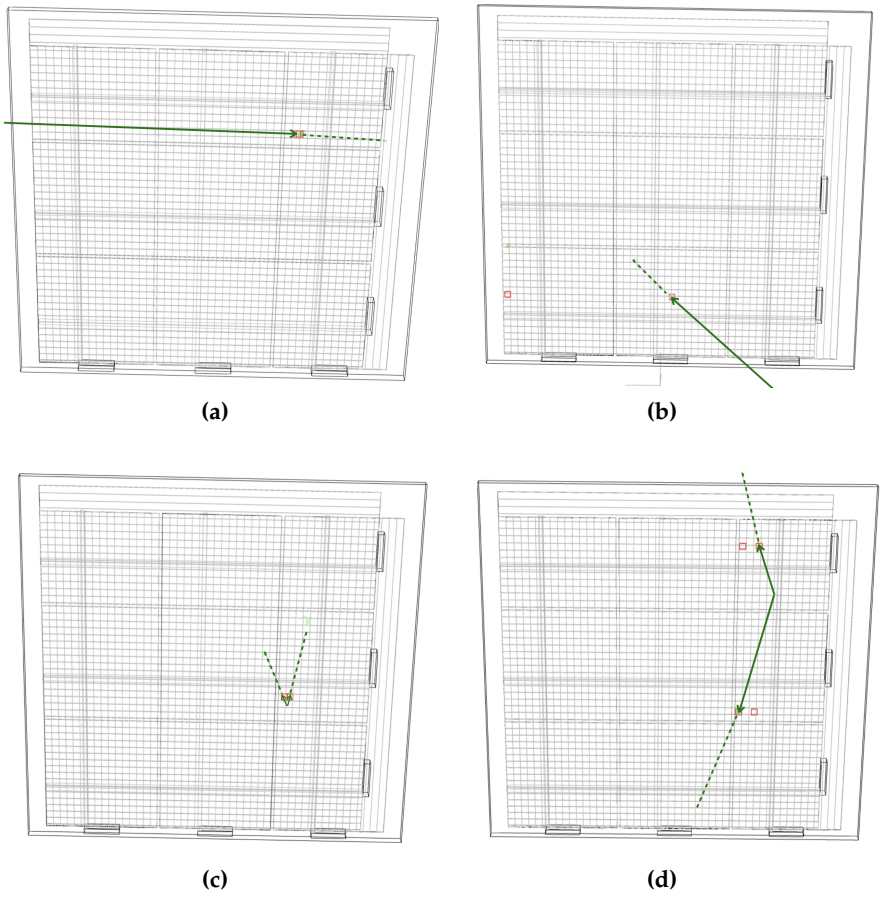


**Figure 10.15** Event Displays of Signal Events in the Overlapping Region of BDT Distributions: (a) An electron/positron intersecting two CRT vertical strips, resulting in two reconstructed hits. (b) An electron/position propagating through the CRT panel with a secondary Compton photon triggering only a vertical strip, leading to two reconstructed hits. (c) Electron and positron propagating through the CRT panel, only two closely spaced hits are reconstructed due to the angle and the vertex. (d) An electron-positron pair with a large opening angle propagating through the CRT panel at big intersection angles.

The second maximum, at a BDT score of 0.062, gives a significance of 0.822 and is used for selection. After this selection, approximately 16.86 signal events and 404 background events remain. For reference, in the box selection, only 17 signal events were left after applying the four-hit selection. However, the background was reduced from 1,572 events to 404, representing a significant improvement.

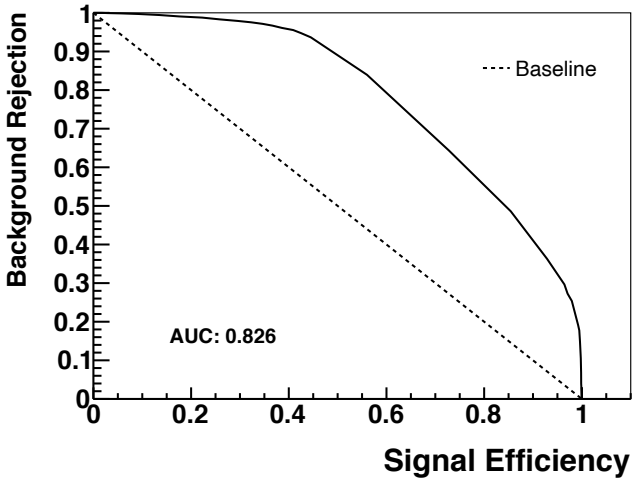


**Figure 10.16** The ROC curve for the BDT classifier. The baseline is drawn in a dashed line.

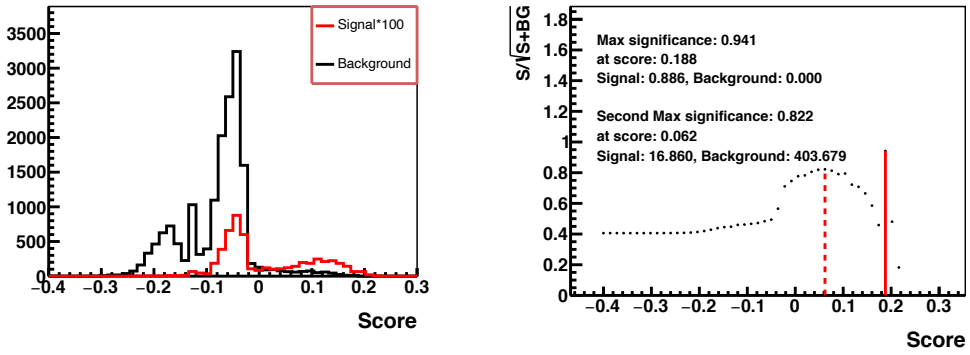


**Figure 10.17** Left: the distribution of the BDT score, with both signal and background normalised to 2.95 $\times 10^{20}$ POT. Right: the modified significance $S/\sqrt{S+BG}$ as a function of the BDT score.

## 10.5 Signal-like Background Events

Around 400 background events remain after the selections. The neutrino interaction types that produce these signal-like background events are investigated, as shown in Figure 10.18. The majority of signal-like background events are generated from RES and DIS interactions, with smaller contributions from QE, COH, and MEC.

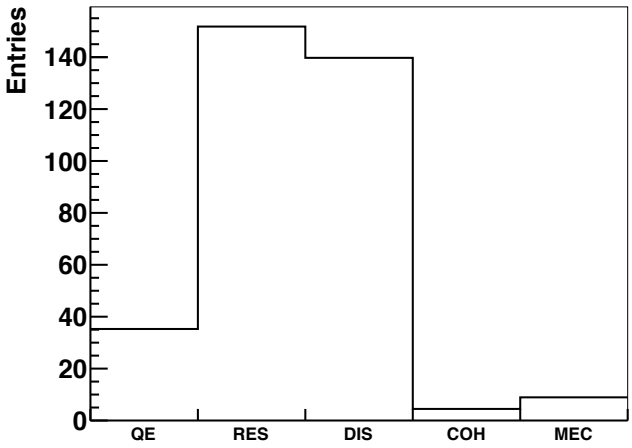


**Figure 10.18** Interaction type of the signal-like background events after selection.

**QE and MEC** Signal-like background events are introduced by leptons, predominantly muons, though electrons are also possible, produced by neutrino interactions in the surrounding concrete. For a muon, as it propagates through the concrete, a secondary particle, typically an electron, can be produced via muon ionisation or decay near the surface. This secondary electron may either escape the concrete directly and interact with the downstream panel or undergo a series of electromagnetic interactions. In the latter case, the electron generally first emits a photon via Bremsstrahlung. The photon can then produce an electron-positron pair through pair production in the concrete, air, or upon contact with the CRT panel. One of these electrons deposits energy and creates a CRT hit, while the other escapes. In the case of an electron as the primary lepton, signal-like background events can be caused either by the primary electron and its secondary particles or by the secondary particles generated through electromagnetic interactions of the electron.

**RES, DIS, and COH** The same causes observed for QE and MEC interactions can also occur in RES, DIS, and COH interactions. In addition, pion production in these processes leads to an increased number of signal-like background events. A significant source of background is the decay of a $\pi^0$ particle into a photon, which then undergoes electromagnetic interactions, eventually leading to the detection of electron-positron pairs by the CRT through pair production. In another scenario, both a primary muon and a primary pion can hit the downstream panel, generating signal-like events. Although secondary particles produced by these muon and pion interactions are more likely to be detected by the CRT. It has also been observed that a muon and a proton with momentum above 1 GeV, where the proton behaves as a MIP, can also be misclassified as signal events.

In summary, combining all neutrino interactions, the majority of signal-like background events are caused by secondary particles produced by the primary lepton or pion as they propagate towards the CRT.

## 10.6 Uncertainties on the Background

The uncertainties can be categorised into **statistical** and **systematic uncertainties**. Statistical uncertainty depends on the number of measurements. For a binned histogram, the statistical uncertainty per bin is calculated as the Poisson error, given by $\sqrt{N}$, where $N$ is the number of entries in the bin.

For systematic uncertainties, the approach depends on the impact of the uncertainty. Some are related to the overall rate of the sample and are thus trivially assumed to follow a flat distribution across a binned histogram. For other types of systematic uncertainties, the **multisim** technique is employed for calculation.

The **multisim** technique, like the **unisim** technique introduced in Section 6.8, is an alternative approach for estimating systematic uncertainties, particularly when the uncertainties depend on multiple parameters. Similar to the unisim method, a central value (CV) sample is first produced with all parameters set to their nominal values. Then, all parameters are randomly sampled based on their uncertainties, with these newly sampled parameters referred to as a **universe**. This parameter-sampling process is typically repeated multiple times, generating multiple universes, hence the method is called the multisim technique.

Subsequently, histograms are generated for both the CV universe and all sampled universes. The histograms from the sampled universes reflect the variations due to

the modified parameters. The covariance matrix between the bins can be defined as:

$$E_{ij} = \frac{1}{N}\sum_{s=0}^{N}(x_i^s - x_i^{CV})(x_j^s - x_j^{CV}), \tag{10.3}$$

where $i$ and $j$ are bin indices, $x_i^{CV}$ is the entry for bin $i$ in the CV universe, $x_i^s$ is the entry for bin $i$ in universe $s$, and $N$ is the total number of sampled universes. The uncertainty is $\sigma_i = \sqrt{E_{ii}}$ for the $i_{th}$ bin.

Generating samples from all universes can be computationally heavy. Therefore, alternative approaches have been developed to mitigate this problem. For systematics related to flux, neutrino modelling, and reinteraction modelling in SBN experiments, the multisim approach is implemented using re-weighting tools, which provide $N$ weights per event in the CV sample for $N$ universes. As of the time of writing this thesis, this tool has not been fully implemented in SBND; however, an attempt [253] was made to estimate these systematic uncertainties, and it will be used for this analysis for the time being. For systematics related to reconstruction effects, an alternative approach involves manually smearing the selection handles by their uncertainties $N$ times and re-simulating the sample to generate $N$ universes.

The following sections will describe the sources of different systematics and the calculation of uncertainty from each source. Since the signal is predominantly affected by statistical uncertainties, the systematic uncertainties are calculated only for the background samples.

### 10.6.1 Neutrino Flux

Neutrino flux uncertainties can be grouped into three main categories. The first arises from uncertainties in modelling hadron production ($\pi, K$), resulting from proton collisions with the Beryllium target. Once produced, these hadrons can further interact with the target or the focusing horn, adding additional modelling uncertainties. The final source comes from uncertainties in the current applied to the beam's focusing horn, which further affects the accuracy of the flux simulation.

As described in Section 4.2, the flux simulation was developed by the MiniBooNE experiment and is used by SBN experiments. This simulation incorporates all relevant uncertainties and provides a tool to reweight the flux prediction using 13 parameters [170]. Systematic uncertainties related to the flux can be estimated by using this reweighting tool to generate multiple universes. Previous results indicate that the flux uncertainty is approximately 13% [253], and this value is applied for this analysis. A more precise calculation of the neutrino flux uncertainties will be performed in the future.

### 10.6.2 Neutrino Model

As described in Section 5.2.3, the GENIE generator is used to model neutrino interactions. Various models are implemented within GENIE to simulate these interactions, and each model its own set of parameters with associated uncertainties. These uncertainties can introduce systematic errors into the analysis. The systematic uncertainty in the model predictions can be estimated using the multisim method, with reweightable parameters provided by the GENIE software [204]. An estimation of the systematic uncertainty due to neutrino interactions is approximately 13% [253]. The dedicated calculation of systematic uncertainties related to the neutrino model is planned as part of future work.

### 10.6.3 Reinteraction Model

Primary particles produced by neutrino interactions propagate through various media, such as concrete, air, or polystyrene. During propagation, these primary particles can potentially re-interact with the surrounding medium. These reinteractions are simulated using the GEANT 4 toolkit, as described in Section 5.3.1. The `Geant4Reweight` tool [254] was developed to use the multisim approach to estimate the systematic uncertainties associated with these reinteractions.

Previous results from studies with argon suggest that these uncertainties are on the order of 1% [253]. For this analysis, reinteraction uncertainties are expected to be more significant, as the CRT primarily detects secondary particles produced by these reinteractions. Therefore, the systematic uncertainties are estimated to be 5% for the time being and a dedicated production is planned to calculate these more precisely.

### 10.6.4 Reconstruction Effects

The BDT variables (selection handles) rely on reconstruction information, where each reconstruction has a resolution compared to the true values. The resolution can introduce a source of systematic uncertainty. In Section 9.2.2 and Section 9.3, the resolutions for **position, time**, and **deposited energy** reconstruction are presented. To estimate the systematic uncertainties regarding each handle, the multisim technique is applied. Since no specific tool has been developed for handling reconstruction effects, the multisim approach is implemented by smearing each handle with an offset generated by a Gaussian random generator based on the associated resolution to create the universes. For each universe, the offsets for each handle are fixed at the same values. A workflow has been developed specifically to automate the generation of the universes. For all three handles, 100 universes are generated for the systematics uncertainty calculation.

Figures 10.19, 10.20, and 10.21 display the BDT distributions for the generated universes compared to the CV-universe, after smearing the position, time, and deposited energy handles, respectively. Among these handles, deposited energy introduces the largest systematic uncertainties, which is expected given that the energy resolution is around 25%. The contributions from position and time systematics are approximately 5% and 15%, respectively. Although the last two bins show slightly higher uncertainty, they are primarily dominated by statistical fluctuations of these universe samples.

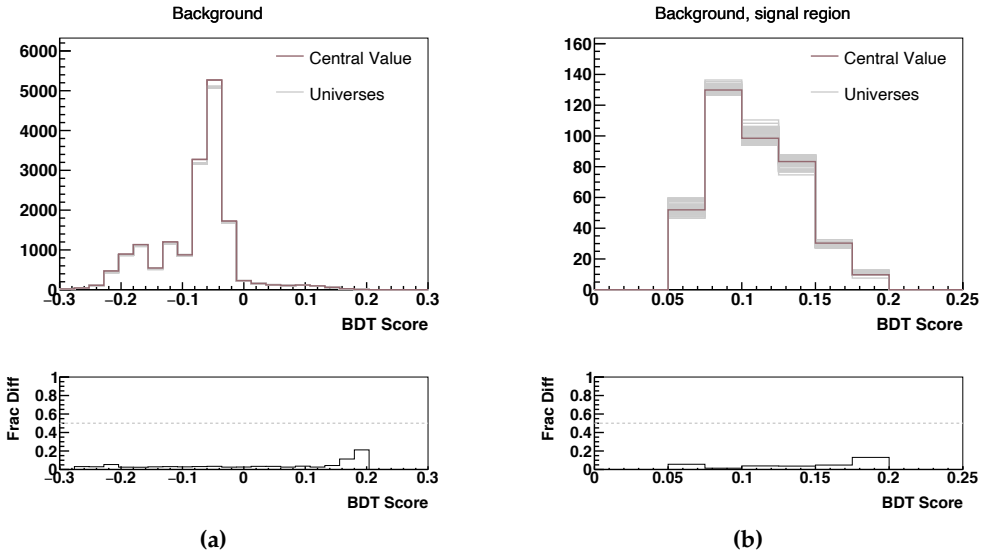


**Figure 10.19** Distribution of the BDT score for the various position-smeared universes compared to the CV for (a) all events and (b) a zoomed-in view of the signal region.

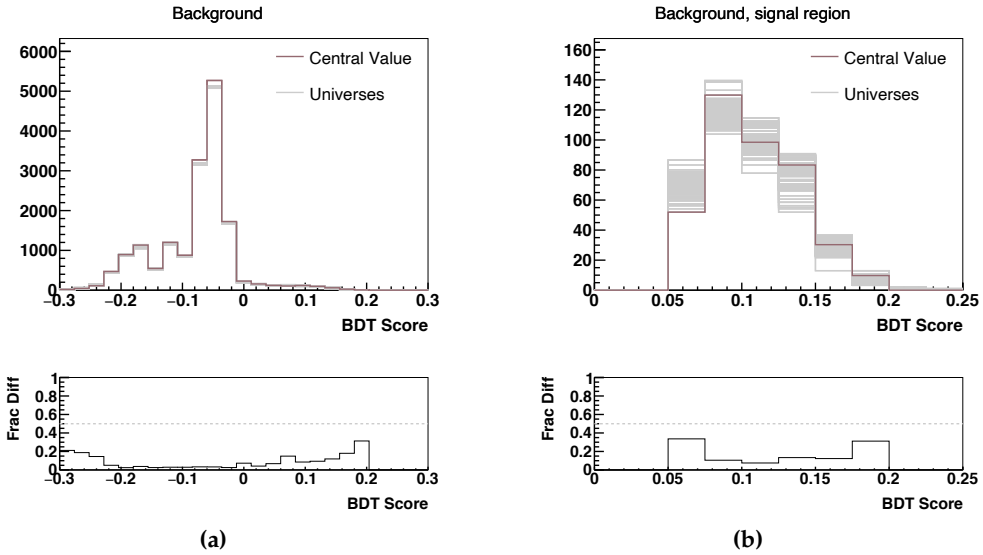


**Figure 10.20** Distribution of the BDT score for the various time-smeared universes compared to the CV for (a) all events and (b) a zoomed-in view of the signal region.

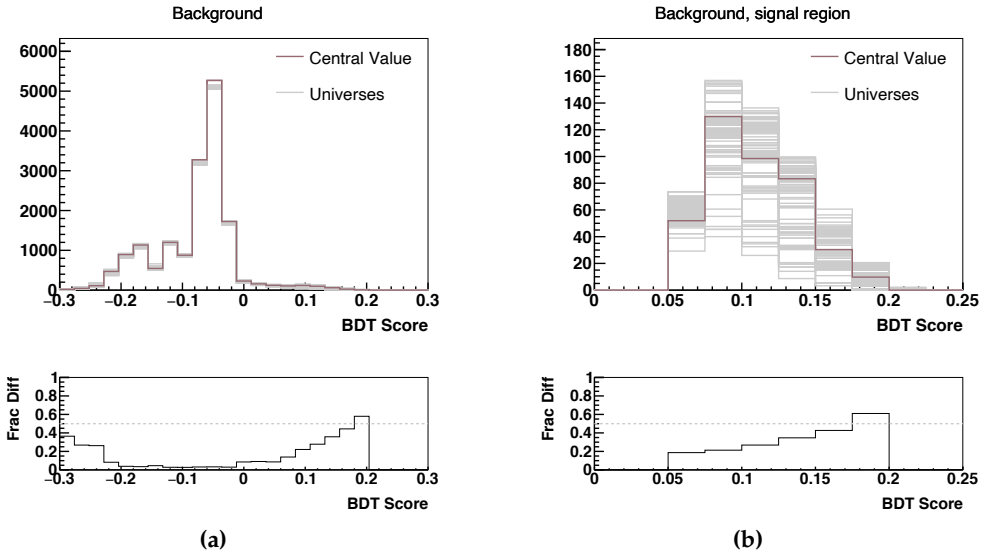


**Figure 10.21** Distribution of the BDT score for the various deposited-energy-smeared universes compared to the CV for (a) all events and (b) a zoomed-in view of the signal region.

### 10.6.5 POT Counting

The number of Protons on Target (POT) determines the number of events. The rate of protons arriving upstream of the target is measured by a toroid monitor, which is capable of measuring POT with an accuracy of 2% [255]. For this analysis, a flat distribution with a 2% uncertainty is assumed for POT counting.

### 10.6.6 Contributions summary

Figure 10.22 shows the total combined uncertainties on the background BDT score in the left panel, along with a zoomed-in view of the signal region on the right. The combined uncertainty is approximately 40%, with deposited energy reconstruction effects being the dominant source. This large systematic uncertainty highlights the need for a more thorough understanding of each contributing source. In future work, dedicated calculations of systematic uncertainties related to flux, the neutrino model, and the reinteraction model for this experimental configuration will be performed. Once these are determined, a covariance matrix will be constructed to further constrain and reduce the overall uncertainty.

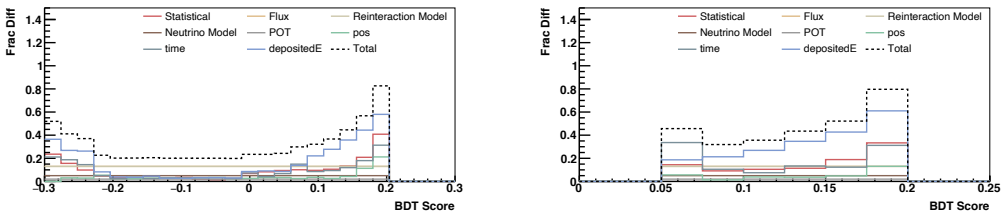


**(a)** **(b)**

**Figure 10.22** The total fractional uncertainties as a function of the BDT score for (a) all events and (b) a zoomed-in view of the signal region.

## 10.7 Data-MC Agreement

With the combined uncertainties, the simulation samples were further compared to the data. Although no cosmic contribution was identified in the simulation, running the analysis workflow on the data revealed a substantial contribution from the cosmic window, which is defined with the same duration but outside the beam spill. This indicates that cosmic ray interactions are underestimated in the simulation. Understanding the deficiencies in the cosmic simulation will be an important aspect of future work.

For now, the beam spill data are corrected by subtracting the cosmic window data to estimate the dirt neutrino background, which is then compared with the background model, as shown in Figure 10.23. Overall, the results show good agreement between the MC and data in the lowest BDT scores, but excesses are observed in some bins at higher scores. These discrepancies will require further investigations.

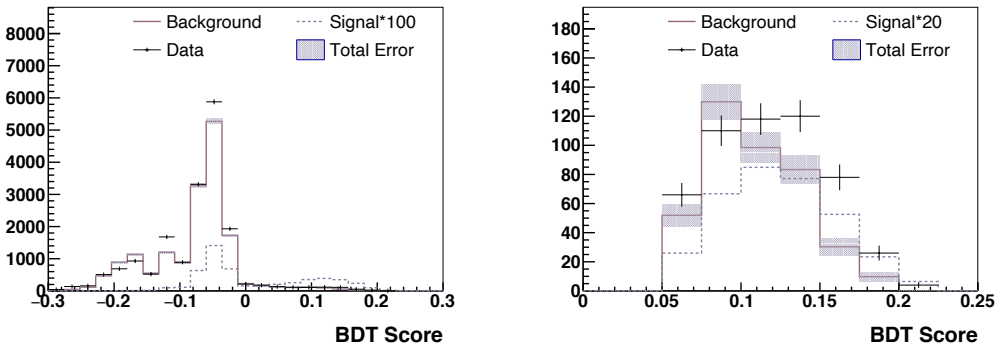


(a) (b)

**Figure 10.23** The BDT score from the MC compared with data, with combined statistical and systematic uncertainties shown for both (a) all events and (b) a zoomed-in view of the signal region.

## 10.8 Summary and Future Work

In this chapter, a search for long-lived dark neutrinos and an extended model-independent search was performed using the CRT Beam Telescope detector. The dark neutrinos are produced via SM neutrino upscattering, propagate, and decay into lepton pairs. Depending on where the decay occurs, dark neutrinos can be classified as long-lived or short-lived. This chapter focused on the long-lived dark neutrino search, where the decay occurs between the two panels, with the considered lepton pair being $e^-e^+$.

This analysis employs a novel detector setup, and significant work has been done by the author to enable a proper analysis. A "box-cut" selection was initially developed to understand the SM neutrino background in the context of CRT, air, and concrete. Due to the limited selection handles available, the BDT method was applied to maximise selection efficiency. The BDT significantly improved the significance; however, since the dark neutrino signal is produced via SM neutrino interactions and the Beam Telescope detector is positioned too low relative to the neutrino beam centre, many events were lost during minimal selections.

There is still work required to finalise this analysis. As mentioned in the chapter, part of the systematic uncertainties have derived from a previous attempt, and a thorough calculation of these uncertainties is needed for the final limit exclusion plot using data. Additionally, further investigation is necessary to fully understand the data-MC agreement.

# 11

# Model-Independent Searches with the SBND CRT Beam Telescope

The analysis of the baseline long-lived dark neutrino model presented in the previous chapter has shown that after applying the selection cuts insufficient signal events would remain compared with the background. This means that the detector may be sensitive to models where the coupling is higher resulting in a larger signal production rate. However, this is non-trivial for dark neutrino models because the coupling constant also affects the lifetime of the dark neutrino, significantly altering the decay location.

Meanwhile, the dark neutrino model produces an electron-positron pair signature in the detector, a signature that could also be generated by other BSM particles, such as HNLs and dark photons, suggesting a model-independent approach could be feasible. The results from the dark neutrino model can be projected onto a model-independent search using the framework introduced in Section 2.5. This approach considers a generic long-lived BSM particle, providing more flexibility in adjusting the BSM-SM coupling and therefore the expected event rate.

This chapter will describe the method used to expand the dark neutrino results into a model-independent long-lived particle search, including the calculations of scaling factors for different lifetimes with statistical tests, and the principles of these tests will be explained. Additionally, the sensitivity of the Beam Telescope was determined for different lifetimes, and these results will be discussed. This search was performed in collaboration with phenomenologists K. J. Kelly (Texas A&M University) and P. A. N. Machado (FNAL).

## 11.1 Principle of Statistic Method Used

The end-to-end scaling factor calculation is performed using the `pyhf` package [256, 257], which implements likelihood-based hypothesis testing [258]. Hypothesis testing is a statistical method that assesses the consistency between the observed data and the expected background distribution, combined with the signal distribution with a scaling factor. In this method, the test statistic distribution is constructed using likelihood functions that represent probability distributions for different hypotheses under varying parameters. By scanning through different scaling factors and calculating the confidence level (CL) using the $CL_s$ method [259, 260], the scaling factor that satisfies the predefined 90% CL can be determined.

### 11.1.1 Hypotheses Definition

The first step in a statistical test is to define the hypotheses. A hypothesis $H$ can be constructed using the signal scaling factor $\mu$, which is an unconstrained parameter typically referred to as the **parameter of interest**. The other parameters in the hypothesis are collectively represented as $\boldsymbol{\theta}$ and are known as **nuisance parameters**.

In a BSM search, two hypotheses are typically involved: one representing the background only and another representing a superposition of background and signal. Following `pyhf` nomenclature, the hypothesis with the superposition of signal and background is referred to as the **null hypothesis**, while the background-only scenario is called the **alternative hypothesis**. This counterintuitive definition and naming is introduced to avoid hypothesis rejection by fluctuations in dominant background samples. In a summary, these hypotheses can be expressed using parameters as:

$$\begin{aligned} \textbf{null hypothesis} &: H_{s+b} = H(\mu = 1, \boldsymbol{\theta}), \\ \textbf{alternative hypothesis} &: H_b = H(\mu = 0, \boldsymbol{\theta}), \end{aligned} \tag{11.1}$$

### 11.1.2 Likelihood-based Test Statistic

Both hypotheses will be tested using a frequentist approach to quantify the level of agreement with the observed data. Since binned BDT score histograms after selections for both signal and background samples are used as input for the statistical test, the **likelihood** function $L(\mu, \boldsymbol{\theta})$ is chosen to form the test statistic. This function represents the probability of observing the data given a hypothesis $H(\mu, \boldsymbol{\theta})$.

To test the null hypothesis, the likelihood for each bin is given by a Poisson distribution:

$$L(\mu) = \frac{e^{-(\mu s+b)}(\mu s + b)^n}{n!}, \tag{11.2}$$

where $s$ and $b$ are the expected numbers of signal and background events for that bin, and $n$ is the number of observed data events. Assuming the entries in each histogram bin are independent, the likelihood for the entire histogram (i.e., for all bins) is the product of the likelihoods for each bin. This can be expressed as [258]:

$$L(\mu, \boldsymbol{\theta}) = \prod_{i=1}^{N} \frac{(\mu s_i + b_i)^{n_i}}{n_i!} e^{-(\mu s_i + b_i)} \prod_{\theta \in \boldsymbol{\theta}} c_\theta(a_\theta \mid \theta), \tag{11.3}$$

where the first product term is the likelihood for $N$ bins, and the second product term represents the contribution from nuisance parameters $\boldsymbol{\theta}$, with a constraint function $c_\theta(a_\theta \mid \theta)$ with the measurement $a_\theta$ constraining each nuisance parameter $\theta$.

For a tested value of $\mu$, the profile likelihood ratio is defined as [258]:

$$\lambda(\mu) = \frac{L(\mu, \hat{\hat{\boldsymbol{\theta}}}(\mu))}{L(\hat{\mu}, \hat{\boldsymbol{\theta}})}, \tag{11.4}$$

where the numerator is the maximised likelihood function for the tested value $\mu$, with $\hat{\hat{\boldsymbol{\theta}}}(\mu)$ being the nuisance parameter values that maximise the likelihood for the given $\mu$. The denominator in Equation 11.4 corresponds to the maximised likelihood function with both $\mu$ and $\boldsymbol{\theta}$ unconstrained, determined by the best fit to the observed data. In this case, $\hat{\mu}$ and $\hat{\boldsymbol{\theta}}$ represent the best-fit values for the signal scaling factor and nuisance parameters, respectively.

The scaling factor $\mu$ can only take non-negative values since the signal process can only increase the number of observed events. If the best fit of the data yields a negative value for $\hat{\mu}$, the denominator in Equation 11.4 is constrained to $\hat{\mu} = 0$. Thus, Equation 11.4 takes the form [258]:

$$\tilde{\lambda}(\mu) = \begin{cases} \frac{L(\mu, \hat{\hat{\boldsymbol{\theta}}}(\mu))}{L(0, \hat{\hat{\boldsymbol{\theta}}}(0))} & \hat{\mu} < 0, \\ \frac{L(\mu, \hat{\hat{\boldsymbol{\theta}}}(\mu))}{L(\hat{\mu}, \hat{\boldsymbol{\theta}})} & \hat{\mu} \geq 0, \end{cases} \tag{11.5}$$

where $\hat{\boldsymbol{\theta}}(0)$ are nuisance parameters when $\hat{\mu} = 0$.

The test statistics can be constructed as [258]:

$$\tilde{q}_\mu = \begin{cases} -2 \ln \tilde{\lambda}(\mu), & \hat{\mu} \leq \mu, \\ 0, & \hat{\mu} > \mu. \end{cases} \tag{11.6}$$

The region where $\hat{\mu} > \mu$ arises from upward fluctuations in the observed data. To account for this, the test statistic $\tilde{q}_\mu$ is set to 0 in such cases.

To test the agreement between the two hypotheses and the observed data, $p$-values are used to quantify the level of agreement. The $p$-values for both hypotheses can be calculated from the probability density function (PDF) of the test statistic, $f(\tilde{q}|\mu')$, where $\mu'$ represent a different strength and $\mu' \neq \mu$. The p-value calculation takes the following form:

$$\begin{aligned} p_{s+b}(\mu', \boldsymbol{\theta}) &= \int_{\tilde{q}_{\mu,\text{obs}}}^{\infty} f(\tilde{q}_\mu \mid \mu') d\tilde{q}_\mu, \\ p_b(0, \boldsymbol{\theta}) &= \int_0^{\tilde{q}_{\mu,\text{obs}}} f(\tilde{q}_\mu \mid 0) d\tilde{q}_\mu. \end{aligned} \tag{11.7}$$

The probability density function (PDF) typically does not have an analytical expression, so alternative methods are necessary to generate the PDF distribution. By default, the `pyhf` package uses **asymptotic approximations**, which assume that $\hat{\mu}$ follows a Gaussian distribution with a mean of $\mu'$ and a standard deviation of $\sigma$. Another common method is known as **toy throwing**, where a large number of pseudo-experiments, or "toys," are generated by randomly sampling the nuisance parameters $\boldsymbol{\theta}$ within their allowed constraints. Each toy produces a possible value of $\tilde{q}(\mu)$, and a significant number of toys are required to build an accurate distribution.

The toy throwing method is computationally intensive, which is why the asymptotic approximations approach is used by default in `pyhf`. A comparison of these different approaches will be conducted as part of future work.

### 11.1.3 The $CL_s$ Method

The $p$-value under the null hypothesis $H_{s+b}$ can be calculated, and if $p_{s+b} < \alpha$, the null hypothesis can be excluded with a confidence level of $1 - \alpha$. However, if the background is poorly modelled, fluctuations in the background model can lead to false exclusions, potentially resulting in an incorrect rejection of the null hypothesis.

The $CL_s$ method is a modified frequentist approach commonly used in particle physics to set upper limits and calculate discovery significance [259, 260]. It is defined using the $p$-values from the two previously defined hypotheses as follows:

$$CL_s = \frac{CL_{s+b}}{CL_b} = \frac{p_{s+b}}{1 - p_b}. \tag{11.8}$$

Because $1 - p_b$ ranges from 0 to 1, the $CL_s$ value is always greater than $p_{s+b}$. This makes the $CL_s$ method more conservative in quantifying significance compared to the traditional $p$-value approach. A 90% confidence level (CL) means that $CL_s < (1 - 0.9)$, and therefore the number to set for statistical test for $CL_s$ method will be 0.1.

## 11.2 Scaling Factor Calculation

For a given model, `pyhf` scans over a range of $\mu$ values and outputs the value of $\mu$ that is closest to achieving a 90% confidence level (CL). The constraint on the nuisance parameters, $c_\theta(a_\theta \mid \theta)$, is defined by the uncertainties of the histogram. Depending on the type of uncertainties, the constraint can take different forms. Since the systematic uncertainties for this analysis have not been fully calculated, only statistical uncertainty is currently accounted for during testing.

In addition, for the sensitivity calculation, the tested dataset uses simulated background. For future limit exclusion results, the CRT Beam Telescope data will be used. The base model for calculating the scaling factor $\mu$ at 90% CL is the BSM model with a 400 MeV mass. Since the signal obtained from the dark neutrino is very small, and `pyhf` can only scale down by default, an initial scaling factor of 100 was applied before the test. An example is shown in Figure 11.1, where the $CL_s$ quantity is calculated by scanning $\mu$ values up to 0.05. By the intersection with the $CL_s$ line (illustrated in red), the corresponding value of $\mu$ is determined to be 1.9046 after correcting for the pre-scaling factor of 100. In this way, for each tested model, the scaling factor can be calculated and subsequently interpreted to generate the sensitivity plot.

## 11.3 Different Lifetime Assumptions

To map out the sensitivity for the model-independent search in the Beam Telescope detector, the mass of the generic long-lived BSM particle is fixed at 400 MeV, while the particle's lifetime is varied. A new sample with different lifetimes is simulated by reweighting each event using a scaling factor $r$, given by:

$$r = \frac{e^{\frac{-l}{\gamma * \beta * l_{\text{new, unboosted}}}}}{e^{\frac{-l}{\gamma * \beta * l_{\text{old, unboosted}}}}}, \tag{11.9}$$

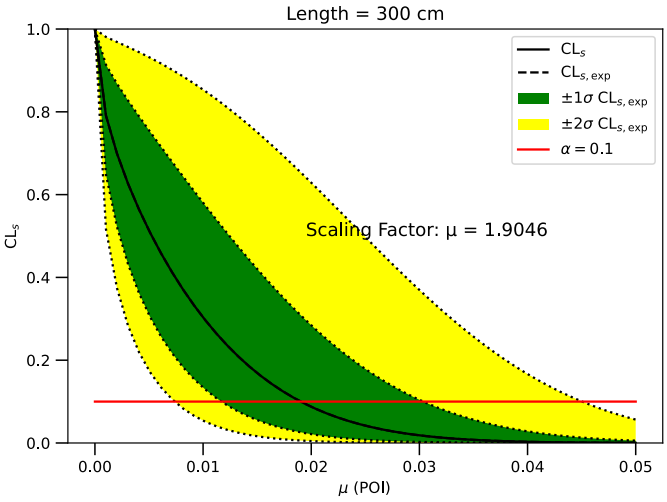


**Figure 11.1** The $CL_s$ value as a function of the signal strength factor $\mu$. The observed and expected $CL_s$ curves overlap, as the background simulation is used as test data. The expected $\pm 1\sigma$ and $\pm 2\sigma$ deviations are shown as green and yellow shaded regions, respectively. The red horizontal line represents the 90% confidence level (CL).

Where $\gamma = E/m$, $\beta = \sqrt{1 - 1/\gamma^2}$, $l$ is the decay length, and $l_{\text{old, unboosted}}$ is the initial un-boosted decay length, set to 306.53 cm. A total of twelve new un-boosted decay lengths were considered to either increase or decrease $l_{\text{old, unboosted}}$. For each considered lifetime, a new Dark neutrino BDT with the same set of variables is trained, with selections made based on the maximum $S/\sqrt{BG}$. The selected region of the BDT distribution is then used as input for the statistical test to calculate the scaling factor. The BDT score distributions, selections, and statistical test results for each considered lifetime are shown in Appendix D.

| Lifetime (unboosted) [cm] | 3.0635 | 30.635 | 50 | 100 | 306.35 | 1000 | 2000 |
|---|---|---|---|---|---|---|---|
| $\mu$ at 90% CL | N/A | 155.9418 | 53.7548 | 11.5847 | 1.9046 | 0.4535 | 0.4035 |
| Lifetime (unboosted) [cm] | 3063.5 | 4000 | 5000 | 7000 | 9000 | 10000 | N/A |
| $\mu$ at 90% CL | 0.4454 | 0.3417 | 0.3870 | 0.3282 | 0.3244 | 0.2647 | N/A |

**Table 11.1** Calculated scaling factor of signal strength $\mu$ for different unboosted lifetimes.

The scaling factors are listed in Table 11.1. The N/A result for the tested unboosted lifetime of 3.0635 cm occurs because the lifetime is too short, resulting in the decay vertex not occurring between the two panels. Consequently, the particle cannot be considered long-lived, causing the BDT designed for long-lived particles to fail.

## 11.4 Sensitivity Results

The model used to calculate the scaling factor assumes a specific scattering cross-section for generation via neutrino upscattering. Scaling up the signal rate corresponds to an increase in this cross-section. Therefore, the sensitivity plot can be represented by mapping the cross-sections, derived from the scaling factor, which represents the product of the production rate of long-lived BSM particles and their decay rate into an $e^-e^+$ pair, as a function of the particle's lifetime. The parameter space explored is fairly general.

Figure 11.2 shows the 90% CL sensitivity in the parameter space for the model-independent search using the SBND CRT Beam Telescope. A conservative exclusion limit from MiniBooNE was estimated by phenomenologists and compared with the CRT Beam Telescope sensitivity. As this is the first exploration of BSM particles in this specific parameter space, we are still determining the best way to compare these results with existing studies, which will be done in collaboration with the phenomenologists involved in this analysis. At this early stage, it appears that there is a region of the phase space excluded by this measurement.

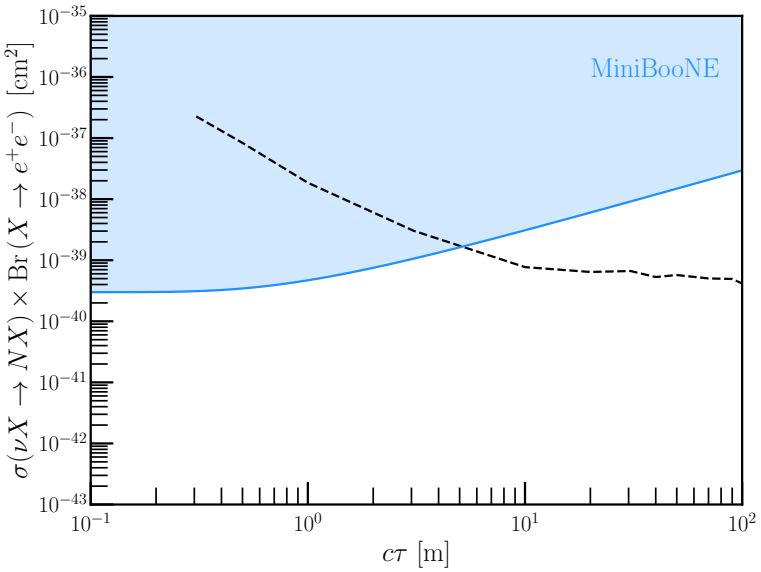


**Figure 11.2** Sensitivity plot for the model-independent search, showing the product of the production rate of long-lived BSM particles and their decay rate into an $e^-e^+$ pair, as a function of the particle's lifetime.

## 11.5 Summary and Future Work

This chapter presented a search for a generic long-lived particle using the SBND CRT Beam Telescope detector. By interpreting the dark neutrino results within a model-independent framework via a common $e^-e^+$ signature, the model-independent search results can be inferred from the dark neutrino analysis. The model-independent approach offers greater flexibility in adjusting the scaling factor, which helps mitigate the problem of having too few signal events for dark neutrinos.

The scaling factor was calculated using statistical tests, and various lifetimes were tested to generate the sensitivity plot for the model-independent search using the CRT Beam Telescope detector setup. The sensitivity plot was presented in this chapter and compared with a conservative MiniBooNE exclusion limit. Since this parameter space is being explored for the first time, we will collaborate with phenomenologists to translate existing results to the parameter space explored in this study as part of future work.

# 12

# Conclusions and Outlook

Modern particle physics detectors are typically complex and comprise various subsystems to enable high-precision particle identification. In the case of a LArTPC detector for neutrino experiments, the design of these detectors has expanded to include three main subsystems: the TPC, the PDS, and the CRT. While the combination of these subsystems maximises particle detection efficiency, each subsystem is intricate enough on its own to explore different aspects of physics. This thesis primarily focuses on the PDS of MicroBooNE and the CRT system of SBND.

Scintillation light is predominantly used for event triggering in LArTPC experiments, but in recent years, it has been recognised that it could have broader applications. Therefore, having a good understanding of light propagation and detection and the accuracy of its simulation is crucial. In Chapter 6, we present a novel method to measure the light yield using point-like isolated protons. This method allows for testing different simulation approaches and evaluating the assumptions used in the simulation. Two different Rayleigh scattering lengths were tested and compared with data, with a preference for a 100 cm Rayleigh scattering length determined using MicroBooNE data, and a hint that the true length might be even longer. This method can also be applied for the calibration of light signals in other experiments, such as SBND.

The CRT system in SBND is designed to tag cosmic ray activity. Chapter 8 details the commissioning work on the characteristics of the SiPM response to a single photoelectron. This process was used to commission the modules prior to installation, and the response data will be stored in a database for future reconstruction efforts.

If one is creative enough, a simple technology like the CRT and a basic setup like the CRT Beam Telescope can be used for intriguing BSM searches. What began as an off-hand idea has since evolved, with significant work needed to make the concept more realistic. In Chapter 9, we described the simulation, reconstruction, and calibration efforts that were developed to lay the groundwork for the BSM search.

Finally, in Chapter 10, the dark neutrino search using the Beam Telescope detector was presented. The journey of conducting this analysis came with many surprises. Neutrinos proved to be surprisingly active, with interactions occurring in concrete, air, and even the CRT panels. Additionally, reinteractions during particle propagation introduced unexpected background events. The detector's relatively low position and the smaller size of the CRT panels contributed to unexpected signal loss. Despite the limited selection handles provided by the CRT, a BDT classifier with improved performance was successfully developed.

However, even with the BDT, the signal remained relatively low compared with the background, and the constraints of the dark neutrino model made it difficult to naively increase the signal rate. As a result, in Chapter 11, the dark neutrino results were re-interpreted in a model-independent search framework, focusing only on the predicted final state without relying on a specific model. The scaling factors for the model-independent search were calculated, and the sensitivity of the CRT Beam Telescope particles' lifetime was established.

To finalise the model-independent BSM analysis, a few missing pieces still need to be addressed. First, the systematic uncertainties related to flux, the neutrino model, and the reinteraction model need to be calculated. Additionally, a thorough understanding of the data-MC agreement is required. Once these elements are in place, a final limit exclusion plot can be generated for the SBND CRT Beam Telescope, which is anticipated to be published.

# Appendix A

# Total Light Yield Map in the $y-z$ Plane with Different $x$ Position

This appendix shows the light yield map in the $y$-$z$ plane at different $x$ positions to examine uniformity. When the drift position is within 100 cm, the light yield changes significantly with location, as shown in Figure A.1. As the position moves further away from the PMTs, the light yield becomes more uniform.

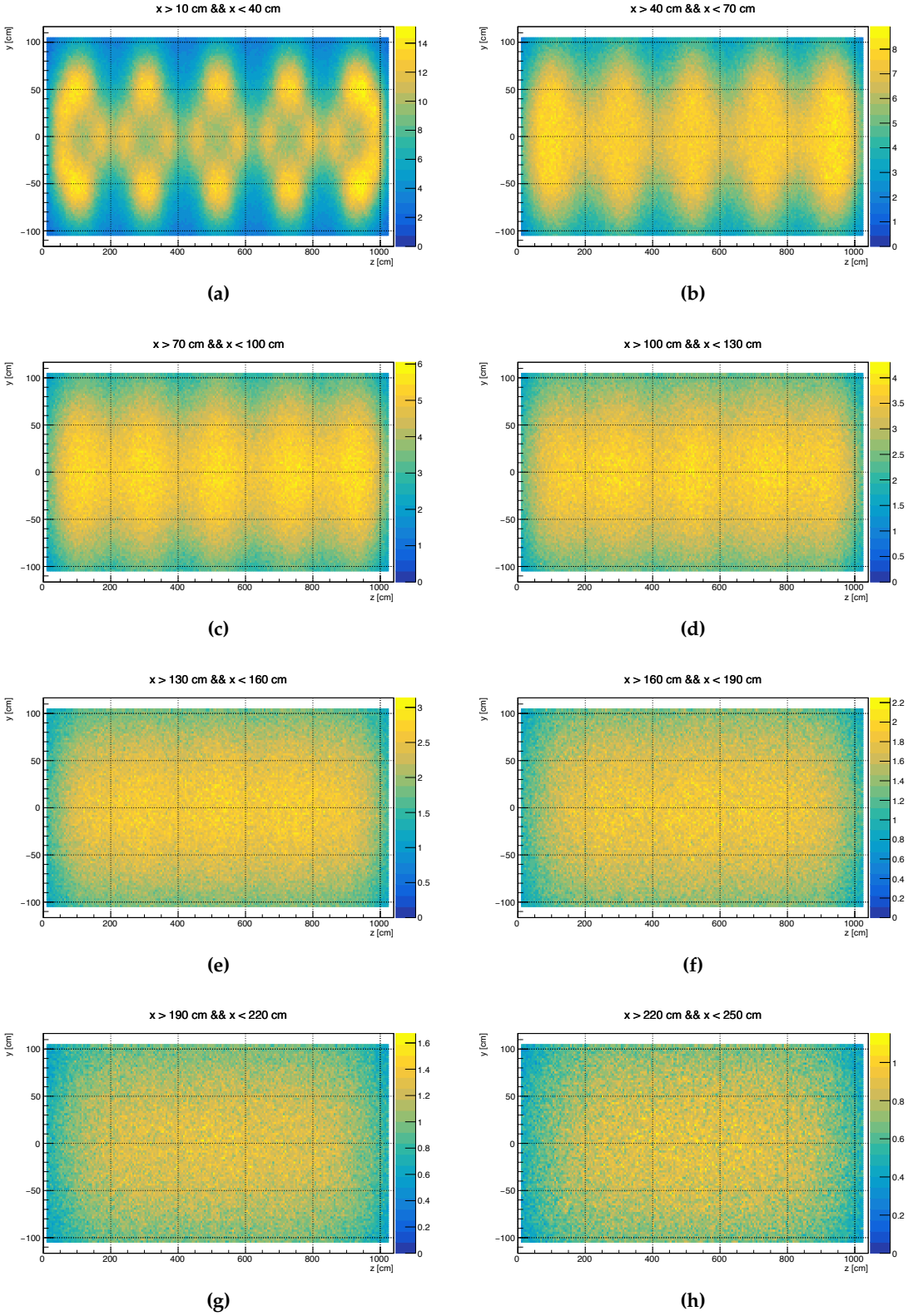


**(a)** **(b)** **(c)** **(d)** **(e)** **(f)** **(g)** **(h)**

**Figure A.1** Light yield map in $y - z$ plane with various drift positions.

# Appendix B

# FEB configurations for Single PE Response Measurement

This appendix details how to set the configuration for CRT channels during data collection. This is achieved by modifying the array on a channel-by-channel basis, as illustrated below:

```
FEBConfiguration_singlePEVoltage140.channel_configuration:
[
    [ 0, 0, 1, 140, 1, 52, 47, 0, 0, 1], # Channel 0
    ...
]
```

Each of 32 lines in the array represents one specific configuration for one channel. There are 10 numbers in each line:

- The $1^{st}$ and $2^{nd}$ numbers are used to tune the threshold for the channel, range from 0 to 15
- The $3^{rd}$ number is used to swap the bias voltage range, either 2.5 V or 4.5 V; 1 means 4.5 V.
- The $4^{th}$ number is used to tune the bias setting of the SiPM, ranging from 0 to 255.
- The $5^{th}$ number is used to enable/disable the channel to fire the trigger. Setting this number to be 0 is to prevent the channel from firing the trigger.

- The $6^{th}$ and $7^{th}$ numbers are the amplifier settings for the high ADC and low ADC region. The $6^{th}$ number is used for increase the amplifier for the single PE response measurement. The interpretation of the values can be found in Figure B.1.

- The $8^{th}$ and $9^{th}$ numbers enable the charge injection for calibration of the amplifiers for the high ADC and low ADC region.

- The $10^{th}$ value is set to 1 to enable the preamp. If the channel is extremely noise, disabling the preamplifier effectively kills it and keeps the noise from spreading to other channels.

| setting | setting in binary | Cfeedback (fF) | gain HG amplifier | gain LG amplifier |
|---|---|---|---|---|
| 63 | 111111 | 0 | 0 | 0 |
| 62 | 111110 | 25 | 60.00 | 600.00 |
| 61 | 111101 | 50 | 30.00 | 300.00 |
| 60 | 111100 | 75 | 20.00 | 200.00 |
| 59 | 111011 | 100 | 15.00 | 150.00 |
| 58 | 111010 | 125 | 12.00 | 120.00 |
| 57 | 111001 | 150 | 10.00 | 100.00 |
| 56 | 111000 | 175 | 8.57 | 85.71 |
| 55 | 110111 | 200 | 7.50 | 75.00 |
| 54 | 110110 | 225 | 6.67 | 66.67 |
| 53 | 110101 | 250 | 6.00 | 60.00 |
| 52 | 110100 | 275 | 5.45 | 54.55 |
| 51 | 110011 | 300 | 5.00 | 50.00 |
| 50 | 110010 | 325 | 4.62 | 46.15 |
| 49 | 110001 | 350 | 4.29 | 42.86 |
| 48 | 110000 | 375 | 4.00 | 40.00 |
| 47 | 101111 | 400 | 3.75 | 37.50 |
| 46 | 101110 | 425 | 3.53 | 35.29 |
| 45 | 101101 | 450 | 3.33 | 33.33 |
| 44 | 101100 | 475 | 3.16 | 31.58 |
| 43 | 101011 | 500 | 3.00 | 30.00 |
| 42 | 101010 | 525 | 2.86 | 28.57 |
| 41 | 101001 | 550 | 2.73 | 27.27 |
| 40 | 101000 | 575 | 2.61 | 26.09 |
| 39 | 100111 | 600 | 2.50 | 25.00 |
| 38 | 100110 | 625 | 2.40 | 24.00 |
| 37 | 100101 | 650 | 2.31 | 23.08 |
| 36 | 100100 | 675 | 2.22 | 22.22 |
| 35 | 100011 | 700 | 2.14 | 21.43 |
| 34 | 100010 | 725 | 2.07 | 20.69 |
| 33 | 100001 | 750 | 2.00 | 20.00 |
| 32 | 100000 | 775 | 1.94 | 19.35 |
| 31 | 11111 | 800 | 1.88 | 18.75 |

**Figure B.1** Interpretation of the gain settings

# Appendix C

# Additional CRT Reconstruction Plots

## C.1 PE Corrections Relative to True Energy Depositions

Figure C.1 shows that when true energy depositions are present behind the reconstructed CRT hits, the corrected PE is uniform across the entire distance to the readout. In contrast, if no real particles are associated with the hits, the uncorrected PE is uniformly distributed. In this case, the corrections lead to over-correction, resulting in a non-uniform distribution across the distance.

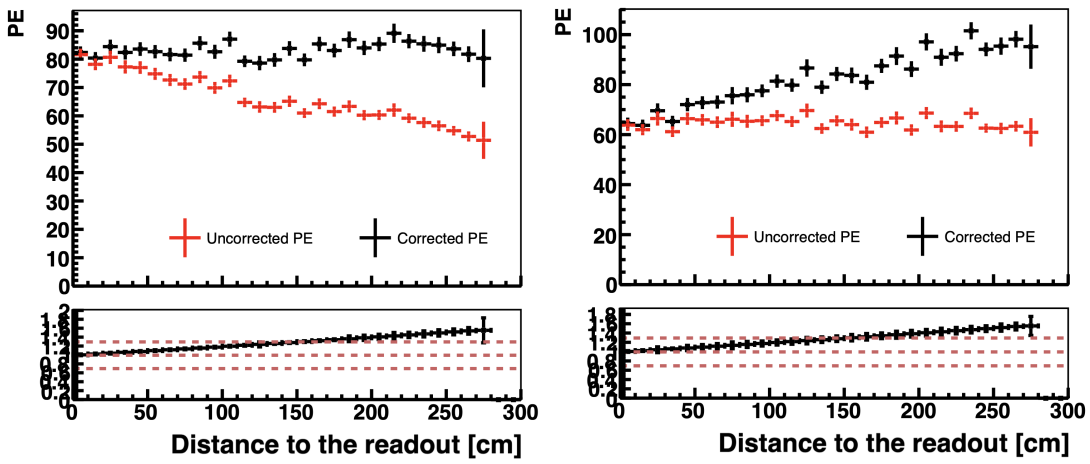


(a) (b)

**Figure C.1** Corrected vs. uncorrected PE for (a) with real hits behind and (b) without real hits behind.

## C.2 Different Physics List Comparison for Upstream CRT panel

Figure C.2 illustrates a comparison of different physics lists used in the GEANT4 simulation for the upstream panel. Figure C.2 (b) shows that the high precision list QGSP_BERT_HP performs better than the others.

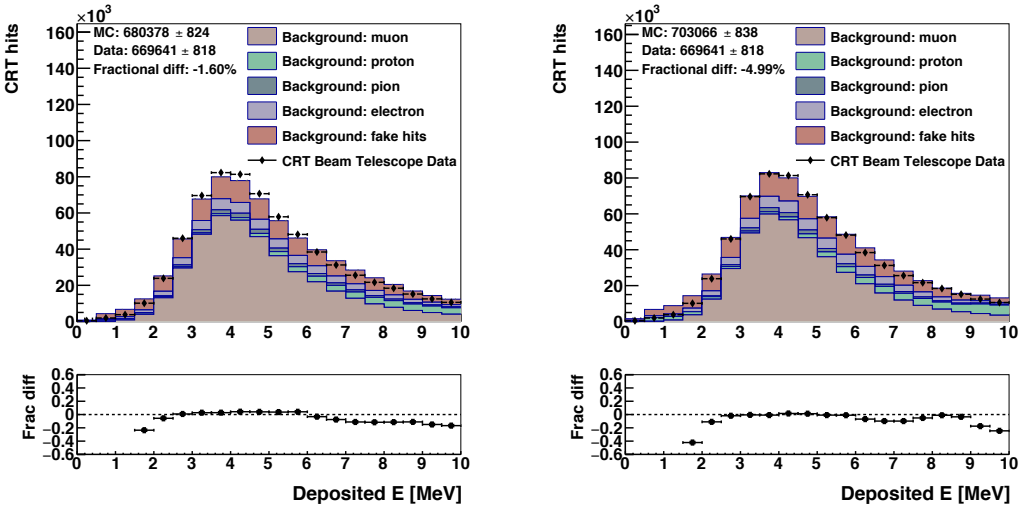


**Figure C.2** Distribution of deposited energy with (a) QGSP_BERT list and (b) QGSP_BERT_HP list in GEANT 4 simulation.

# Appendix D

# Additional Plots for Dark Neutrinos Searches

## D.1 Long-lived Dark Neutrino with Mass of 140 MeV

Figure D.1 shows the procedure for optimizing the selection criteria for the dark neutrino signal, assuming a mass of 140 MeV.

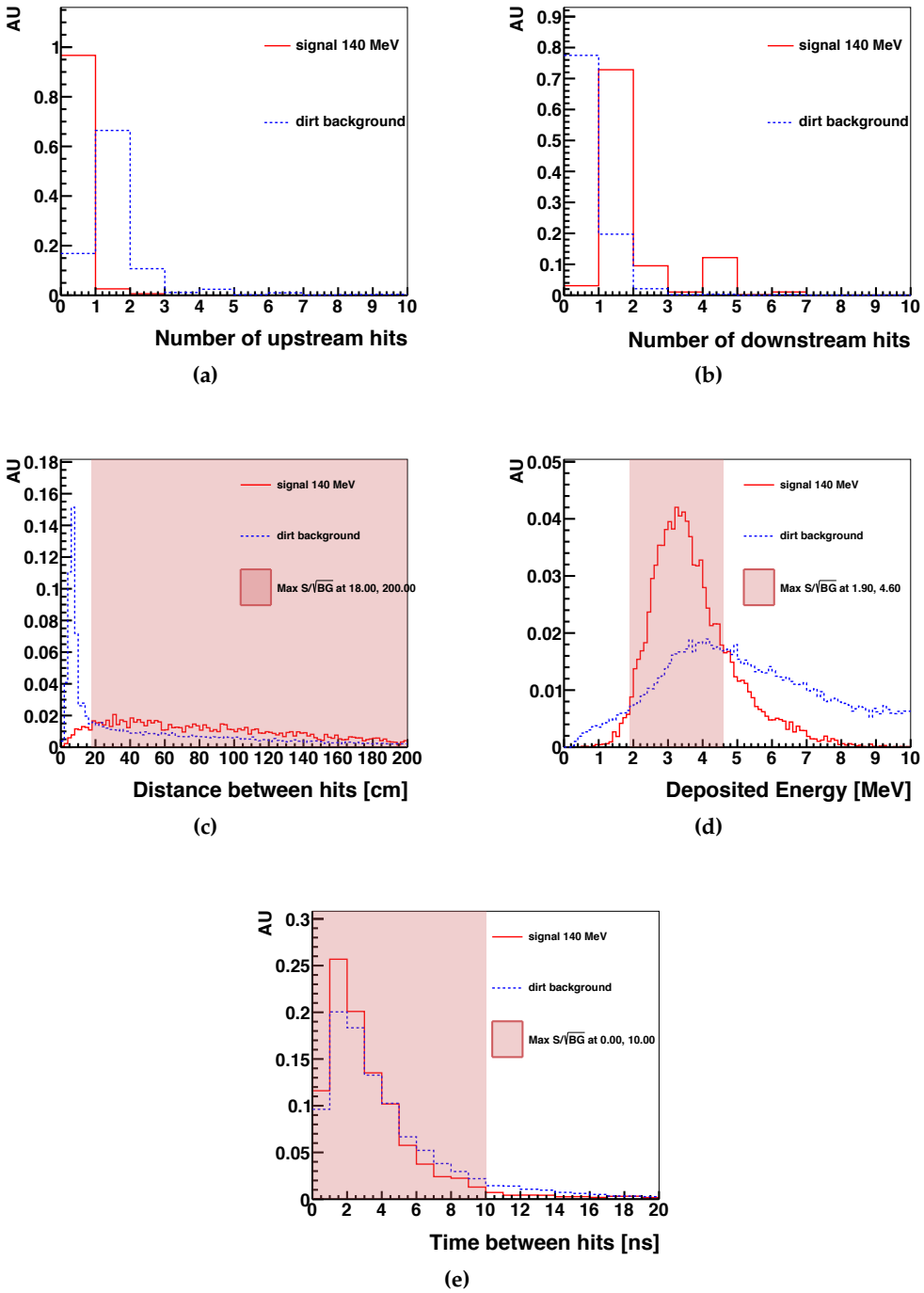


**Figure D.1** Distributions of selections of 140 MeV signal compared with the dirt background.

## D.2 BDT Distribution for Long-lived Model-Independent Searches

Figure D.2- D.5 show the distribution of the trained BDT score for each unboosted decay length assumption. The selections on the BDT score are determined by maximizing $S/\sqrt{BG}$, and the BDT scores for these selections are listed in Table D.1.

| Lifetime (unboosted) [cm] | 3.0635 | 30.635 | 50 | 100 | 306.35 | 1000 | 2000 |
|---|---|---|---|---|---|---|---|
| $\mu$ at 90% CL | N/A | 0.02 | 0.062 | 0.062 | 0.062 | 0.062 | 0.048 |
| Lifetime (unboosted) [cm] | 3063.5 | 4000 | 5000 | 7000 | 9000 | 10000 | |
| $\mu$ at 90% CL | 0.062 | 0.02 | 0.034 | 0.062 | 0.02 | 0.006 | |

**Table D.1** The selection on BDT scores with the maximised $S/\sqrt{BG}$.

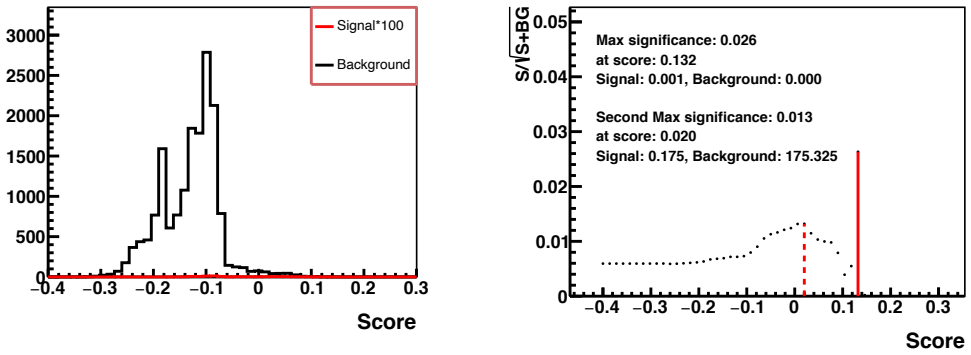


(a)

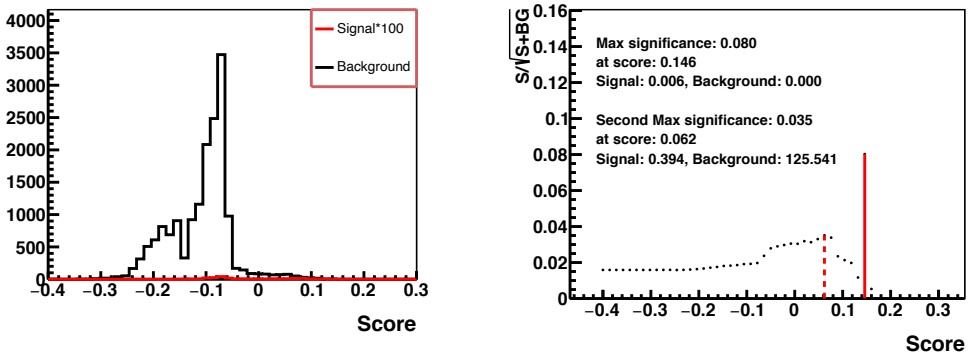


(b)

**Figure D.2** BDT distribution (left columns) and the significance as a function of the BDT score (right columns) for (a) 30.635 cm (b) 50 cm.

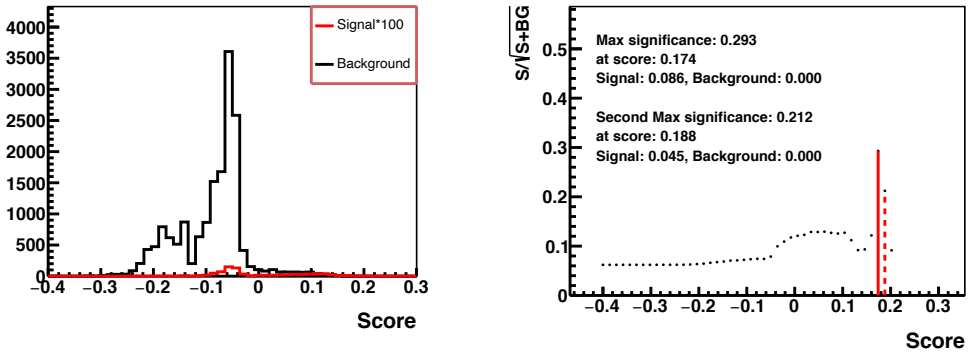


(a)

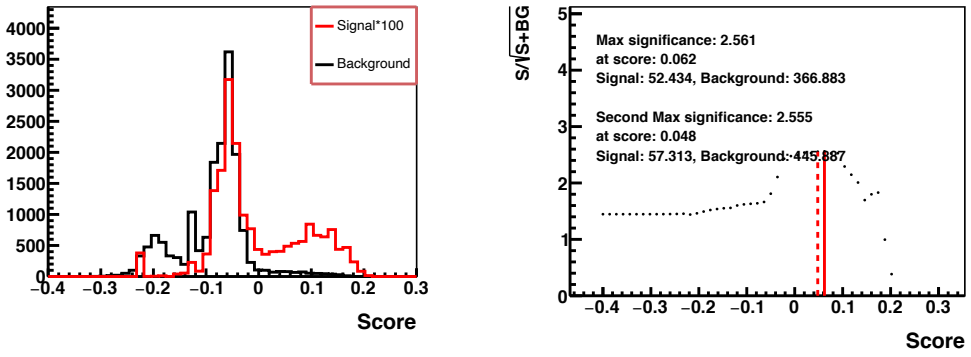


(b)

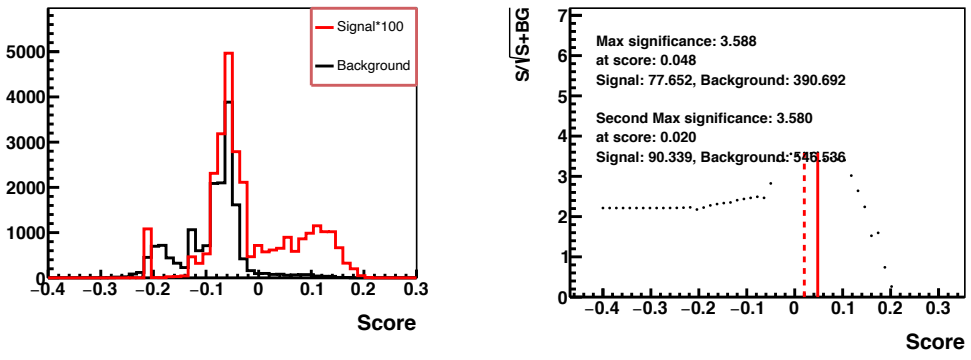


(c)

**Figure D.3** BDT distribution (left columns) and the significance as a function of the BDT score (right columns) for (a) 100 cm (b) 1000 cm and (c) 2000 cm.

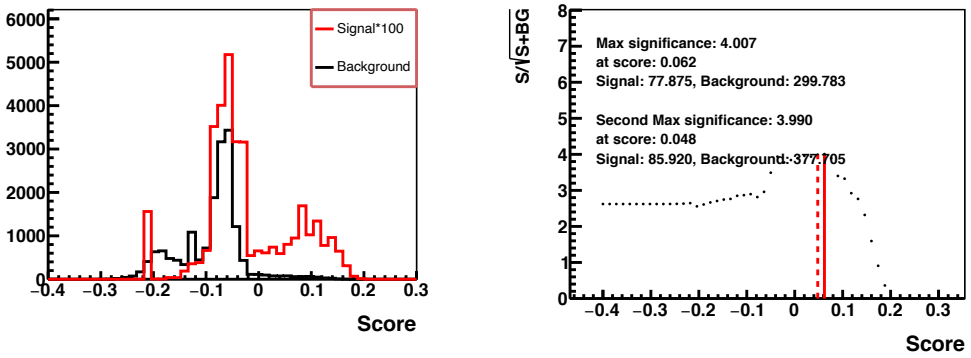


(a)

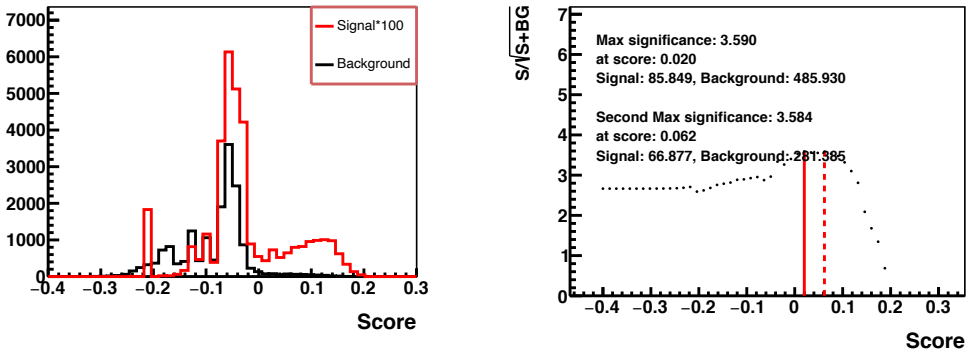


(b)

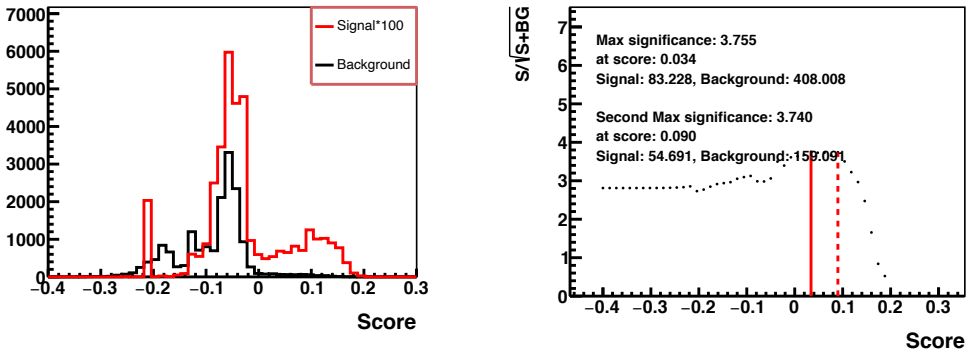


(c)

**Figure D.4** BDT distribution (left columns) and the significance as a function of the BDT score (right columns) for and (a) 3063.5 cm (b) 4000 cm and (c) 5000 cm.

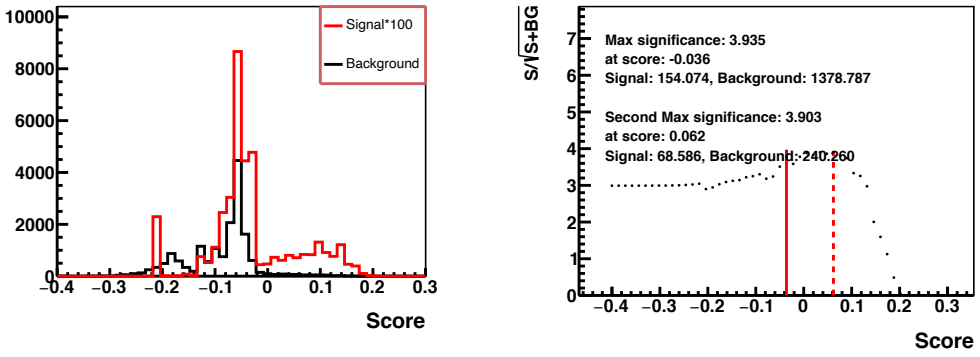


(a)

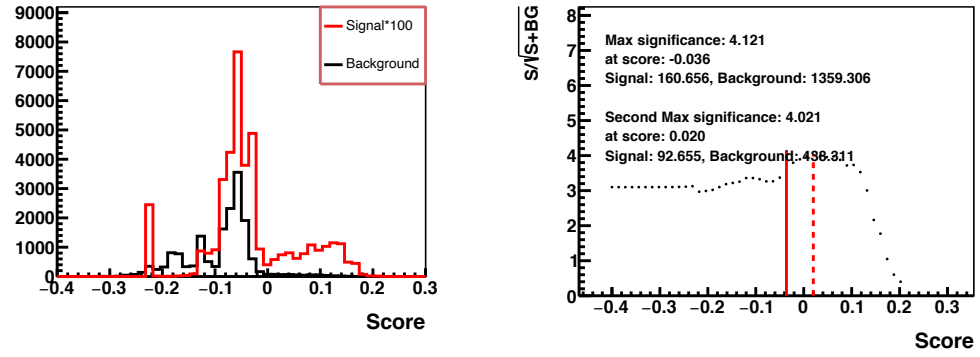


(b)

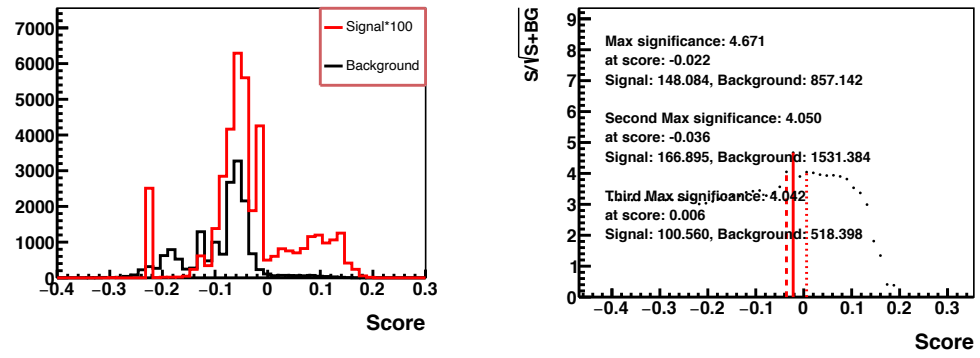


(c)

**Figure D.5** BDT distribution (left columns) and the significance as a function of the BDT score (right columns) for (a) 7000 cm (b) 9000 cm and (c) 10000 cm.

## D.3 Scaling Factor Calculated From Statistical Test

Figure D.6 and D.7 illustrate the signal scaling factor obtained from statistical tests using the `pyhf` package.

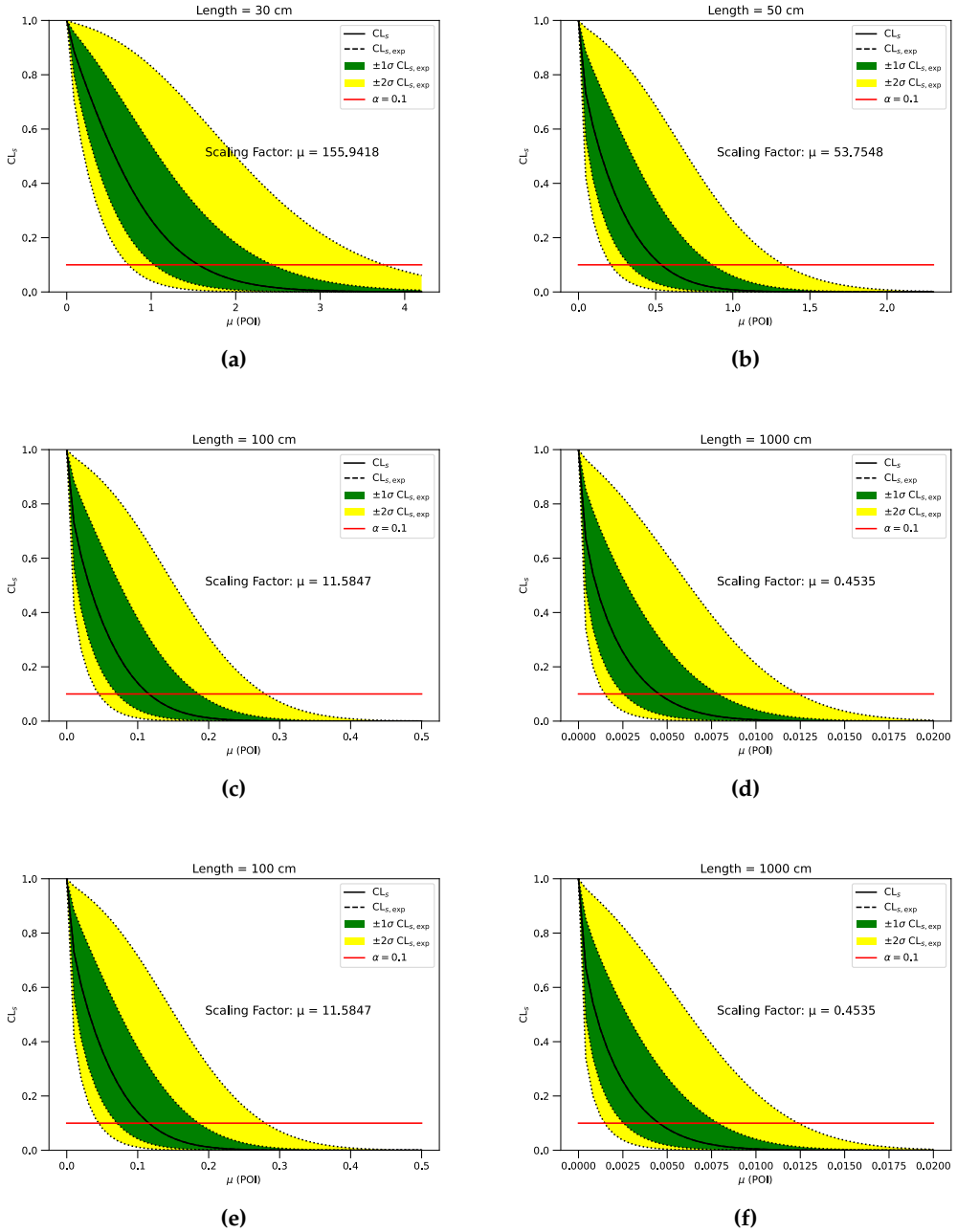


**Figure D.6** The $CL_s$ value as a function of the signal strength factor $\mu$ for different unboosted decay length.å

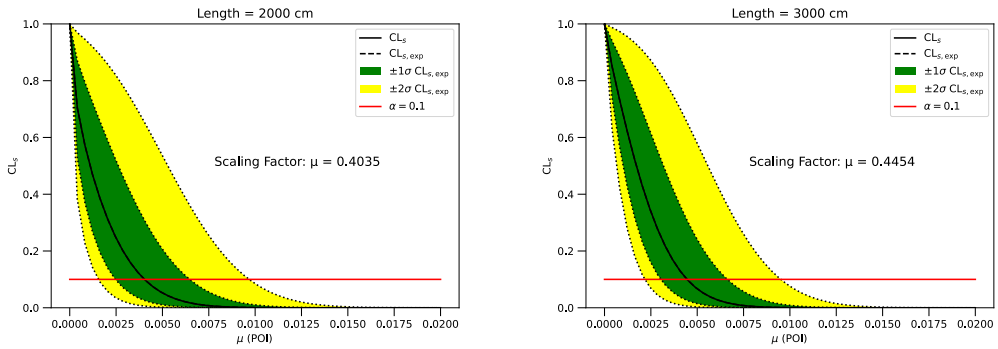


**(a)** **(b)**

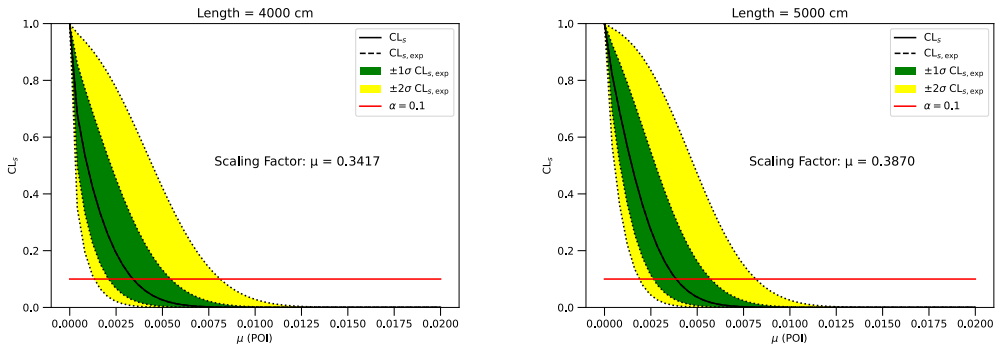


**(c)** **(d)**

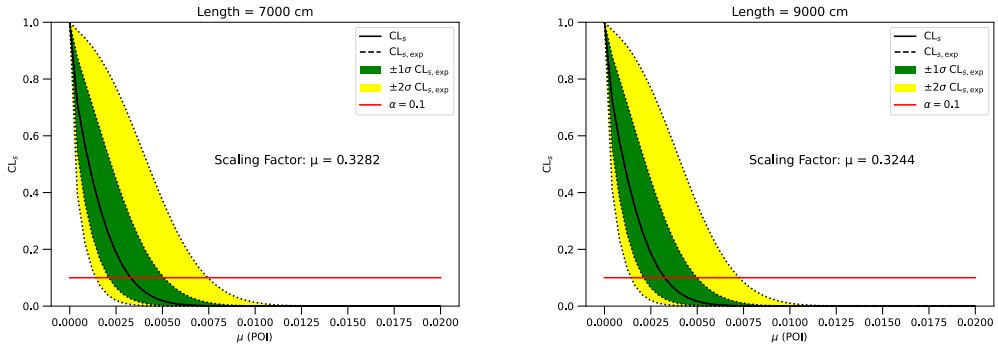


**(e)** **(f)**

**Figure D.7** (Continued) The $CL_s$ value as a function of the signal strength factor $\mu$ for different unboosted decay lengths.

# Appendix E

# Preliminary Results: Short-lived Dark Neutrino in the SBND CRT Beam Telescope

This section presents preliminary results for the short-lived dark neutrino searches in the CRT Beam Telescope detector. Similar to the long-lived dark neutrino case, the signal kinematics will be shown first. At the time of writing, only preliminary box selections have been developed for this scenario. These selections will be refined and finalised in future work.

Table E.1 lists the generated samples of three masses of dark neutrino considered in this analysis.

| $m_{N_D}$ [MeV] | Number of Events |
|---|---|
| 250 | 366.98 |
| 400 | 21384.51 |
| 600 | 9873.41 |

**Table E.1** Details of the dark neutrino MC simulation samples generated for short-lived dark neutrinos are provided. The number of events is not an integer due to the weight applied to each event.

## E.1 Signal Kinematics

The lepton pair for the short-lived dark neutrino search is chosen to be muon pairs. This choice is made because the dark neutrinos decay within the upstream dirt, making it difficult for electrons to escape and propagate through the detector. Three masses are considered: 250 MeV, 400 MeV, and 600 MeV. Figure E.1 illustrates the kinetic energy distributions for muons and anti-muons for these three mass cases. The average kinetic energies are approximately 230 MeV for 250 MeV dark neutrinos, 330 MeV for 400 MeV dark neutrinos, and 500 MeV for 600 MeV dark neutrinos.

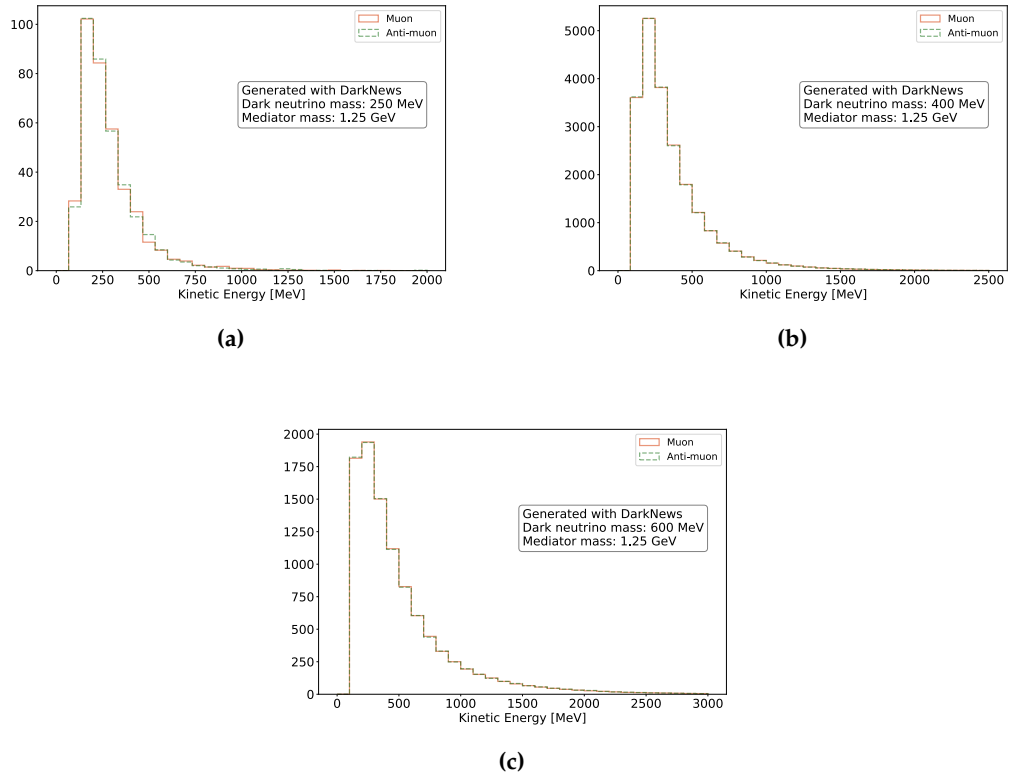


**Figure E.1** The kinetic energy distribution of muons and anti-muons for dark neutrino masses of (a) 250 MeV, (b) 400 MeV and (c) 600 MeV.

The opening angle between muons and anti-muons is shown in Figure E.2 for all three mass cases. Similar to the long-lived dark neutrino scenario, lower masses result in greater boosting of the lepton pairs, leading to smaller opening angles. However, in the short-lived case, the variation in opening angle with mass is more pronounced. The 250 MeV mass is significantly more boosted compared to the other mass assumptions, resulting in much smaller opening angles.

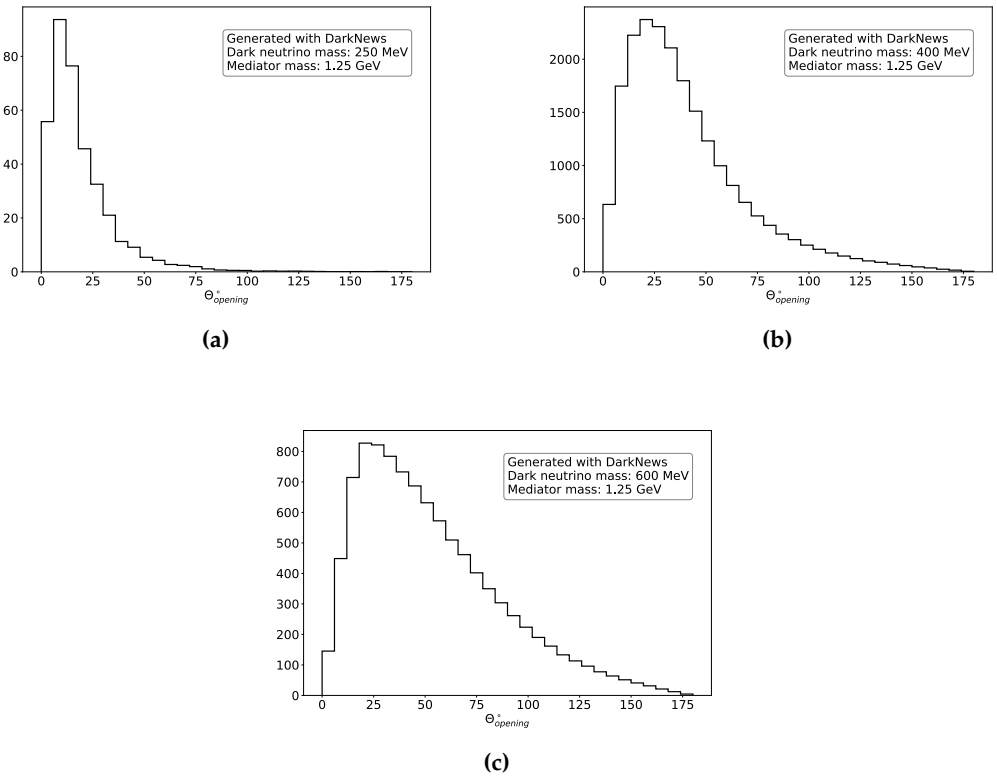


**Figure E.2** Opening angles between muons and anti-muons for dark neutrino masses of (a) 250 MeV, (b) 400 MeV and (c) 600 MeV.

## E.2 Event Selection

This section describes the event selection process designed for the short-lived dark neutrino signal. These selections were developed using the dark neutrino MC sample with a 400 MeV mass, alongside the full neutrino MC (dirt) background.

### E.2.1 Minimal Selections

Similar to the long-lived dark neutrino selections, the first stage involves a set of minimal selections. The initial requirement is that events must interact with either panel during the beam spill. Since short-lived dark neutrinos decay in front of the upstream panel, producing a $\mu^{-}\mu^{+}$ pair, four reconstructed hits are expected in the upstream panel and four in the downstream panel, respectively.

However, the detector setup is positioned below the beam centre, leading to the loss of many events with the minimal selections. Additionally, because the downstream panel is smaller than the upstream panel and the $\mu^-\mu^+$ pair is not highly boosted, many events hit the upstream panel but miss the downstream panel, as shown in Figure E.3.

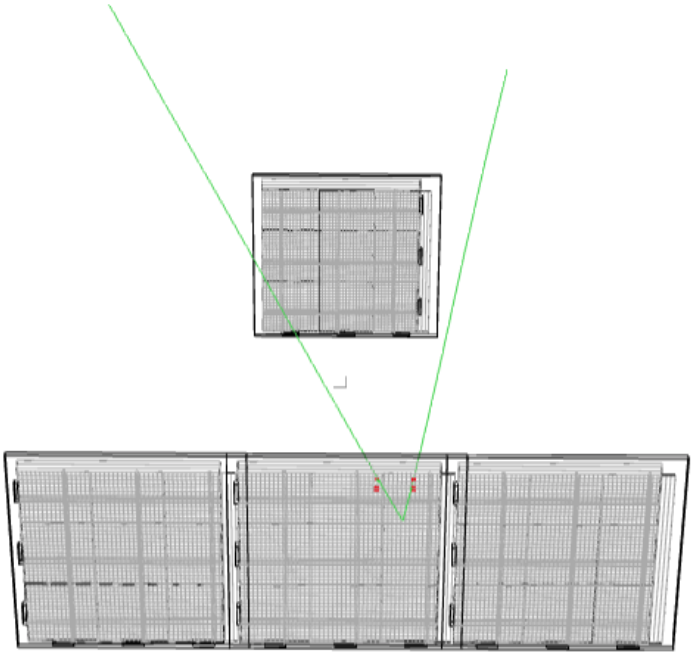

**Figure E.3** An event display illustrates that a signal event hits the upstream panel but not the downstream panel.

### E.2.2 Topological Selection

The topological selection involves two cuts because the produced $\mu^-\mu^+$ pair originates from the same vertex with an opening angle.

#### Area Selection

The first selection simply calculates the area formed by the four hits in the upstream panel and the four hits in the downstream panel. The area in the upstream panel is required to be smaller than that of the downstream panel.

### Similarity Ratio Selection

As shown in Figure E.4 (a), if two particles are produced from the same vertex, the two rectangles formed by the hits on the parallel planes should be similar to each other. Therefore, a similarity ratio $r_{\text{Similarity}}$ is defined as:

$$r_{\text{Similarity}} = \frac{a/a'}{b/b'}, \tag{E.1}$$

where $a$ and $b$ are the width and length of the upstream rectangle, and $a'$ and $b'$ are the width and length of the downstream rectangle.

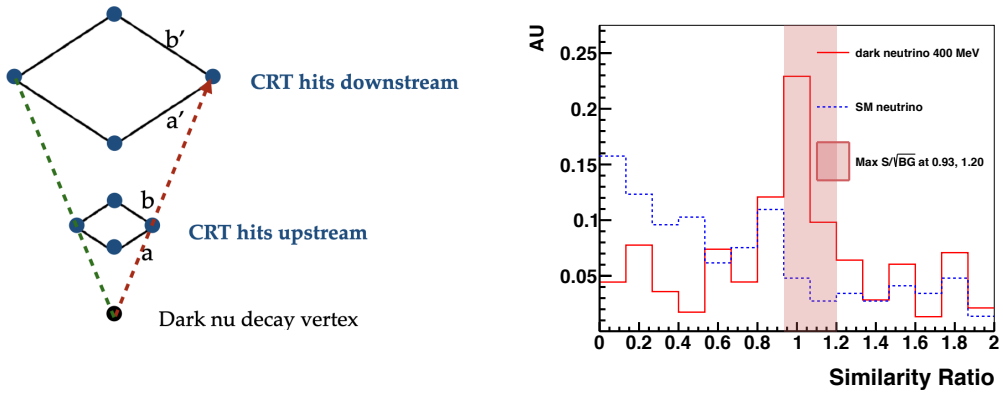


(a) (b)

**Figure E.4** (a) A schematic diagram illustrating a pair of charged particles interacting with two CRT panels parallel to each other, with $a, b$ and $a', b'$ representing the width and length of the rectangles formed in each plane. (b) The distribution of the similarity ratio for both signal and background.

Figure E.4 (b) shows the similarity ratio for both signal and background. The signal peaks around 1 but with significant smearing, while the background is more dominant around 0. Several potential reasons may explain why the similarity ratio distribution for the signal is smeared. First, the position reconstruction resolution is around 1.88 cm, and for candidates passing the minimal selections, the four hits are likely very close to each other, as shown in Figure E.5. Therefore, even a small change in position can have a significant impact on the similarity ratio.

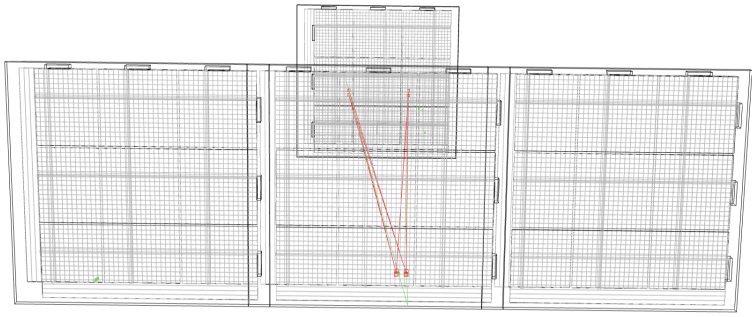

**Figure E.5** An event display of an event with a similarity ratio outside the selection region.

### E.2.3 Time of Flight Selection

The next selection handle involves using time of flight (t.o.f) to further distinguish the signal from the background. Figure E.6 shows the t.o.f distribution for both signal and background. The minimal distance between the upstream and downstream panels is 9.46 m, so for a particle travelling at the speed of light, the t.o.f should be above 32 ns. However, unphysical values are observed in the current calculation. A correction, such as reconstruction unfolding to retrieve the true underlying distribution, will be addressed in future work.

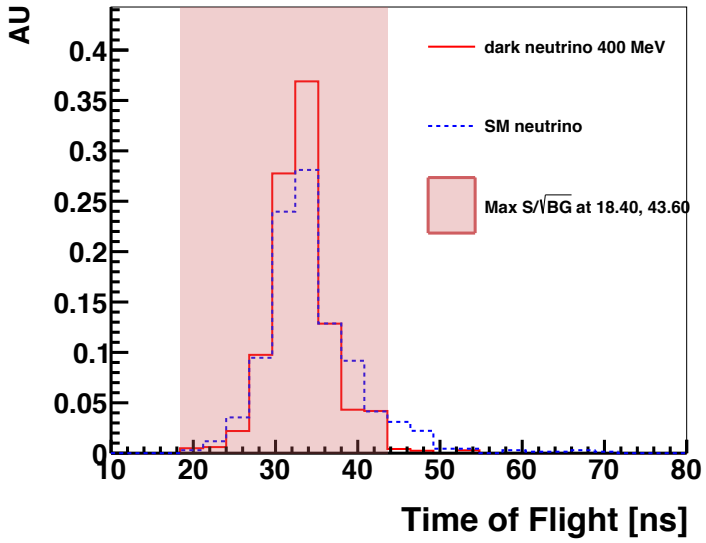


**Figure E.6** Time of flight for dark neutrino signal and background.

### E.2.4 Deposited Energy Selection

Since the dark neutrino decays into a $\mu^-\mu^+$ pair, which are minimum ionizing particles (MIPs), the deposited energy is used for further selection. Figure E.7 shows the distribution of deposited energy for the selected hits in the upstream and downstream panels, respectively. The selection is made based on the maximum significance $S/\sqrt{BG}$.

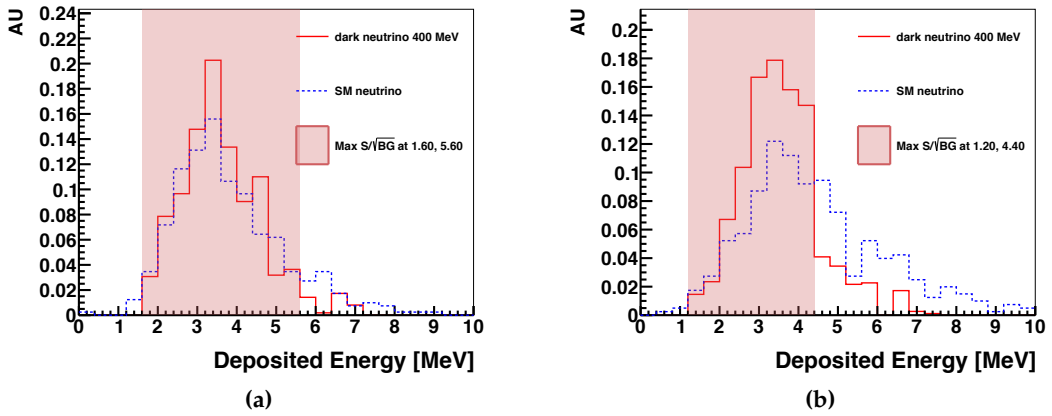


**Figure E.7** The deposited energy for selected hits for (a) upstream and (b) downstream panel.

### E.2.5 Summary of Selection

Table E.2 shows preliminary results illustrating the number of events remaining after each selection stage. While the dark neutrino with 400 MeV appears to be the most promising case, like other masses considered, most signal events are lost during the minimal selections. The similarity ratio proves to be a powerful tool for eliminating the majority of the background, though it also significantly reduces the signal. These selection handles will need to be revisited and improved in future work.

| | Dirt neutrino | Dark neutrino 250MeV | Dark neutrino 400MeV | Dark neutrino 600MeV |
|---|---|---|---|---|
| **Deposited energy in detector within beam spil** | 560273 (100.000 %) | 3.1882 (100.000 %) | 279.396 (100.000 %) | 170.148 (100.000 %) |
| **Four reco hits in the upstream** | 12362.2 (2.206 %) | 0.609198 (19.108 %) | 53.3196 (19.084 %) | 24.0396 (14.129 %) |
| **Four reco hits in the downstream** | 28.7449 (0.005 %) | 0.0174604 (0.548 %) | 1.00728 (0.361 %) | 0.278351 (0.164 %) |
| **upstream hit area < downstream hit area** | 22.805 (0.004 %) | 0.0174604 (0.548 %) | 1.00727 (0.361 %) | 0.264043 (0.155 %) |
| **Similarity Ratio** | 1.27284 (0.000 %) | 0 (0.000 %) | 0.270128 (0.097 %) | 0.0609833 (0.036 %) |
| **t.o.f** | 0.742487 (0.000 %) | 0 (0.000 %) | 0.255113 (0.091 %) | 0.0580964 (0.034 %) |
| **Deposited energy** | 0.10607 (0.000 %) | 0 (0.000 %) | 0.0725392 (0.026 %) | 0.0333992 (0.020 %) |

**Table E.2** Numbers of events at each stage of the event selection for the short-lived dark neutrino case (normalised to 2.95 $\times 10^{20}$ POT).

## E.3 Remaining Background

Even though the cut-flow table suggests that a background-free search could be possible with enhanced signal strength, further examination of the remaining background reveals surviving events involving a muon and a pion, as shown in Figure E.8. These events closely resemble the signal, and without the introduction of additional selection handles, removing them will be challenging.

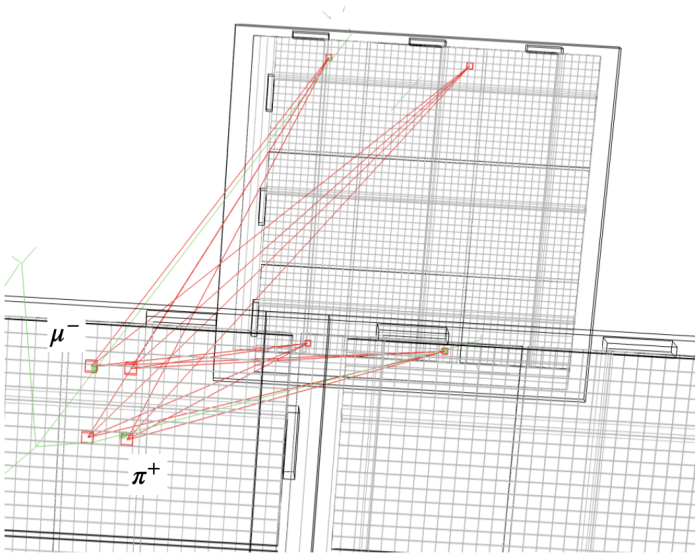


**Figure E.8** An event display demonstrating the remaining background after selections.

# Bibliography


[1] W. Pauli, "Pauli letter collection: letter to Lise Meitner".

[2] *Standard model*, https://www.physik.uzh.ch/en/groups/serra/outreach/StandardModel.html, Accessed: 2024-08-29.

[3] M. Kleesiek et al., "$\beta$-Decay Spectrum, Response Function and Statistical Model for Neutrino Mass Measurements with the KATRIN Experiment", Eur. Phys. J. C **79**, 204 (2019).

[4] J. S. Chadwick, "The existence of a neutron", Proceedings of The Royal Society A: Mathematical, Physical and Engineering Sciences **136**, 692–708 (1932).

[5] E. Fermi, "Tentativo di una teoria dei raggi beta", Nuovo Cimento 11 (1934) 1 **11**, 1–19 (1934).

[6] F. Perrin, "Possibilité d'émission de particules neutres de masse intrinsèque nulle dans les radioactivités beta", Comptes-Rendus 197 (1933) 1625 (1933).

[7] H. Bethe and R. Peierls, "The 'neutrino'", Nature **133**, 532 (1934).

[8] F. Reines and C. L. Cowan, "Detection of the free neutrino", Phys. Rev. **92**, 830–831 (1953).

[9] C. L. Cowan et al., "Detection of the free neutrino: A Confirmation", Science **124**, 103–104 (1956).

[10] B. Pontecorvo, "Inverse beta process", Camb. Monogr. Part. Phys. Nucl. Phys. Cosmol. **1**, 25–31 (1946).

[11] L. W. Alvarez, "A proposed experimental test of the neutrino theory", (1949) 10.2172/929771.

[12] R. Davis, "Nuclear recoil following neutrino emission from beryllium 7", Phys. Rev. **86**, 976–985 (1952).

[13] R. Davis Jr., "Attempt to detect the antineutrinos from a nuclear reactor by the Cl37(anti-nu,e-) A37 reaction", Phys. Rev. **97**, 766–769 (1955).

[14] M. Konopinski, "The universal fermi interaction", Phys. Rev. **92**, 1045–1049 (1953).

[15] S. H. Neddermeyer and C. D. Anderson, "Note on the nature of cosmic-ray particles", Phys. Rev. **51**, 884–886 (1937).

[16] J. C. Street and E. C. Stevenson, "New evidence for the existence of a particle of mass intermediate between the proton and electron", Phys. Rev. **52**, 1003–1004 (1937).

[17] Y. Nishina et al., "On the nature of cosmic-ray particles", Phys. Rev. **52**, 1198–1199 (1937).

[18]S. Sakata and T. Inoue, "Progress of theoretical physics 1", Phys. Rev., 143 (1946).

[19]M. Conversi et al., "On the disintegration of negative mesons", Phys. Rev. **71**, 209–210 (1947).

[20]G. Feinberg, "Decays of the mu Meson in the Intermediate-Meson Theory", Phys. Rev. **110**, 1482–1483 (1958).

[21]M. S. Athar and S. K. Singh, *The physics of neutrinos interactions* (Cambridge University Press, Cambridge, 2020).

[22]G. Danby et al., "Observation of high-energy neutrino reactions and the existence of two kinds of neutrinos", Phys. Rev. Lett. **9**, 36–44 (1962).

[23]M. L. Perl et al., "Evidence for Anomalous Lepton Production in e+ - e- Annihilation", Phys. Rev. Lett. **35**, 1489–1492 (1975).

[24]K. Kodama et al., "Observation of tau neutrino interactions", Phys. Lett. B **504**, 218–224 (2001).

[25]T. Patzak, "First direct observation of the tau-neutrino", Europhys. News **32**, 56–57 (2001).

[26]L. Di Lella and C. Rubbia, "The Discovery of the W and Z Particles", Adv. Ser. Direct. High Energy Phys. **23**, 137–163 (2015).

[27]S. Schael et al., "Precision electroweak measurements on the $Z$ resonance", Phys. Rept. **427**, 257–454 (2006).

[28]J. A. Formaggio and G. P. Zeller, "From ev to eev: neutrino cross sections across energy scales", Rev. Mod. Phys. **84**, 1307–1341 (2012).

[29]J. N. Bahcall, "Solar neutrinos. i. theoretical", Phys. Rev. Lett. **12**, 300–302 (1964).

[30]R. Davis, "A review of the homestake solar neutrino experiment", Progress in Particle and Nuclear Physics **32**, 13–32 (1994).

[31]K. Hirata et al., "Experimental study of the atmospheric neutrino flux", Physics Letters B **205**, 416–420 (1988).

[32]Y. Fukuda et al., "Evidence for oscillation of atmospheric neutrinos", Phys. Rev. Lett. **81**, 1562–1567 (1998).

[33]B. Pontecorvo, "Inverse beta processes and nonconservation of lepton charge", Zh. Eksp. Teor. Fiz. **34**, 247 (1957).

[34]Z. Maki et al., "Remarks on the unified model of elementary particles", Prog. Theor. Phys. **28**, 870–880 (1962).

[35]B. Pontecorvo, "Neutrino Experiments and the Problem of Conservation of Leptonic Charge", Zh. Eksp. Teor. Fiz. **53**, 1717–1725 (1967).

[36]A. Bellerive et al., "The sudbury neutrino observatory", Nuclear Physics B **908**, Neutrino Oscillations: Celebrating the Nobel Prize in Physics 2015, 30–51 (2016).

[37]T. Araki et al., "Measurement of neutrino oscillation with kamland: evidence of spectral distortion", Phys. Rev. Lett. **94**, 081801 (2005).

[38]M. Tanabashi et al., "Review of particle physics", Phys. Rev. D **98**, 030001 (2018).

[39]L. Wolfenstein, "Neutrino Oscillations in Matter", Phys. Rev. D **17**, 2369–2374 (1978).

[40]A. Y. Smirnov, "The Mikheyev-Smirnov-Wolfenstein (MSW) Effect", in International Conference on History of the Neutrino: 1930-2018 (Jan. 2019).

[41]K. J. Kelly, *The MiniBooNE Anomaly*, https://indico.ph.ed.ac.uk/event/107/contributions/1460/attachments/930/1259/KJK_SBNTH_Dec21.pdf, Mini SBN-Theory workshop, 2021.

[42]E. Richard et al., "Measurements of the atmospheric neutrino flux by super-kamiokande: energy spectra, geomagnetic effects, and solar modulation", Phys. Rev. D **94**, 052001 (2016).

[43]Y. Fukuda et al., "Measurement of the flux and zenith angle distribution of upward through going muons by Super-Kamiokande", Phys. Rev. Lett. **82**, 2644–2648 (1999).

[44]M. Guler et al., "An appearance experiment to search for $\nu_\mu$ $\nu_\tau$ oscillations in the CNGS beam: experimental proposal", CERN report (2000).

[45]N. Agafonova et al., "Observation of a first $\nu_\tau$ candidate event in the OPERA experiment in the CNGS beam", Physics Letters B **691**, 138–145 (2010).

[46]Q. R. Ahmad et al., "Measurement of the rate of $\nu_e + d \rightarrow p + p + e^-$ interactions produced by $^8$B solar neutrinos at the Sudbury Neutrino Observatory", Phys. Rev. Lett. **87**, 071301 (2001).

[47]Q. R. Ahmad et al., "Direct evidence for neutrino flavor transformation from neutral current interactions in the Sudbury Neutrino Observatory", Phys. Rev. Lett. **89**, 011301 (2002).

[48]P. A. Zyla et al., "Review of Particle Physics", PTEP **2020**, 083C01 (2020).

[49]B. Aharmim et al., "Combined analysis of all three phases of solar neutrino data from the sudbury neutrino observatory", Phys. Rev. C **88**, 025501 (2013).

[50]K. Eguchi et al., "First results from kamland: evidence for reactor antineutrino disappearance", Phys. Rev. Lett. **90**, 021802 (2003).

[51]F. P. An et al., "Observation of electron-antineutrino disappearance at Daya Bay", Phys. Rev. Lett. **108**, 171803 (2012).

[52]J. K. Ahn et al., "Observation of Reactor Electron Antineutrino Disappearance in the RENO Experiment", Phys. Rev. Lett. **108**, 191802 (2012).

[53]Y. Abe et al., "Indication of Reactor $\bar{\nu}_e$ Disappearance in the Double Chooz Experiment", Phys. Rev. Lett. **108**, 131801 (2012).

[54]P. A. M. Dirac and R. H. Fowler, "The quantum theory of the electron", Proceedings of the Royal Society of London. Series A, Containing Papers of a Mathematical and Physical Character **117**, 610–624 (1928).

[55]M. Goldhaber et al., "Helicity of Neutrinos", Phys. Rev. **109**, 1015–1017 (1958).

[56]D. Gorbunov and M. Shaposhnikov, "How to find neutral leptons of the $\nu$MSM?", JHEP **10**, [Erratum: JHEP 11, 101 (2013)], 015 (2007).

[57]E. Majorana, "Teoria simmetrica dell'elettrone e del positrone", Nuovo Cim. **14**, 171–184 (1937).

[58]M. Agostini et al., "Final Results of GERDA on the Search for Neutrinoless Double-$\beta$ Decay", Phys. Rev. Lett. **125**, 252502 (2020).

[59]S. Abe et al., "Search for the Majorana Nature of Neutrinos in the Inverted Mass Ordering Region with KamLAND-Zen", Phys. Rev. Lett. **130**, 051801 (2023).

[60]D. Q. Adams et al., "New Direct Limit on Neutrinoless Double Beta Decay Half-Life of Te128 with CUORE", Phys. Rev. Lett. **129**, 222501 (2022).

[61]J. J. Gomez-Cadenas, "The NEXT experiment", Nucl. Part. Phys. Proc. **273-275**, 1732–1739 (2016).

[62]N. Abgrall et al., "The Large Enriched Germanium Experiment for Neutrinoless Double Beta Decay (LEGEND)", AIP Conf. Proc. **1894**, edited by O. Civitarese et al., 020027 (2017).

[63]V. Albanese et al., "The SNO+ experiment", JINST **16**, P08059 (2021).

[64]Sakharov, A. D., "Violation of CP Invariance, C asymmetry, and baryon asymmetry of the universe", Pisma Zh. Eksp. Teor. Fiz. **5**, 32–35 (1967).

[65]C. S. Wu et al., "Experimental Test of Parity Conservation in Beta Decay", Phys. Rev. **105**, 1413–1415 (1957).

[66]J. H. Christenson et al., "Evidence for the $2\pi$ Decay of the $K_2^0$ Meson", Phys. Rev. Lett. **13**, 138–140 (1964).

[67]M. Kobayashi and T. Maskawa, "CP Violation in the Renormalizable Theory of Weak Interaction", Prog. Theor. Phys. **49**, 652–657 (1973).

[68]Fukugita, M. and Yanagida, T., "Baryogenesis Without Grand Unification", Phys. Lett. B **174**, 45–47 (1986).

[69]Davidson, Sacha and Nardi, Enrico and Nir, Yosef, "Leptogenesis", Phys. Rept. **466**, 105–177 (2008).

[70]V. Barger et al., "Matter effects on three-neutrino oscillations", Phys. Rev. D **22**, 2718–2726 (1980).

[71]S. F. King and C. Luhn, "Neutrino Mass and Mixing with Discrete Symmetry", Rept. Prog. Phys. **76**, 056201 (2013).

[72]A. Loureiro et al., "Upper bound of neutrino masses from combined cosmological observations and particle physics experiments", Phys. Rev. Lett. **123**, 081301 (2019).

[73]M. Aker et al., "Direct neutrino-mass measurement based on 259 days of KATRIN data", arXiv:2406.13516 (2024).

[74]F. Vissani, "Signal of neutrinoless double beta decay, neutrino spectrum and oscillation scenarios", JHEP **06**, 022 (1999).

[75]H. Päs and W. Rodejohann, "Neutrinoless Double Beta Decay", New J. Phys. **17**, 115010 (2015).

[76]M. A. Acero et al., "Improved measurement of neutrino oscillation parameters by the NOvA experiment", Phys. Rev. D **106**, 032004 (2022).

[77]K. Abe et al., "Measurements of neutrino oscillation parameters from the T2K experiment using $3.6 \times 10^{21}$ protons on target", Eur. Phys. J. C **83**, 782 (2023).

[78]J. Wolcott, "New NOvA results with 10 years of data", in XXXI International Conference on Neutrino Physics and Astrophysics (Aug. 2024).

[79]B. Abi et al., "Deep Underground Neutrino Experiment (DUNE), Far Detector Technical Design Report, Volume I Introduction to DUNE", JINST **15**, T08008 (2020).

[80]B. Abi et al., "Deep Underground Neutrino Experiment (DUNE), Far Detector Technical Design Report, Volume II: DUNE Physics", arXiv:2002.03005 (2020).

[81]K. Abe et al., "Hyper-Kamiokande Design Report", arXiv:1805.04163 (2018).

[82]A. Abusleme et al., "JUNO physics and detector", Prog. Part. Nucl. Phys. **123**, 103927 (2022).

[83]M. G. Aartsen et al., "Combined sensitivity to the neutrino mass ordering with JUNO, the IceCube Upgrade, and PINGU", Phys. Rev. D **101**, 032006 (2020).

[84]S. Adrian-Martinez et al., "Letter of intent for KM3NeT 2.0", J. Phys. G **43**, 084001 (2016).

[85]F. Kaether et al., "Reanalysis of the GALLEX solar neutrino flux and source experiments", Phys. Lett. B **685**, 47–54 (2010).

[86]J. N. Abdurashitov et al., "Measurement of the solar neutrino capture rate with gallium metal. III: Results for the 2002–2007 data-taking period", Phys. Rev. C **80**, 015807 (2009).

[87]G. Mention et al., "The Reactor Antineutrino Anomaly", Phys. Rev. D **83**, 073006 (2011).

[88]A. Aguilar et al., "Evidence for neutrino oscillations from the observation of $\bar{\nu}_e$ appearance in a $\bar{\nu}_\mu$ beam", Phys. Rev. D **64**, 112007 (2001).

[89]M. Sorel et al., "Combined analysis of short-baseline neutrino experiments in the $(3+1)$ and $(3+2)$ sterile neutrino oscillation hypotheses", Phys. Rev. D **70**, 073004 (2004).

[90]G. Karagiorgi et al., "Viability of Delta m**2 ~ 1- eV**2 sterile neutrino mixing models in light of MiniBooNE electron neutrino and antineutrino data from the Booster and NuMI beamlines", Phys. Rev. D **80**, [Erratum: Phys.Rev.D 81, 039902 (2010)], 073001 (2009).

[91]S. Gariazzo et al., "Updated Global 3+1 Analysis of Short-BaseLine Neutrino Oscillations", JHEP **06**, 135 (2017).

[92]A. A. Aguilar-Arevalo et al., "The MiniBooNE Detector", Nucl. Instrum. Meth. A **599**, 28–46 (2009).

[93]A. A. Aguilar-Arevalo et al., "A Search for Electron Neutrino Appearance at the $\Delta m^2 \sim 1eV^2$ Scale", Phys. Rev. Lett. **98**, 231801 (2007).

[94]A. A. Aguilar-Arevalo et al., "Updated MiniBooNE neutrino oscillation results with increased data and new background studies", Phys. Rev. D **103**, 052002 (2021).

[95]P. Abratenko et al., "Measurement of the flux-averaged inclusive charged-current electron neutrino and antineutrino cross section on argon using the NuMI beam and the MicroBooNE detector", Phys. Rev. D **104**, 052002 (2021).

[96]P. Abratenko et al., "Search for Neutrino-Induced Neutral-Current Δ Radiative Decay in MicroBooNE and a First Test of the MiniBooNE Low Energy Excess under a Single-Photon Hypothesis", Phys. Rev. Lett. **128**, 111801 (2022).

[97]P. Abratenko et al., "Search for an anomalous excess of inclusive charged-current $\nu_e$ interactions in the MicroBooNE experiment using Wire-Cell reconstruction", Phys. Rev. D **105**, 112005 (2022).

[98]P. Abratenko et al., "Search for an anomalous excess of charged-current quasielastic $\nu$e interactions with the MicroBooNE experiment using Deep-Learning-based reconstruction", Phys. Rev. D **105**, 112003 (2022).

[99]P. Abratenko et al., "Search for an anomalous excess of charged-current $\nu$e interactions without pions in the final state with the MicroBooNE experiment", Phys. Rev. D **105**, 112004 (2022).

[100]P. Abratenko et al., "Search for an Excess of Electron Neutrino Interactions in MicroBooNE Using Multiple Final-State Topologies", Phys. Rev. Lett. **128**, 241801 (2022).

[101]The MicroBooNE Collaboration, "First search for an anomalous excess of charged-current $\nu_e$ interactions without visible pions using the full MicroBooNE dataset", MICROBOONE-NOTE-1127-PUB1 (2024).

[102]The MicroBooNE Collaboration, "Search for anomalous neutral current coherent-like single-photon production in MicroBooNE", MICROBOONE-NOTE-1131-PUB (2024).

[103]The MicroBooNE Collaboration, "Progress towards an expanded search for neutral-current delta radiative decays in microboone", MICROBOONE-NOTE-1126-PUB (2024).

[104]The MicroBooNE Collaboration, "An update on MicroBooNE's inclusive single photon low energy excess search", MICROBOONE-NOTE-1125-PUB (2024).

[105]P. Abratenko et al., "First Constraints on Light Sterile Neutrino Oscillations from Combined Appearance and Disappearance Searches with the MicroBooNE Detector", Phys. Rev. Lett. **130**, 011801 (2023).

[106]E. Bertuzzo et al., "Dark neutrino portal to explain MiniBooNE excess", Physical Review Letters **121** (2018) 10.1103/physrevlett.121.241801.

[107]A. Cooper-Sarkar et al., "Search for heavy neutrino decays in the bebc beam dump experiment", Physics Letters B **160**, 207–211 (1985).

[108]P. Ilten et al., "Serendipity in dark photon searches", JHEP **06**, 004 (2018).

[109]A. Atre et al., "The Search for Heavy Majorana Neutrinos", JHEP **05**, 030 (2009).

[110]A. de Gouvêa and A. Kobach, "Global Constraints on a Heavy Neutrino", Phys. Rev. D **93**, 033005 (2016).

[111]G. Bernardi et al., "Further limits on heavy neutrino couplings", Physics Letters B **203**, 332–334 (1988).

[112]A. Vaitaitis et al., "Search for neutral heavy leptons in a high-energy neutrino beam", Phys. Rev. Lett. **83**, 4943–4946 (1999).

[113]E. Gallas et al., "Search for neutral weakly interacting massive particles in the fermilab tevatron wideband neutrino beam", Phys. Rev. D **52**, 6–14 (1995).

[114]P. Vilain et al., "Search for heavy isosinglet neutrinos", Physics Letters B **343**, 453–458 (1995).

[115]G. W. Bennett et al., "Final report of the e821 muon anomalous magnetic moment measurement at bnl", Phys. Rev. D **73**, 072003 (2006).

[116]B. Abi et al., "Measurement of the positive muon anomalous magnetic moment to 0.46 ppm", Phys. Rev. Lett. **126**, 141801 (2021).

[117]A. M. Abdullahi et al., "The present and future status of heavy neutral leptons", J. Phys. G **50**, 020501 (2023).

[118]K. J. Kelly et al., "Heavy axion opportunities at the DUNE near detector", Phys. Rev. D **103**, 095002 (2021).

[119]V. Brdar et al., "Axionlike Particles at Future Neutrino Experiments: Closing the Cosmological Triangle", Phys. Rev. Lett. **126**, 201801 (2021).

[120]B. Patt and F. Wilczek, "Higgs-field portal into hidden sectors", arXiv:hep-ph/0605188 (2006).

[121]B. Batell et al., "Keeping it simple: simplified frameworks for long-lived particles at neutrino facilities", JHEP **08**, 092 (2023).

[122]P. Abratenko et al., "Search for a higgs portal scalar decaying to electron-positron pairs in the microboone detector", Phys. Rev. Lett. **127**, 151803 (2021).

[123]K. Abe et al., "Search for heavy neutrinos with the T2K near detector ND280", Phys. Rev. D **100**, 052006 (2019).

[124]P. Coloma et al., "New constraints on Heavy Neutral Leptons from Super-Kamiokande data", Eur. Phys. J. C **80**, 235 (2020).

[125]A. V. Artamonov et al., "Study of the decay $K^+ \to \pi^+ \nu\bar{\nu}$ in the momentum region $140 < P_\pi < 199$ MeV/c", Phys. Rev. D **79**, 092004 (2009).

[126]A. V. Artamonov et al., "Search for heavy neutrinos in $K^+ \to \mu^+ \nu_H$ decays", Phys. Rev. D **91**, [Erratum: Phys.Rev.D 91, 059903 (2015)], 052001 (2015).

[127]E. Cortina Gil et al., "Search for heavy neutral lepton production in K+ decays to positrons", Phys. Lett. B **807**, 135599 (2020).

[128]E. Cortina Gil et al., "Search for a feebly interacting particle $X$ in the decay $K^+ \to \pi^+ X$", JHEP **03**, 058 (2021).

[129]E. Cortina Gil et al., "Search for $K^+$ decays to a muon and invisible particles", Phys. Lett. B **816**, 136259 (2021).

[130]C. Anderson et al., "The ArgoNeuT detector in the NuMI low-energy beam line at Fermilab", Journal of Instrumentation **7**, P10019 (2012).

[131]M. G. Schorr and F. L. Torney, "Solid non-crystalline scintillation phosphors", Phys. Rev. **80**, 474–474 (1950).

[132]P. A. Amaudruz et al., "The T2K Fine-Grained Detectors", Nucl. Instrum. Meth. A **696**, 1–31 (2012).

[133]M. Auger et al., "A Novel Cosmic Ray Tagger System for Liquid Argon TPC Neutrino Detectors", Instruments **1**, 2 (2017).

[134]S. Berns et al., "A novel polystyrene-based scintillator production process involving additive manufacturing", JINST **15**, 10 (2020).

[135]T. Poschl et al., "Measurement of ionization quenching in plastic scintillators", Nuclear Instruments and Methods in Physics Research Section A: Accelerators, Spectrometers, Detectors and Associated Equipment **988**, 164865 (2021).

[136]J. B. Birks, "Scintillations from organic crystals: specific fluorescence and relative response to different radiations", Proceedings of the Physical Society. Section A **64**, 874 (1951).

[137]C. N. Chou, "The nature of the saturation effect of fluorescent scintillators", Phys. Rev. **87**, 904–905 (1952).

[138]G. T. Wright, "Scintillation response of organic phosphors", Phys. Rev. **91**, 1282–1283 (1953).

[139]R. Voltz et al., "Influence of the Nature of Ionizing Particles on the Specific Luminescence of Organic Scintillators", The Journal of Chemical Physics **45**, 3306–3311 (1966).

[140]T. Doke, "Fundamental Properties of Liquid Argon, Krypton and Xenon as Radiation Detector Media", Portugal. Phys. **12**, 9–48 (1981).

[141]E. Morikawa et al., "Argon, krypton, and xenon excimer luminescence: From the dilute gas to the condensed phase", The Journal of Chemical Physics **91**, 1469–1477 (1989).

[142]A. Hitachi et al., "Effect of ionization density on the time dependence of luminescence from liquid argon and xenon", Phys. Rev. B **27**, 5279–5285 (1983).

[143]S. Kubota et al., "Dynamical behavior of free electrons in the recombination process in liquid argon, krypton, and xenon", Phys. Rev. B **20**, 3486–3496 (1979).

[144]H. Cao et al., "Measurement of Scintillation and Ionization Yield and Scintillation Pulse Shape from Nuclear Recoils in Liquid Argon", Phys. Rev. D **91**, 092007 (2015).

[145]M. G. Boulay and A. Hime, "Technique for direct detection of weakly interacting massive particles using scintillation time discrimination in liquid argon", Astropart. Phys. **25**, 179–182 (2006).

[146]P. J. Green, "Light and Dark in Liquid Argon Time Projection Chamber Neutrino Detectors", PhD thesis (Manchester U., Manchester U., 2022).

[147]E. Grace and J. A. Nikkel, "Index of refraction, Rayleigh scattering length, and Sellmeier coefficients in solid and liquid argon and xenon", Nucl. Instrum. Meth. A **867**, 204–208 (2017).

[148]P. Agnes et al., "Simulation of argon response and light detection in the DarkSide-50 dual phase TPC", JINST **12**, P10015 (2017).

[149]A. Neumeier et al., "Attenuation measurements of vacuum ultraviolet light in liquid argon revisited", Nucl. Instrum. Meth. A **800**, 70–81 (2015).

[150]M. Babicz et al., "A measurement of the group velocity of scintillation light in liquid argon", JINST **15**, P09009 (2020).

[151]S. Himi et al., "LIQUID AND SOLID ARGON, AND NITROGEN DOPED LIQUID AND SOLID ARGON SCINTILLATORS", Nucl. Instrum. Meth. **203**, 153–157 (1982).

[152]R. Acciarri et al., "Effects of Nitrogen contamination in liquid Argon", JINST **5**, P06003 (2010).

[153]B. J. P. Jones et al., "A measurement of the absorption of liquid argon scintillation light by dissolved nitrogen at the part-per-million level", Journal of Instrumentation **8**, P07011–P07011 (2013).

[154]R. Acciarri et al., "Effects of nitrogen and oxygen contamination in liquid argon", Nuclear Physics B - Proceedings Supplements **197**, 11th Topical Seminar on Innovative Particle and Radiation Detectors (IPRD08), 70–73 (2009).

[155]M. Miyajima et al., "Average energy expended per ion pair in liquid argon", Phys. Rev. A **9**, 1438–1443 (1974).

[156]E. Shibamura et al., "Drift velocities of electrons, saturation characteristics of ionization and W-values for conversion electrons in liquid argon, liquid argon-gas mixtures and liquid xenon", Nucl. Instrum. Meth. **131**, 249–258 (1975).

[157]L. Onsager, "Initial recombination of ions", Phys. Rev. **54**, 554–557 (1938).

[158]R. Acciarri et al., "A Study of Electron Recombination Using Highly Ionizing Particles in the ArgoNeuT Liquid Argon TPC", JINST **8**, P08005 (2013).

[159]P. Cennini et al., "Performance of a three-ton liquid argon time projection chamber", Nuclear Instruments and Methods in Physics Research Section A: Accelerators, Spectrometers, Detectors and Associated Equipment **345**, 230–243 (1994).

[160]J. Thomas and D. A. Imel, "Recombination of electron-ion pairs in liquid argon and liquid xenon", Phys. Rev. A **36**, 614–616 (1987).

[161]Y. Li et al., "Measurement of longitudinal electron diffusion in liquid argon", Nuclear Instruments and Methods in Physics Research Section A: Accelerators, Spectrometers, Detectors and Associated Equipment **816**, 160–170 (2016).

[162]P. Abratenko et al., "Measurement of the longitudinal diffusion of ionization electrons in the MicroBooNE detector", JINST **16**, P09025 (2021).

[163]V. Atrazhev and I. Timoshkin, "Transport of electrons in atomic liquids in high electric fields", IEEE Transactions on Dielectrics and Electrical Insulation **5**, 450–457 (1998).

[164]N. Gee et al., "Ion and electron mobilities in cryogenic liquids: Argon, nitrogen, methane, and ethane", Journal of Applied Physics **57**, 1097–1101 (1985).

[165]P. Abratenko et al., "Measurement of space charge effects in the MicroBooNE LArTPC using cosmic muons", JINST **15**, P12037 (2020).

[166]V. M. Basque, "Understanding and Enhancing The Performance of LArTPC Neutrino Detectors for Neutrino Measurements and Beyond the Standard Model Searches", PhD thesis (Manchester U., Manchester U., 2021).

[167]R. Acciarri et al., "Oxygen contamination in liquid Argon: Combined effects on ionization electron charge and scintillation light", JINST **5**, P05003 (2010).

[168]A. Bettini et al., "A Study of the factors affecting the electron lifetime in ultrapure liquid argon", Nucl. Instrum. Meth. A **305**, 177–186 (1991).

[169]P. A. Machado et al., "The Short-Baseline Neutrino Program at Fermilab", Annual Review of Nuclear and Particle Science **69**, 363–387 (2019).

[170]A. A. Aguilar-Arevalo et al., "The Neutrino Flux Prediction at MiniBooNE", Phys. Rev. D **79**, 072002 (2009).

[171]B. Pontecorvo, "Electron and Muon Neutrinos", Zh. Eksp. Teor. Fiz. **37**, 1751–1757 (1959).

[172]R. Acciarri et al., "A Proposal for a Three Detector Short-Baseline Neutrino Oscillation Program in the Fermilab Booster Neutrino Beam", arxiv:1503.01520 (2015).

[173]M. G. Catanesi et al., "Measurement of the production cross-section of positive pions in the collision of 8.9-GeV/c protons on beryllium", Eur. Phys. J. C **52**, 29–53 (2007).

[174]R. A and T. R. H., "SKYSHINE-A PAPERTIGER?", Particle Accelerators **7**, 23–39 (1975).

[175]C. Llewellyn Smith, "Neutrino reactions at accelerator energies", Physics Reports **3**, 261–379 (1972).

[176]A. A. Aguilar-Arevalo et al., "Bringing the SciBar detector to the booster neutrino beam", FERMILAB-PROPOSAL-0954 (2006).

[177]C. Rubbia, "The Liquid Argon Time Projection Chamber: A New Concept for Neutrino Detectors", EP Internal Report 77-8 (1977).

[178]J. N. Marx and D. R. Nygren, "The Time Projection Chamber", Physics Today **31**, 46–53 (1978).

[179]D. R. Nygren, "Origin and development of the TPC idea", Nucl. Instrum. Meth. A **907**, 22–30 (2018).

[180]W. J. Willis and V. Radeka, "Liquid Argon Ionization Chambers as Total Absorption Detectors", Nucl. Instrum. Meth. **120**, 221–236 (1974).

[181]R. Acciarri et al., "Design and Construction of the MicroBooNE Detector", JINST **12**, P02017 (2017).

[182]B. Abi et al., "First results on ProtoDUNE-SP liquid argon time projection chamber performance from a beam test at the CERN Neutrino Platform", JINST **15**, P12004 (2020).

[183]R. Acciarri et al., "Construction of precision wire readout planes for the Short-Baseline Near Detector (SBND)", JINST **15**, P06033 (2020).

[184]P. Abratenko et al., "First demonstration of O(1 ns) timing resolution in the MicroBooNE liquid argon time projection chamber", Phys. Rev. D **108**, 052010 (2023).

[185]The MicroBooNE Collaboration, "Establishing a Pure Sample of Side-Piercing Through-Going Cosmic-Ray Muons for LArTPC Calibration in MicroBooNE", MICROBOONE-NOTE-1028-PUB.

[186]R. Acciarri et al., "Noise Characterization and Filtering in the MicroBooNE Liquid Argon TPC", JINST **12**, P08003 (2017).

[187]C. Adams et al., "Calibration of the charge and energy loss per unit length of the MicroBooNE liquid argon time projection chamber using muons and protons", JINST **15**, P03022 (2020).

[188]A. Smith, "Measurement of the muon-neutrino charged-current single charged-pion cross-section on argon with the microboone detector", PhD thesis (Apollo - University of Cambridge Repository, 2021).

[189]W. Foreman et al., "Calorimetry for low-energy electrons using charge and light in liquid argon", Phys. Rev. D **101**, 012010 (2020).

[190]The MicroBooNE Collaboration, "PMT Gain Calibration In MicroBooNE", MICROBOONE-NOTE-1064-TECH.

[191]T. Briese et al., "Testing of Cryogenic Photomultiplier Tubes for the MicroBooNE Experiment", JINST **8**, T07005 (2013).

[192]M. Adamowski et al., "Development of cryogenic installations for large liquid argon neutrino detectors", IOP Conf. Ser. Mater. Sci. Eng. **101**, edited by P. Kittel and M. Sumption, 012029 (2015).

[193]P. Abratenko et al., "Scintillation light in SBND: simulation, reconstruction, and expected performance of the photon detection system", Eur. Phys. J. C **84**, 1046 (2024).

[194]A. Machado et al., "The X-ARAPUCA: an improvement of the ARAPUCA device", JINST **13**, C04026–C04026 (2018).

[195]H. V. Souza et al., "Liquid argon characterization of the X-ARAPUCA with alpha particles, gamma rays and cosmic muons", JINST **16**, P11002 (2021).

[196]E. L. Snider and G. Petrillo, "LArSoft: Toolkit for Simulation, Reconstruction and Analysis of Liquid Argon TPC Neutrino Detectors", J. Phys. Conf. Ser. **898**, edited by R. Mount and C. Tull, 042057 (2017).

[197]C. Green et al., "The art framework", Journal of Physics: Conference Series **396**, 022020 (2012).

[198]R. Brun and F. Rademakers, "Root — an object oriented data analysis framework", Nuclear Instruments and Methods in Physics Research Section A: Accelerators, Spectrometers, Detectors and Associated Equipment **389**, New Computing Techniques in Physics Research V, 81–86 (1997).

[199]C. Andreopoulos et al., "The GENIE Neutrino Monte Carlo Generator", Nucl. Instrum. Meth. A **614**, 87–104 (2010).

[200]D. Heck et al., "CORSIKA: A Monte Carlo code to simulate extensive air showers", FZKA-6019 (1998).

[201]S. Agostinelli et al., "GEANT4–a simulation toolkit", Nucl. Instrum. Meth. A **506**, 250–303 (2003).

[202]R. Chytracek et al., "Geometry description markup language for physics simulation and analysis applications", IEEE Transactions on Nuclear Science **53**, 2892–2896 (2006).

[203]C. Adams et al., "Measurement of the atmospheric muon rate with the MicroBooNE Liquid Argon TPC", JINST **16**, P04004 (2021).

[204]C. Andreopoulos et al., "The GENIE Neutrino Monte Carlo Generator: Physics and User Manual", arXiv:1510.05494 (2015).

[205]O. Buss et al., "Transport-theoretical description of nuclear reactions", Physics Reports **512**, Transport-theoretical Description of Nuclear Reactions, 1–124 (2012).

[206]Y. Hayato, "A neutrino interaction simulation program library NEUT", Acta Phys. Polon. B **40**, edited by A. Ankowski and J. Sobczyk, 2477–2489 (2009).

[207]J. Zmuda et al., "NuWro Monte Carlo generator of neutrino interactions - first electron scattering results", Acta Phys. Polon. B **46**, 2329 (2015).

[208]J. Tena-Vidal et al., "Neutrino-nucleus CC0$\pi$ cross-section tuning in GENIE v3", Phys. Rev. D **106**, 112001 (2022).

[209]R. S. Jones, "Muon-neutrino disappearance with multiple liquid argon time projection chambers in the Fermilab Booster neutrino beam.", PhD thesis (U. Liverpool (main), University of Liverpool, Liverpool U., 2021).

[210]L. Alvarez-Ruso et al., "Recent highlights from GENIE v3", Eur. Phys. J. ST **230**, 4449–4467 (2021).

[211]J. Nieves et al., "Inclusive Charged–Current Neutrino–Nucleus Reactions", Phys. Rev. C **83**, 045501 (2011).

[212]C. Berger and L. M. Sehgal, "Lepton mass effects in single pion production by neutrinos", Phys. Rev. D **76**, 113004 (2007).

[213]A. Bodek and U. K. Yang, "Higher twist, xi(omega) scaling, and effective LO PDFs for lepton scattering in the few GeV region", J. Phys. G **29**, edited by K. Long and R. Edgecock, 1899–1906 (2003).

[214]T. Yang et al., "A Hadronization Model for Few-GeV Neutrino Interactions", Eur. Phys. J. C **63**, 1–10 (2009).

[215]T. Katori and S. Mandalia, "PYTHIA hadronization process tuning in the GENIE neutrino interaction generator", J. Phys. G **42**, 115004 (2015).

[216]A. M. Abdullahi et al., "DarkNews: A Python-based event generator for heavy neutral lepton production in neutrino-nucleus scattering", Comput. Phys. Commun. **297**, 109075 (2024).

[217]J. Li and M. Del Tutto, *Searching for Dark Neutrinos in the SBND Beam Telescope*, SBND internal slides, 2024.

[218]D. H. Wright and M. H. Kelsey, "The Geant4 Bertini Cascade", Nucl. Instrum. Meth. A **804**, 175–188 (2015).

[219]J. Yarba, "Recent developments and validation of Geant4 hadronic physics", J. Phys. Conf. Ser. **396**, edited by M. Ernst et al., 022060 (2012).

[220]G. Folger and J. P. Wellisch, "String parton models in GEANT4", eConf **C0303241**, MOMT007 (2003).

[221]R. Veenhof, "Garfield, recent developments", Nuclear Instruments and Methods in Physics Research Section A: Accelerators, Spectrometers, Detectors and Associated Equipment **419**, 726–730 (1998).

[222]C. Adams et al., "Ionization electron signal processing in single phase lartpcs. part i. algorithm description and quantitative evaluation with microboone simulation", Journal of Instrumentation **13**, P07006 (2018).

[223]The MicroBooNE Collaboration, "Novel approach for evaluating detector systematics in the MicroBooNE LArTPC", MICROBOONE-NOTE-1075-PUB.

[224]D. Garcia-Gamez et al., "Predicting Transport Effects of Scintillation Light Signals in Large-Scale Liquid Argon Detectors", Eur. Phys. J. C **81**, 349 (2021).

[225]T. K. Gaisser and A. M. Hillas, "Reliability of the method of constant intensity cuts for reconstructing the average development of vertical showers", in International cosmic ray conference, 8 vols. (January 1977), p. 353.

[226]J. S. Marshall and M. A. Thomson, "The Pandora Software Development Kit for Pattern Recognition", Eur. Phys. J. C **75**, 439 (2015).

[227]R. Acciarri et al., "The Pandora multi-algorithm approach to automated pattern recognition of cosmic-ray muon and neutrino events in the MicroBooNE detector", Eur. Phys. J. C **78**, 82 (2018).

[228]H. Bichsel, "Straggling in thin silicon detectors", Rev. Mod. Phys. **60**, 663–699 (1988).

[229]S. Berkman et al., *Measurement of $\nu_e$ interactions at low energy with the MicroBooNE Experiment*, MicroBooNE internal note.

[230]M. Del Tutto, "First Measurements of Inclusive Muon Neutrino Charged Current Differential Cross Sections on Argon at 0.8 GeV Average Neutrino Energy with the MicroBooNE Detector", PhD thesis (Oxford U., 2019).

[231]P. Abratenko et al., "Calorimetric classification of track-like signatures in liquid argon tpcs using microboone data", Journal of High Energy Physics **2021** (2021) 10.1007/JHEP12(2021)153.

[232]The MicroBooNE Collaboration, "Measuring light yield with isolated protons in MicroBooNE", MICROBOONE-NOTE-1119-PUB.

[233]C. Adams et al., "A method to determine the electric field of liquid argon time projection chambers using a UV laser system and its application in MicroBooNE", JINST **15**, P07010 (2020).

[234]The MicroBooNE Collaboration, "Novel Approach for Evaluating Detector Systematics in the MicroBooNE LArTPC", MICROBOONE-NOTE-1075-PUB.

[235]*Plastic scintillating fibers*, https://www.kuraray.com/uploads/5a717515df6f5/PR0150_psf01.pdf, Accessed: 2024-11-11.

[236]*Hamamatsu s12825-050p*, http://www.hamamatsu.com/jp/en/S12571-050P.html, Accessed: 2023-09-13.

[237]C. Adams et al., "Design and construction of the MicroBooNE Cosmic Ray Tagger system", JINST **14**, P04004 (2019).

[238]M. Auger et al., "Multi-channel front-end board for SiPM readout", JINST **11**, P10005 (2016).

[239]J. Fleury et al., "Petiroc and Citiroc: front-end ASICs for SiPM read-out and ToF applications", JINST **9**, C01049 (2014).

[240]*Amd/xilinx spartan 6 fpgas*, https://www.amd.com/en/products/adaptive-socs-and-fpgas/fpga/spartan-6.html, Accessed: 2024-11-11.

[241]The SBND Collaboration, *SBND Cosmic Ray Tagger Beam Telescope Test Setup*, SBND internal note.

[242]K. Biery et al., "Flexible and Scalable Data-Acquisition Using the artdaq Toolkit", in 21st IEEE Real Time Conference (June 2018).

[243]*CAEN V1730 Reference*, https://www.caen.it/products/v1730/, Accessed: 2024-11-11.

[244]G. V. Stenico, "SBND Trigger System: Status and MTC/A Configuration", Physical Sciences Forum **8** (2023) 10.3390/psf2023008060.

[245]T. Kroupova, "SBND Hardware Trigger System", PoS **TAUP2023**, 190 (2024).

[246]*TSpectrum Class Reference*, https://root.cern.ch/doc/master/classTSpectrum.html, Accessed: 2023-09-13.

[247]I. Kreslo et al., *SBND Cosmic Ray Tracker Design and Performance Technical Note*, SBND internal note, 2019.

[248]A. Mastbaum and M. Del Tutto, *SBND Cosmic Ray Tracker Simulation*, SBND internal note, 2022.

[249]A. Aloisio et al., "FPGA implementation of a high-resolution time-to-digital converter", in 2007 ieee nuclear science symposium conference record, Vol. 1 (2007), pp. 504–507.

[250]I. Kreslo, *Fist CRT Measurements in SBND Building*, SBND Internal Slides, 2017.

[251]K. Albertsson et al., "Machine Learning in High Energy Physics Community White Paper", J. Phys. Conf. Ser. **1085**, 022008 (2018).

[252]A. Hoecker et al., "TMVA - Toolkit for Multivariate Data Analysis", arXiv:physics/0703039 (2009).

[253]H. G. Lay, "Preparing for Precision: Neutral Current Neutral Pion Production in the Short-Baseline Near Detector", PhD thesis (Lancaster University, 2024).

[254]J. Calcutt et al., "Geant4Reweight: a framework for evaluating and propagating hadronic interaction uncertainties in Geant4", Journal of Instrumentation **16**, P08042 (2021).

[255]A. A. Aguilar-Arevalo et al., "Neutrino flux prediction at MiniBooNE", Phys. Rev. D **79**, 072002 (2009).

[256]L. Heinrich et al., *Pyhf: v0.7.6, version 0.7.6*, 2021.

[257]L. Heinrich et al., *Pyhf: pure-python implementation of HistFactory statistical models*, 2021.

[258]G. Cowan et al., "Asymptotic formulae for likelihood-based tests of new physics", Eur. Phys. J. C **71**, [Erratum: Eur.Phys.J.C 73, 2501 (2013)], 1554 (2011).

[259]T. Junk, "Confidence level computation for combining searches with small statistics", Nuclear Instruments and Methods in Physics Research Section A: Accelerators, Spectrometers, Detectors and Associated Equipment **434**, 435–443 (1999).

[260] A. L. Read, "Presentation of search results: the CLs technique", Journal of Physics G: Nuclear and Particle Physics **28**, 2693 (2002).